

Report 4241

A STATISTICAL DESCRIPTION OF PRESSURE AND VELOCITY FIELDS AT THE TRAILING EDGES OF A FLAT STRUT

ADA 028771

DAVID W. TAYLOR NAVAL SHIP RESEARCH AND DEVELOPMENT CENTER

Bethesda, Md. 20884



12
P.S.

A STATISTICAL DESCRIPTION OF PRESSURE AND VELOCITY
FIELDS AT THE TRAILING EDGES OF A FLAT STRUT

by
William K. Blake



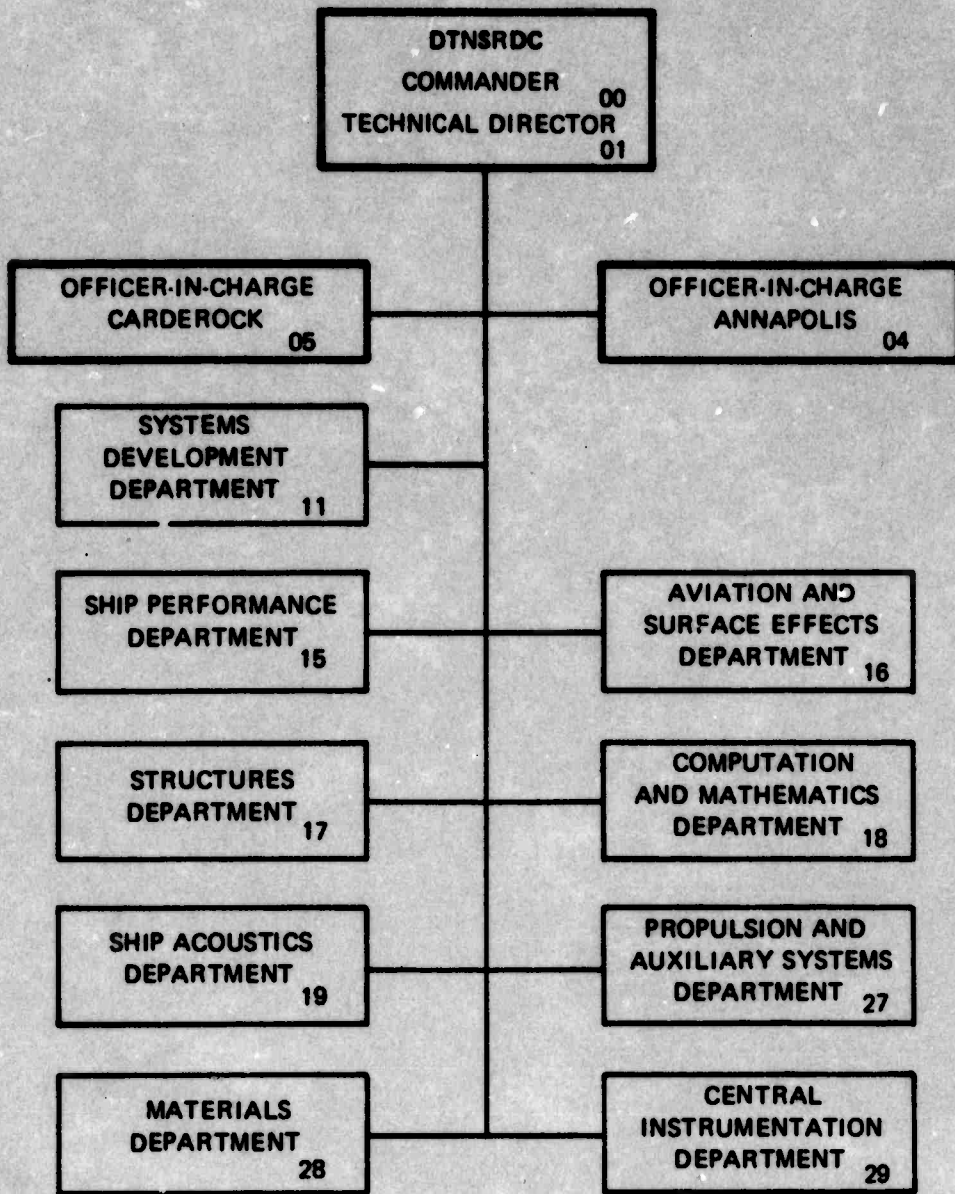
APPROVED FOR PUBLIC RELEASE: DISTRIBUTION UNLIMITED

SHIP ACOUSTICS DEPARTMENT
RESEARCH AND DEVELOPMENT REPORT

December 1975

Report 4241

MAJOR DTNSRDC ORGANIZATIONAL COMPONENTS



ACCESSION BY	
NTIS	Write Section <input checked="" type="checkbox"/>
DOC	Buff Section <input type="checkbox"/>
UNANNOUNCED	<input type="checkbox"/>
JUSTIFICATION	
BY	
DISTRIBUTION/AVAILABILITY CODES	
Orig.	Avail. end/or SPECIAL
A	

UNCLASSIFIED

SECURITY CLASSIFICATION OF THIS PAGE(When Data Entered)

(Block 10)

Task 18184, Work Unit 1-1942-080
Subproject SF43-452-702
Work Unit 1-1942-069
Subproject ZR.011 08 01

(Block 20 continued)

boundary-layer characteristics; streamwise turbulence intensities; and fluctuating surface pressures have been spatially mapped in the region of each edge. Correspondence between surface pressures and turbulent fields in both the immediate vicinity and the far wake of each edge were determined by correlation analyses. Results show a mechanism of pressure production which is common to both random and periodic pressures. They also indicate that the mechanism differs from that which produces attached boundary-layer--wall-pressure fluctuations. The level and chordwise variations of periodic pressures are shown to be determined, through a nearly unique functional form, by the strength and formation length of vortices. Furthermore, the vortex shedding frequency is shown to be expressible in alternative dimensionless forms based on either near- or far-wake variables. In the cases of random wake generation, the surface pressures are generated by both a large-scale eddy structure and a smaller scale convected field. The large eddies are formed in the separation process at the edge; but they do not form the coherent wavelike wake structure which is shown to be necessary for the generation of periodic pressures. Although the broadband intensities of the turbulence in the near wakes of both types of edge have been found to be comparable, a coherent wake structure is seen to exist behind only those edges sustaining periodic pressures.

UNCLASSIFIED

SECURITY CLASSIFICATION OF THIS PAGE(When Data Entered)

TABLE OF CONTENTS

	Page
ADMINISTRATIVE INFORMATION	1
1. INTRODUCTION	1
2. FACILITY AND INSTRUMENT DESCRIPTIONS	5
2.1 STRUT AND TRAILING EDGES	6
2.2 INSTRUMENTATION	6
2.3 STATISTICAL PRECISION	9
3. CHARACTERISTICS OF FLOW INCIDENT ON EDGES	10
4. PRESSURES AND VELOCITIES GENERATED BY PERIODIC VORTEX STREETS	17
4.1 WAKES OF BLUNT TRAILING EDGES	17
4.2 WAKE BEHIND 45-DEGREE--ROUNDED-BEVELED TRAILING EDGE	25
4.3 CHORDWISE DISTRIBUTION OF FLUCTUATING PRESSURE	31
4.4 VORTEX SHEDDING FREQUENCY: UNIVERSAL STROUHAL NUMBERS	33
4.5 SUMMARY: PERIODIC VORTEX STREETS	38
5. SEPARATED FLOW AT BEVELED TRAILING EDGES	39
5.1 TURBULENT FLOW NEAR 25-DEGREE--KNUCKLE- BEVELED EDGE	39
5.2 TURBULENT FLOW NEAR 25-DEGREE--ROUNDED- BEVELED EDGE	46
6. PRESSURE FLUCTUATIONS ON NONSINGING EDGES	49
6.1 PRESSURES ON 25-DEGREE--ROUNDED- BEVELED EDGE	49
6.2 PRESSURES ON 25-DEGREE--KNUCKLE-BEVELED EDGE	58
7. SUMMARY: TRAILING EDGES AND UNSTEADY PRESSURES	65
APPENDIX A - VARIANCE OF ESTIMATE OF CROSS SPECTRAL DENSITY	129
APPENDIX B - DIMENSIONLESS PROFILES OF MEAN AND TURBULENT VELOCITIES	133

	Page
APPENDIX C - STABILITY ANALYSIS OF WAKES	141
ACKNOWLEDGMENTS	147
REFERENCES	152

LIST OF FIGURES

1 - Strut, Showing Orientation of Trailing Edges and Locations of Microphones	69
2 - Ratio of Response of Probe Tubes to Response of a 1/2-Inch Microphone	70
3 - Relative Phases between Probe Microphones with Damping and a 1/2-Inch Microphone Reference	71
4 - Standard Deviation of Cross Spectral Density of Uncorrelated Random-Noise Signals	72
5 - Cross-Section Shape and Static Pressure Distribution on Strut with 25-Degree--Rounded-Beveled Edge	73
6 - Mean and Turbulent Velocity Profiles for Positions 4, Open Points, and B, Closed Points, on Strut with 25-Degree--Rounded-Trailing Edge	74
7 - Spectra of Longitudinal Turbulent Velocity at Position B on Knuckle Edge at $U_{\infty} = 100$ Feet per Second	75
8 - Normalized Mean Velocity Profiles Incident on Trailing Edges	76
9 - Narrowband Mean-Square Pressures, Measured in 62.5-Hertz Bands at Forward Chordwise Locations of Knuckle-Trailing Edge at $U_{\infty} = 50$ Feet per Second	77
10 - Narrowband Mean-Square Pressures, Measured in 62.5-Hertz Bands at Chordwise Locations Forward of Knuckle-Trailing Edge for $U_{\infty} = 100$ Feet per Second	78
11 - Wall Pressure Spectral Densities at Position B, Normalized on Local Wall Shear, Displacement Thickness, and U_{∞}	79

	Page
12 - Normalized Magnitude of Longitudinal Cross Spectral Density at Position B	80
13 - Normalized Lateral Cross Spectral Density at Position B	81
14 - Flow Patterns and Pressure Distributions at Trailing Edge of Blunt Trailing Edge at $U_{\infty} = 100$ Feet per Second	82
15 - Mean-Square Pressures, Measured on Blunt Edge in 12.5-Hertz Bands at Tip, $r_x = -0.3$ Inch, and at Position 6, $r_x = -13$ Inch, Flagged Points; for $U_{\infty} = 50$ Feet per Second, Open Points, $\Delta\omega_f/U_s = 0.178$; and for $U_{\infty} = 100$ Feet per Second, Closed Points, $\Delta\omega_f/U_s = 0.09$	83
16 - Pressure Velocity Correlations behind Blunt Edge at $U_{\infty} = 100$ Feet per Second; r_x Is Measured Relative to Edge	84
17 - Wake Structure, Fluctuating Surface Pressure Distribution, and Vortex Phase Speeds behind Blunt Edge	85
18 - Lateral Spatial Correlation of Fluctuating Trailing-Edge Pressure, Measured at 100 Feet per Second	86
19 - Flow Patterns and Static Pressure Distribution at 45-Degree--Rounded Trailing Edge of Strut	87
20 - Dimensionless Longitudinal Velocity Spectral Densities, Measured in Formation Region of Near Wake from 45-Degree--Rounded-Beveled Edge	88
21 - Mean-Square Pressures, Measured on the 45-Degree Rounded Edge in 12.5-Hertz Bands at Positions G and 6, Flagged Points; for $U_{\infty} = 50$ Feet per Second, Open Points, $\Delta\omega_o/U_s = 0.09$; and for 100 Feet per Second, Closed Points, $\Delta\omega_o/U_s = 0.045$	89
22 - Pressure-Velocity Correlations in Wake behind 45-Degree--Rounded-Beveled Edge at $U_{\infty} = 50$ Feet per Second; r_x Measured from Tip	90

	Page
23 - Pressure-Velocity Correlations behind 45-Degree-- Rounded-Beveled Edge at $U_{\infty} = 100$ Feet per Second; Distances r_x are Measured from Tip of Edge	91
24 - Vortex Geometry in Near Wake, Corresponding to Pressure- Velocity Correlations for Upper Shear Layer	92
25 - Mean-Square Pressures Measured at various Streamwise Distances x Forward of Trailing-Edge Stagnation Point x_s	93
26 - Chordwise Distribution of Fluctuating Pressures Normalized on Flow-Separation Speed U_s , Vortex Strength, and Formation Length	94
27 - Dimensionless Vortex-Shedding Frequencies Based on Momentum Thickness	95
28 - Universal Strouhal Number of Bearman (1967) versus U_s/U_{∞} for Blunt and 45-Degree--Rounded-Trailing Edges	96
29 - Flow Patterns and Static Pressure Distributions on 25-Degree--Knuckle-Beveled Edge	97
30 - Space-Time Velocity Correlations above Position F on 25-Degree--Knuckle Edge at $U_{\infty} = 50$ Feet per Second	98
31 - Space-Time Velocity Correlations above Position F on 25- Degree--Knuckle Edge, Using Vertical Separations of Probes	99
32 - Spectra of Longitudinal Turbulent Velocity at Positions F and H on Knuckle Edge	100
33 - Momentum Balance for 25-Degree Knuckle Edge at $U_{\infty} = 100$ Feet per Second	102
34 - Flow Patterns at $U_{\infty} = 100$ Feet per Second and Pressure Distribution Near 25-Degree--Rounded-Beveled Edge	103
35 - Momentum Balance for 25-Degree--Rounded-Beveled Edge at 100 Feet per Second	104

	Page
36 - Autospectra of Turbulent Velocity Fluctuations over 25-Degree--Rounded-Beveled Edge	105
37 - Autospectra at Position F on 25-Degree--Rounded- Beveled Edge Nondimensionalized on Distance from Wall	108
38 - Dimensionless Pressure Spectra on 25-Degree-- Rounded-Beveled Trailing Edge	109
39 - Comparison of Various Measurements of Autospectra of Wall Pressures in Adverse Pressure Gradients	110
40 - Normalized Longitudinal Cross Spectral Density Magnitudes of Fluctuating Surface Pressures on 25- Degree--Rounded-Beveled Edge	111
41 - Wall Pressure Convection Velocities at Two Positions on Strut with 25-Degree--Rounded-Beveled Trailing Edge	112
42 - Normalized Lateral Cross Spectral Density Magnitudes of Fluctuating Surface Pressure at Position E1 on 25-Degree--Rounded-Beveled Edge	113
43 - Broadband Space-Time Correlations of Pressures at Position E1 on 25-Degree--Rounded-Trailing Edge	114
44 - Pressure-Velocity Correlations at Position B on 25-Degree--Rounded Edge	115
45 - Pressure-Velocity Correlations at Position F on Rounded Edge	116
46 - Broadband Space-Time Cross Correlations of Pressure at Position G and Fluctuating Velocity in Wake of 25- Degree--Rounded Edge at 60 Feet per Second	118
47 - Narrowband Mean-Square Pressure Levels, Measured in 62.5-Hertz Bands at Various Positions on 25-Degree Knuckle Edge	119
48 - Dimensionless Pressure Spectra of 25-Degree--Knuckle- Trailing Edge	120

	Page
49 - Broadband Space-Time Correlations of Pressures at Position F on 25-Degree Knuckle; Separations Measured from Position F, $\delta^* = 0.05$ Foot	121
50 - Broadband Correlation of Pressures at Positions F and G on 25-Degree Knuckle with $U_\infty = 100$ Feet per Second, $r_s/\delta^* = 1.66--\delta^*$ Evaluated at Position F	122
51 - Broadband Space-Time Correlations of Pressure and Velocity above 25-Degree Knuckle Edge	123
52 - Broadband Space-Time Correlations on 25-Degree Knuckle Edge of Pressures at Position F and Velocities in Wake for $U_\infty = 100$ Feet per Second	124
53 - Correspondence of Pressure-Velocity Correlation with Mean Shear for Position F on 25-Degree Knuckle Edge at 100 Feet per Second	124
54 - Correspondence of Pressure-Velocity Correlation with Mean Shear for Position G on 25-Degree Rounded Edge at 60 Feet per Second	125
55 - Normalized Cross Spectral Density Magnitudes (ϕ) and Phases (α) for Knuckle Edge	126
56 - Normalized Pressure-Velocity Cross Spectral Densities for Pressures at Position F on Knuckle Edge at 100 Feet per Second	127
57 - Comparison of Autospectra of Pressures on 25-Degree Wedge with Cross Spectrum of Pressures on Opposite Sides of Trailing Edge	128
58 - Mean and Turbulent Velocity Profiles at Position G on 45-Degree--Rounded-Beveled Edge	134
59 - Mean Velocity Profiles on 25-Degree--Rounded-Beveled Edge at $U_\infty = 100$ Feet per Second	135
60 - Mean Velocity Profiles on 25-Degree--Rounded-Beveled Edge at $U_\infty = 60$ Feet per Second	136
61 - Turbulence Intensity Profiles above 25-Degree--Rounded-Beveled Edge at $U_\infty = 60$ Feet per Second	136

	Page
62 - Turbulence Intensity Profiles above 25-Degree-- Rounded-Beveled Trailing Edge at $U_{\infty} = 100$ Feet per Second	137
63 - Mean Velocity Profiles above 25-Degree Knuckle Edge at $U_{\infty} = 50$ Feet per Second	137
64 - Mean Velocity Profiles above 25-Degree Knuckle Edge at 100 Feet per Second	138
65 - Turbulence Intensity Profiles above 25-Degree-- Knuckle-Trailing Edge at $U_{\infty} = 50$ Feet per Second	138
66 - Turbulence Intensity Profiles above 25-Degree-- Knuckle-Trailing Edge at $U_{\infty} = 100$ Feet per Second	139
67 - Mean Velocity Profiles Which Approximate Those Measured behind the 45-Degree--Rounded-Trailing Edge at Various Positions r_x	148
68 - Diagram of the Stability of a Two-Dimensional Wake: $P = 0.69$ and $U_m = 0.31$	149
69 - Cross Wake Distribution of Streamline Velocity Perturbations for Velocity Profile $P = 0.69$ and $U_m = 0.31$	149
70 - Amplification Factors Computed for Velocity Profiles of Figure 67	150
71 - Streamline Variations of Measured and Calculated Disturbances, $\frac{-1}{u} \frac{d^2}{dx^2} / U_o$, and Calculated Growth Rates, $\alpha C_I / C_R$, for Profiles of Figure 67	151

LIST OF TABLES

1 - Mean Boundary-Layer Properties for 25-Degree Knuckle Trailing Edge	14
2 - Mean Boundary-Layer Properties for 25-Degree Round Trailing Edge	14
3 - Strouhal Numbers	37
4 - Shear-Layer Length and Frequency Scales	144

NOTATION

C_f	Wall-shear coefficient
C_p	Local pressure coefficient, Equation (1)
$(C_p)_b$	Base pressure coefficient
f	Frequency = $\omega/2\pi$
H	Shape factor, δ^*/θ
h	Thickness of the strut upstream from the trailing edge
l_f	Vortex formation length
P	Static pressure
P_∞	Static pressure far from the strut
$\overline{p^2}$	Broadband mean-square pressure level
$\overline{p^2}(f)$	Mean-square pressure, filtered in a specified frequency band
$R_{pp}(\vec{r}, \tau)$	Space-time cross-correlation between pressure and velocity normalized on rms pressures at each measurement point, Equation (13)
$R_{pu}(\vec{r}, \tau)$	Space-time cross-correlation between pressure and velocity normalized on rms pressure and local mean velocity U_o ; see Equation (11)
$\vec{r}=(r_s, r_z, r_n)$	Separation coordinates aligned with local strut surface
$\vec{r}=(r_x, r_z, r_y)$	Separation coordinates
s	Streamwise coordinate measured in the plane of the surface of the strut
\bar{U}_c	Convection velocity determined from broadband, space-time correlations
U_c	Convection velocity determined from cross spectral density phase; for periodic processes $U_c = \bar{U}_c$

U_o	Local mean free-stream velocity
U_s	$U_\infty \sqrt{1-C_{p_b}}$
U_∞	Mean velocity incident on the strut
$U(y)$	Local mean velocity
$\overline{u^2}$	Broadband turbulence intensity, mean square
$\overline{u^2}(f_s)$	Filtered turbulence intensity
x	Distances measured from the leading edge in the plane of the strut
y_f	Value of y_o at vortex formation
y_o	Cross-wake separation between turbulence maxima, as illustrated in Figures 17 and 24
α	Cross spectrum phase
δ	Boundary-layer thickness
δ^*	Displacement thickness defined by Equation (2)
θ	Momentum thickness defined by Equation (4)
ν	Kinematic viscosity of the fluid
ρ	Fluid density
τ_w	Local wall shear coefficient
$\Phi_{uu}(\omega)$	Autospectral density of velocity fluctuations
ω	Frequency
$Q_\infty = 1/2 \sigma U_\infty^2$	

ADMINISTRATIVE INFORMATION

The work reported herein was funded by the Naval Sea Systems Command under Subproject SF43-452-702, Task 18184, Work Unit 1-1942-080 and by the David W. Taylor Naval Ship Research and Development Center In-House Research Program under Subproject ZR 011 08 01, Work Unit 1-1942-069.

1. INTRODUCTION

Influences of trailing-edge shapes on vortex-induced vibrations of turbine blades were the subjects of an early investigation by Heskestad and Olberts (1960).¹ In that series of measurements it was found that the most severe hydroelastic vibrations of a flat plate were induced by blunted trailing edges and edges symmetrically beveled or tapered with large included angles at the apices. The lowest levels of vibration occurred for edges which were unsymmetrically beveled with relatively small included angles and a large curvature at the juncture of the beveled edge with the main surface of the strut. Toebs and Eagleson (1961)² not only characterized some effects of trailing-edge geometry on vibrations but also experimentally demonstrated some aspects of self-excitation in the hydroelastic behavior of flat plates. Eagleson et al. (1962)³ related those results to the development of periodic disturbances in the wake, finding that the strengths of shed vortices could be reduced by increasing the taper of the edge. They also found that if the plate were allowed to vibrate, the amplitude of motion induced by trailing-edge flow would decrease commensurately with the observed reduction in the strength of shed vortices.

¹Heskestad, G. and D.R. Olberts, "Influence of Trailing Edge Geometry on Hydraulic-Turbine-Blade Vibration Resulting from Vortex Excitation," Transactions of the American Society of Mechanical Engineers, Journal of Engineering For Power, Vol. 82, pp. 103-110 (Apr 1960). A complete listing of references is given on page(s) 152.

²Toebs, G.H. and P.S. Eagleson, "Hydroelastic Vibrations of Flat Plates Related to Trailing Edge Geometry," Transactions of the American Society of Mechanical Engineers, Journal of Basic Engineering, pp. 1-8 (1961).

³Eagleson, P.S. et al., "Turbulence In the Early Wake of a Fixed Flat Plate," Massachusetts Institute of Technology Hydrodynamics Laboratory Report 46 (Feb 1961).

More recently, Greenway and Wood (1973)⁴ performed a series of flow-visualization experiments to establish the flow structures at the trailing edges of stationary and oscillating flat struts. In those measurements the edges were blunt and unsymmetrically beveled with various included angles. The effect of beveling was found to destabilize the vortex structure in the wake but not to influence greatly the strengths of shed vortices. Greenway and Wood calculated strengths of shed vortices from particle trajectories in photographs. For included angles of less than 30 deg, regularity in the wake was found to be nearly absent for rigid struts. These visualization results corroborated with the Heskestad and Olberts hydroelastic data and led to speculation by Greenway and Wood that a reduction in vibration amplitude arose because of randomization of the periodic forces on the strut rather than from a reduction in the mean-square amplitude of the forces.

The influence of splitter plates in altering the formation of periodic vortex streets in the wakes of flat struts was examined by Bearman (1965).⁵ Splitter plates interfered with interaction of separated free-shear layers at bluff trailing edges. Measurements of velocity fluctuations in the wakes for increasing splitter-plate lengths demonstrated that the disturbances reached maxima at increasing distances downstream from the edge. Locations of maximal disturbances were found by smoke visualization to coincide with points between the positions of the first and second vortices. For long enough splitter plates, Bearman⁵ found that discrete vortex formation could be eliminated.

The frequency of vortex formation in wakes formed by blunt trailing edges was first examined by Gongwer (1952),⁶ who proposed a particularly

⁴Greenway, M.E. and C.J. Wood, "The Effect of a Beveled Trailing Edge on Vortex Shedding and Vibration," *Journal of Fluid Mechanics*, Vol. 61, pp. 323-335 (1973).

⁵Bearman, P.W., "Investigation of the Flow Behind a Two-Dimensional Model with a Blunt Trailing Edge and Fitted with Splitter Plates," *Journal of Fluid Mechanics*, Vol. 21, pp. 241-255 (1965).

⁶Gongwer, G.A., "A Study of Vanes Singing In Water," *Journal of Applied Mechanics*, Vol. 19 (1952).

simple form of dimensionless frequency or Strouhal number. He found by experiment that the shedding frequency scaled well on the free-stream velocity and a length that was the sum of the edge thickness and the momentum thicknesses of the boundary layers forming the wake. Later, Bearman⁵ found for a blunt edge with a given length of splitter-plate that the Strouhal number formed with the trailing-edge thickness and free-stream velocity was nearly constant over a wide speed range. He found, however, that the Strouhal number varied considerably as the splitter-plate length was increased. He also found that the static base-pressure coefficient varied with splitter length but not with Reynolds number. A relationship between shedding frequency and static base pressure was shown by Bearman (1967).⁷ In that paper Bearman noted that earlier definition of Strouhal number by Roshko (1954)⁸ did not fit his 1965 results without modification. The definition by Roshko⁸ was based on the estimated distance between parallel, separated, free-shear layers in the wake. This distance was analytically determined by the notched hodograph method from the potential flow around bluff, two-dimensional cylinders. The modification by Bearman⁷ replaced this distance with the estimated cross wake separation between vortex centers in the fully developed far wake. This vortex separation was determined by use of the Kronauer (1964)⁹ hypothesis that a minimum vortex drag coefficient is exerted on the wake-producing body and this coefficient uniquely determines the spatial arrangement of vortices. From measured streamwise vortex separations, Bearman⁷ calculated the cross wake separations. His defined Strouhal number appeared to be a universal function of the mean base-pressure coefficient for data collected by a number of investigators on

⁷Bearman, P.W., "On Vortex Street Wakes," *Journal of Fluid Mechanics*, Vol. 28, pp. 625-641 (1967).

⁸Roshko, A., "On the Drag and Shedding Frequency of Two-Dimensional Bluff Bodies," *National Advisory Committee for Aeronautics Technical Note 3969* (1954).

⁹Kronauer, R.E., "Predicting Eddy Frequency in Separated Wakes," Paper presented at the International Union of Theoretical and Applied Mathematics Symposium on Concentrated Vortex Motions in Fluids, University of Michigan, Ann Arbor, Mich. (6-11 Jul 1964); also, referred to by Bearman (1967).

various blunt bodies with and without splitter plates. In the definitions made by both Roshko⁸ and Bearman,⁷ the characteristic velocity is that existing just outside the boundary layers on the body at the point of separation.

These investigations have shown how details of the wake structure determine vortex shedding frequencies and how trailing-edge shape influences the interactions of separated shear layers. When the shear layers are decoupled, vortex formation appears to become disordered; this disorder modifies the frequency of formation of vortices as well as the base pressure or the drag coefficient of the resultant vortex street. What these investigations do not disclose, however, is the level and time dependence of dynamic pressures which are exerted on a shedding body for the various trailing-edge shapes. Many investigations of the oscillatory lift coefficients on shedding cylinders have been made, but very little information exists for streamlined aerofoils with vortex shedding. Recently, however, Hanson (1970)¹⁰ measured the mean and fluctuating base pressures as well as the near-wake characteristics behind lifting airfoils. His results demonstrated that a relationship exists among the mean base pressure coefficient, the distance of vortex formation downstream of the edge λ_f , and the momentum thickness of the wake θ . The mean base pressure coefficient was found to increase linearly with the ratio θ/λ_f . Apparently, pressure recovery of the flow near the edge is associated with an increase in the formation length. Hanson also found that the vortex shedding frequency could be scaled on momentum thickness of the wake more adequately than a geometric length, characteristic of the trailing edge.

This report is a description of measurements of fluctuating pressures on trailing edges of flat struts and of fluctuating velocities in wakes that generate those pressures. The measurements were made on a family of edge shapes, similar to those of Heskestad and Olberts¹ and of

¹⁰Hanson, C.E., "An Investigation of the Near-Wake Properties Associated with Periodic Vortex Shedding from Airfoils," Massachusetts Institute of Technology Acoustics and Vibration Laboratory Report 76234-5 (1970).

Greenway and Wood.⁴ The edges (Figure 1) were selected for the range of random to periodic wakes that they produced. Cross spectral densities of the pressures on the edges as well as cross correlations and cross spectra of those pressures with velocity disturbances in the shear layers near the edges will demonstrate the relationship of the pressures with the near wake-formation regions of each edge. Chordwise distributions of fluctuating pressure will be shown, and Strouhal number definitions will be reviewed. For the trailing edges considered, interrelationships will be drawn among those which generate periodic surface pressures and those which do not.

2. FACILITY AND INSTRUMENT DESCRIPTIONS

All measurements were performed in the Anechoic Flow Facility (AFF) of the David W. Taylor Naval Ship Research and Development Center (the Center). This facility combines a low-turbulence wind tunnel with an anechoic chamber. The broadband turbulence intensity level in the tunnel at a centerline speed of 150 ft/sec has been shown by DeMetz and Casarella (1973)¹¹ to be about 0.08 percent. The test section is 21 feet and 1 inch in length and has a cross-section of 8 by 8 feet with corner fillets to maintain one-dimensional flow throughout. Pressure gradients which are caused by turbulent boundary-layer growth are reduced by tapering the test section walls. Flow speeds may be controlled within ± 0.5 percent with a maximum velocity of 200 feet per second. Measurements have been made at the end of the test section where it is jointed by an anechoic chamber designed for a 150-Hz lower acoustic cutoff frequency. A description of the acoustic and aerodynamic characteristics of the facility has been given by Bowers (1973).¹²

¹¹DeMetz, F.C. and M.J. Casarella, "An Experimental Study of the Intermittent Properties of the Boundary Layer Pressure Field During Transition on a Flat Plate," NSRDC Report 4140 (Nov 1973).

¹²Bowers, B.E., "The Anechoic Flow Facility-Aerodynamic Calibration and Evaluation (U)," NSRDC Evaluation Report SAD-48E-1942 (May 1973).

2.1 STRUT AND TRAILING EDGES

The working strut (Figure 1) had a circular leading edge which, due to laminar separation, tripped the turbulent boundary layer on the downstream flat section. Excluding the removable trailing-edge sections, the strut was 3 feet in chord with a uniform thickness of 2 inches and a span of 4 feet. Four trailing edges were used; one was squared off, and three were unsymmetrically beveled. Of the beveled edges, two had an included tip angle of 25 deg and a length of 6 1/4 inches; the other had an included tip angle of 45 deg and a length of 4 inches. The 45-deg edge and one of the 25-deg edges were faired with 5- and 10-inch radii, respectively, to give a continuously increasing pressure gradient. The other 25-deg edge had a knuckle, 2-inches from the strut attachment point; see Figure 1. Both the strut and the trailing edges were constructed from pine and plywood and were painted to maintain a smooth surface.

The strut was rigidly fastened in a vertical position to the floor of the tunnel at the end of the upstream test section, adjacent to the anechoic chamber. An end plate in the form of a plywood panel 8 feet long and 5 feet wide was attached to the top of the strut and to the walls of the tunnel. The end plate and tunnel floor together with the vertical strut resembled a sidewise H. The arrangement effectively divided the tunnel in half. The measured values of fluctuating wall pressures on the blunt trailing edge of the strut were uniform over an 8-inch spanwise section, showing that the flow was essentially two dimensional across the span of the strut.

2.2 INSTRUMENTATION

Static Pressure Measurements

The static pressure variation along the chord was measured using pressure taps at discrete points along both sides of the strut, including the stagnation point. Depending on the trailing edge, there were up to 22 tap locations. Each pressure tap consisted of 1-inch long and 1/8-inch-OD, 1/16-inch-ID, copper tubing, glued into position so that its tip was sealed flush with the surface of the strut. Removable panels on one side of the strut, permitted attachment of flexible plastic tubes which ran down through the strut and under the tunnel floor to a bank of manometers.

Surface Pressure Fluctuation Measurements

The flow-induced, surface-pressure fluctuations on the strut were measured using a 1/8-inch condenser microphone (Bruel and Kjaer (B & K) Model 4138) whose sensing area was reduced by placing a cap perforated with a 1/32-inch-diameter hole in its center over the diaphragm of the microphone. The 1/8-inch condenser microphone was connected to the cathode follower (B & K Model 2619) through a 1/4-inch, right-angle adaptor (B & K Model UA 0122) which was modified to accept the 1/8-inch microphone. The pinhole perforating the center of this cap led to a small cavity above the diaphragm. The frequency response of the pinhole microphone was measured by comparing the response of the microphone with and without pinhole caps to identical free-field sound fields. The relative phase shift between the microphones was also measured in this manner. The Helmholtz resonance frequency caused by the cavity was measured at 17.5 kilohertz. Response of the pinhole microphone was from flat to 1 dB from 65 Hz to 10 kHz, and the relative phase shift was from zero to 5 deg at 8 kHz, and 14 deg at 10 kilohertz.

The 1/8-inch condenser microphones with pinhole caps were flush mounted to various positions along the strut and trailing edges at the positions indicated in Figure 1. The autospectra as well as the longitudinal (streamline) and lateral (spanwise) cross spectral densities of pressures were measured at these locations. The dimensions of the microphone positions will be described as the measurements are presented.

Besides the 1/8-inch microphone, a 1/2-inch microphone (B & K Model 4133) with a probe-tube extension (B & K Model UA 0040) was used to measure the pressure spectra at narrow thicknesses of the trailing edge as well as the tip. The probe tube acts as a low-pass filter between the microphone and the fluctuating pressure source. Three 3/64-inch-diameter probe tubes were calibrated with lengths of 1 1/2, 3, and 4 7/16 inches; all obtained a flat amplitude response to 2 kHz and approximately a linear-phase response. Calibration of the probe tube with proper damping was accomplished by using a B & K coupler that

accepted a probe tube, a 1/2-inch microphone, and a small sound source. The volume of the coupler is much smaller than the wavelength of sound, thereby producing a uniform sound pressure level in the chamber over the frequency range of interest. The source was driven by a frequency analyzer (General Radio Model 1900) connected in the tracking mode. The signals from both the 1/2-inch microphone and the probe tube were fed back into the analyzer for frequency analysis and were displayed on a graphic level recorder (General Radio). The response of the tube was adjusted by placing damping material (steel wool) into the probe tube and comparing the amplitude and phase response of the probe tube with that of the 1/2-inch microphone. Responses are shown in Figures 2 and 3.

Velocity Measurements

Turbulent velocity fluctuations were measured using a heat flux system (Thermo-Systems Model 1010), constant temperature anemometer, and a linearizer (Thermo-Systems Model 1005B). The anemometer was calibrated for wind speeds using a venturi meter. A 0.0005-inch, platinum-iridium alloy wire with a 0.3-msec time constant was used for the sensing element which was attached to an 18-inch probe support. The probe support was positioned by an electromechanical linear actuator to within 0.01 inch, ± 0.005 inch, by reading a dc voltage, fed back from a linear potentiometer. Probe and probe supports were aerodynamically shaped to minimize vibration from vortex shedding from the supports. Turbulence intensities were measured using a B & K true rms meter.

Auto and Cross Spectrum and Correlation Analyses

All of the wall pressure auto and cross spectral densities as well as the pressure-velocity, cross spectral densities were obtained with a real-time analyzer system (Time Data Type 1923/A). The spectral densities were determined digitally, using a fast Fourier-transform algorithm with a Hanning window. Sample sizes of at least 256 were used

with effective analysis bands, ranging from 12.5 to 62.5 hertz. The bandwidths of analyses were constant over each complete frequency range, which was either from 0 to 2 or from 0 to 20 kilohertz. Some velocity spectral densities were obtained in 1/10-octave bands using a sound and vibration analyzer (General Radio Model 1564).

Broadband correlations were made with a digital correlator (Hewlett Packard Model 3721A). This instrument displayed both auto and cross correlation functions at 100 computed points with time delays from 100 μ sec to 100 sec possible. The digital equivalent of resistor-capacitor circuit (RC) averaging was used.

2.3 STATISTICAL PRECISION

Figure 4 shows measured and theoretical expressions for the standard deviation of cross spectral density estimates of random signals. The measurement was conducted by correlating two broadband signals, which were known to be uncorrelated, using the real-time analyzer. The computed values of the normalized cross spectrum, theoretically zero, were estimate errors which decreased with increasing sample size N. For each sample size a value of the computed cross-spectrum was selected. This value exceeded 80 percent of the estimates of the spectrum, and it was interpreted as an 80-percent confidence limit on the error of a cross spectral density estimate. A theoretical estimate, whose derivation is presented in Appendix A, is

$$\frac{|\sigma(\phi_{xy})|}{\phi_{xx}(f)} = \frac{1}{\sqrt{N}} \left(1 + 2 \frac{\phi_{xy}(f)}{\phi_{xx}(f)} - \frac{|\phi_{xy}(f)|^2}{(\phi_{xx}(f))^2} \right)^{1/2}$$

where $\phi_{xx}(f) = \phi_{yy}(f)$ is the true autospectral density of the input

$\phi_{xy}(f)$ is the true cross spectral density

$\sigma(\phi_{xy})$ is the standard deviation of the cross spectrum estimate.

3. CHARACTERISTICS OF FLOW INCIDENT ON EDGES

The measurements described in this section served to establish that the turbulent flow field, incident on the edges, was typical of that which exists in fully developed boundary layers on flat surfaces. Measurements of the correlations between fluctuating wall pressures at different chordwise points as well as of turbulent velocity were made. These compared favorably to the measured statistics of other investigators; they, therefore, confirmed proper experimental technique, and standardized the incident flow.

Figure 5 shows the chordwise static pressure distribution and the cross-section shape of the strut, which was outfitted with the 25-deg--rounded trailing edge. The static pressures are expressed as a coefficient

$$-C_p = \frac{P_\infty - P}{1/2 \rho U_\infty^2} \approx \left(\frac{U_o}{U_\infty} \right)^2 - 1 \quad (1)$$

which, in the absence of a local pressure gradient across the boundary layer, can be interpreted in terms of the local free-stream velocity on the strut U_o . In Equation (1) P_∞ is the ambient pressure far from the strut, P is the local static pressure on the strut, ρ is the fluid density, and U_∞ is the mean velocity upstream of and incident on the strut. Locations 1 through 6 in Figure 5 designate single microphone locations for which the static pressure distribution was trivially altered by modifying the edges. Measurements at all these locations were made only once in the course of the experiment, and representative checks were made for each edge. The lettered locations near the trailing edge are those for which the static pressure was influenced to varying degrees by the different edges; measurements were performed at those locations for all edges. The edges were attached to the main strut 36 inches from the leading edge.

The results in Figure 5 show a sharp static pressure minimum forward of microphone position 1, followed by a steep adverse pressure gradient. Flow visualization with oil streaks at 100 ft/sec disclosed a separation region extending from approximately 1 inch to 3 inches downstream from the leading edge. It is conjectured that laminar separation was caused by the circular leading edge. Short separation bubbles on leading edges of airfoils as discussed by Chang (1970)¹³ play the role of causing transition for the downstream boundary layer. In this type of flow the separated laminar shear layer becomes turbulent before reattachment. Likely, the free-stream turbulence level of the wind tunnel (0.08 percent) was low enough to permit laminar separation to occur. The flow around the cylindrical leading edge in the present case is probably somewhat similar to that around the forward quadrant of a circular cylinder. In that case (Chang)¹³ laminar separation occurs, 82 deg removed from the forward stagnation point for Reynolds numbers, based-diameter, less than 2×10^5 . Turbulent separation occurs further around for Reynolds numbers greater than 7×10^5 . In the present instance, for $U_\infty = 100$ ft/sec the Reynolds number based on the diameter of the leading edge, $h = 2$ inches, is 1.02×10^5 . The conjecture of laminar separation, then, seems reasonable.

Further downstream, the static pressure varies slightly, becoming somewhat favorable forward of the trailing edge. Magnitudes of the favorable and adverse pressure gradients at the trailing edge are dependent on the shape of the trailing edge; each edge will be discussed in detail later in the report. For all except the blunt trailing edge, the favorable pressure gradient from $x = 28$ inches to $x = 34$ inches shown in Figure 5 is typical. Therefore, the statistics of the boundary layer for all positions 1 through B are expected to be unaltered by changing the beveled trailing edges but, perhaps, slightly modified by the blunt edge. This difference in local static pressure is thought to be caused by the slight change in camber brought about by the use of unsymmetrical versus symmetrical edges.

¹³Chang, P.K., "Separation of Flow," Pergamon Press, Oxford, England (1970).

The mean and turbulent velocity profiles for positions 4 and B are shown in Figure 6. The mean velocity $U(y)$ and root-mean-square turbulent velocity u'^2 are expressed as fractions of the local free-stream velocity U_0 . Distance normal to the plane of the strut y is normalized on the boundary-layer thickness δ , which is defined by $U(\delta) = 0.99 U_0$. The mean velocity profiles appear to be similar, indicating that an equilibrium boundary layer has been formed on the strut. The Prandtl (Schlichting (1960)¹⁴) 1/7-power law for the mean velocity distribution is also shown, and it compares favorably with the results. This comparison further shows that the mean velocity in the boundary layer is similar to that on a flat plate. Also, the Klebanoff (1955)¹⁵ longitudinal turbulence intensities are shown; levels in the outer region of the boundary layer on the strut are higher than those of Klebanoff. That they decrease from position 4 to position B suggests that these levels are caused by large-scale disturbances associated with the leading-edge separation. Close to the wall $y/\delta < 0.15$, the measured intensities are lower than those measured by Klebanoff.¹⁵ The discrepancy could be due to a probe-wall interference or possibly (but less likely) to the effect of upstream history determined by the leading-edge separation.

Spectral densities of the turbulent velocities at selected locations in the boundary layer at position B on the knuckle edge are shown in Figure 7. The spectra are normalized on the local mean velocity $U(y)$, the boundary-layer-displacement thickness

$$\delta^* = \int_0^{\delta} \left[1 - \frac{U(y)}{U_0} \right] dy \quad (2)$$

and the mean square velocity $\overline{u'^2}$. They are two sided so that

¹⁴Schlichting, H., "Boundary Layer Theory," McGraw-Hill Fourth Edition, New York (1960).

¹⁵Klebanoff, P.S., "Characteristics of Turbulence in a Boundary Layer with Zero Pressure Gradient," National Advisory Committee for Aeronautics Report 1247 (1955).

$$1 = \int_{-\infty}^{\infty} \frac{\phi_{uu}(\omega) U(y)}{u^2 \delta^*} d \left[\frac{\omega \delta^*}{U(y)} \right] \quad (3)$$

where ω is the radian frequency. Near the wall for $y/\delta = 0.028$, the normalized spectrum is deficient in low-frequency intensity, compared to spectra further from the wall. Generally the spectra are comparable to those measured elsewhere, e.g., Klebanoff,¹⁵ and Blake (1970).¹⁶

Tables 1 and 2 give mean boundary-layer properties, measured elsewhere on the strut with 25-deg knuckle and round trailing edges. The momentum thicknesses

$$\theta = \int_0^{\delta} \frac{U(y)}{U_o} \left[1 - \frac{U(y)}{U_o} \right] dy \quad (4)$$

and the shape factors

$$H = \delta^*/\theta \quad (5)$$

are shown with δ and δ^* for each location. At position B for 100 feet/sec the boundary layer on the 25-deg knuckle edge is slightly thicker than that at the same location for the 25-deg round edge.

The mean velocity profiles at positions A and B forward of the 25-deg round trailing edge are plotted logarithmically for 100 ft/sec in Figure 8. Velocities are normalized on the friction velocity

$$U_{\tau} = \sqrt{\tau_w/\rho} \quad (6)$$

where τ_w is the local wall shear. The value of U_{τ} was determined by curve fitting to the law of the wall as described by Perry and Joubert (1963).¹⁷

¹⁶Blake, W.K., "Turbulent Boundary Layer Wall Pressure Fluctuations on Smooth and Rough Walls," Massachusetts Institute of Technology Acoustics and Vibration Laboratory Report 70208-1 (1969).

¹⁷Perry, A.E. and P.N. Joubert, Journal of Fluid Mechanics, Vol. 17, p. 193 (1963).

TABLE 1 - MEAN BOUNDARY-LAYER PROPERTIES FOR 25-DEGREE KNUCKLE TRAILING EDGE

50 Feet per Second					100 Feet per Second			
Pos	δ	δ^*	θ	H	δ	δ^*	θ	H
A					0.65	0.09	0.073	1.23
B					0.67	0.103	0.074	1.4
C					0.62	0.0705	0.0564	1.245
D	0.90	0.084	0.0795	1.055	0.56	0.05	0.0475	1.06
E					0.5	0.07	0.0525	1.34
E-1	1.33	0.45	0.135	3.4	0.88	0.316	0.114	2.765
F	1.6	0.81	0.181	4.47	1.29	0.596	0.217	2.75

All dimensions are in inches, $H = \delta^*/\theta$.

TABLE 2 - MEAN BOUNDARY-LAYER PROPERTIES FOR 25-DEGREE ROUND TRAILING EDGE

60 Feet per Second					100 Feet per Second			
Pos	δ	δ^*	θ	H	δ	δ^*	θ	H
4	0.575	0.0735	0.061	1.21	0.435	0.0603	0.048	1.26
A								
B	0.8	0.093	0.08	1.17	0.63	0.073	0.059	1.23
B-1					0.615	0.0668	0.0565	1.16
C					0.5	0.045	0.04	1.14
DE	0.8	0.0915	0.059	1.56	0.62	0.093	0.0495	1.88
E-1	0.95	0.157	0.082	1.93	0.65	0.118	0.0676	1.74
F	1.35	0.285	0.133	2.12	0.95	0.231	0.095	2.43
G	1.96	0.52	0.215	2.42	1.36	0.451	0.129	3.47

All dimensions are in inches, $H = \delta^*/\theta$.

The local wall-shear coefficient at $x = 32$ inches and $U_\infty = 100$ ft/sec

$$C_f = \tau_w / 1/2 \rho U_o^2 \quad (7)$$

was found to be $C_f = 3.2 \times 10^{-3}$, somewhat lower than that given by Schlichting¹⁴ for a naturally developed boundary layer on a smooth wall at this Reynolds number $U_\infty x / \nu$.

The mean-square-wall-pressure fluctuations, measured in 62.5-Hz frequency bands at positions 1 through 6, $\overline{p^2}(f)$, are shown in Figure 9 as fractions of free-stream dynamic head q_∞ and a function of frequency f for $U_\infty = 50$ feet per second. At position 1 the narrowband pressures at low frequencies decrease from an undetermined maximum at $f < 120$ Hz and then show a broad peak at 2700 hertz. The levels at position 2 are broadband; at locations which are further removed from the leading edge, the levels continue to decrease slightly. At 100 ft/sec the narrowband wall pressures (Figure 10) at position 1 are more broadband than at 50 ft/sec; however, they are substantially higher than at other locations on the strut. There is a broad "hump" centered on 4500 Hz, followed by f^{-2} behavior. The oscilloscope trace of the unfiltered signal showed that between $U_\infty = 75$ and 100 ft/sec, as speed was increased slowly and continuously, the pressure fluctuations "jumped" markedly. This suggests that the disturbances at position 1 which are associated with the leading-edge separation changed in character as the speed was increased from 50 to 100 feet per second. Perhaps the separated shear-layer reattachment occurred immediately above position 1 at 100 ft/sec and a little downstream from position 1 at 50 feet per second. The presence of the peaks at 2700 and 4500 Hz indicates the occurrence of pulsation associated with the laminar separation reattachment whose frequency increases nearly linearly with U_∞ . The pressure spectra at locations downstream from position 1 are more uniformly behaved through position B.

To determine how the wall pressures behave in relation to earlier work, the spectra at position B for 2 speeds have been normalized on the

local wall shear coefficient, the displacement thickness, and inflow U_∞ in Figure 11. Normalization has been made so that

$$\overline{p^2}/\tau_w^2 = \int_{-\infty}^{\infty} \frac{\phi(\omega)U_\infty}{\tau_w^2 \delta^*} d \left(\frac{\omega\delta^*}{U_\infty} \right) \quad (8)$$

The results compare favorably to those of Blake (1970)^{16,18} for a boundary layer on a smooth, flat wall. For $\omega\delta^*/U_\infty > 4$ the results diverge because of the spatial averaging of small-scale disturbances over the microphone face as discussed by Corcos (1963).¹⁹ Those effects become most severe when $\omega d/U_c > 2$, where d is the diameter of the microphone, and $U_c \approx 0.6 U_\infty$ is the convection velocity of disturbances across the microphone considered in Section 6. For the current case, $d = 0.3 \delta^*$, $U_c \approx 0.6 U_\infty$ (Section 4), and $\omega\delta^*/U_\infty \approx 4$ so that $\omega d/U_c \approx 2$. The spectra also diverge slightly at low dimensionless frequencies. This divergence was not observed in earlier work (Blake^{16,18}), and in this case it may be due to the influence of the leading-edge separation. It could also be associated with the fact that the current measurements were obtained at a lower Reynolds number $N_{Re_\theta} = U_\infty \theta/\nu$ than in the earlier work. Nonetheless these dimensionless spectra are considered to be in good agreement with the earlier ones.

The spatial cross spectral densities of wall pressures at position B were measured with a pair of microphones separated in the streamline direction by a variable distance r_x . The magnitudes of the cross spectrum $|\phi(r_x, 0, \omega)|$ are normalized on the autospectrum $\phi(\omega)$ and are plotted against the phase $\alpha(r_x, \omega)$ in Figure 12. For separations of $r_x = 3\delta^*$ and $r_x = 6\delta^*$, the magnitude is a function of phase; this behavior is typical of pressure fluctuations on smooth walls. The dotted curve in Figure 12 is from the data of Blake¹⁸ which were obtained on the smooth wall

¹⁸Blake, W.K., "Turbulent Boundary-Layer Wall Pressure Fluctuations on Smooth and Rough Walls," Journal of Fluid Mechanics, Vol. 44, p. 1 (1970).

¹⁹Corcos, G.M., "On the Resolution of Pressure in Turbulence," Journal of the Acoustical Society of America, Vol. 35, p. 192 (1963).

beneath a boundary layer of substantially larger Reynolds number. The phase of the cross spectrum has been interpreted by Corcos¹⁹ in terms of a convection velocity U_c (note $r_x = r_s$)

$$\alpha(r_x, \omega) = \omega r_x / U_c \quad (9a)$$

or in terms of a characteristic wavelength λ_c

$$\alpha(r_x, \omega) = 2\pi r_x / \lambda_c \quad (9b)$$

Using this interpretation, the data in Figure 12 suggest that in the present case the coherence of disturbances diminishes to 0.1 within two wavelengths, compared to three wavelengths beneath the boundary layer at high Reynolds number. The convection velocities which were determined from the phases will be discussed in Section 6. Cross spectral densities for a lateral separation of $r_z = 3\delta^*$ are shown in Figure 13. For $\omega r_z / U_c > 1.5$ they are similar to those measured on other smooth walls; for $\omega r_z / U_c < 1.5$ they are less than those measured by Blake;¹⁸ however, the discrepancy may be related to an additional separation dependence as noted by Bull (1967).²⁰

4. PRESSURES AND VELOCITIES GENERATED BY PERIODIC VORTEX STREETS

Disturbances in the wakes of both the blunt trailing edge and the rounded 45-deg trailing edge were characterized by the development of periodic vortex streets. In this section we will consider first the particular details of the flow off each edge separately and second the general characteristics of the periodic disturbances.

4.1 WAKES OF BLUNT TRAILING EDGES

The wake structures behind blunt trailing edges have been determined in detail by Bearman^{5,7} and Greenway and Wood.⁴ Current measurements on the blunt edge corroborate and extend those results, and they serve as a basis for interpreting the other measurements to be described later.

²⁰Bull, M.K., "Wall Pressure Fluctuations Associated with Subsonic Turbulent Boundary Layer Flow," Journal of Fluid Mechanics, Vol. 28, p. 719 (1967).

The characteristics of the flow field of the blunt trailing edge are shown in Figure 14. The descriptions begin 29 inches downstream from the leading edge and extend 4 1/2 inches downstream from the trailing edge. The static pressure distribution, shown at the top of the figure, becomes favorable near the edge; the base pressure coefficient which was measured at numerous locations on the base including the centerline of the strut was

$$- C_{p_b} = 0.51$$

It was uniform across the thickness of the edge and the span. The Reynolds number, based on chord $U_\infty w/\nu$, where w is the chord, extended to 2×10^6 . For the experiments of Bearman⁵ it extended to 2.85×10^5 , and in the case of Greenway and Wood⁴ it extended to 1.4×10^4 for their flow visualizations and to 1.3×10^6 for their wind tunnel measurements.

The vortex shedding frequency for the current strut, measured both with fluctuating pressures on the strut and with the velocity fluctuations in the wake, was found to be linearly dependent on U_∞ . To compare shedding frequencies in this and earlier work, we note the Strouhal number based on the strut thickness h , which is

$$N_{st} = f_s h / U_\infty = 0.23 \quad (10)$$

This number* is somewhat smaller than that of Greenway and Wood⁴ at a low Reynolds number $N_{st} = 0.286$; however, it is in agreement with their value of $N_{st} = 0.24$ obtained at a high Reynolds number. This difference is probably caused by laminar separation at the trailing edges at their low Reynolds number; also, the shed boundary layers in this and the Greenway and Wood cases are dissimilar. The current value compares favorably with the Bearman⁵ value, $N_{st} = 0.24$, for a blunt edge without a splitter plate. All of the previously mentioned differences in dimensionless shedding

* In this case the definition is practically equivalent to that of Gongwer⁶ which replaces h by h plus the sum of the momentum thicknesses of the boundary layers shed off the edge. Thus, $h+2\theta=2.1$ inch and $f_s(h+2\theta)/U_\infty = 0.25$ which is somewhat greater than the value 0.19 obtained by Gongwer.

frequency are most likely due to variations in the wake thicknesses occurring in the various experiments, and they reflect the observation (Bearman)⁷ that Equation (10) is not a universal scaling number. One of the purposes of this report is to review various frequency-scaling hypotheses in light of the current measurements.

The mean velocity profiles of the flow on the strut and in the near wake of the strut are shown at the center of Figure 14. At the bottom of Figure 14 are shown the vertical profiles of root-mean-square filtered fluctuating velocity u^2 ^{1/2} (f_s); the turbulence velocities were filtered in 1/10-octave bands centered on the shedding frequency f_s . Within 0.5 inch of the strut the profiles display sharp maxima near the corners of the edge and broader peaks closer to the centerline of the wake. The sharp peaks in intensity are associated with the primary disturbances in the shear layers, while the peaks near the centerline are probably caused by a secondary vortex system. For $x > 0.5$ inch, the profiles of u^2 ^{1/2} (f_s) display two maxima which broaden in spatial extent as the disturbances are convected away from the strut. The locus of the filtered intensity maxima is sketched in the center of Figure 14; it is situated a distance which we shall call $y = y_0/2$ above the centerline of the wake.

The root-mean-square fluctuating pressure, filtered in a 12.5-Hz band centered on the shedding frequency p^2 ^{1/2} (f_s), was measured at increasing distances from the trailing edge. The pressures, normalized on the dynamic head of the inflow, are shown in the upper part of Figure 14. The fluctuating pressures on one side of the strut were in common phase, showing no convection as was expected. The frequency spectra of fluctuating pressure on the surface of the strut (Figure 15) displayed a single dominant peak at $f = f_s$. (This figure will be more fully described later.) An autospectrum of the fluctuating base pressure displayed a single peak at $f = 2f_s$. The narrowband, root-mean-square base pressure, filtered at $f = 2f_s$, is also shown in Figure 14.

The growth of coherent disturbances in the near wake can be deduced from correlations of fluctuating pressure on the edge with fluctuating velocity at specific locations in the wake. The magnitudes of the fluctuating pressures generated by the wake should depend on both the strength of the vortices shed into the wake and the proximity of the vortices to the edge. The frequency of the pressures is the same as the rate of formation of vortices, and this is given by the ratio of the local speed of convected vortices relative to the fixed edge to the streamwise spacing of adjacent vortices in a single row. The cross-wake spatial variation of local fluctuating velocity in a vortex street has been related to the geometry of the configuration of the vortices by Schaefer and Eskinazi (1959).²¹ They have shown that the maximum of u^2 (f_s), i.e., $y = y_0/2$, coincides with the locus of the peripheries of the vortex cores rather than the locus of centers of the vortices. The diameter of each vortex core was shown to extend approximately from the position of maximum filtered velocity to the centerline of the wake. The strength of the vortex is proportional to the product of the diameter of the vortex core and the tangential velocity at the extremity of the core. Therefore, measurements of the correlation between the fluctuating surface pressure and the fluctuating velocity along the $y = y_0/2$ are expected to reflect the structure of vortices in the wake.

This measurement was performed by moving an anemometer probe along the locus of filtered turbulence maxima in the upper side of the wake that is shown in Figure 14. The space-time correlation of pressure and velocity is written

$$\tilde{R}_{pu}(r_x, \tau) = \frac{p(r_{x_1} = -0.375, t) u(r_x, t + \tau)}{p_e^{1/2} U_0} \quad (11)$$

²¹Schaefer, J.W. and S. Eskinazi, "An Analysis of the Vortex Street Generated in a Viscous Fluid," Journal of Fluid Mechanics, Vol. 6, p. 241 (1959).

where $p_e(t) = p(f_x = -0.375 \text{ in.}, t)$ is the unfiltered fluctuating pressure as close as possible to the tip

$$r_{x_1} = -0.375 \text{ inch}$$

t is time

$u(r_x, t)$ is the local velocity along $y = y_0/2$

r_x is measured downstream of the trailing edge.

The correlation has been normalized on the root-mean-square fluctuating pressure at the tip and the local free-stream velocity U_0 . By using U_0 rather than the local root-mean-square velocity $u^2 1/2 (f_s)$ as a normalizing factor, we can determine the influences of specific locations of the wake on the fluctuating pressure. The measured correlations for $U_\infty = 100 \text{ ft/sec}$ are shown in Figure 16. The upper curve is the spatial correlation, which reaches a value $R_{pu}(r_x, 0) = -0.25$ at $r_x = 0.5 \text{ inch}$ and a value $R_{pu}(r_x, 0) = +0.25$ at $r_x = 2.1 \text{ inch}$. Zero crossings occur at $r_x = 1.1 \text{ inch}$ and $r_x = 3.5 \text{ inch}$. The maximum values of $u^2 1/2 (f_s)/U_0$, taken from Figure 14, show an absolute maximum at $r_x = 1.3 \text{ inch}$; the intensities grow from $u^2 1/2 = 0.16 U_0$ to a maximum $0.29 U_0$. This, according to the Bearman⁵ criterion, signifies the end of the vortex formation region. The correlation coefficient evaluated at constant phase is determined by $R_{pu}(r_x, \tau_m)$, where τ_m increases from zero, and it essentially correlates the pressure with a single vortex as it moves downstream. We shall call this the moving-eddy correlation, and it shows that although the coherence is greatest at the end of the formation region $r_x = \lambda_f$, its magnitude essentially follows that of $u^2 1/2 (f_s)$. The correlation coefficient based on $u^2 1/2 (f_c)$, therefore, is unity which simply means that the pressure is caused entirely by a fully coherent vortex street. The values of the time delay τ_m for the moving-eddy correlation are shown at the location of Figure 17. The varying slope in the curve of τ_m versus r_x shows that when the vortex begins to form from the free shear layer, the pressure is generated instantaneously on the surface of the strut. As the vortex continues to

form, it begins to move downstream from the strut while its strength increases. This acceleration continues until $r_x = 1.3$ inch, at which point the acceleration diminishes, and it begins to move with a slowly varying speed of convection. The convection velocity, defined as $\bar{U}_c = \Delta r_x / \Delta \tau_m$ at this point is $\bar{U}_c \approx 0.64 U_o$. This convection velocity, based on the moving-eddy correlation, was also obtained by using a pair of hot wire anemometers and forming velocity space-time correlations. The points obtained in the near wake have been included in part d of Figure 16, and they fully corroborate the pressure-velocity correlation. In the far wake, i.e., for $r_x = 9$ inches or $r_x/h = 4.5$, the velocity correlations give $\bar{U}_c = 0.81 U_o$. According to the Bearman⁷ measurements of velocity correlations, the convection velocity of disturbances in the wake became constant and equal to $0.88 U_\infty$ for $r_x/h > 4$.

To construct a geometric picture of the vortex structure we use the convection velocities, determined from the data of Figure 16, and the frequency of shedding f_s to determine streamline vortex separations b from the relationship

$$\bar{U}_c = f_s b$$

Convection velocities are shown at the bottom of Figure 17. In the near wake, the spatial correlation of Figure 16a is interpreted to show that the first, growing vortex is formed at $r_x = 0.5$ inch downstream from the edge. At the same time, the vortex, shed one-half cycle earlier from the opposite corner of the edge and grown to full strength, has moved to $r_x = 2.1$ inches. The cross wake position of the vortex centers in the near wake can be estimated by using the Schaefer and Eskinazi (1959)²¹ semiempirical result, which roughly locates the vortex cores between $y = 0$ and $y = y_o/2$. Using these guidelines, locations of vortices in the near wake can be estimated and they are shown in Figure 15. In this diagram the circles signify vortex core sizes, and the arrows show the direction of circulation. The diagram shows the size of the first vortex,

not fully grown at $r_x = 0.5$ inch, which could not be established using the previously described criteria so the size shown in the figure is the largest that can be accommodated by the geometry. The dotted line is the locus of the secondary maxima of u^2 (f_s)^{1/2}, and it is interpreted as the boundary of the region of secondary flow at the trailing edge.

Also shown in Figure 17 is the streamwise distribution of the root-mean-square fluctuating pressure, which has been normalized on the dynamic head of the free stream. It is shown that the wake-induced pressure diminishes to one-third its value at the tip within only one trailing-edge thickness. These levels were obtained from dimensionless spectra such as those in Figure 15. In the latter figure the frequency of shedding has been made dimensionless on the cross-wake distance between filtered turbulence maxima $y_o = y_f$, evaluated at $r_x = \ell_f$ and a speed U_s , characteristic of the shear-layer at the point of separation. This speed has been defined by Roshko⁸ through the theory of potential flow to be related to the static base-pressure coefficient by

$$U_s = U_\infty \sqrt{1 - C_{p_b}} \quad (12)$$

The dimensionless filtered-pressure levels show a maximum at a dimensionless frequency $\omega_s y_f / U_s = 1$. The bandwidth of the pressure levels appears greater for a speed of 50 than for 100 ft/sec; however, at both speeds the bandwidths of the measured pressures are controlled by the filter for which the dimensionless bandwidths are $\Delta\omega y_f / U_s = 0.09$ and 0.18 for 100 and 50 ft/sec, respectively. Also apparent are the lower magnitude harmonics of the fundamental pressure fluctuations. For $\omega y_f / U_s < 3$, the broadband-pressure levels at the tip are a factor of 6 to 10 in excess of those measured upstream at position 6, $r_x = -13$ inches. At the latter position, spectrum levels are typical of those measured in turbulent boundary layers with vanishing streamline pressure gradient.

Correlations of the periodic pressures along the span were determined at a speed of $U_\infty = 100$ ft/sec for microphone separations to $r_z = 4$ h.

These correlations have been normalized on the mean-square pressure, which was uniform along that portion of the span used for the measurement.

This correlation is written

$$R_{pp}(r_z, \tau) = \frac{\langle p(z, t) p(z+r_z, t+\tau) \rangle}{[p_z^2(z, t) p_z^2(t, z+r_z)]^{1/2}} \quad (13)$$

and the measurements behave as $A \cos(\omega_s \tau + \alpha)$, where A and α are separation-dependent amplitude and phase functions approaching unity and zero, respectively, as $r_z \rightarrow 0$. The space-time correlations indicated that A was a slowly varying function of time delay τ . The correlations at $\tau = 0$ produced the lateral coherence function $A \cos \alpha$; at time delays $\tau_m = \alpha/\omega_s$, they produced the maximum correlation amplitude A . The angle α is related to the yaw angle ϕ made by the vortex filaments with the trailing edge by the relationship $\alpha = (\omega_s r_z \tan \phi)/U_s$. The data shown in Figure 18 are for both of these correlation functions. The scatter for $R_{pp}(r_z, \tau = 0)$ was caused by the slow variation of this function with time, reflecting that ϕ was not constant. The phase of the correlation α , in fact, varied between zero and the absolute value reflected by the data given in Figure 18. This was determined by measuring the correlation with short averaging times. The data indicate that the vortex filaments were shed at yaw angles to $\phi = 17$ degrees. Since $|R_{pp}(r_z, 0)| \leq R_{pp}(r_z, \tau_m)$, the data of Figure 18 show that for $r_z > 4$ h the lateral correlation will have some negative values with an absolute value less than 0.2. A correlation length defined as

$$l_z = \int_{-\infty}^{\infty} |R_{pp}(r_z, 0)| dr_z \quad (14)$$

is indicated by the data to be on the order of $\lambda_z \approx 4 h$. Similarly defined correlation lengths have been found for vortex streets behind cylinders to be as low as 3 and as large as 10 cylinder diameters, and they depend on Reynolds number.

4.2 WAKE BEHIND 45-DEGREE--ROUNDED-BEVELED TRAILING EDGE

Our discussion of this edge will parallel that of the blunt edge. When the trailing edge is unsymmetrically rounded, using the 45-deg angle and a 5-inch fairing radius of curvature as shown in Figure 1, the separation point for the boundary layer on the curved side becomes less distinct. This degree of disorder as well as the streamwise displacement of the free-shear layer formation points detunes interaction. Characteristics of the boundary layer and near-wake are shown in Figure 19. The figure shows a favorable pressure gradient upstream from tap 11, followed by an adverse gradient downstream from this point and constant pressure downstream from tap 13. Observation of oil-streak patterns disclosed concentrations of oil along spanwise-oriented lines at taps 13 and 17. The former is interpreted as an upper separation point; the latter, as the stagnation point for the trailing edge. The constant static pressure and the oil-film patterns indicate that flow is separated downstream from tap 13.

The center diagram of Figure 19 shows the mean velocity profiles in the trailing-edge region. The profile at position G is given in dimensionless form in Appendix B. Speeds measured at various points above the surface have been made dimensionless by using a local approximation of the free-stream speed U_∞ , which was determined at each measurement station. The bulge in the profile at tap 11, showing a somewhat higher speed near the wall than in the outer flow reflects the negative pressure coefficient at this point. It is apparent that Equation (1) is not satisfied by the data because unity minus the square of the measured U_0/U_∞ , where U_0 is the local maximum speed just outside the

boundary layer, does not equal the minimum pressure coefficient at the corresponding point. The discrepancy is probably due to an error in measuring U_∞ , determined at this chordwise location about 1.5 inches above the surface.

The velocity profiles show the flow reversal, which is characteristic of regions of separated flow. Profiles of broadband, root-mean-square velocity fluctuations are also shown, and they display local maxima at distances from the wall corresponding to maxima in the vertical gradient of mean velocity dU/dy . The velocity spectral densities, measured at $U_\infty = 100$ ft/sec, disclosed a periodic contribution at $\omega = \omega_s$, which is interpreted as due to a vortex street. Profiles of narrowband fluctuating velocity, filtered in 1/10-octave bands at the shedding frequency $\omega = \omega_s$, $u^2 \frac{1}{2} (f_s)/U_o$, are shown at the bottom of Figure 19. Above the surface of the edge and in the wake at downstream distances $r_x > 1$ inch, there are maxima corresponding to maxima in dU/dy . Very near the edge, there are secondary maxima which are proposed to be associated with a secondary vortex system similar to that already proposed behind the blunt edge. In contrast to the wake of the blunt edge, however, there is an asymmetry in the wake which persists at least 5 inches downstream from the trailing edge. In this case, local maxima in filtered intensities occur at the upper and lower cross wake positions $y = y_u$ and $y = y_l$, respectively. The characteristic cross wake dimension is, then, $y_o = y_u - y_l$.

A characteristic shedding velocity U_s will again be defined in terms of the pressure coefficient $-C_{p_s}$ beneath the separated boundary layer downstream from tap 13. Following the Roshko⁸ definition we write

$$U_s = U_\infty \sqrt{1 - C_{p_s}} \quad (12)$$

This is the same as the separation velocity of the blunt edge. Spectral densities of the wake-velocity fluctuations $\Phi_u(\omega)$ are nondimensionalized on the wake variables y and U_s in Figure 20 (the spacing y_f will be calculated later). The mean-square velocity is

$$\overline{u^2} = \int_{-\infty}^{\infty} \phi_{uu}(\omega) d\omega \quad (15)$$

At a distance $r_x = 1.25$ inch downstream from the edge, and $2y/h = 1.10$ above the tip, the dimensionless spectra show the periodic contribution at $\omega_s y_f / U_s = 1$ for $U_\infty = 100$ and 50 ft/sec. The intensity of the contribution is substantially higher at 100 than at 50 feet per second. Velocity fluctuations at $U_\infty = 50$ ft/sec and $2y/h = 0$ are entirely broadband. A similar nondimensionalization of fluctuating surface pressures on the edge also shows a periodic contribution at $\omega_s y_f / U_s = 1$. Figure 21 shows the dimensionless spectra of narrow-frequency-band (12.5-Hz) levels of mean-square spectra at positions 6 and G. For $U_\infty = 100$ ft/sec, the periodic contribution is greatest at position G and substantially diminished at position 6. At 50 ft/sec, the spectrum at position G shows a broadly peaked contribution which contrasts the weak periodicity indicated by the velocity spectrum of Figure 20. It appears that the pressure fluctuations extant on the edge at 50 ft/sec are determined more by local separation than by the vorticity in the wake field. At 100 ft/sec, the pressures generated by the wake field are dominant.

Further corroboration for this hypothesis is given by the space-time cross-correlations between the unfiltered trailing-edge pressure at position G and the wake-velocity fluctuations filtered in 1/10-octave bands at $f = f_s$, similar to those of the previous section. For $U_\infty = 50$ ft/sec, correlations between the pressure fluctuations at position G and the wake velocities along $y = y_u$ and $y = y_l$ are shown in Figure 22. Normalized on the root-mean-square pressure at G and the mean velocity U_0 , the spatial correlation along the locus (r_x, y_u) shows a minimum of $R_{pu}(0, r_x, y_u) = -0.04$ over the edge whose absolute value is never exceeded for $r_x > 0$. This shows that instantaneously the pressure at position G is dominated locally by separation. The correlations also

show that the shear layers along y_u and y_l interact to form a coherent wake; however, the level of coherence with the pressure at position G decreases as r_x increases. The spatial correlation indicates that the formation of vortices from the upper and lower shear layers, although facilitated by mutual interaction of the layers, does not involve total entrainment of one layer by the other. Figure 22a suggests that the upper layer forms a vortex first near $r_x = 1$ while the lower layer forms a vortex near $r_x = 1.5$ inch. This indicates a lag on the order of one-eighth wavelength. Further downstream, the mutual interaction brings the vortices into a more coherent alignment.

This interpretation of the spatial correlation is also supported by the growth of the root-mean-square--filtered-velocity fluctuations of Figure 19. The local maximum values of filtered disturbances for both shear layers are shown as a function of r_x in Figure 22b. Along $y = y_u$ the disturbances filtered at $\omega = \omega_s$ grow to a maximum at a distance between $1.5 \text{ inch} < r_x < 3 \text{ inch}$, downstream but along $y = y_l$ the disturbances grow to a maximum at $r_x = 1$ inch. The growth and streamwise coherence of the disturbances shown by Figures 22a and 22b indicate that the development of regularly spaced vortices is weakened by the relatively independent behavior of the upper and lower shear layers as compared to that behavior of those shed from the blunt edge.

The growth and decay of a given eddy as it moves downstream from position G as indicated by the moving eddy correlation is shown in Figures 22c and 22d. The time τ_m has been defined from the maximum magnitude of the space-time correlation as

$$|\tilde{R}_{pu}(r_x, \tau_m)| > |\tilde{R}_{pu}(r_x, \tau)|$$

where r_x is fixed. Along the trajectory of the upper shear layer $y = y_u$, the absolute value of the correlation grows to give a minimum at $r_x = 1.5$ inch, $R_{pu}(1.5 \text{ in.}, \tau_m) = -0.052$. Along the lower trajectory,

the value of the space-time correlation is taken at the time delay of maximum positive correlation since we are interested in a contribution 180 deg out of phase with the observed eddy at $y = y_u$. This phase reversal is dictated by the necessity for the vortices of each shear layer to be of opposite sign. The correlations in the upper and lower shear layers do not become matched until $r_x > 2$ inches; the time delays τ_m become nearly equal at this distance.

The behavior of the near wake for the 45-deg round edge is strongly dependent on Reynolds number as can be seen now by reference to Figure 23. The correlation measurements were repeated for $U_\infty = 100$ feet per second. In contrast to the case of low speed, the disturbances from both layers are seen to grow to maxima at $1.5 \text{ inch} < r_x < 2 \text{ inches}$ with the spatial correlation increasing dramatically with distance downstream from the tip of the trailing edge. In this case $\tilde{R}_{pu}(r_x, 0) \leq 0.1$, and $r_x > 0$, compared to $\tilde{R}_{pu}(r_x, 0) \leq 0.023$ for $r_x > 0$. The contribution to the total pressure fluctuation by the local separation is notably reduced, compared to the contribution at $U_\infty = 50 \text{ ft/sec}$ as shown by the lower correlation magnitude for $r_x < 0$. It is worthwhile to note that the root-mean-square pressure that was used to normalize the correlation is the broadband pressure, $\overline{p^2}^{1/2}$. Reference to Figure 21 shows that while the periodic pressures are higher and dominate the signal at $U_\infty = 100 \text{ ft/sec}$, the broadband pressures are dominant at $U_\infty = 50 \text{ feet per second}$. For this reason, $\overline{p^2}^{1/2} / q_\infty = 1.13 \times 10^{-2}$ at 100 ft/sec; however, $\overline{p^2}^{1/2} / q_\infty = 2.6 \times 10^{-2}$ at 50 feet per second. Thus it appears that even though a development of the periodic wake is weak at low speeds, the continuous spectrum pressures due to the local separation are important. The moving-eddy correlation $\tilde{R}_{pu}(r_x, \tau_m)$ for $U_\infty = 100 \text{ ft/sec}$ not only reflects the pronounced wake development but the values of τ_m show small $\Delta\tau_m / \Delta r_x$ for small r_x . This is behavior quite similar to that observed for the blunt edge. Also, the values of $\tilde{R}_{pu}(r_x, \tau_m)$ for the upper and lower shear layers are more nearly matched at $U_\infty = 100 \text{ feet per second}$.

A wake structure for $U_\infty = 100$ ft/sec as deduced from the measurements is shown in Figure 24. As in Section 4.1, cores of the vortices are assumed to be bounded by the lines

$$y_u > y > \frac{y_u + y_\ell}{2} \quad \text{and}$$

$$\frac{y_u + y_\ell}{2} > y > y_\ell$$

with a streamwise spacing given by $\tilde{R}_{pu}(r_x, 0)$ in Figure 23. The dotted line near the trailing edge circumscribes both the region of flow reversal as well as the locus of secondary maxima in $u^{1/2}(f_s)$ as shown in

Figure 19 for small r_x . Root-mean-square filtered pressures $\overline{p^2}^{1/2}(f_s)/q_\infty$ are shown to have a maximum at position $G(r_x = -1.1)$. At the downstream position ($r_x = -0.4$) the periodic contributions are missing; this position is nearly coincident with the stagnation point $r_x = -0.6$. The convection velocities

$$\frac{\overline{U_c}}{U_\infty} = \frac{1}{U_\infty} \frac{\Delta r_x}{\Delta \tau_m} \quad (16)$$

as determined from Figure 23 show a maximum at $r_x = 0.8$ along $y = y_u$. Here the velocity disturbance is approximately 180 deg out of phase with the fluctuating pressure at G, and its phase slowly varies as the eddy moves downstream. Along the lower layer $y = y_\ell$, an opposite behavior appears; the disturbance convection velocity decreases slightly. This contrasting behavior could be caused by an uncertainty in determining the peak in the space-time correlation and would be discounted altogether, except that Hanson¹⁰ made a similar observation in the wake behind a notched, lifting airfoil. He observed convection velocities on the

order of $1.7 U_s$. The current measurement indicates that the upper disturbance speeds up briefly, while the lower disturbance is convected at a lower speed. The formation length defined as the distance from the stagnation point on the foil to the value of r_x for the maximum in the filtered velocity fluctuation, is taken to be $\ell_f = 2.3$ inches. This nearly corresponds to the location of the minimum shear layer spacing $y_o = y_u - y_l = y_f$.

4.3 CHORDWISE DISTRIBUTION OF FLUCTUATING PRESSURE

Figures 17 and 24 show that the root-mean-square pressures on each edge decrease with increasing upstream distance from the extremity of the edge. In Figure 25, mean-square filtered, 12.5-Hz pressures* for each edge are shown together as a function of distance from the stagnation point ($x-x_s$). The measurements were made on each edge for two speeds, and the pressures, normalized on the dynamic head, have been grouped for a given edge shape. The chordwise variation for the blunt edge is less dependent on speed than for the 45-deg round edge. This difference could be due to the occurrence of three dimensionality associated with a finite, spanwise correlation of the vortex streets. In this regard, recall that Figure 18 gives a spanwise correlation length $\ell_c = 4 h = 8$ inch. The data of Figure 25 show that forward of the blunt edge for $(x-x_s) > 10$ inches, the rate of decrease of pressure with further distance is more pronounced. This suggests a three dimensionality effect on the chordwise pressure distribution which may be speed dependent. On the 45-deg round edge, the less rapid reduction in fluctuating pressure with distance at $U_\infty = 200$ ft/sec could be attributed to greater spanwise coherence at the greater speed. Unfortunately, spanwise correlation measurements were not made for this edge.

A dimensional argument for scaling these pressure distributions is derived from the estimated wake structures in Figures 17 and 24. For

* Filter bandwidth was greater than bandwidths of pressures.

a vortex situated at λ_f downstream from the stagnation point, the local pressure exerted on the strut at x is assumed to be determined in a general functional form by

$$\frac{p(x, x_s)}{\rho} = -U_s \frac{\kappa}{\lambda_f} g\left(\frac{x-x_s}{\lambda_f}\right) \quad (17)$$

where U_s is the shedding velocity defined earlier on the basis of the static pressure coefficient in the trailing-edge separation region

$x-x_s$ is the position of the vortex relative to the edge

κ is the strength of the vortex.

The influence function $g((x-x_s)/\lambda_f)$ specifies that the pressure at a point is governed only by the distance to the vortex. The function is, in general, dependent on the shape of the edge. For a periodic vortex sheet, the individual vortices are correlated with a specific spatial relationship so that the formation length, which locates the first vortex pair relative to the edge, is a dominant space variable.

The characteristic strengths of the vortices in the wake are determined by the core radii r_o given in Figures 17 and 24 and the root-mean-square filtered intensities u^2 $^{1/2}$ (f_s) of Figures 16 and 23. The second vortex is considered to be characteristic of the wake because for each edge it is the first vortex immediately downstream from formation. In the case of the blunt edge, $4r_o/h \approx 0.8$, and u^2 $^{1/2}$ (f_s) = $0.29 U_o$ so that we approximate

$$\kappa = \sqrt{2} \cdot 2\pi u^2$$

$$\kappa = 0.52 U_o h \quad (18)$$

as the typical vortex strength. Greenway and Wood⁴ have estimated that

$$0.5 < \kappa/U_{\infty}h < 1.2$$

from their flow visualization of blunt-edge flows at chordwise Reynolds numbers of 1.4×10^4 . At the decade higher Reynolds number of the current measurements, taking $U_o \approx U_{\infty}$, the vortex strength appears to be slightly reduced. For the 45-deg round edge, $4r_o/h \approx 0.5$, and $u^{1/2}(f_s) = 0.11 U_o$, so that $\kappa = 0.12 U_o h$. Thus rounding the trailing edge not only decorrelated the wake but also reduced the coherent vortex strength.

The normalization of Equation (17) describes a universal distribution function. To test its validity, the data of Figure 25 have been replotted in a dimensionless form, utilizing l_f as a length scale in Figure 26. The pressures appear to be well defined by these variables-- some points for 200 ft/sec have been ignored in this representation. Using reciprocals of integral powers of distance we find that a series combination of $(x-x_s)^{-1}$ and $(x-x_s)^{-3}$ would probably describe the dimensionless distribution over a significant range of the variable $(x-x_s)/l_f$.

4.4 VORTEX SHEDDING FREQUENCY: UNIVERSAL STROUHAL NUMBER

The vortex shedding frequency has been shown by Figures 15 and 20 or 21 to scale on the shedding speed U_s and the near-wake length scale y_f . An alternative nondimensionalization which has been suggested by Hanson¹⁰ involves the momentum thickness of the wake at formation θ_f where

$$\theta_f = \int_{-\infty}^{\infty} \left(1 - \frac{U(y)}{U_o} \right) dy$$

His data for lifting airfoils show that the Strouhal number

$$S_{\theta} = f_s \theta_f / U_s$$

is a universal function of the Reynolds number $U_s \theta_f / \nu$. However, the data for the current edges only partially support this definition of Strouhal number.

Figure 27 shows the Hanson results as dots together with the points which apply to the current experiments. The curve drawn through the points follows the empirical equation

$$S_{\theta} N_{R_{e_{\theta}}} = 0.0728 [N_{R_{e_{\theta}}} - 1038] \quad (19)$$

which was determined by Hanson and which is similar to that determined by Roshko.⁸ The dimensionless frequency for the shedding from the blunt trailing edge is only one-half that given by the 45-deg, round edge and by Equation (19). Apparently, the momentum thickness of the wake at formation is not a universally applicable length scale for the shedding frequency. A distinguishing feature of blunt edge, compared to the 45-deg, round edge and the edges of the Hanson study, seems to be the base-pressure coefficient which is $(-C_p)_B = 0.51$ in the first case and less than $(-C_p)_B = 0.3$ in all of the later cases. The Bearman⁵ and Hanson¹⁰ investigations with splitter plates have shown that an increase in base-pressure coefficient accompanies a reduction in formation length. Also, a relatively low base-pressure coefficient represents more complete pressure recovery by the flow and this in turn implies that less momentum has been transferred to the wake in the form of fluid unsteadiness at the trailing edge. The loss of momentum from the mean flow downstream from the edge, which determines θ_f , must be balanced by the increase of unsteady fluid momentum. The growth of the regular disturbances associated with periodic vortex streets is undoubtedly accelerated by the presence of this unsteady motion; however, it is

probably not fully governed by it. Thus the wake momentum thickness, while being representative of the overall loss of momentum from the mean flow, may not be expressive of the dynamical conditions necessary for the formation of a periodic vortex street. The conditions favorable for the formation of regular disturbances might be expected to be governed by θ_f rather than by a geometric dimension of the trailing edge, e.g., the lateral distance between the flow separation points, if the vortices are formed far enough downstream from the trailing edge that extraneous flow disturbances associated with the immediate separation region decay. This is probably not the case for very blunt trailing edges with high base-pressure coefficients where vortices are formed close to the edge but may be possible for smoother edges with lower C_{p_b} .

The formation of the regular vortex street from the shear layers leaving the shedding body will depend on the level of vorticity associated with each layer as it is shed as well as on the cross-wake distance between the layers. The following discussion will show the motivation for suggesting y_f as an alternative to θ_f as a length scale. Some theoretical work has been performed to examine the influences of these factors. Abernathy and Kronauer (1962)²² have performed calculations of the growth of disturbances in idealized parallel shear layers. The degree of shear-layer interaction for a given streamwise wavelength of disturbance was shown to depend on the separation of the layers. A breakdown in the shear layers, due to instability to small disturbances, was shown to occur with the resultant formation of identically structured concentrations of vorticity. The spatial structure of these disturbances, which resembled that of a von Kármán vortex street, motivated Abernathy and Kronauer²² to speculate that there is a unique relationship between the wavelength of the initial disturbance and shear-layer separation distance which is most likely to generate a periodic vortex street. Physically, thin sheets of vorticity, such as those which are assumed

²²Abernathy, F.H. and R.E. Kronauer, "The Formation of Vortex Streets," Journal of Fluid Mechanics, Vol. 13, pp. 1-20 (1962).

in the idealized calculations of Abernathy and Kronauer,²² appear to have existed only in the immediate vicinity of the blunt trailing edge as shown in Figure 14. They are not apparent at all behind the 45-deg round edge (Figure 19) where the shear layers are relatively thick. To examine the stability of disturbances in wakes which are characterized by thick shear layers similar to those of the round edge (Figure 19) a stability analysis has been performed by Sato and Kuriki (1961).²³ They found that at large Reynolds numbers, small disturbances of a wide range of wavelengths could be amplified and that the rate of the amplification was determined by the inflection points in the mean velocity profile. The calculations were verified by measuring disturbances in the wake of a thin flat plate. The distance between the inflection points of the Sato and Kuriki²³ profile was essentially analogous to the shear layer separation of Abernathy and Kronauer.²² Also, the amplitudes of the growing disturbances were observed by the Sato and Kuriki²³ combined measurement and calculation to be maximum at the inflection points of the mean velocity profile.

The wake stability calculations described in Appendix C were performed for a variety of profile shapes of the general form of those in Figure 19. They have further demonstrated that the frequency of the least stable disturbances in each case depends more on separation of the inflection points than on the momentum thickness of the wake. The momentum thickness of each profile is shown to be not uniquely related to the shear-layer separation for the set of profiles considered.

These considerations motivate the selection of y_f as an alternative to θ_f as a near wake-length scale for the spectra of Figures 15 and 20 or 21. Use of U_s as a speed scale is motivated by the view that it is representative of the speed of the shear layer as it leaves the shedding body. Further evidence from past investigations for the use of this frequency scaling is scant because y_f is not available in the literature.

²³Sato, H. and K. Kuriki, "The Mechanism of Transition in the Wake of a Thin Flat Plate Placed Parallel to a Uniform Flow," Journal of Fluid Mechanics, Vol. 11, p. 321 (1961).

Neither the formation length nor y_f were determined in earlier investigations other than those of Bearman⁵ and of Hanson.¹⁰ The measurements of Hanson¹⁰ which are among the most extensive in this regard are not complete enough to determine y_f very precisely. Table 3 shows the best estimates of $\omega_s y_f / U_s$ which can be extracted from data by Bearman and Hanson.

TABLE 3 - STROUHAL NUMBERS

Edge Shape	$\omega_s y_f / U_s$	Position of y_f
Blunt ⁵	0.97	1.0 l_f
Blunt with splitter plate, ⁵ $l/h=1$	0.92	1.0 l_f
Notched lifting ¹⁰ ($N_{Re\theta} = 6900$)	0.78	0.3 l_f
Notched lifting ¹⁰ ($N_{Re\theta} = 4800$)	0.83	0.5 l_f
Splitter, ¹⁰ $l/h=1$ ($N_{Re\theta} = 5930$)	0.91	0.4 l_f
Splitter, ¹⁰ $l/h=1$ ($N_{Re\theta} = 9800$)	0.94	0.5 l_f

The wake position downstream from the trailing edge at which y_f is estimated has also been listed. It is pertinent to note that the lowest value of $\omega_s y_f / U_s$ occurs for the case of y_f measured only 0.3 l_f downstream from the edge. Because of wake spreading we would expect the actual value of y_f to be somewhat greater than that used here. This nondimensionalization appears to scale the shedding frequency within 20 percent.

Bearman⁷ has suggested an alternative scaling based on far-wake variables. This scaling is based on the Kronauer⁹ stability criterion which states that the stable cross-wake spacing b of the vortices in a wake with a periodic vortex street is of such a nature that a minimum

drag is exerted on the body. The Bearman universal Strouhal number $S_B = f_s b / U_s$ was determined from the far-wake data of both the blunt and 45-deg-round edges using his calculation procedure. The values are shown in Figure 28 as a function of shedding velocity U_s / U_∞ ; agreement with the trend of earlier data continues to support the Bearman definition.

4.5 SUMMARY: PERIODIC VORTEX STREETS

The temporally periodic pressures that are generated on a strut by the formation of a von Kármán vortex street have been quantitatively related to the position of the first fully formed vortex in the wake as well as to the strengths of the vortices. This relationship gives the chordwise variation of the magnitude of the pressure as a function of the distance upstream from the edge stagnation point expressed in multiples of the vortex formation length. This similarity function appears to be independent of both the speed and the edge geometry over the range of variables considered. Some influence of the spanwise coherence of the vortex street on the chordwise behavior is indicated. A spanwise coherence length of approximately four edge thicknesses was observed for the blunt edge. For a fixed formation length, the magnitude of the pressure is directly proportional to the strengths of the vortices. Development of the vortex street was suppressed at low speeds behind the 45-deg-round edge; disturbances decayed as they were convected downstream from the edge. In this case periodic pressures could not be detected on the strut. At higher speeds the spatial wavelike growth of disturbances, typical of the blunt-edge wake, was detected, and periodic pressures were generated. At the lower speeds, however, even though the periodic disturbances were suppressed, high-level, continuous-spectrum pressures were generated by the local boundary-layer separation.

The frequency of vortex shedding was found to be given by two Strouhal numbers which are based on either the near- or far-wake variables. The near-wake momentum thickness was verified as a

characteristic length for the shapes with low base-pressure coefficients. The estimated shear layer separation at the end of the formation region was found to be a characteristic length with more general application. The Bearman⁷ far-wake Strouhal number, based on the Kronauer⁹ stability criterion, was found to agree with the current data.

5. SEPARATED FLOW AT BEVELED TRAILING EDGES

The remainder of the report will be concerned with flow near the nonsinging edges of Figure 1. In these cases the boundary layers incident on the edges experience adverse pressure gradients before being shed by the strut. For nonsymmetrical edges, the flow on one side of the strut separates far enough upstream from the apex, or tip, of the trailing edge that periodic vortex street are not formed. This section describes the mean and unsteady velocities that occur on two trailing edges; Section 6 will describe the characteristics of fluctuating pressures that are generated for each case in the separation process. The purpose of these sections is to account for the separated flow field which has been shown in the last section to induce high-level, continuous-spectrum pressures.

5.1 TURBULENT FLOW NEAR 25-DEGREE-- KNUCKLE-BEVELED EDGE

As the boundary layer approaches the edge, it first experiences a favorable pressure gradient, followed by an adverse gradient just downstream from the knuckle. This is shown in Figure 29 for the two tunnel speeds $U_{\infty} = 50$ and 100 feet per second. The pressure recovery appears to be more apparent at the higher speed since the pressure coefficients are less negative at 100 than at 50 feet per second. Boundary-layer characteristics were obtained at the positions A through F on the surface of the edge as well as in the near wake downstream from the edge. These positions are shown for reference in Figure 29. Before discussing the measurements it is appropriate to mention that an oil-streak experiment--identical to that described in Sections 3 and 4--showed separation at position E. Oil accumulated in a streak

one-tenth of an inch in width at the downstream edge of the knuckle. The streaks were stagnant downstream from position F. This indicates a steady separation at the knuckle followed by a large-scale and intermittent separation zone further downstream.

Results of a survey of the boundary layer on the edge, performed at $U_{\infty} = 100$ ft/sec, are shown in Figure 29. Expanded and normalized versions for speeds of 50 and 100 ft/sec are shown in Appendix B. Table 1 gives thickness parameters for the boundary layer. At position E, which is one-tenth of an inch downstream from the knuckle, no evidence of the flow reversal that accompanies separation could be found. A single hot wire anemometer probe is expected to sense the absolute value of the mean velocity in the boundary layer; however, a sign change in the vertical gradient $\frac{d|U|}{dy}$, where $|U|$ is the magnitude of the mean velocity in the boundary layer, should indicate a reversal in flow. This sign change was not detected at any location on the trailing edge. The profile at position F shows a vanishing velocity gradient near the wall and that at position H shows a nearly vanishing gradient at the tip of the edge. The linearized, broadband, root-mean-square turbulence intensities of the boundary layers are also shown as dotted lines for each location. These profiles show two important features. The first is the display of local maxima in turbulence intensity which coincide with maxima in the vertical gradients in mean velocity. These local maxima show absolute maxima in excess of $\overline{u^2}^{1/2} / U_0 = 0.23$, which occurs near position H. The intensity at position I is comparable to that at position H. The second feature is that near the wall; where $dU/dy = 0$, the gradient $\frac{d}{dy} \left(\frac{\overline{u^2}^{1/2}}{U_0} \right)$ also vanishes. Furthermore, at position F the root-mean-square turbulence intensity in this region near the wall is approximately one half the measured local mean velocity. Peak fluctuations of velocity, therefore, probably exceed

the mean velocity near the wall. Lines of constant speed, which describe streamlines, have been drawn in Figure 29. The dashed line encloses the region near the wall for which $dU/dy \approx 0$.

The short dashed lines in the drawings of the mean velocity profiles at positions F and H reflect the interpretation that the flow near the wall is oscillatory. The nature of this oscillation is shown by reference to the space-time correlation of the streamwise component of velocity at position F. A pair of anemometer probes was positioned a distance n above and in the plane with the surface of the strut. In the plane of the edge surface, therefore, the probes were separated in the streamwise direction a distance $r_s = 0.5$ inch and in the lateral direction a distance $r_z = 0.13$ inch. Since the probes were at a common height from the edge, they were nominally separated a distance $r_n = 0$. Correlations were measured at various distances above the wall as the probes were traversed together along the y axis. The correlations were normalized as

$$R_{uu}(\bar{x}, \bar{r}, \tau) = \frac{u(\bar{x}, t) u(\bar{x} + \bar{r}, t + \tau)}{[u^2(\bar{x}, t) u^2(\bar{x} + \bar{r}, t)]^{1/2}} \quad (20)$$

Coordinates \bar{x} pertain to the location of the reference probe. The separation coordinates \bar{r} are measured in the plane of the edge. The interpretation of Favre, Gaviglio, and Dumas (1957)^{24,25} is given to the correlations. The results are shown in Figure 30 for reference probe distances $y = 0.1, 0.25, 0.15, 1.0$ inch from the wall at position F and for $U_\infty = 50$ feet per second. Reference to Figure 29* shows that the position $y = 0.5$ nearly corresponds to the local maximum in turbulence intensity at position F. At a greater distance above the edge, $y = \delta = 1.0$ inch, the cross correlation shows a maximum at a time delay

²⁴Favre, A.J. et al., "Space Time Double Correlations in a Turbulent Boundary Layer," Journal of Fluid Mechanics, Vol. 2, p. 313 (1957).

²⁵Favre, A.J. et al., "Further Space-Time Correlations of Velocity in a Turbulence Boundary Layer," Journal of Fluid Mechanics, Vol. 3, p. 344 (1957).

*Velocity profiles for $U_\infty = 50$ ft/sec and for and for $U_\infty = 100$ ft/sec are similar.

$t_c = 0.7 \times 10^{-3}$ seconds. This defines a convection velocity

$$\frac{\bar{U}_c}{U_\infty} = (r_s/\tau_c)U_\infty = 1.2 \quad (21)$$

That $\bar{U}_c > U_\infty$ is of no concern, since the direction of the vector or mean flow probably does not coincide with the direction of the vector of separation so that the measured convection velocity deviates from the actual convection velocity, e.g., U' by

$$U_c = U'/\cos \theta \quad (22)$$

where θ is the angle between the vectors just mentioned. At the maximum of turbulence intensity $y = 0.5$ inch, maximum correlation is reduced considerably, and it occurs at a larger time delay. This is consistent with slower convection closer to the wall. Still closer to the wall at $y = 0.25$ inch, corresponding to the outer limit of the region where $dU/dy = 0$, the maximum correlation is increased, and it occurs at $\tau = 0$. This indicates that the fluid disturbances here occur simultaneously at both probes. Near the wall, at $y = 0.1$ inch, the maximum correlation increases in magnitude, yet it remains at $\tau = 0$. The correlations near the wall are marked by a skewness toward negative time delays. This lack of symmetry in correlation can be explained by suggesting that two velocity components exist in the flow at this position. The strongest component, with the largest correlation at $\tau = 0$, is not convected; a weaker component, indicated by a reduced maximum correlation value at $\tau < 0$, is convected upstream or opposite to the direction of mean flow.

Correlations between probes positioned vertically, $r_s = 0$ and $r_n \neq 0$, are shown in Figure 31. The reference probe is set at $y = 0.1$ inch above the edge. For $r_n = 0.22$ inch, the space-time correlation at $\tau = 0$ is positive. For $r_n = 0.44$ inch, the correlation at $\tau = 0$ is small and negative. At this separation one probe is situated 0.1 inch

above the wall, and the other is set at the point of maximum turbulence intensity. The small and negative correlation at $\tau = 0$ shows that a large and positive--directed downstream--velocity disturbance in the shear layer is weakly associated with a small and negative--directed upstream--velocity disturbance near the wall. The increased negative correlation magnitudes at $\tau = -12$ msec show that this positive velocity disturbance in the shear layer is followed by a negative--directed upstream--disturbance of moderate magnitude. The velocities in the outer flow and those near the surface are in quadrature; a streamline-directed velocity in the outer flow is correlated with a deceleration of the inner flow.

Figure 32 shows spectral densities of the fluctuating velocities* in the region of the trailing edge, normalized on the total mean-square velocity as described by Equation (3). At position F, the dimensionless spectra appear to be similar at all distances from the wall. This suggests that eddies are convected at a velocity proportional and nearly equal to $U(y)$, since a wave number $\omega/U(y)$ can be used to describe the data. Furthermore, this wave number can be nondimensionalized on δ^+ to give dimensionless spectra which are typical of those measured in turbulent boundary layers on flat surfaces. This can be seen by comparing to spectra obtained at position B. Also, we see that the normalization applies for two velocities.

For distances above the wall greater than 0.3δ , this normalization of the spectra can be expected because the space-time correlations (Figure 30) show that the turbulence is convected at velocities which are comparable to those in the boundary layer. Closer to the wall, the correlations in Figure 30 show that for the most part, the disturbances at two streamwise-separated locations are recorded

* It is to be noted that these spectra as well as those in Figure 33 were not all measured in the Anechoic Flow Facility. Some were measured in another, smaller facility during preliminary stages of this work. In the smaller facility slight blockage effects caused thinner boundary layers than those under discussion; however, the dimensionless mean- and turbulent-velocity profiles were basically identical in the two facilities. Thus the dimensionless spectra from those measurements are included here. Where spectrum measurements in the two facilities could be made, the dimensionless data agreed.

simultaneously rather than being convected. The convection indicated by the existence of the dimensionless spectra for $y < 0.3 \delta$ apparently plays only a small part in the near-wall turbulence dynamics. At these distances from the wall, the turbulence is distributed over wave numbers which are large compared to a displacement thickness.

Also apparent in the spectra of Figure 32 are certain peaks at different low dimensionless frequencies which actually occur at the same low frequency. Normalized on the free-stream velocity, the peaks occur at $\omega \delta^*/U_\infty \approx 0.25$. Returning to the correlations of Figure 30, we see that the zero crossing of the correlation for $y = 0.06 \delta$ occurs at $\tau U_\infty / \delta^* = 24$, which corresponds to a characteristic frequency $2\pi \delta^* / U_\infty \tau = 0.26$. The correspondence of these frequencies shows that a large-scale, low-frequency disturbance coexists with small-scale, high-wave-number, convected disturbances. Furthermore, the low-frequency disturbances have a vertical scale between 0.22 and 0.44 inch, indicated by the sign change in the correlations of Figure 31. Examination of the flow pattern at position F (in Figure 29) shows that this distance from the surface corresponds to the upper extremity of the estimated separation region.

The further connection between these measurements and the vortex structure was made using a "visualization" with a series of cotton tufts which were mounted to the strut. Long tufts, 2 inches in length, moved in an intermittent rotary pattern which was alternated with the tufts being swept downstream. Then, in an instant, they resumed their rotary motion. Short tufts, about 0.5 inch in length, were buffeted in an oscillatory motion up and downstream.

These observations present a picture of an unsteady large vortex which is formed and then swept downstream. The core size of this vortex is probably on the order indicated by the closed curve in Figure 29. The process is only weakly periodic, occurring at the approximate frequency $\omega \delta^* / U_\infty \approx 0.25$, or $\omega h / U_\infty \approx 0.6$, where h is the thickness of the trailing edge as indicated by velocity spectra.

We conclude this section with a brief examination of the momentum balance of the boundary layer as it approaches the trailing edge. Bidwell (1951)²⁶ has derived a momentum integral equation for thick boundary layers with streamwise nonuniformity. His relationship gives the wall-shear coefficient as

$$\frac{C_f}{2} - \frac{d\theta}{ds} + \frac{dC_p}{ds} \left(\frac{1+H/2}{1-C_p} \right) = - \frac{1}{U_o^2} \int_0^\delta \overline{\frac{\partial u^2}{\partial s}} dy$$

$$+ \frac{1}{U_o^2} \int_0^\delta \int_0^y \frac{\partial}{\partial s} \left(\overline{\frac{\partial uv}{\partial s}} + \overline{\frac{\partial v^2}{\partial y}} \right) dy dy - \frac{\delta}{U_o^2} \int_0^\delta \frac{\partial^2 \overline{uv}}{\partial s^2} dy \quad (23)$$

All the terms in the equation have been previously defined, except v , which is the vertical (normal) velocity fluctuation. Bidwell assumed that $\overline{v^2}$ vanishes at $y = 0$ and $y = \delta$. In equilibrium boundary layers the terms on the right hand side are negligible, compared to those on the left and so they are neglected. In Figure 33 the mean momentum terms are shown for the flow near the edge at $U_\infty = 100$ feet per second. Upstream of position E, the difference between the momentum loss

$\left(\frac{d\theta}{ds} \right)$ and the pressure gradient terms agrees with the wall-shear coefficient, determined by the curve-fitting procedure outlined in Section 3. At position E, the difference between the mean momentum terms becomes more significant and indicative of the momentum lost from the mean motion and converted into the momentum of unsteady Reynolds stress terms.

²⁶Bidwell, J.M., "Application of the von Kármán Momentum Theorem to Turbulent Boundary Layers," National Advisory Committee for Aeronautics TM 2571 (1951).

5.2 TURBULENT FLOW NEAR 25-DEGREE-- ROUNDED-BEVELED EDGE

The surveys of the boundary layer and the static pressure distribution on the 25-deg--rounded-beveled edge are shown in Figure 34. Downstream of position F, the static pressure was nearly constant for speeds $U_\infty = 60$ and 100 ft/sec; however, the gradient of pressure was adverse downstream 37 inches from the leading edge. The mean velocity defects $U_0 - U(y)$ (for $U_\infty = 100$ ft/sec) increase markedly downstream from this point, while the fluctuating velocities increase to an apparent maximum in the vicinity of positions H and I. The balance of mean momentum (Figure 35) shows that lost mean momentum is not compensated by the pressure gradient at locations downstream from position E-1. This suggests that the boundary layer separated downstream from this point. An examination of the mean velocity profiles, however, shows that the normal gradient $\frac{dU}{dn}$ vanishes somewhere between positions F and G, suggesting that separation occurs in that region. Apparently, the separation occurred near position F. Flow visualization by oil streaks demonstrated that flow separation occurred just upstream from position F. Distinct flow reversal was not clearly disclosed because the very low velocities near the wall were insufficient to cause significant movement of the oil. In drawing streamlines in Figure 34, position F has been selected as the separation point. Inequality of the mean momentum terms at this position as shown in Figure 35 is probably due to the generation of Reynolds stresses as Bidwell²⁶ has pointed out.

Table 2 gives the mean properties of the boundary layer on the rounded trailing edge. Dimensionless velocity profiles are shown in Appendix B. The favorable pressure gradient upstream from position C causes the boundary layer to contract so that its momentum and displacement thicknesses decrease, and the shape factor decreases to 1.14. Although the mean momentum balance (Figure 35) suggests that this is accompanied by an increase in C_f , compared to the values of local skin friction at positions A and B. The survey of the boundary layer was not made with close enough streamwise separations for the calculated momentum integrals to give local values of C_f precisely.

Related investigations are those of Schloemer (1967)²⁷ and of Burton (1973)²⁸ in which boundary-layer turbulence and wall-pressure fluctuations were measured on surfaces with both favorable and adverse pressure gradients. Although the surfaces on which their measurements were made were not trailing edges, the pressure gradients of their measurements can be compared to those of this study. Figure 35 shows that the favorable (negative) gradients of the momentum balance in the current study are significantly greater in magnitude than those examined earlier,* while the range of adverse (positive) gradients examined in the Burton measurement is representative of the attached boundary layer on the 25-deg--rounded-beveled trailing edge. The favorable gradient of the current discussion is more severe than the gradients of the earlier two.

The frequency spectra of the longitudinal velocity fluctuations in the boundary layer show the same property of local convection that has been shown for boundary layers with vanishing pressure gradients. Spectra, normalized as in Equation (3), are shown in Figure 36; the measurements were all obtained in the region of adverse gradient. At position DE, the dimensionless spectra at high frequencies are similar to those which were obtained on the region of the strut for which $\frac{\partial P}{\partial s} \approx 0$. This similarity implies that the small length scale is δ^* , which is typical of the high-frequency turbulence. Also, the dimensionless spectra show that low-frequency motion which probably is caused by large-scale motion is reduced near the wall, i.e., near $y \approx 0.014\delta$, compared

²⁷Schloemer, H.H., "Effects of Pressure Gradients on Turbulent Wall Pressure Fluctuations," Journal of the Acoustical Society of America, Vol. 42, pp. 93-113 (1967).

²⁸Burton, T.E., "Wall Pressure Fluctuations at Smooth and Rough Walls Beneath a Turbulent Boundary Layer with Favorable and Adverse Free-Stream Pressure Gradients," Massachusetts Institute of Technology Acoustics and Vibration Laboratory Report 70208-9 (1973).

* Since pressure coefficients were unavailable in that reporting, the approximation $C_p \approx 0$ was made in order to calculate the momentum terms.

to levels at distances from the wall on the order of δ^* . Near the point of separation at position F, the dimensionless spectra at different heights above the wall are separated into two groups. For $y/\delta > 0.13$ to 0.15 the turbulence is controlled by lower frequency (larger scale) disturbances than at points closer to the wall. An alternative nondimensionalization, suggested by Bradshaw (1967),²⁹ replaces the displacement thickness by the distance from the wall. This operation was performed on the spectra of Figure 36b, and it resulted in a collapse of high-frequency levels into two groups; the first for $y/\delta = 0.025, 0.033, 0.296,$ and 0.466 and the second for $y/\delta = 0.127$ and 0.152 ; see Figure 37. At the latter two distances from the wall, the curvature of the profile of mean velocity nearly vanishes, i.e., $\partial^2 U/\partial y^2 \approx 0$; see Appendix B. Spectra which may be nondimensionalized in this manner have been suggested by Bradshaw to be controlled by eddies in the near-wall region whose sizes are proportional to distance from the wall. At the location above the wall where the mean velocity gradient is maximum, the disturbances appear to be dominated by higher-frequency, wave number, components compared to those at other locations. Also in contrast to the spectra measured at position B, the $k^{-5/3}$ dependence occurs over a very restricted range of wave numbers. In the region of the separated boundary layer, position G, Figure 36c shows that the nondimensionalization on δ^* gives spectra which are generally similar throughout the boundary layer. Also, the spectra are similar to those both at position B and at position F on the knuckle edge for $0.8 < \omega\delta^*/U(y) < 6$. For wave numbers outside this range, the dimensionless spectra at position F on the knuckle edge are dissimilar; however, they are generally greater than those at position G on the round edge. Thus, the large-scale motion on the knuckle edge is more intense than that occurring in the separated region of the rounded edge.

A review of Figures 7, 32, and 36 shows that over the range $1 < \omega\delta^*/U(y) < 6$, the dimensionless spectra are generally similar and

²⁹Chandiramani, K.L., "Interpretation of Wall Pressure Measurements Under a Turbulent Boundary Layer," Bolt Beranek and Newman, Inc., Report 1310 (1965).

behave approximately as $[\omega\delta^*/U(y)]^{-5/3}$. This dependence on wave number suggests the existence of an inertial subrange, analogous to that which exists in isotropic turbulence. At higher frequencies the wave number dependence increases, while at lower wave numbers the spectra occasionally show various peaks. In both of these extreme ranges, spectra are notably dissimilar at different locations along the streamline and at varying distances from the wall. If we interpret the dimensionless wave number as $2\pi\delta^*/\lambda_x$, where λ_x is the streamwise length scale of convected eddies, the spectra of Figures 32, 33, and 36 show that the intensity of the large turbulent eddies for which $\lambda_x > 2\pi\delta^*$ are position-dependent. The lack of similarity of spectra at low wave numbers at a given position on either of the trailing edges indicates that these larger eddies are not convected at velocities proportional to $U(y)$. Within the fully separated flow on both edges, the dimensionless spectra are similar; this would suggest that δ^* is a spatial scale for the turbulent disturbances at some frequencies.

6. PRESSURE FLUCTUATIONS ON NONSINGING EDGES

For both 25-deg--beveled-trailing edges, frequency distribution and spatial coherence of pressures have been measured. Furthermore, coherence of pressures with turbulence in the locally separated flow will be discussed to establish a mechanism for generation of the pressures.

6.1 PRESSURES ON 25-DEGREE--ROUNDED-BEVELED EDGE

Autospectral Densities

The boundary-layer flow on this edge has just been shown to be both attached with an adverse (positive) pressure gradient and separated. The statistics of the fluctuating pressures on this edge are therefore typical of those occurring in attached boundary layers with adverse pressure gradients (Burton²⁸ and Schloemer²⁷) as well as those beneath fully separated flows; see Section 6.2.

The region of flow separation on this edge was too small in its spatial extent to permit correlation measurements. Thus a discussion of those pressure statistics will be largely deferred until Section 6.2 so that we will first concentrate on the statistics beneath the attached portion of the boundary layer. In Figure 38 the spectral densities of pressure fluctuations have been normalized on the free-stream dynamic head and the local displacement thickness. The dimensionless pressure spectra at positions A and B are identical, and they have been shown to be typical of pressures beneath boundary layers on smooth surfaces in zero pressure gradient. Position C is in the region of favorable gradient, and the spectrum levels are slightly lower than those at position A. For the other measurement locations as the static pressure gradient increased, the pressure fluctuations became more dominated by low-frequency disturbances. At separation the pressure levels were the highest at $\omega\delta^*/U_\infty \approx 0.4$. The spread in dimensionless spectrum levels exhibited in Figure 38 is a factor of 5. Burton²⁸ has shown spread of a factor of 10 for the range of static pressure gradients shown in Figure 35. A comparison of the dimensionless spectra just upstream of separation of position E-1 of the current measurements and those of earlier studies is shown in Figure 39. The spectra are designated according to the dimensionless pressure gradient parameter of Figure 35. The spectra at $\theta \frac{\Delta C_p}{\Delta s} \frac{1+H/2}{1-C_p} \approx 19$ are notably dissimilar, and the difference in shape is possibly due to the influence of the upstream boundary-layer history.

In comparing the current experiment with that by Burton, we find that in addition to differences in $N_{R_{e\theta}}$ at the measurement points, the momentum thickness upstream from the region of pressure gradient (position C) is $\theta \approx 0.06$ inch, and $C_f \approx 0.003$ upstream from position C, while for Burton,²⁸ $\theta = 0.28$ inch, and $C_f = 0.001$ at the entrance of the region of his adverse pressure gradient. The maximum values of dimensionless spectra are similar for both boundary layers; however, near $\omega\delta^*/U_\infty = 3$ the spectrum level on the current trailing edge is

roughly a factor of 10 higher than in the Burton case. The spectra in Figure 38 show that as the fluid in the boundary layer of the strut moves into the region of adverse gradient (position DE), the pressure fluctuations first increase above the upstream, baseline, values at zero pressure gradient throughout the frequency range. Further downstream the pressures at low frequencies continue to increase while some reduction occurs at high-dimensionless frequencies. Finally when the flow separates at position G, the spectrum is broad with a peak at $\omega\delta^*/U_\infty = 0.4$. In the Burton case, a gradually increasing adverse pressure gradient was also imposed on the boundary layer without separation; however, the value of C_f for his incident flow was considerably less than in the current case. Thus, since pressure spectrum levels in zero gradient increase with τ_w (Blake,^{16,18} Burton,²⁸ and Section 3 of this report) the upstream, baseline, pressure levels were notably lower in the Burton case than on the trailing edge under discussion. Thus we conclude that upstream history, which affects the growth of the incident boundary layer as well as the local Reynolds number, which is based on local momentum thickness, affects the level of local pressure fluctuations on the rounded-trailing edge in the severely positive pressure gradient.

Figure 39 indicates that the maximum spectrum level attained by the pressure fluctuations reaches the limit $\phi(\omega)U_\infty/q_\infty^2\delta^* \approx 10^{-4}$ while the flow is attached. Higher levels are attained after separation.

Spatial Coherence and Convection

Cross spectral densities of the pressures at the trailing edge were obtained with longitudinally separated microphones. These spectra are normalized on autospectrum levels and are expressed as functions of phase in Figure 40. The representation follows that of Section 3 which was used for the boundary layer with zero pressure gradient. The normalized cross-spectrum represents a coherence which is not a

unique function of the phase $\alpha(r_s, \omega)$. A nearly identical behavior was determined by Burton²⁸ for the smooth wall with adverse pressure gradient.

Corcos,¹⁹ interpretation of the longitudinal phase of Equation (9) was used again to determine the convection velocities of Figure 41. Data in the upper figure were obtained about zero pressure gradient at position B. They are typical of measurements taken elsewhere. For the region of adverse gradient, levels are shown in the lower figure. All separations are referred to the lettered position, and they are in the direction of the free-stream flow. The convection velocities are normalized on U_∞ ; frequencies are expressed as in Figure 38, except that an average of δ^* at the measurement points is used. A comparison of Figures 38 and 41 shows that the measurements are dominated by the flat portion of the pressure spectrum. The convection velocities for pressures in the frequency range $\frac{\omega \delta^*}{U_\infty} > 0.1$ fall into two classes, depending on whether the reference point is DE or E-1. For the reference position DE, U_c/U_∞ approaches 0.8; for $r_s = 1$ inch, Figure 40 shows that the coherence exceeds that measured with E-1, the reference. When E-1 is the reference, the convection velocities approach $0.55 U_\infty$ at the higher dimensionless frequencies. We will assume that the pressures are generated by velocity disturbances which are located in the boundary layer situated a distance y_c from the wall so that $U(y_c) = U_c$. An examination of Figure 37 as well as of the dimensionless data of Appendix B in light of this assumption leads to a specification that the pressures are generated in the region for which streamline velocity fluctuations are largest. This is also the region for which dU/dy is maximum. Interpretation of the cross spectrum as the coherence of a pressure disturbance of wave number ω/U_c leads to the further speculation that the disturbance loses its identity as it passes down the edge. The increased production of Reynolds stresses as the pressure gradient increases is the cause of this disorder. At frequencies of such a nature that $\omega \delta^*/U_\infty < 0.1$, the convection velocities show two other

distinctly different behavior modes. For the separation of 0.5 inch with E-1 the reference location, U_c is increased dramatically with decreasing frequency. Alternatively, when DE is the reference, the convection velocities decrease in agreement with the Burton measurements.

Normalized cross spectral densities with laterally separated microphones are shown in Figure 42 for separation distances ranging from 0.31 to 0.62 inch. The reference location is position E-1. Separations are normalized on the wave number ω/U_c , where U_c is taken from data in Figure 41 for position E-1 with $r_s = 0.5$ inch. The lateral cross spectral density appears to be a universal function of $\omega r_z/U_c$; it is also insensitive to the nature of the boundary layer. This is illustrated by the close similarity between the current data and those of Schloemer²⁷ as well as those for the vanishing pressure gradient in Figure 42 for large separations.

Overall spatial coherence of the pressures is shown by the broadband, space-time correlations for streamline separations relative to position E-1. Figure 43 shows the normalized correlation function, defined as

$$R_{pp}(\bar{r}, \tau) = \frac{\overline{p(x,t)p(x+\bar{r}, t+\tau)}}{[\overline{p^2(x,t)} \overline{p^2(x+\bar{r}, t+\tau)}]^{1/2}} \quad (24)$$

where in this case x is the coordinate of position E-1. For both positive--the reference sensor upstream from the movable sensor--and negative separations, time delays for maximum correlation $U_\infty \tau_m / \delta^*$ are the same. Values of the moving-eddy correlations* $R_{pp}(r_s, 0, \tau_m)$ are larger for positive separations than for negative ones. Convection velocities $r_s / \tau_m U_\infty$ are approximately 0.7. The broadband correlations are dominated by the low-frequency pressures which, according to Figure 41, are convected past position E-1 at relatively high velocities.

*This term is originally due to Chandiramani.²⁹

The rapid loss in coherence in the moving-eddy correlation, which is due to the rapid boundary layer growth, is apparently similar for both speeds. Furthermore, the moving-eddy correlation is less than that previously measured in zero pressure gradient.

To summarize the characteristics of spatial coherence, we note the auto and cross spectra of the pressure fluctuations have shown that while the increased pressure gradient at the trailing edge causes an accelerated increase in the boundary layer thickness, the correlation scales of the pressures relative to δ^* diminish, compared to situations in zero pressure gradient.

The lateral coherence remains somewhat unchanged by the growth of the boundary layer. As the boundary layer nears separation the autospectrum level increases at low frequencies, compared to what it was when the pressure gradient was nearly zero. Just upstream of boundary-layer separation at position E-1, the pressure field is controlled by disturbances for which $\omega\delta^*/U_\infty < 1$. Considering these disturbances as wavelike, along the lines implied by Corcos¹⁹ and (1964)³⁰ and examined by Landahl (1967),³¹ we interpret this upper limit in frequency as a limit in wavelength for which $\omega\delta^*/U_c = k_s \delta^* < 1.8$. This effectively places a limit on wavelengths $2\pi/k_s = \lambda_s$ to greater than $3.5 \delta^*$ with the disturbances located at the position in the boundary layer for which dU/dy is maximum, and $y \approx 0.7 \delta^*$ (0.12δ). This is also the location which has been shown to delineate between velocity disturbances with different dimensionless spectral forms as shown in Figure 35b.

Correlation between Pressure and Velocity Disturbances

In order to establish a relationship between the fluctuating wall pressures and the local boundary layer turbulence as well as to form a basis for comparison between singing and nonsinging trailing edges, a

³⁰Corcos, G.M., "The Structure of the Turbulent Pressure Field in Boundary Layer Flows," Journal of Fluid Mechanics, Vol. 18, pp. 353-378 (1964).

³¹Landahl, M.T., "A Wave-Guide Model for Turbulent Shear Flow," Journal of Fluid Mechanics, Vol. 29, pp. 441-459 (1967).

series of pressure-velocity correlations was determined. Correlations like these have been measured in boundary layers without pressure gradient by Willmarth and Wooldridge (1963)³² and by Burton (1971).³³ In the current experiment, the space-time correlations between wall pressure and velocity disturbances along the streamline were determined for pressures at position B, zero pressure gradient; position F, adverse pressure gradients near separation; and position G, fully separated boundary layer. The correlations are defined more generally than Equation (11) as

$$R_{pu}(x; \bar{r}, \tau) = \frac{\overline{p(x,t) u(x+\bar{r}, t+\tau)}}{[\overline{p^2(x,t) u^2(x+\bar{r}, t+\tau)}]^{1/2}} \quad (25)$$

At position B the correlations for $\bar{r} = (0, r_y)$ are practically the same as those measured in previous investigations at positive values of time delay; however, they differ slightly at negative time delays. The current measurements were made at a lower Reynolds number than in the earlier work, and there seems to be a consistent variation, with N_{Re_θ} shown for correlations at $r_y/\delta^* = 0.58$. Close to the wall $r_y = 0.36 \delta^*$, the pressure is more positively correlated, compared to $r_y = 1.06 \delta^*$. With the larger separation, the pressures are more negatively correlated at negative time delays. As Willmarth and Wooldridge have shown, correlations of this shape may be interpreted as correlations of pressure and streamwise velocity gradient $\partial u/\partial x$. Thus, assuming that the pressure-producing disturbances are a function of $x - U_c t$

³²Willmarth, W.W. and E.W. Wooldridge, "Measurement of the Correlation Between the Fluctuating Velocities and the Fluctuating Pressures in a Thick Turbulent Boundary Layer," Advisory Group for Aerospace Research and Development Report 456 (1963).

³³Burton, T.E., "On the Generation of Wall Pressure Fluctuations for Turbulent Boundary Layers over Rough Walls," Massachusetts Institute of Technology Acoustics and Vibrations Laboratory Report 70208-4 (1971).

$$\frac{\partial}{\partial \tau} R_{pu}(x; \bar{r}, \tau) = -1/\bar{U}_c \frac{\partial R_{pu}}{\partial r_x} = -1/\bar{U}_c R_{pu_x}(x; \bar{r}, \tau)$$

It can be seen by inspection of Figure 44 that R_{pu} will have a maximum near $\tau = 0$, $u_x = \partial u / \partial x$.

According to the Kraichnan (1956)³⁴ analysis, the fluctuating wall pressures beneath homogeneous boundary layers are generated by a source field of volume density $\rho \frac{\partial U}{\partial y} \frac{\partial v}{\partial x}$, which is continuously distributed throughout the boundary layer. This "turbulence mean shear" interaction has been argued by Willmarth and Wooldridge³² and Corcos³⁰ to be responsible for a strong correlation at $\tau = 0$ between pressure and the streamline gradient of the normal velocity $\frac{\partial v}{\partial x}$. This correlation they showed to be strongly positive, and it accompanies a negative correlation maximum with $\partial u / \partial x$. The space-time correlations of Figure 44 are consistent with the Willmarth and Wooldridge³² results for $r_y < \delta^*$. For $r_y = 1.06 \delta^*$, however, the shape of the correlation function suggests that an alternative pressure-producing mechanism exists for eddies in the outer, mixing, region of the boundary layer. It will be shown that this function shape will be typical of the separated boundary layer and so will be further discussed at the end of this section.

Pressure-velocity correlations, which were obtained at position F for $\bar{r} = (0, r_y)$ are shown in Figure 45 for $U_\infty = 60$ and 100 feet per second. At position F the maximum intensity of the turbulence occurs at $y = 0.54 \delta^*$ for $U_\infty = 100$ ft/sec, and $y = 0.52 \delta^*$ for $U_\infty = 60$ feet per second. The general functional dependence on τ as well as the maximum correlations is similar to position B. At a corresponding location in the boundary layer $r_y \approx 0.5 \delta^*$, the maximum coherence is reduced at position F, compared to that at position B. The trend of more negative correlations with increasing r_y is also prevalent at this position.

³⁴Kraichnan, R.H., "Pressure Fluctuations in Turbulent Flow over a Flat Plate," Journal of the Acoustical Society of America, Vol. 28, p. 378 (1956).

Correlations obtained above and downstream from position G at $U_\infty = 60$ ft/sec are shown in Figure 46. In these cases $\bar{r} = (r_x, r_y = 0.1 \text{ in.})$, where r_x is variable. Lettered locations a through d correspond to values of r_x , which are indicated in Figure 37. The locus of correlations is just outside the region of separation. These correlation functions are entirely negative; the level of correlation is high for positions a through d, and it decreases at position e. The temporal width of the correlation peak $\Delta\tau$, measured for coherence to decrease to one-half its maximum value, is $\frac{\Delta\tau U_\infty}{\delta^*} \approx 8$, where δ^* is evaluated at position G. This corresponds to a dimensionless frequency $\frac{\omega\delta^*}{U_\infty} \approx 0.8$, which is comparable to the bandwidth of the autospectrum of fluctuating pressure at position G; see Figure 38. On the basis of this similarity in frequency, it appears that the pressure generated beneath the separated boundary layer is caused by a large-scale velocity field, having a coherent influence that persists slightly downstream from the trailing edge. Also it appears from the functional form of the correlation that the mechanism of pressure generation by the turbulence is different for the separated boundary layer than it is for the attached boundary layer. The magnitude of the absolute value of the correlation is also greater for the separated than it is for the attached boundary layer.

The outer flow at position B is typical of that existing in fully developed boundary layers, and it is characterized by a nearly vanishing mean shear; it has been called wakelike by Coles (1956).³⁵ Although this wake analogy comes about because the mean velocity defect has certain functional similarities with those of fully developed wakes, a wake analogy may also apply to the mechanism of turbulent pressure generation. A large-scale turbulent eddy structure is apparently convected at a velocity nearly equal to U_∞ over the surface and trailing edge. The streamwise components of the velocity field due to the eddies are negatively correlated to the pressure on surface. In Section 4 it was

³⁵ Coles, D., "The Law of the Wake in the Turbulent Boundary Layer," Journal of Fluid Mechanics, Vol. 1, pp. 191-226 (1956).

shown that the surface pressures induced by the wake vorticity were negatively correlated with the streamwise component of velocity; see Figures 16, 22, and 23. For the edges considered thus far, pressures at singing and nonsinging edges are distinguished by the degree of coherence in the separation of the boundary layer. This is reflected in the bandwidth of the pressure autospectrum as well as in the coherence, and the downstream persistence of the coherence, of the pressure with the velocity fluctuations. This coherence is, in turn, dependent on the coherence of the velocity fluctuations in the separated boundary layer and wake.

The shapes of the pressure-velocity correlations at position B for $\tau < 0$ may be due to the influence of a large-scale eddy structure, generated by the laminar separation at the leading edge and convected downstream. The mechanism of the pressure production is the same as that implied by the correlations described previously:

6.2 PRESSURES ON 25-DEGREE--KNUCKLE-BEVELED EDGE

The flow field on this trailing edge has been shown in Section 5 to be partially representative of the separated boundary layer downstream from position G on the 25-deg--rounded-beveled edge. The scale and intensity of the boundary layer and its velocity disturbances was shown to be larger on the knuckle edge. This section is therefore an examination of the statistical structure of the pressure field beneath a separated boundary layer. The scope of the measurements is the same as that for the rounded edge.

Autospectral Densities

The dimensional autospectra $G(f)$ are shown in Figure 47; they were obtained at the lettered positions referenced in Figure 29. At $U_\infty = 50$ ft/sec, the autospectra at positions A through D are similar within a factor of two; this is expected because the boundary-layer--displacement thicknesses are comparable for all these positions; see

Tables 1 and 2. At position E, on the downstream side of the knuckle, the pressures are more dominated by low-frequency disturbances. At positions E-1 and F, the boundary layer is fully separated, and the pressures at low frequencies dominate; they are comparable for both locations. At $U_\infty = 100$ ft/sec, the pressures are again similar at positions A through C and attain intermediate levels at positions D and E. At positions E-1, F, and G the autospectra are nearly identical at low frequencies with some spread for $f > 1$ kilohertz. Beneath the separated boundary layer, the low-frequency, pressure spectrum levels are factors of 30 and 10^3 higher than the pressures beneath the attached flow at speeds of 50 and 100 feet per second, respectively.

For comparison of these pressures to those of the other flow situations, the autospectra are nondimensionalized on the outer flow variables U_∞ and δ^* in Figure 48. It can be seen that the dimensionless broadband, low-frequency pressures are a factor of nearly 10^2 higher than those at position G on the 25-deg--rounded-beveled edge. The spectrum levels in the separation region diminish with $\frac{\omega\delta^*}{U_\infty} > 1$ in similarity to those on the 25-deg rounded edge at position G. A notable feature of the dimensionless autospectra beneath the separated boundary layer on the knuckle edge is that the levels do not scale on the free-stream dynamic head, while the spectrum shapes are quite similar when expressed in terms of $\omega\delta^*/U_\infty$. That the spectrum levels are not dependent on q_∞^2 is surprising in light of the fact that the normalized velocity disturbances u' / U_∞ are similar for both speeds; see Appendix B.

Correlations of Wall Pressures

Space-time correlations of wall pressures on the knuckle trailing edge are shown in Figure 49. The definition of the correlation function has been given by Equation (24). As before, a separation vector pointed upstream is negative; for the correlations of Figure 49, position F is the referenced location. The coherence between pressures at positions

E-1 and F ($r_s = -1$ in.) is nearly 0.5 at speeds $U_\infty = 50$ and 100 feet per second. The mean convection velocity is

$$\bar{U}_c = r_s / \tau_m U_\infty = 0.41$$

which is considerably less than that which has been calculated for pressures beneath fully attached boundary layers. The streamwise and lateral spatial correlations $R_{pp}(r_i, 0)$, where $r_i = r_s$ or r_z , are also shown in Figure 49. Overall, the correlations show the existence of a large-scale convected pressure field that seems to be laterally correlated over two trailing-edge thicknesses while instantaneously extending only a 1/3-trailing-edge thickness upstream. This spatial extent roughly corresponds to the estimated upstream boundary of the separation region; see Figure 29. A correlation between pressures at positions F and G shows convection in two directions. As shown in Figure 50 two contributions, correlated nearly equally, appear to be convected at $\bar{U}_c \approx 0.35 U_\infty$. The functional form of the correlation indicates that the correlation

$$p(x_F, t) \frac{\partial p}{\partial t}(x_G, t + \tau)$$

is a maximum at $\tau = 0$. This means that the pressure at position F is positively correlated with the temporal rate of change of pressure at position G. Comparison of the correlation magnitude between pressures at F and G with that of pressures at F and E-1 ($r_s = \pm 1$ inch) shows comparatively less correlation between pressures at F and G. In Section 5-1, the unsteady character of the velocity fluctuations near the edge was described as due to an unsteady large vortex, alternately formed and swept downstream by formation and ejection of the vortex. Positive correlation between $p(x_F, t)$ and $\frac{\partial}{\partial t} p(x_G, t)$ suggests that pressures at F and G are related to the formation of the vortex and its acceleration preceding ejection. They do not appear to be caused by a simple vortex convection.

Pressure and Velocity Correlations

Further indications of the pressure-producing mechanism of the separated boundary layer are given by correlations defined by Equation (25) with $\bar{r} = (0, r_y)$. The space and time correlations are entirely negative as shown in Figure 51. The lettered locations denote the anemometer-probe positions designated in Figure 29. At $r_y = 0.59\delta^*$, the correlation nearly vanishes, while it is negative at $r_y = 0.034\delta^*$ and $r_y \geq 1.18\delta^*$. The increase in the absolute value of the correlation with increasing r_y is somewhat a result of normalization on local turbulence intensity. This latter factor also decreases with large r_y ; see Figure 29 and Appendix B. The maximum value of the pressure-velocity correlation occurs for $r_y \approx 1.18\delta^*$. That the pressure is partially generated by a convecting vortex field is seen by reference to the correlation in Figure 52. The locus of points g through k roughly corresponds to local maxima in turbulence intensity as shown in Figure 29. It is seen that while intensity decreases with increasing r_x , coherence increases slightly. In comparing the correlations in Figures 46 and 51, we see that the pressures on the 25-deg knuckle edge are much more coherently generated by the near wake than those on the 25-deg--rounded-beveled edge. Also, the pressures are negatively correlated with the streamwise velocity disturbances in similarity with correlations on singing edges, Figures 16, 22, and 23. The spatial correlations of pressure velocity, $R_{pu}(\bar{r}, 0)$ show that $R_{pu} = 0$ at point i, which is just above the tip of the edge. Here, the correlations change from positive to negative values, which is a behavior similar to that shown for the 45-deg--rounded-beveled edge in Figures 22 and 23. The magnitude of the spatial coherence is comparable, i.e., $R_{pu} = -0.02$. On the knuckle edge the disturbances (Figure 31) are generally broadband, showing a small low-frequency peak at $\frac{\omega\delta^*}{U_\infty} \sim 0.15$ to 0.2 -- $\frac{\omega h}{U_\infty} \approx 0.5$, where h is the thickness of the strut--which seems to be more pronounced at position H for $y = 0$ than at position F.

The sets of correlations in Figures 49 through 52 show the existence of a pressure field which is partially generated by a wake that is less structured, compared to that causing the periodic pressures on singing trailing edges. The disturbances do not grow as they move downstream in the wake as do those in the flow region of the singing edges; however, they are generated by the local vorticity caused by the separation through a mechanism of pressure generation that appears to be common to both singing and nonsinging trailing edges. Although the magnitudes of pressures which are generated beneath separated boundary layers on both the knuckle and the rounded trailing edges are quite different, to some degree their mechanisms of generation seem to be similar as can be seen by reference to the pressure-velocity correlations of Figures 46 and 51, 53, and 54. For both edges the pressure-velocity correlations in Figures 53 and 54 are shown for corresponding locations on the edges relative to estimated regions of separation. The correlations are in the form $R_{pu}(r_y, 0)$. For both edges, $R_{pu}(r_y, 0)$ corresponds in shape to the profile of mean shear $\frac{\Delta U/U_\infty}{\Delta y/\delta^*}$ as well as to profiles of u^2/U_0 versus y/δ^* . The vertical extent of the region of maximum correlation appears to be measured by the reciprocal of the shape factor δ^*/θ . Finally $(R_{pu})_{\max}$ for the knuckle edge is three times larger than for the 25-deg--rounded-beveled edge. This similarity in $R_{pu}(r_y, 0)$ with the velocity gradient indicates that the source distributions above the two edges are as similar as are the velocity profiles. The time behavior of each of the local correlation functions suggests the simplified interpretation that pressure-producing disturbances are convected at a constant velocity by a fixed point, and a locally positive (or increased) velocity disturbance is associated with a negative pressure disturbance. This interpretation is drawn from the theory of potential flow. However this is only a contribution to the total pressure. Other contributions are

generated by the disturbances ejected into the wake so that the overall level of the pressure fluctuations is generated by the coherent effect both of the convected wake field and of the local shear layer.

Cross-Spectra of Pressure and Velocity Disturbances

To clarify some of the trends in correlations, cross spectral densities of pressures at two streamline locations and cross spectra between pressure and velocity fluctuations were made to show contributions due to various parts of the near- and far-wake flow layer. Magnitudes and phases of normalized-pressure cross spectral densities are shown in Figure 55 for a variety of streamline separations. The phase has been given Corcos¹⁹ interpretation as stated in Equation (9a). Cross spectra (Figures 55a through 55c) show that two frequency ranges of correlation exist. Overall, from positions E to F, the coherence is greatest near 40 Hz ($\omega h/U_\infty = 0.43$), which roughly corresponds to the frequency of the broad peaks in the velocity spectra of Figure 32. Between positions E-1 and F, the coherence is greatest near 200 Hz ($\omega h/U_\infty = 2.1$). This frequency is a limit below which the autospectrum of pressure maintains its asymptotic low-frequency value. Locally (Figure 55d) the pressures at position F are well correlated throughout the frequency range. The disturbances are convected between positions E and F at speeds $U_c \approx 0.32 U_\infty$; and between E and E-1 at $U_c \approx 0.35 U_\infty$; however, between E-1 and F, $U_c \approx 0.48 U_\infty$. Near position F, $U_c \approx 0.4$ to $0.6 U_\infty$, depending on frequency. These velocities are consistent with those indicated by the broadband correlations. Convection velocities of approximately $0.3 U_\infty$ are somewhat less than the mean velocities in the boundary layer at locations of the maximum streamline velocity fluctuations which are from 0.5 to $0.6 U_\infty$. These low-frequency pressures are therefore convected at speeds more representative of the average mean velocity of the large-scale eddy structure beneath the separated shear layer. The more rapidly convected high-frequency disturbances have apparent sources at the location of maximum streamline velocity fluctuations.

The cross spectra between pressures at F and the local velocities at the points g, h, and i in Figure 29 also show two distinctly different frequency ranges of coherence. In Figure 56, for $r_y = 0.5$ inch and $r_x = 2$ inches, point i, the dependence of phase α versus frequency, has two slopes; the magnitude of the cross spectrum has two peaks. The high-frequency peak is convected at $U_c \approx 0.9 U_\infty$. At lower frequencies, the slope $\partial\alpha/\partial\omega$ is negative; which implies the existence of a negative convection. This interpretation follows a special definition of convection velocity as $U_c = r \left[\frac{\partial\alpha}{\partial\omega} \right]^{-1}$. Strictly, U_c is analogous to a group velocity and becomes identical to U_c (Equation (9a)) when U_c is independent of frequency. For $r_x = 1$ inch, point h, the phase is small and nearly independent of frequency; for $r_x = 0$, point g, the phase is negative at all frequencies. In the last case the resolvent separation vector, which is vertical, has a component in the plane of the edge which is directed upstream, $r_s = -0.21$ inch. The convection velocity is, therefore, small and positive as designated in Figure 56. This is representative of the low speed of inner entrained fluid. That the phase is small for point g suggests that the pressure-producing disturbances in the flow pass points F and G at the same time. The similarity between convection velocities in the cross spectral densities of Figures 55 and 56 show that low-frequency pressures are generated by the low-speed large eddy flow, while the higher frequency pressures $f > 100$ Hz are basically generated by the smaller scale eddies in the shear layer.

Comparisons of Singing and Nonsinging Edges

Finally, the degree of dependence of the fluctuating pressures on the eddy structure in the wake has been further indicated by the cross spectra of pressures on opposite sides of the knuckle trailing edge. Sensors were positioned at E-1 (Figure 29) on opposite sides of the trailing edge, and the cross spectra, measured in 12.5-Hz frequency bands, are shown in Figure 57. The high level of coherence for low frequencies

further supports the hypothesis that these pressures are generated by the large-scale disordered wake field. The frequency has been made dimensionless on h and U_∞ . This thickness is selected here as a convenient scale which is representative of the knuckle-edge--shear-layer separation, and it is used to draw a comparison with the singing spectra in Figures 17 and 21. For frequencies $\frac{\omega y_f}{U_s} > 1$ and $\omega h/U_\infty > 1$ (taking $y_f \approx h$, $U_s \approx U_\infty$) all the pressure spectrum levels decrease. It is to be noted that the narrowband dimensionless pressures in Figures 15, 21, and 57 may all be compared directly. It is interesting that even though the 25-deg knuckle edge did not generate a periodic vortex street in the speed range of the measurements, it did generate high-level pressure fluctuations in a frequency range not far removed from the frequency at which singing would have occurred-- $\omega h/U_\infty$ of order unity.

In the case of the 25-deg rounded edge, the pressures at position G are considerably less than those which are generated by other edges; nonetheless, they are restricted to frequencies $\omega y_f/U_\infty \leq 1$, where y_f is the distance between maxima in turbulent velocity intensities shown in Figure 35, $y_f \approx 0.5$ inch. A complete series of measurements was not made on the 25-deg rounded edge at $U_\infty = 200$ ft/sec, however, at this speed, the pressures at position F began to display a weak tone at $f = 450$ hertz. Assuming that $y_f = 0.5$ inch--suggested by the data at positions H and I in Figure 35--and that $U_s = U_\infty$, this frequency is equivalent to $\omega y_f/U_\infty = 1.2$. Weakly periodic velocity disturbances were also measured in the wake at this speed.

7. SUMMARY: TRAILING EDGES AND UNSTEADY PRESSURES

We have seen that all the edges considered in this report generate high-level--fluctuating-surface pressures, regardless of whether or not periodic disturbances are formed in their wakes. It has also been shown that the periodic disturbances occur with Reynolds-number-dependent strengths on the blunt edge and on the 45- and 25-deg--rounded-beveled edges. The flow near the knuckle edge was not examined over a large

enough range of speeds to determine if periodic pressures would occur at high Reynolds number. When periodic disturbances were not generated, the fluctuating pressures on the edge were distributed over a frequency range bounded by the upper limit of frequency $\omega y_f / U_\infty \approx 1$. The spanwise correlation length of the pressure fluid on the knuckle edge was one-fifth that of the periodic pressure field on the blunt edge. Both the low-frequency random pressures on the one hand and the periodic pressures due to coherent vortex streets on the other hand appear to be generated by large-scale vorticity through a common mechanism. Higher frequency pressures in the random cases appear to be due to a smaller-scale convected vortex structure, which is located at the upper boundary of the region of separation. Contributions to the random velocity disturbances in the separated and nearly separated flow on nonsinging edges which are locally convected appear to be due to a vortex structure whose length scale is governed by the local displacement thickness. The other contributions to the velocities which are not locally convected and which appear to be generated by the near-wake structure occur at frequencies dependent on the shear-layer separation in the near wake.

A comparison of the turbulence intensities and length scales of all edges shows that no correspondence exists between the degree of periodicity of the surface pressures and the value of the maximum broadband intensity of velocity fluctuations at the edge extremity. These intensities cover the range $0.16 \leq \overline{u^2}^{1/2} / U_0 \leq 0.23$. Periodic pressures have been shown by the experiments to require the growth of coherent wavelike disturbances in the wake, and this growth is therefore apparently unrelated to $\overline{u^2}^{1/2} / U_0$. This evidence has been supported by the stability calculations of Appendix C which show the amplification factors of disturbances to be dependent on Reynolds number and $d^2 U / dy^2$.

The remainder of this section will be devoted to the practical questions of

1. Establishing whether or not a given trailing edge will generate a periodic vortex street

2. Estimating the frequencies of pressures that are generated

3. Estimating fluctuating pressure levels and length scales.

Although certain dimensionless factors have been shown in the preceding sections to describe the measurements quite precisely, these quantities are probably not very useful for estimations because they involve parameters which are associated with flow details rather than with overall geometric details. In an estimation process the quantities are not known a priori, and they are, therefore, of little practical value. The results of the measurements will be summarized and approximated below so that some simple formulas may be given.

Minimum Reynolds Number for Periodic Wake Generation

Periodic disturbances were generated on the blunt and both of the rounded-beveled edges above certain onset speeds. Using a definition of Reynolds number based on the wake parameter y_f , these speeds corresponded to $U_\infty y_f/\nu = 5.2 \times 10^4$ for the 25-deg edge, 3.3×10^4 for the 45-deg edge, and 4.1×10^3 for the blunt edge. Length scales are $y_f = 0.25 h$ and $0.6 h$ for the 25- and 45-deg round edge, respectively, and $0.75 h$ for the blunt edge. Although the onset Reynolds numbers are not the same for all edges, there appears to be a consistent increase in onset Reynolds number as the apex angle of the edge is decreased.

Vortex Shedding Frequencies

Although a universal Strouhal number based on a geometric length of the trailing edge has not been isolated in this study, an approximate dimensionless frequency is $f_s y_f/U_\infty \approx 1/2\pi$. The length y_f for the blunt and rounded-beveled edges has been given above. Other dimensionless forms have been proposed by other authors for specific trailing-edge forms, and they may give frequencies more precisely in those cases; however, none appear to have practical and universal application. When shedding does not occur, the random pressures are bounded by the upper limit in frequency $f y_f/U_\infty \approx 1/2\pi$. Here, values of y_f are the same as those given previously; for the 25-deg knuckle-beveled edge, it is approximately 0.6 to 0.8 h.

Fluctuating Pressure Levels

The surface pressure levels exerted on the struts apparently are not governed by any known simple scaling law. In general, at a given speed the level of the periodic pressures on the rounded-beveled edges decreases with a reduction in apex angle. When random pressures were generated on the rounded edges, the broadband mean-square levels were seen to be comparable to $10^{-4} q_{\infty}^2$. For the 25-deg--knuckle-beveled edge, the mean-square levels of the random pressures attained substantially higher levels, approaching $10^{-2} q_{\infty}^2$.

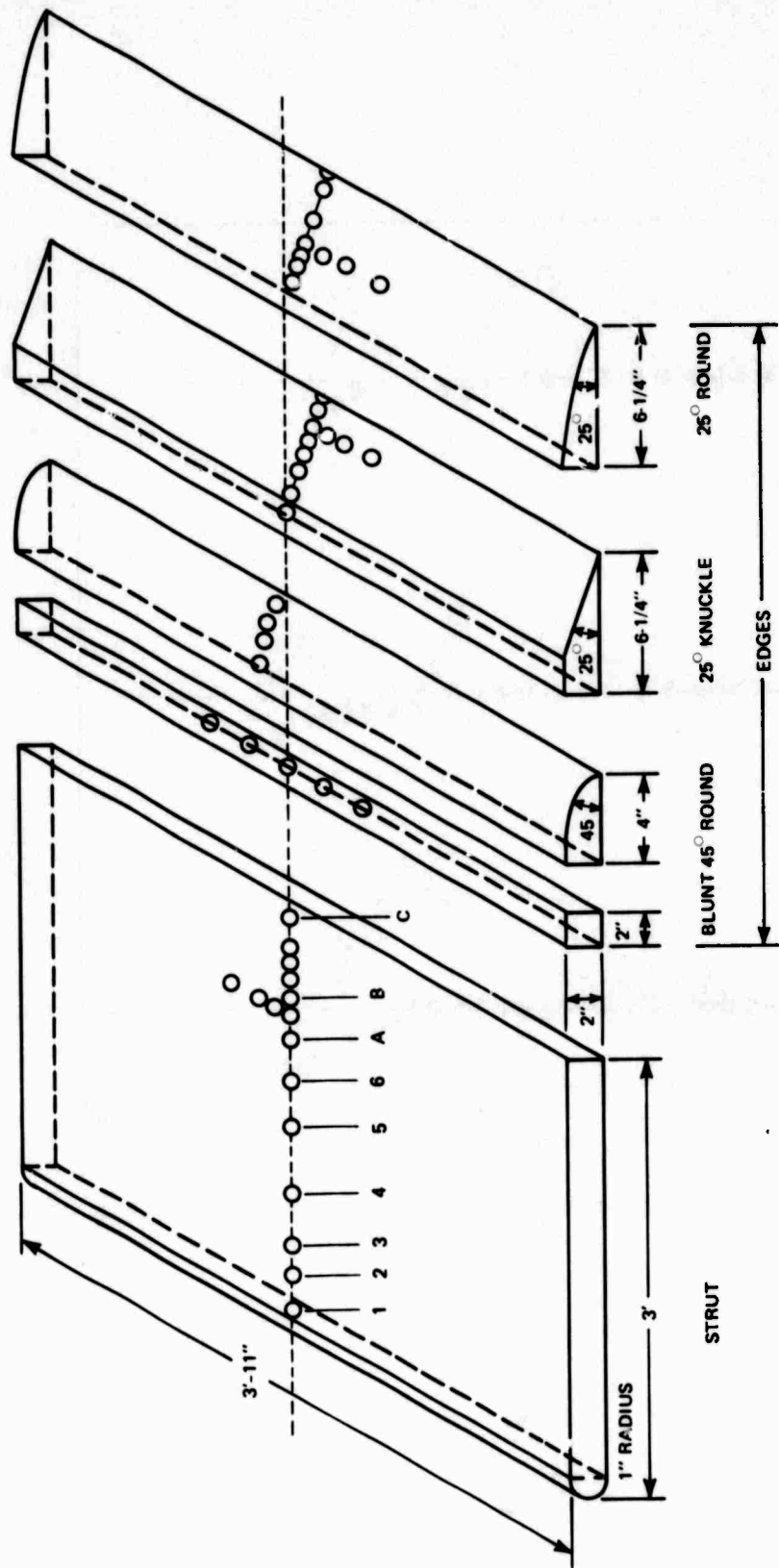


Figure 1 - Strut, Showing Orientation of Trailing Edges and Locations of Microphones

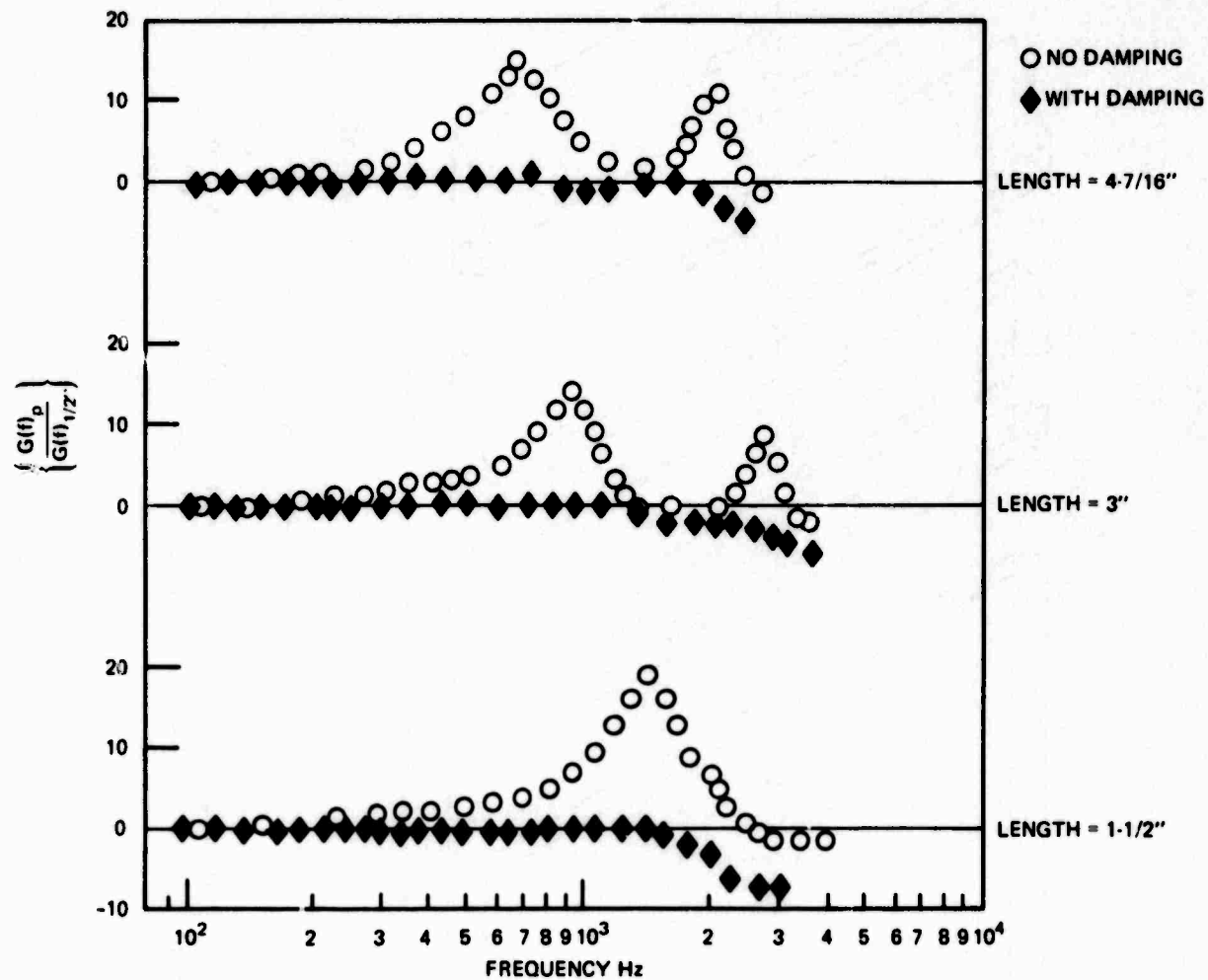


Figure 2 - Ratio of Response of Probe Tubes to Response of a 1/2-Inch Microphone

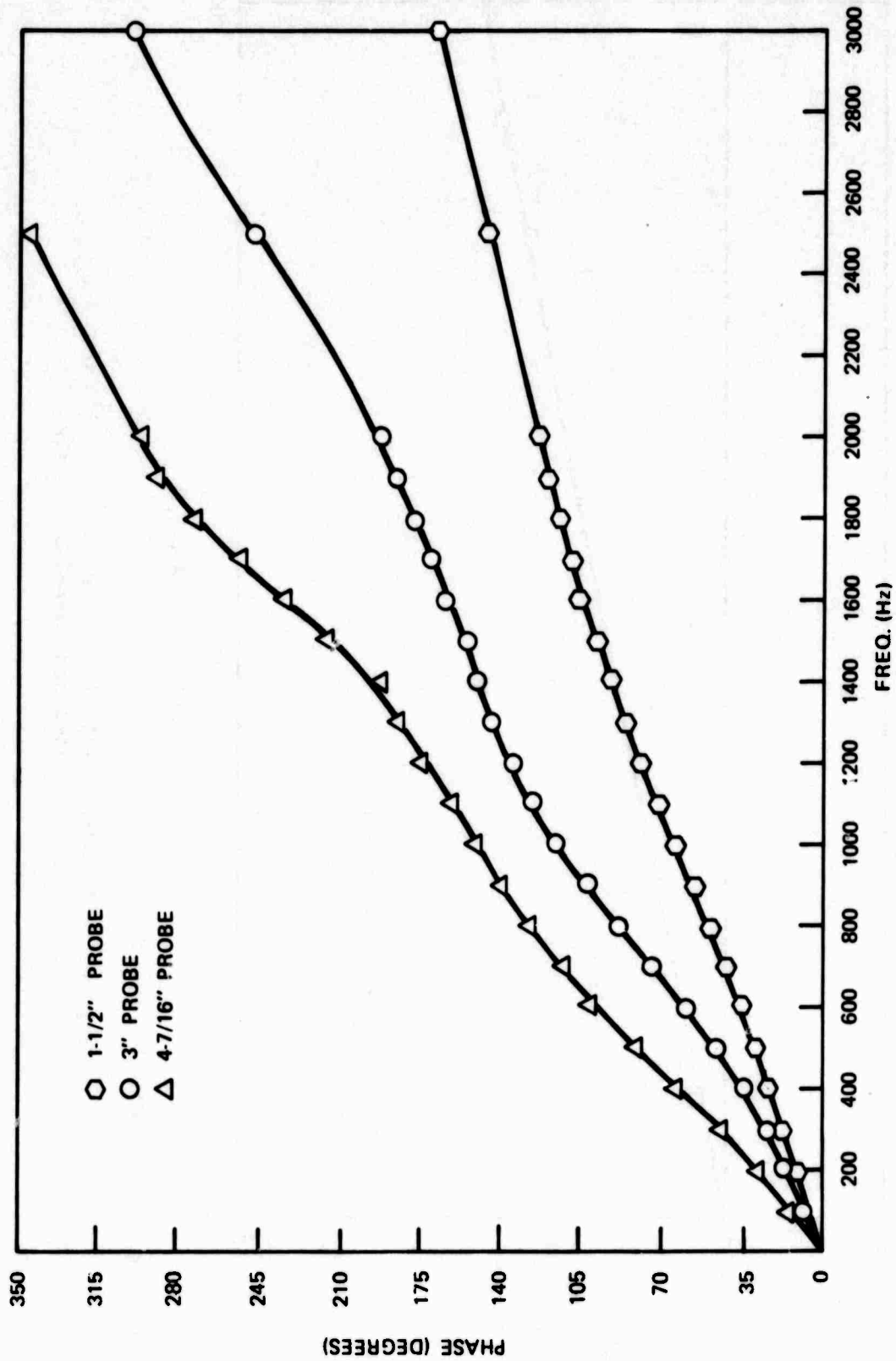
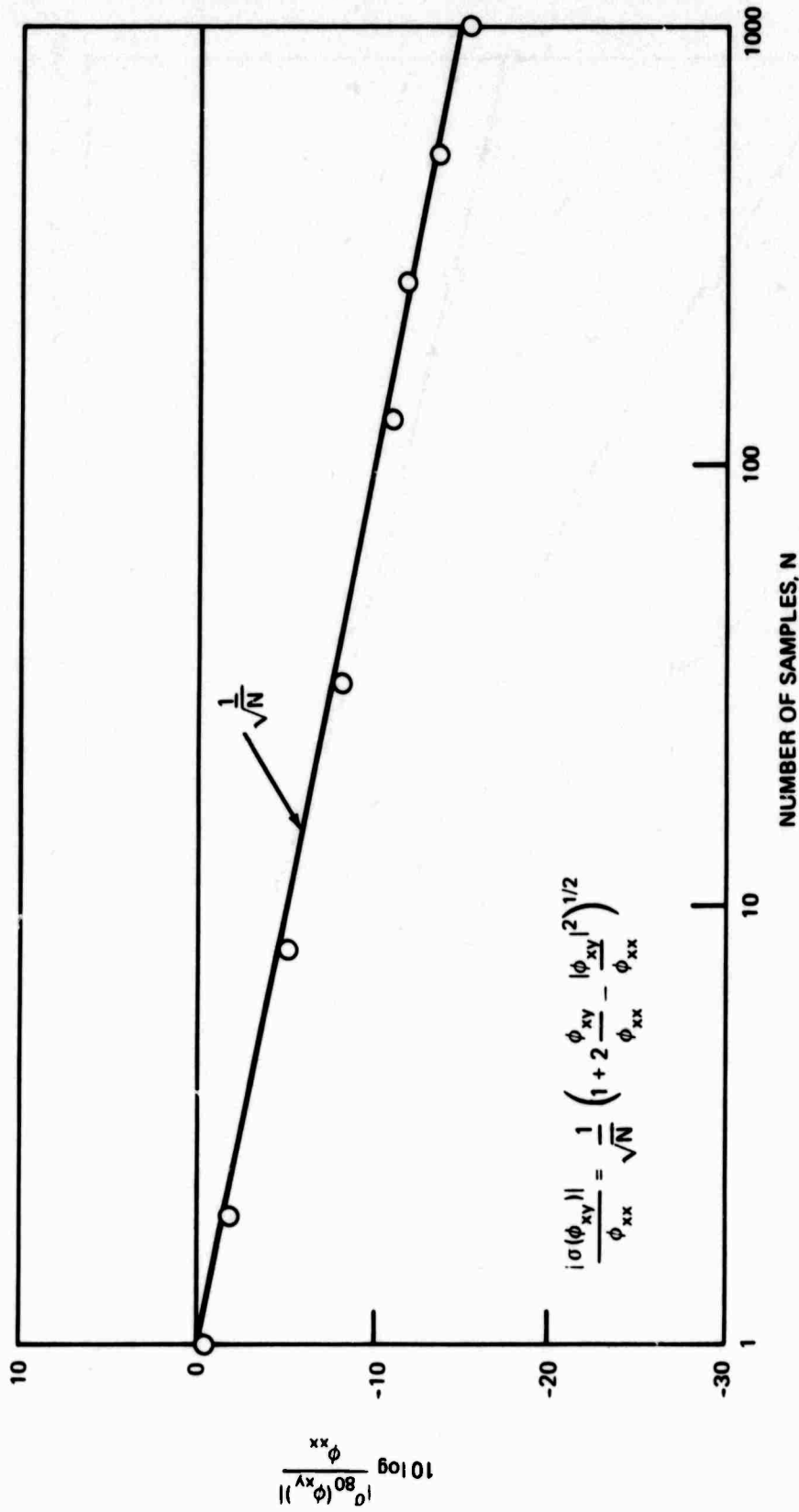


Figure 3 - Relative Phases between Probe Microphones with Damping and a 1/2-Inch Microphone Reference



NOTE: 80% OF CSD ESTIMATES WITHIN 1σ .

Figure 4 - Standard Deviation of Cross Spectral Density of Uncorrelated Random-Noise Signals

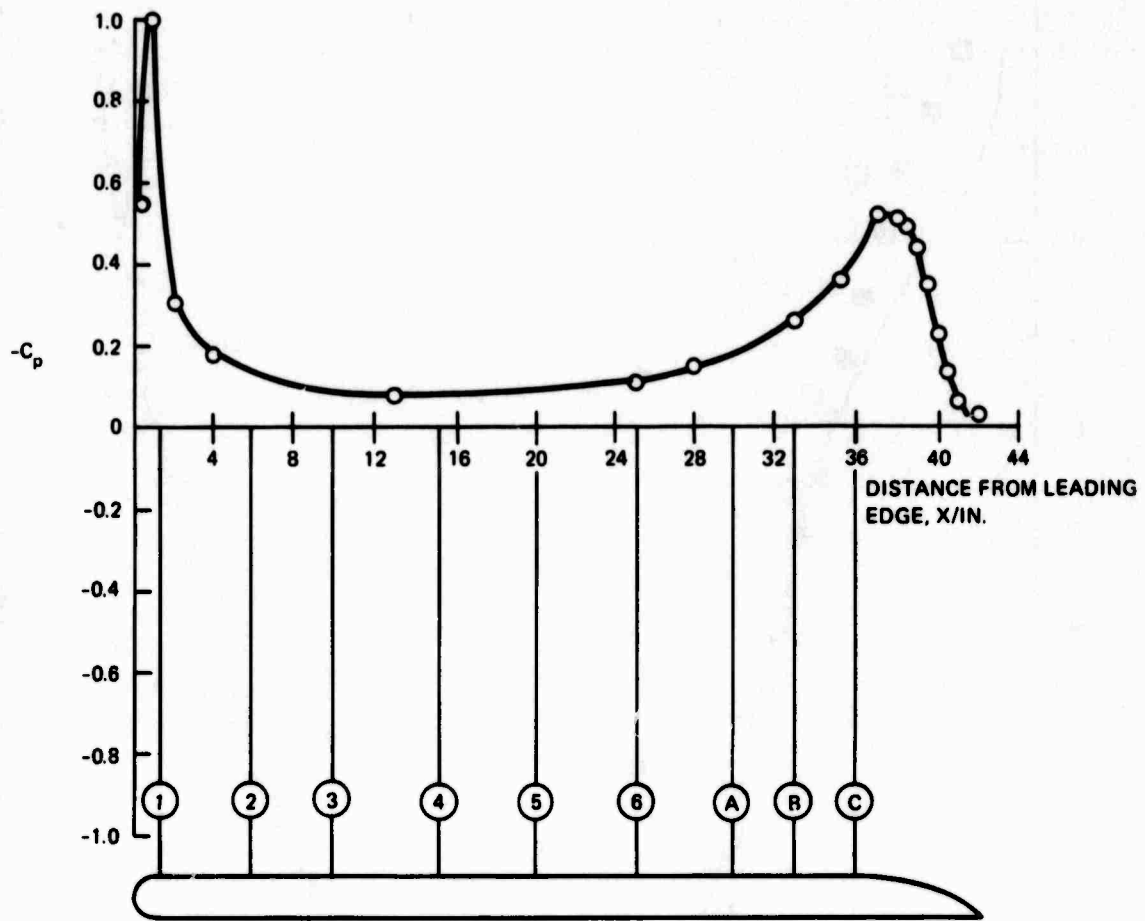


Figure 5 - Cross-Section Shape and Static Pressure Distribution on Strut with 25-Degree--Rounded-Beveled Edge (Also shown are profile of strut and upstream microphone positions)

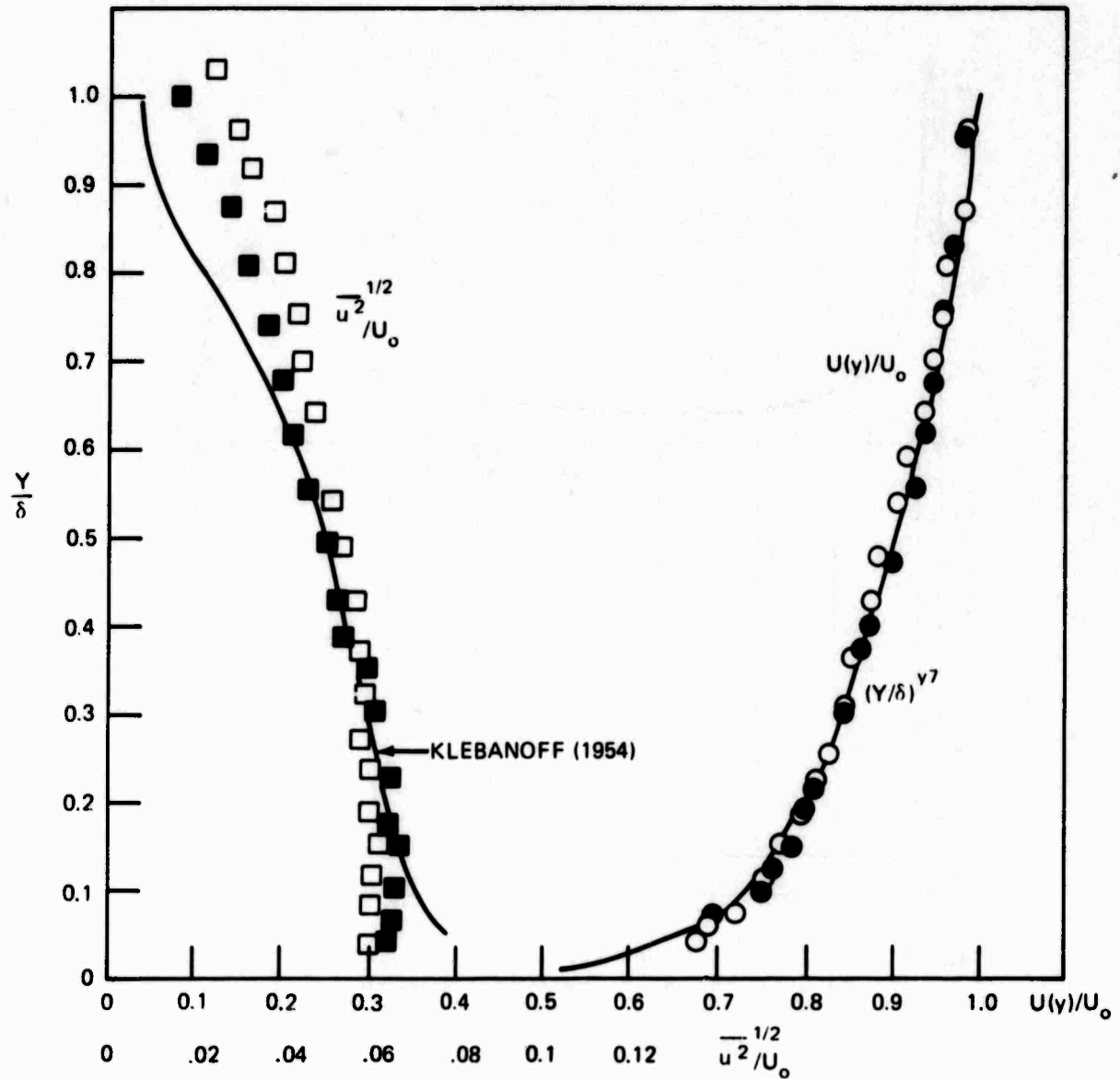


Figure 6 - Mean and Turbulent Velocity Profiles for Positions 4, Open Points, and B, Closed Points, on Strut with 25-Degree--Rounded-Trailing Edge

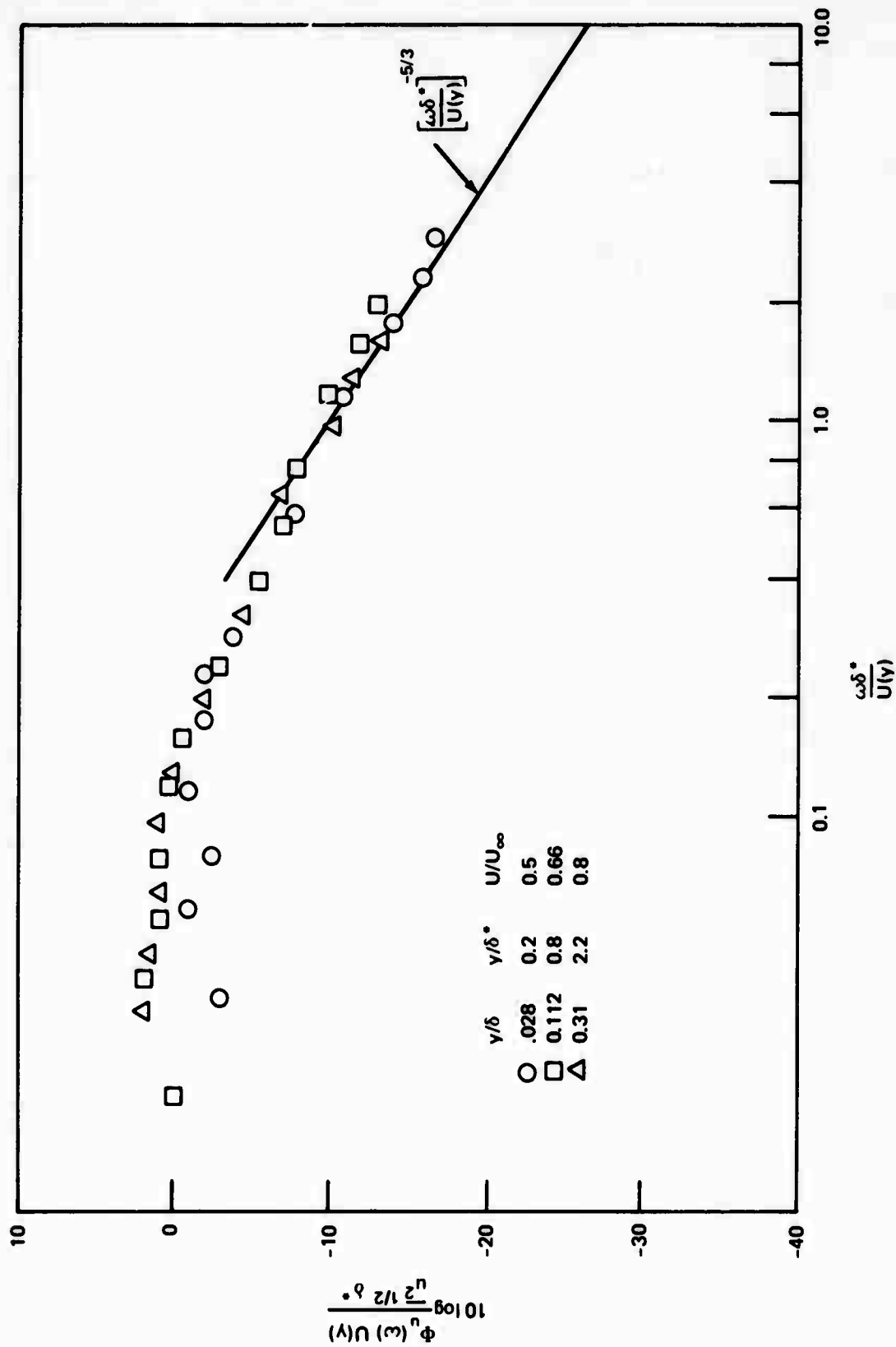


Figure 7 - Spectra of Longitudinal Turbulent Velocity at Position B on Knuckle Edge at $U_\infty = 100$ Feet per Second

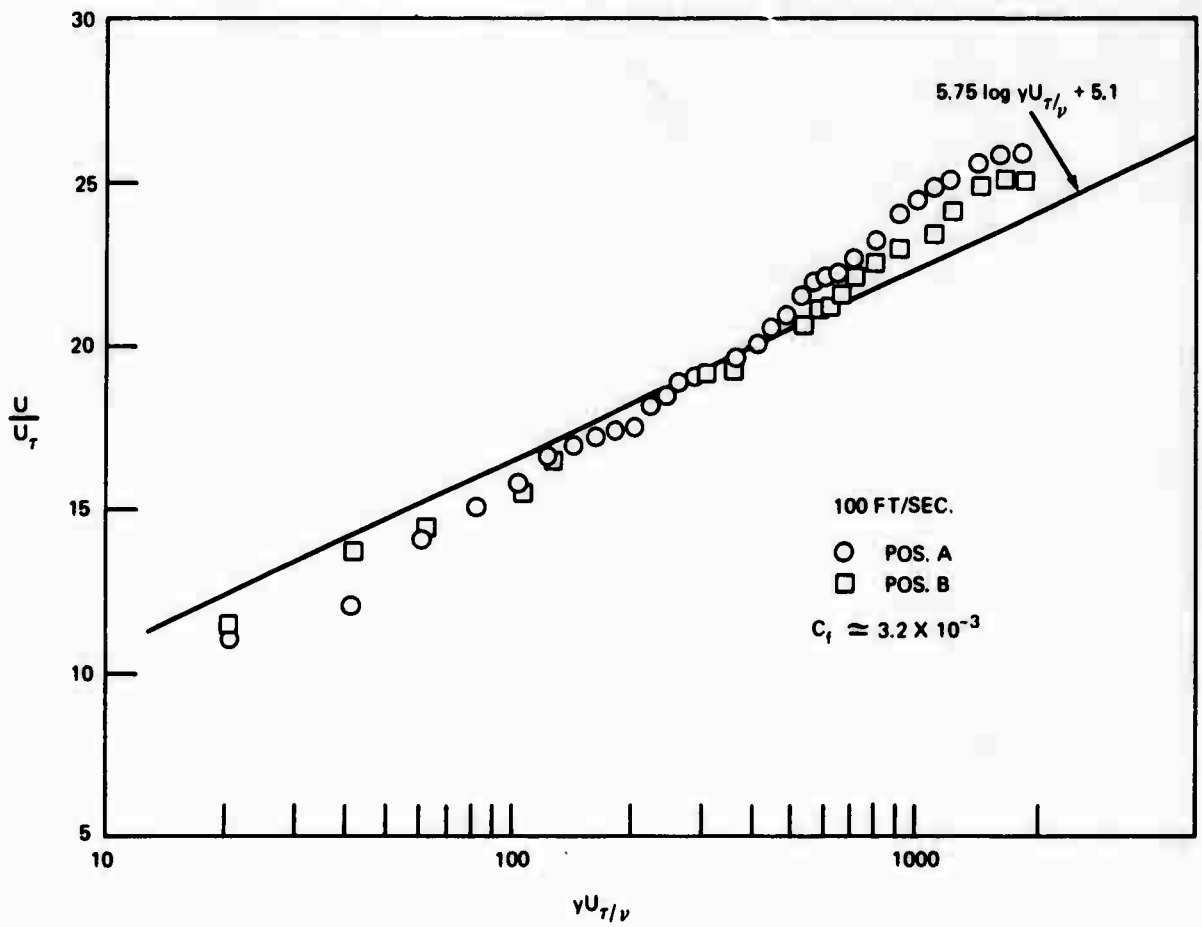


Figure 8 - Normalized Mean Velocity Profiles Incident on Trailing Edges

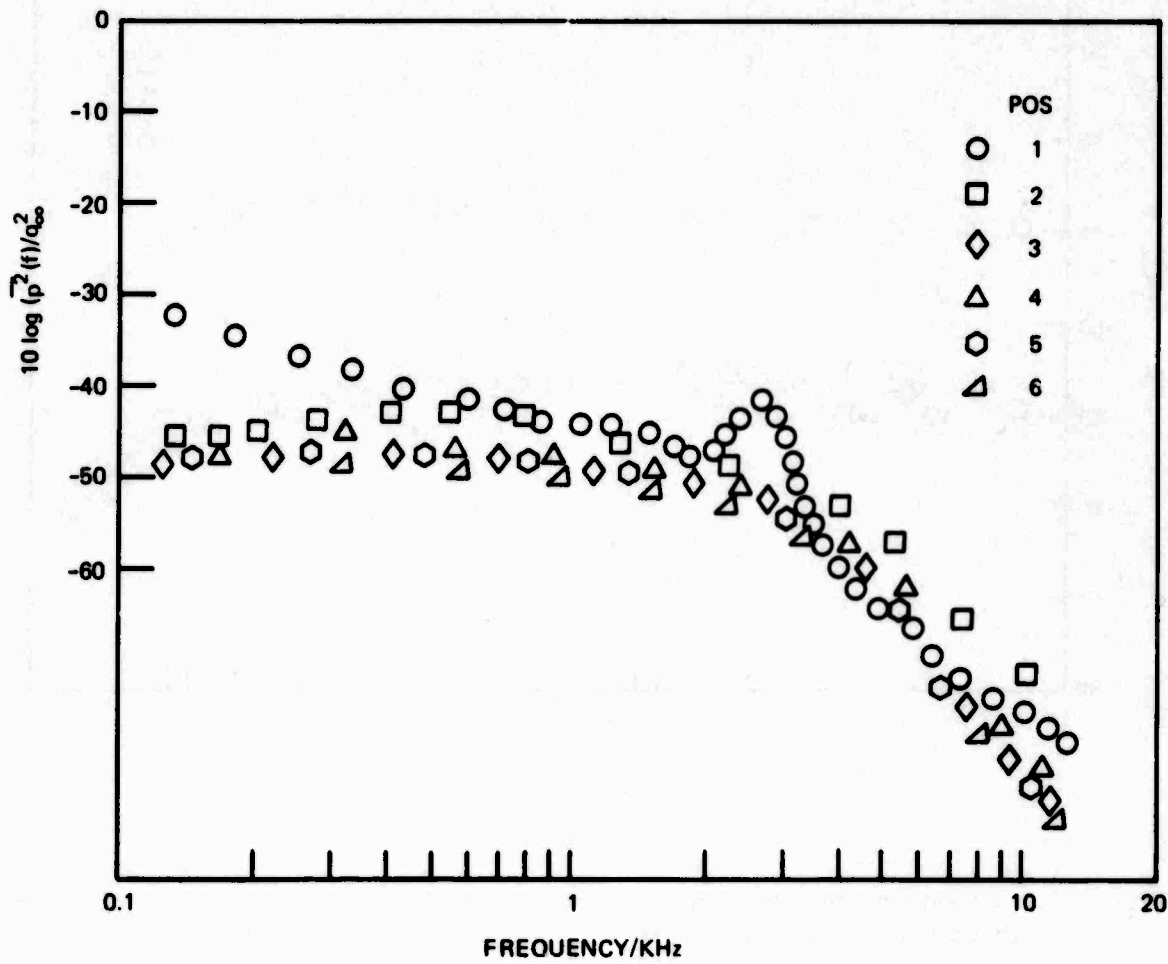


Figure 9 - Narrowband Mean-Square Pressures, Measured in 62.5-Hertz Bands at Forward Chordwise Locations of Knuckle-Trailing Edge at $U_{\infty} = 50$ Feet per Second

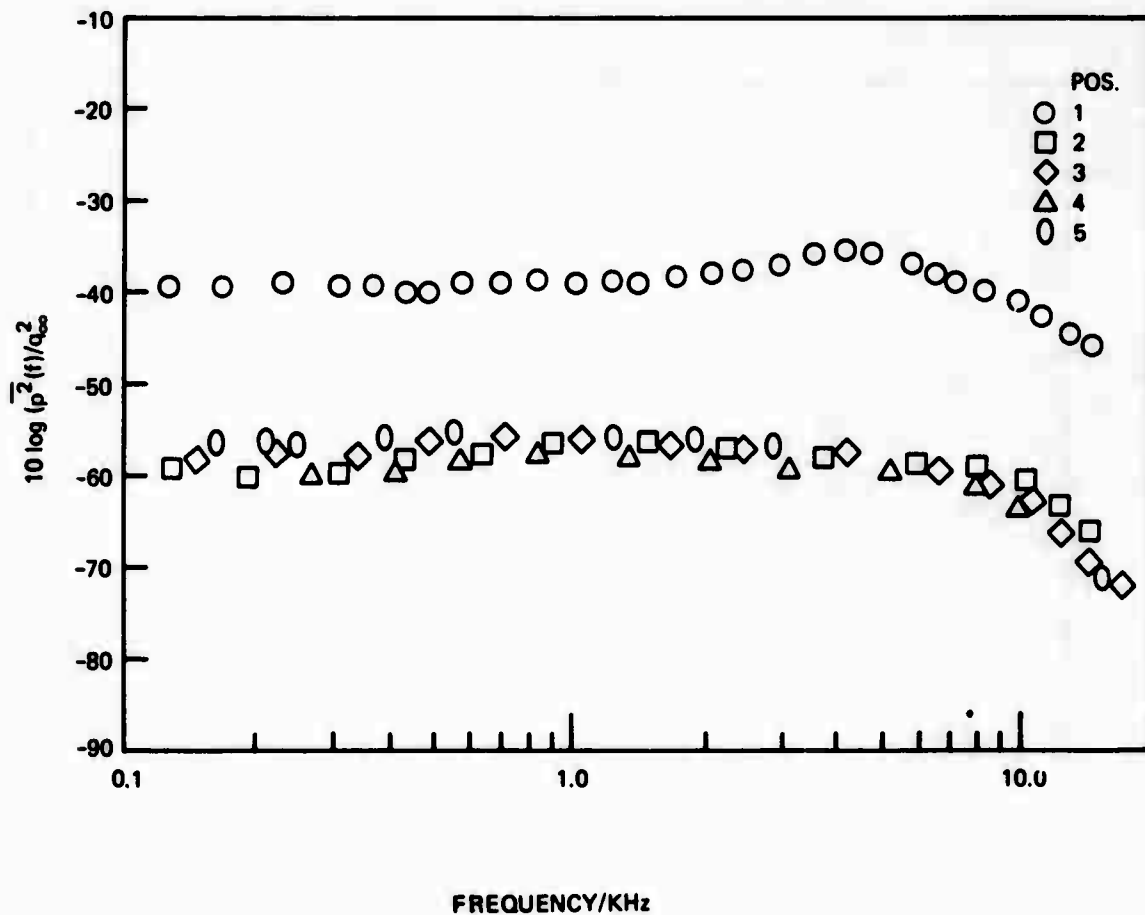


Figure 10 - Narrowband Mean-Square Pressures, Measured in 62.5-Hertz Bands at Chordwise Locations Forward of Knuckle-Trailing Edge for $U_{\infty} = 100$ Feet per Second

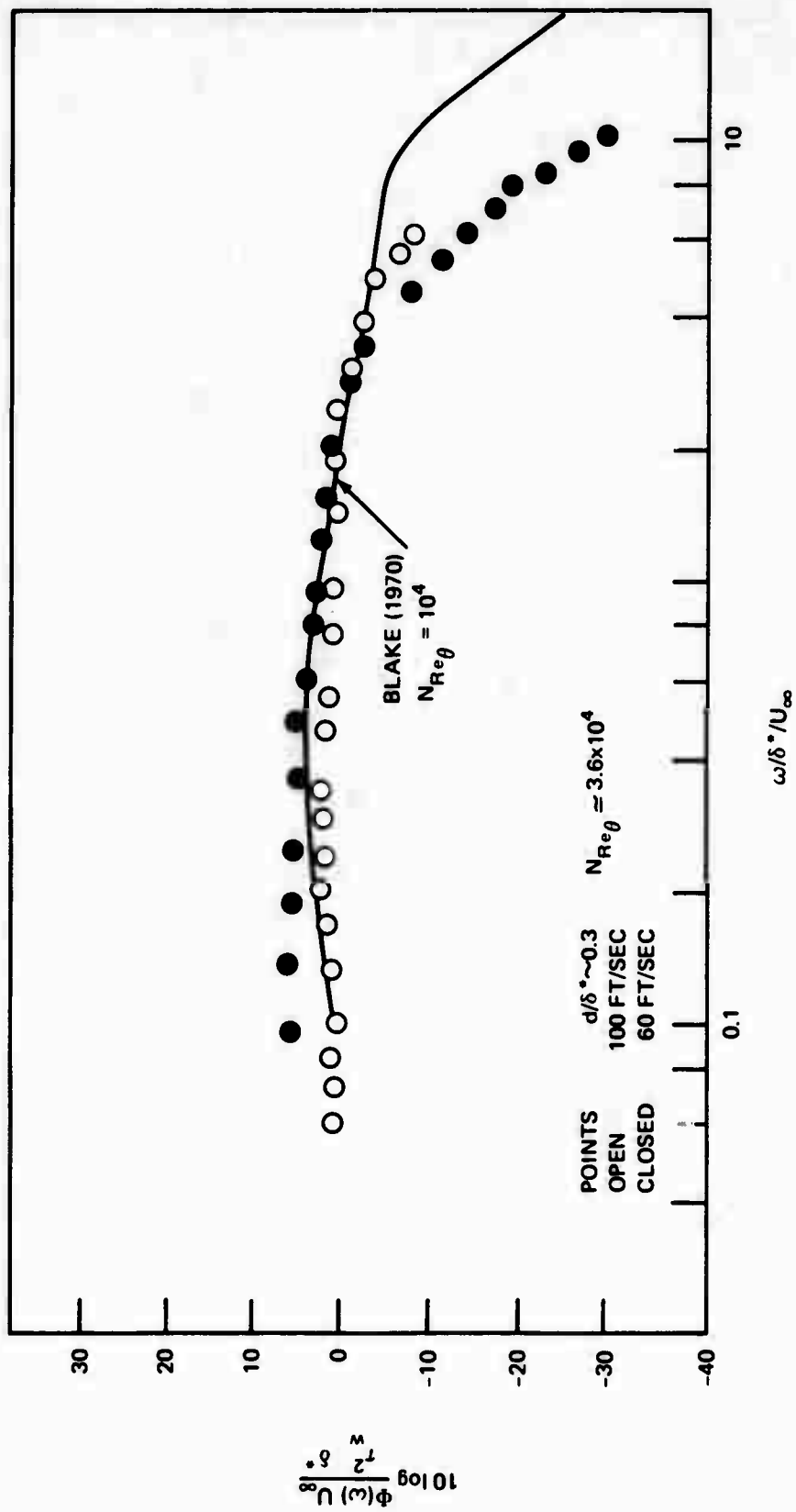


Figure 11 - Wall Pressure Spectral Densities at Position B,
 Normalized on Local Wall Shear, Displacement Thickness,
 and U_∞

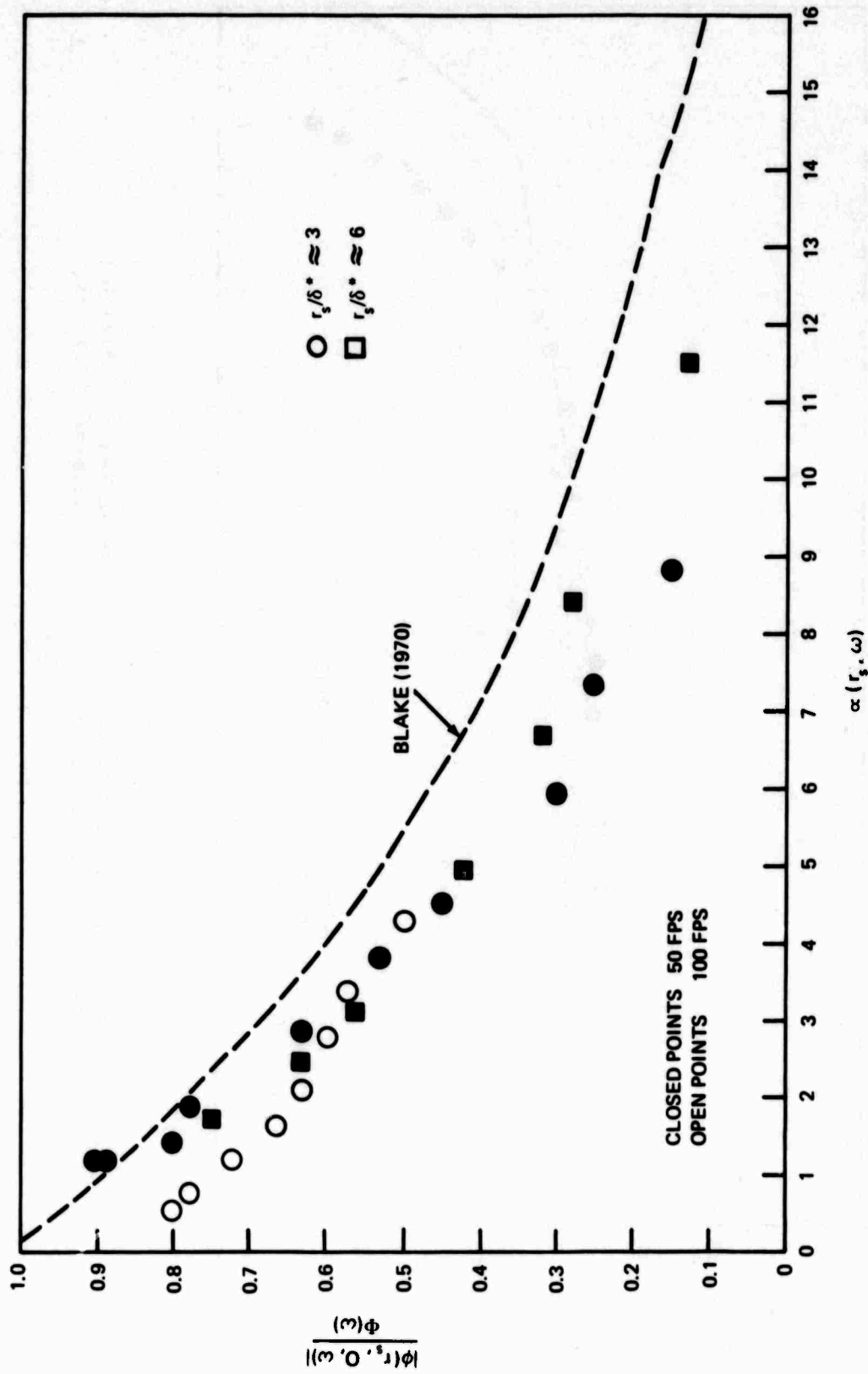


Figure 12 - Normalized Magnitude of Longitudinal Cross Spectral Density at Position B

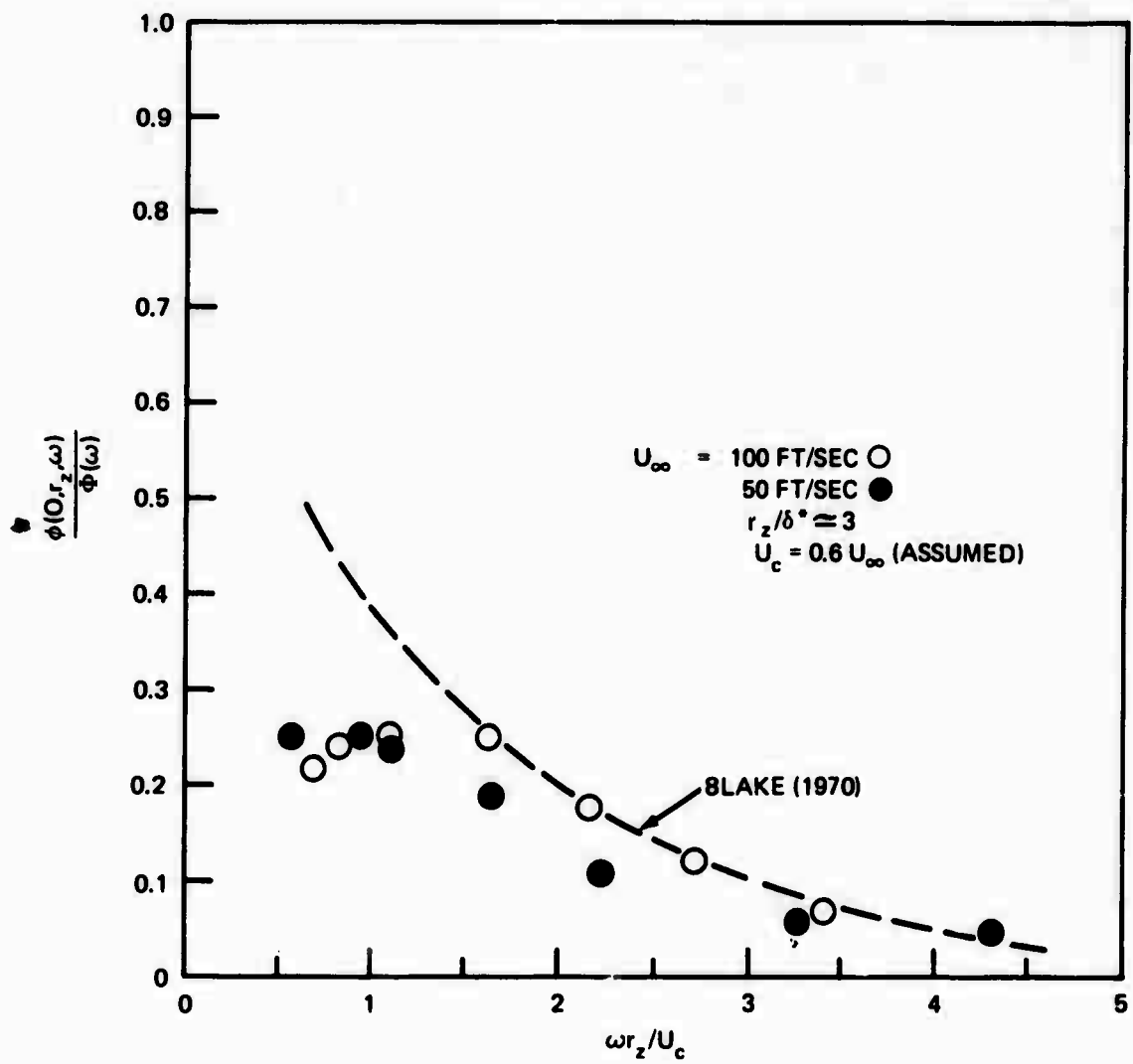


Figure 13 - Normalized Lateral Cross Spectral Density at Position B

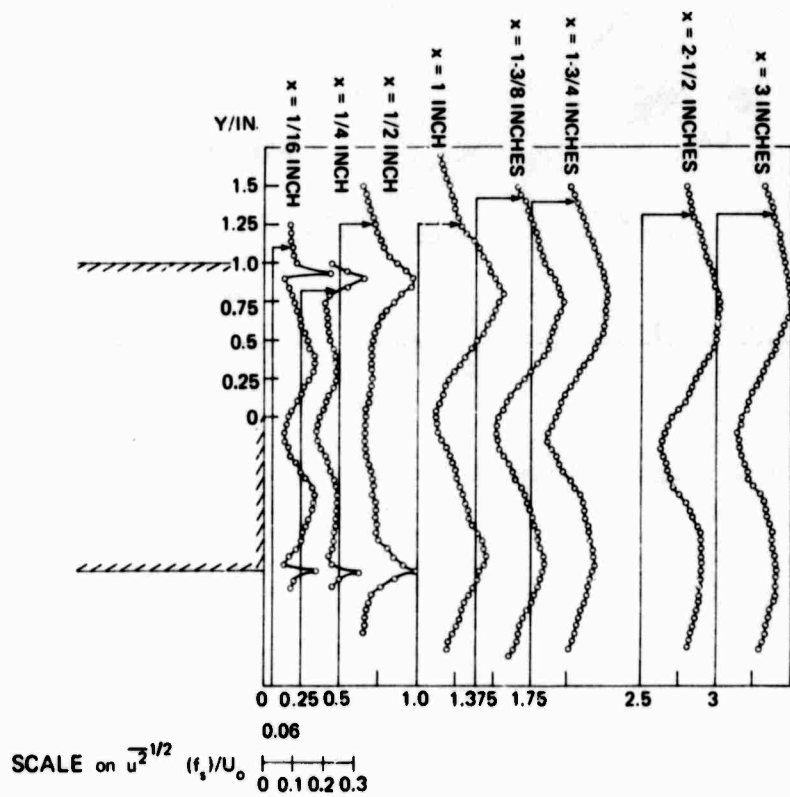
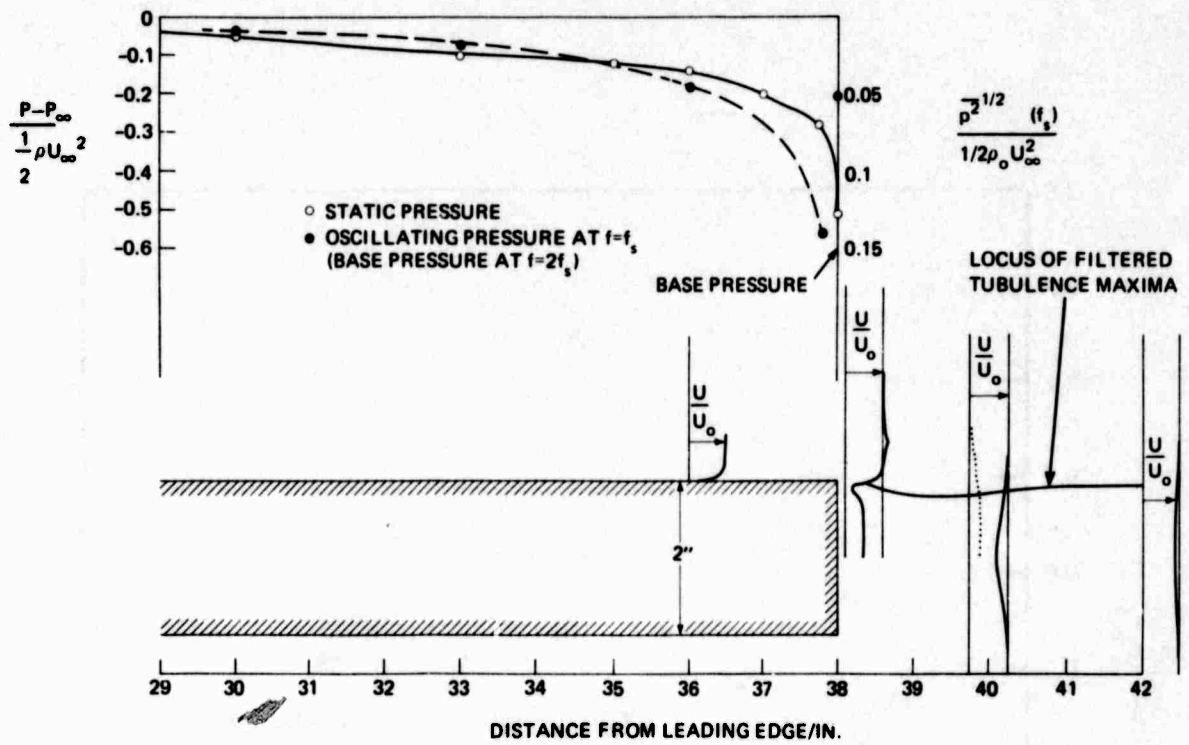


Figure 14 - Flow Patterns and Pressure Distributions at Trailing Edge of Blunt Trailing Edge at $U_\infty = 100$ Feet per Second

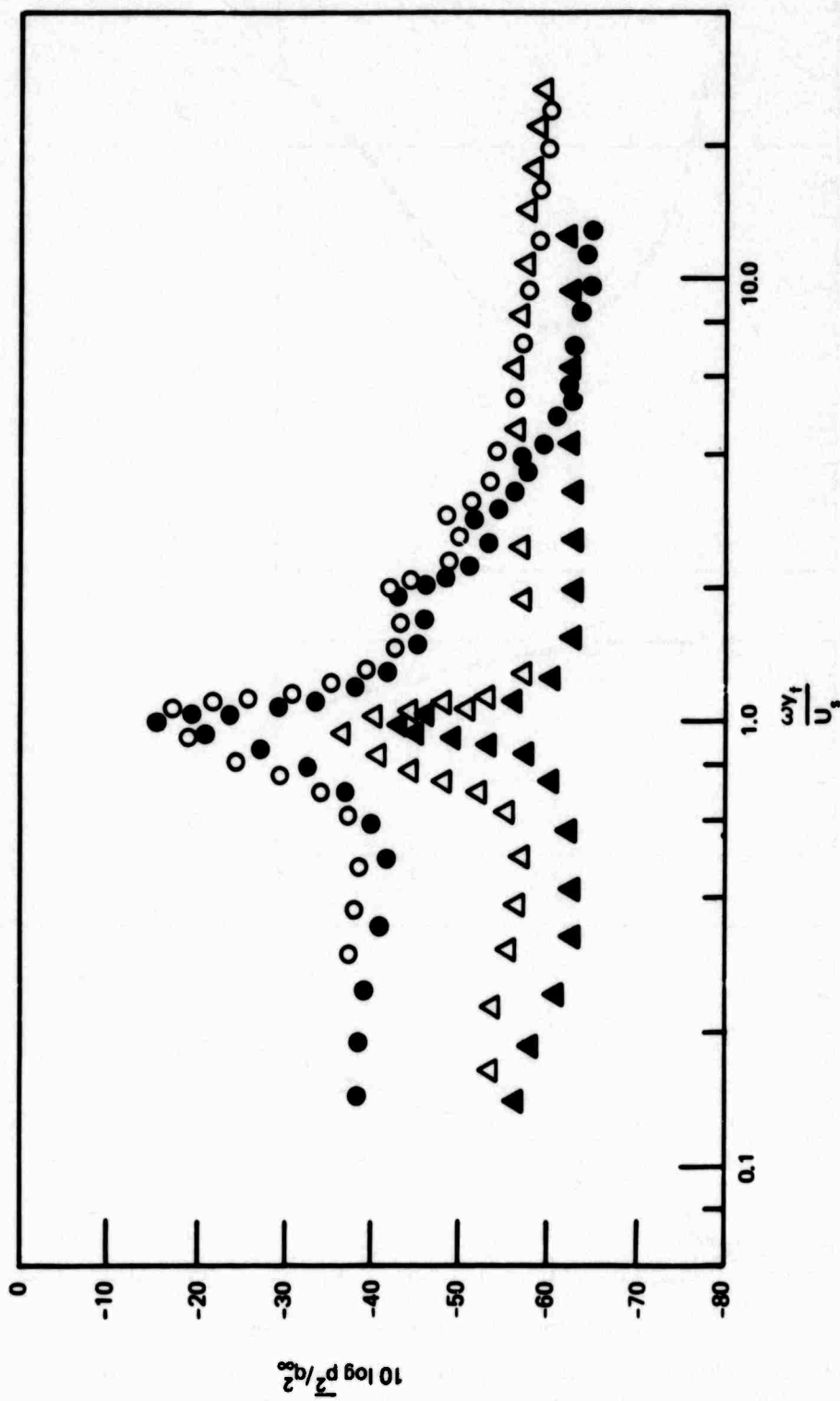


Figure 15 - Mean-Square Pressures, Measured on Blunt Edge in 12.5-Hertz Bands at Tip, $r_x = -0.3$ Inch, and at Position 6, $r_x = -13$ Inch, Flagged Points; for $U_\infty = 50$ Feet per Second, Open Points, $\Delta\omega_f/U_s = 0.178$; and for $U_\infty = 100$ Feet per Second, Closed Points, $\Delta\omega_f/U_s = 0.09$

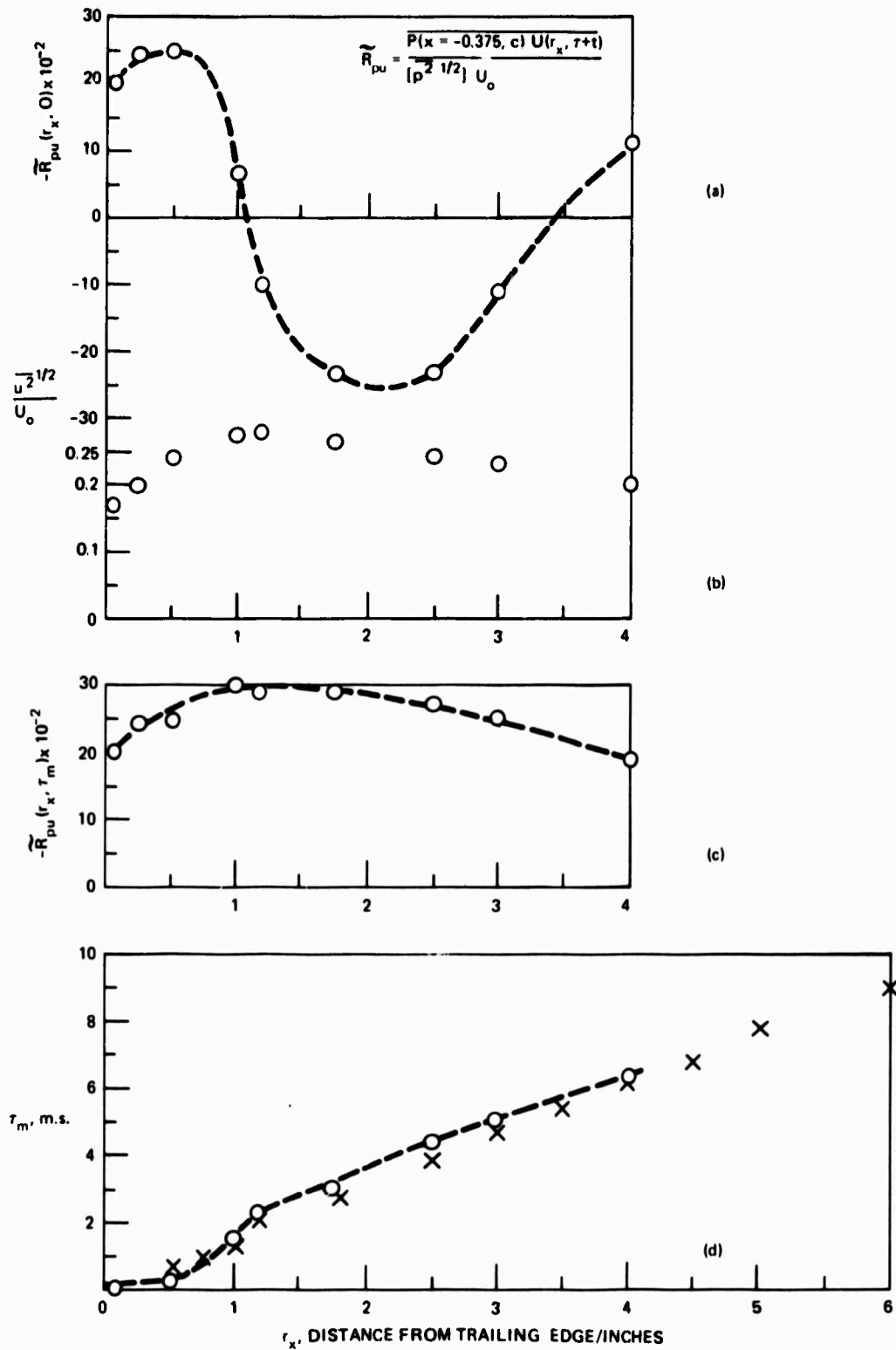


Figure 16 - Pressure Velocity Correlations behind Blunt Edge at $U_\infty = 100$ Feet per Second; r_x Is Measured Relative to Edge
(In diagram (d) open points were obtained from R_{pu} ; cross points from R_{uu} .)

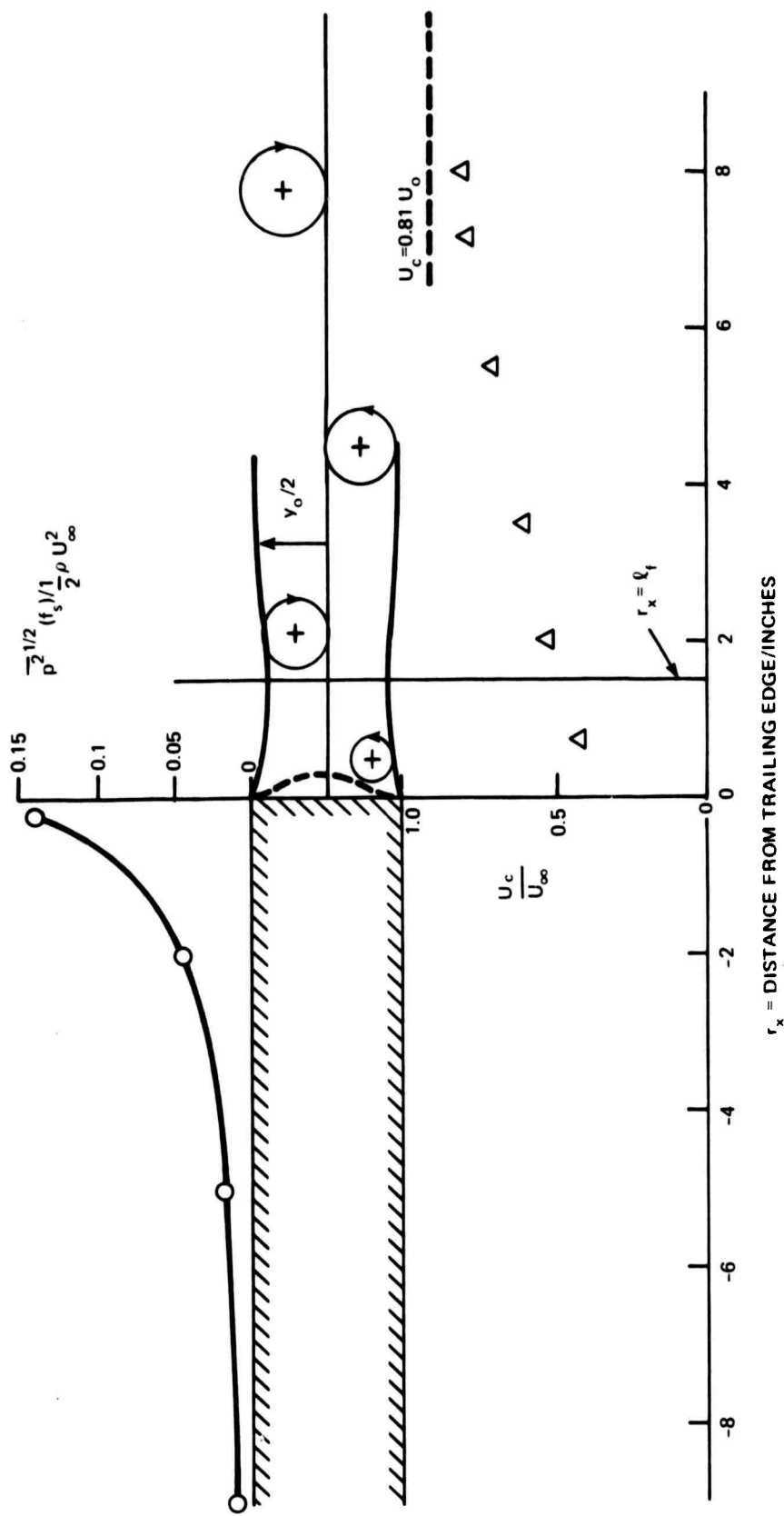


Figure 17 - Wake Structure, Fluctuating Surface Pressure Distribution, and Vortex Phase Speeds behind Blunt Edge

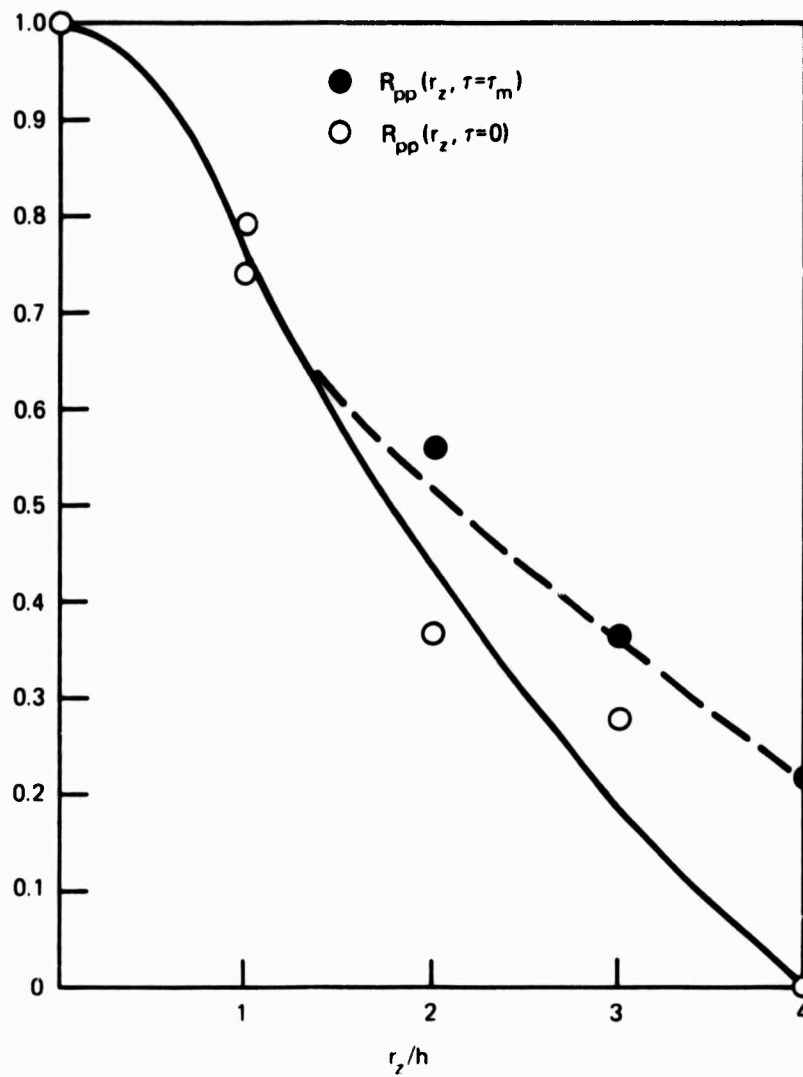


Figure 18 - Lateral Spatial Correlation of Fluctuating Trailing-Edge Pressure, Measured at 100 Feet per Second

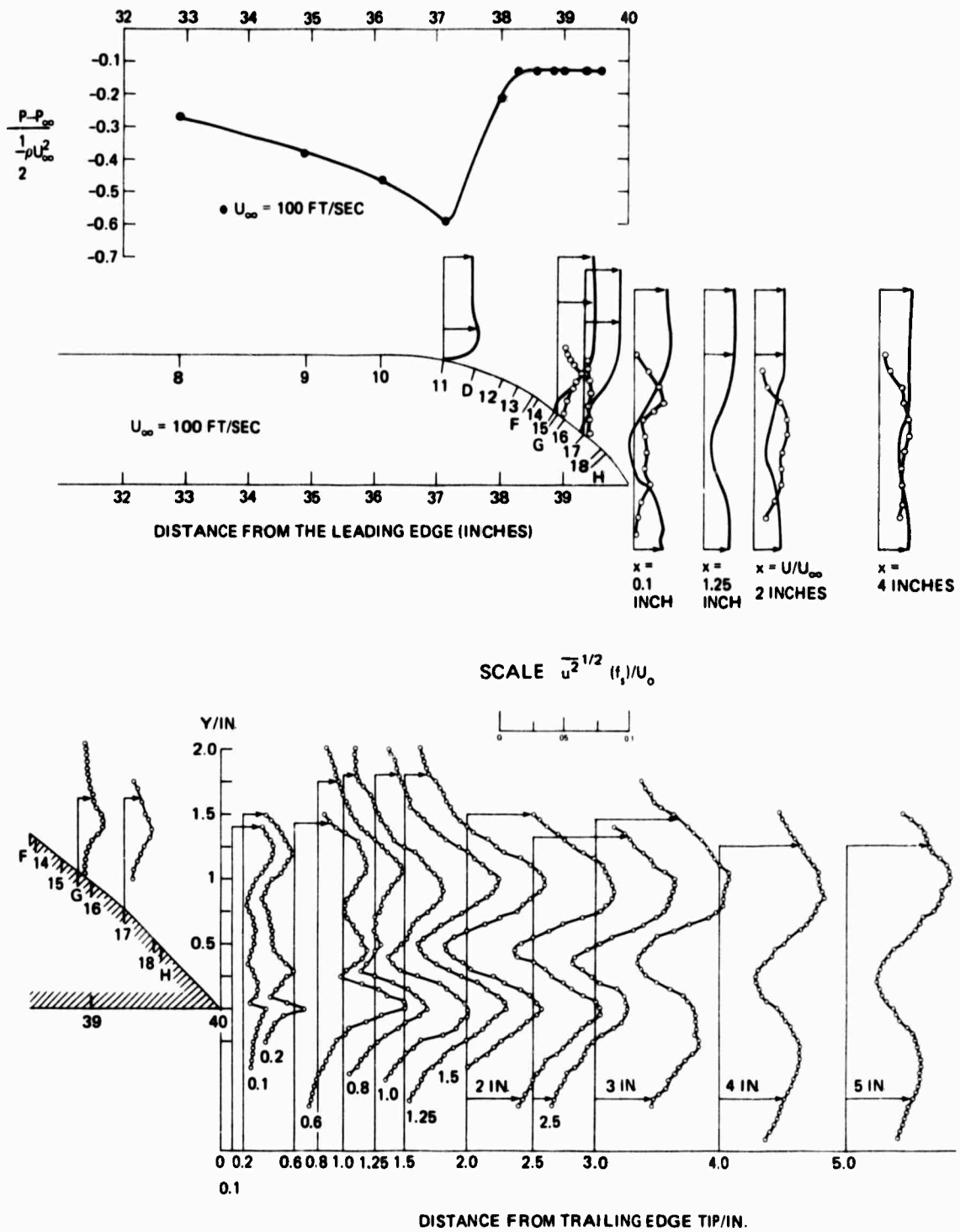


Figure 19 - Flow Patterns and Static Pressure Distribution at 45-Degree--
 Rounded Trailing Edge of Strut
 (Numbers denote pressure tap locations;
 letters denote microphone locations.)

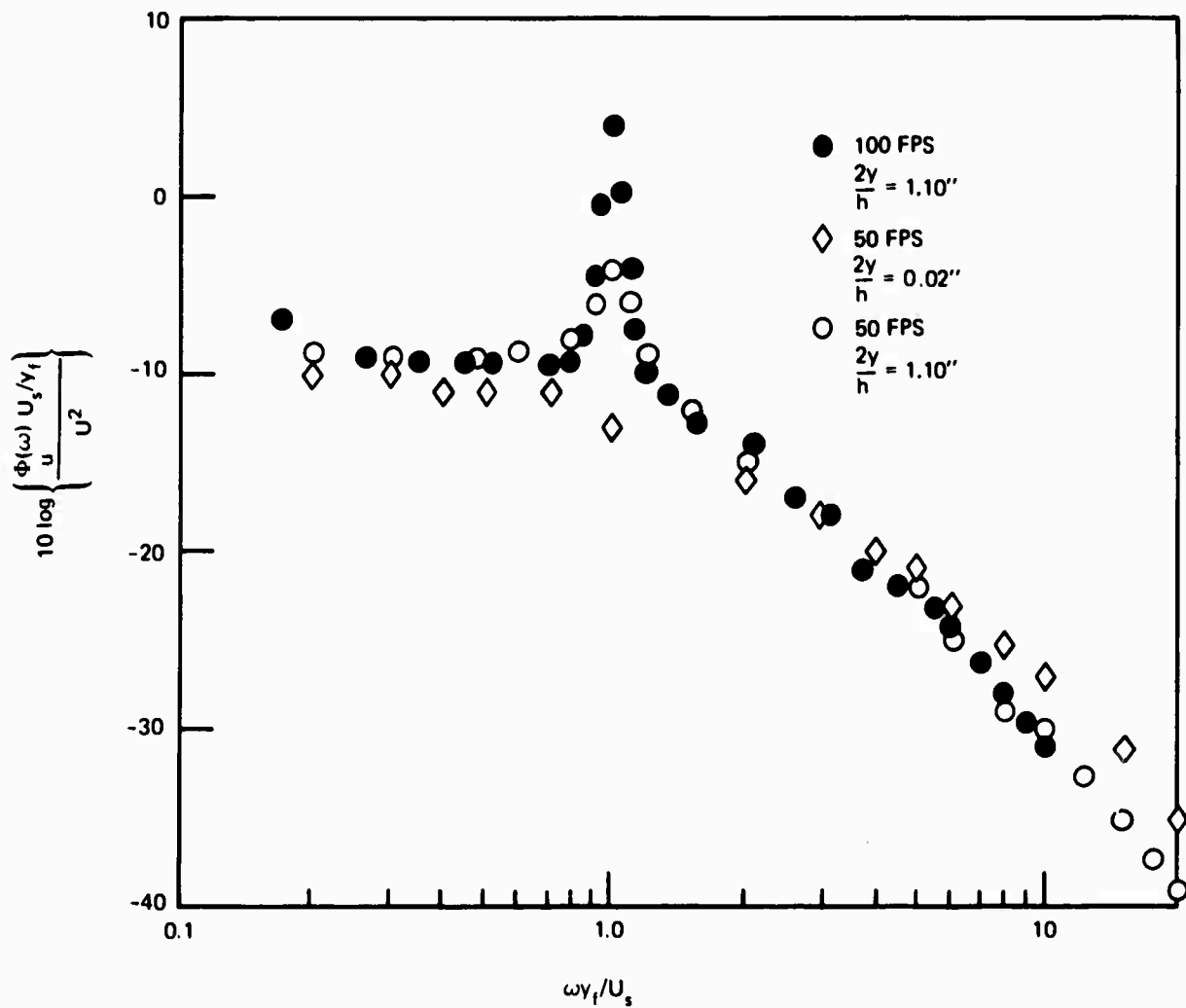


Figure 20 - Dimensionless Longitudinal Velocity Spectral Densities,
 Measured in Formation Region of Near Wake from
 45-Degree--Rounded-Beveled Edge
 (Co-ordinate position, $r_x = 1.25$ inch.)

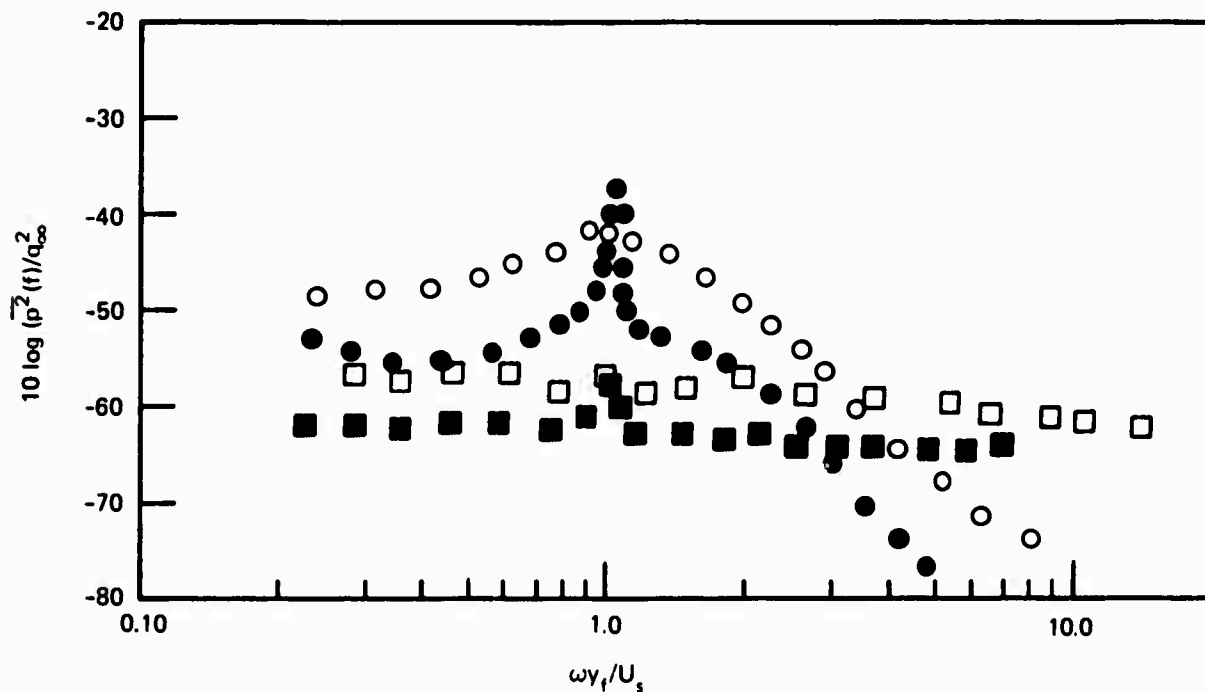


Figure 21 - Mean-Square Pressures, Measured on the 45-Degree Rounded Edge
in 12.5-Hertz Bands at Positions G and 6, Flagged Points;
for $U_\infty = 50$ Feet per Second, Open Points, $\Delta\omega_o/U_s = 0.09$;
and for 100 Feet per Second, Closed Points,
 $\Delta\omega_o/U_s = 0.045$

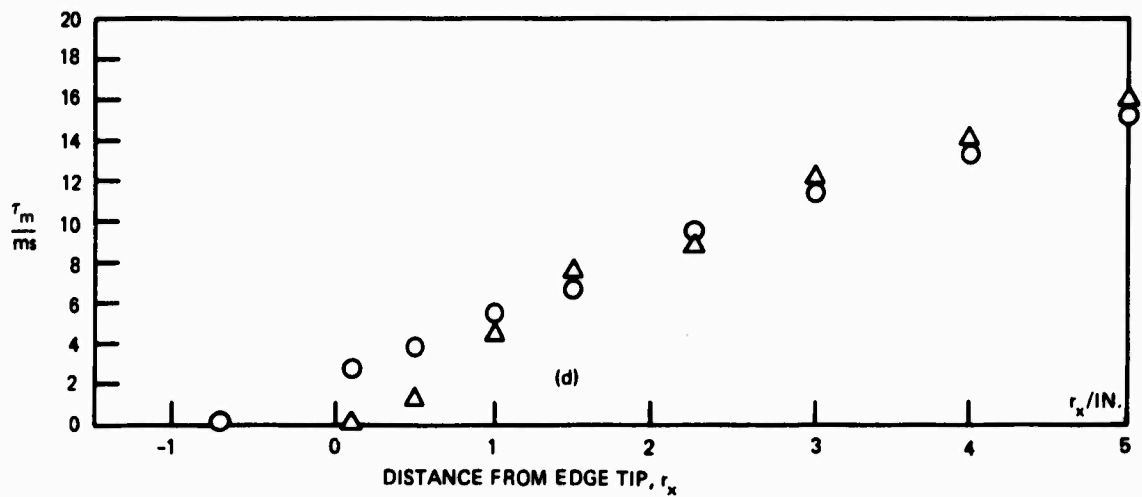
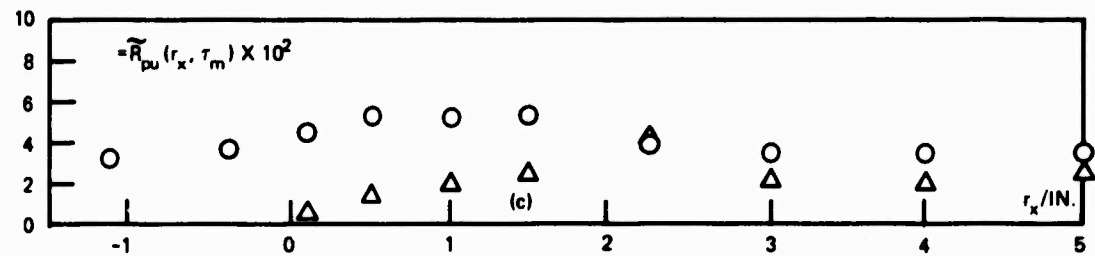
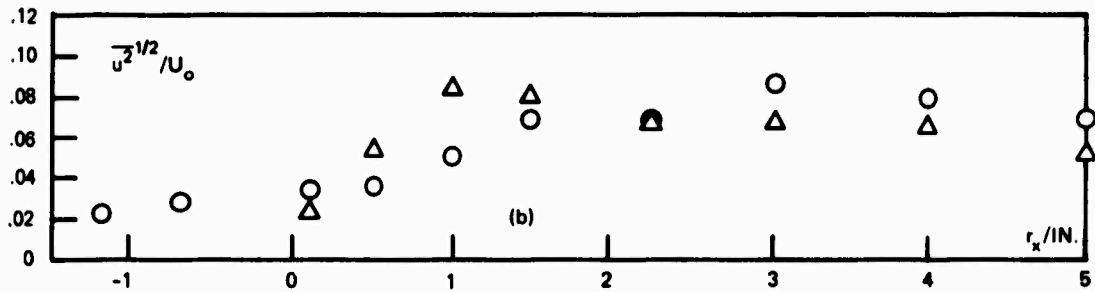
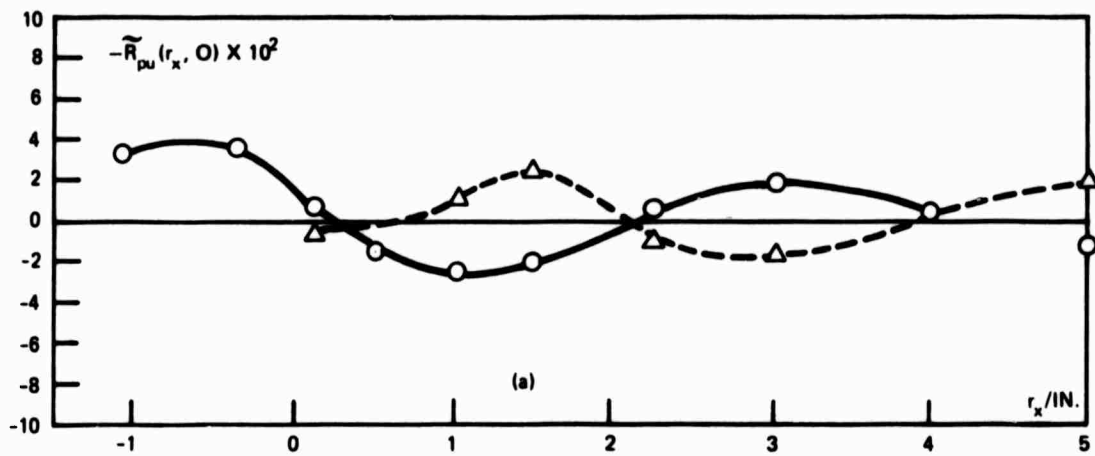


Figure 22 - Pressure-Velocity Correlations in Wake behind 45-Degree--Rounded-Beveled Edge at $U_\infty = 50$ Feet per Second; r_x Measured from Tip (Points marked 0 along $y = y_u$; Δ along $y = y_\ell$)

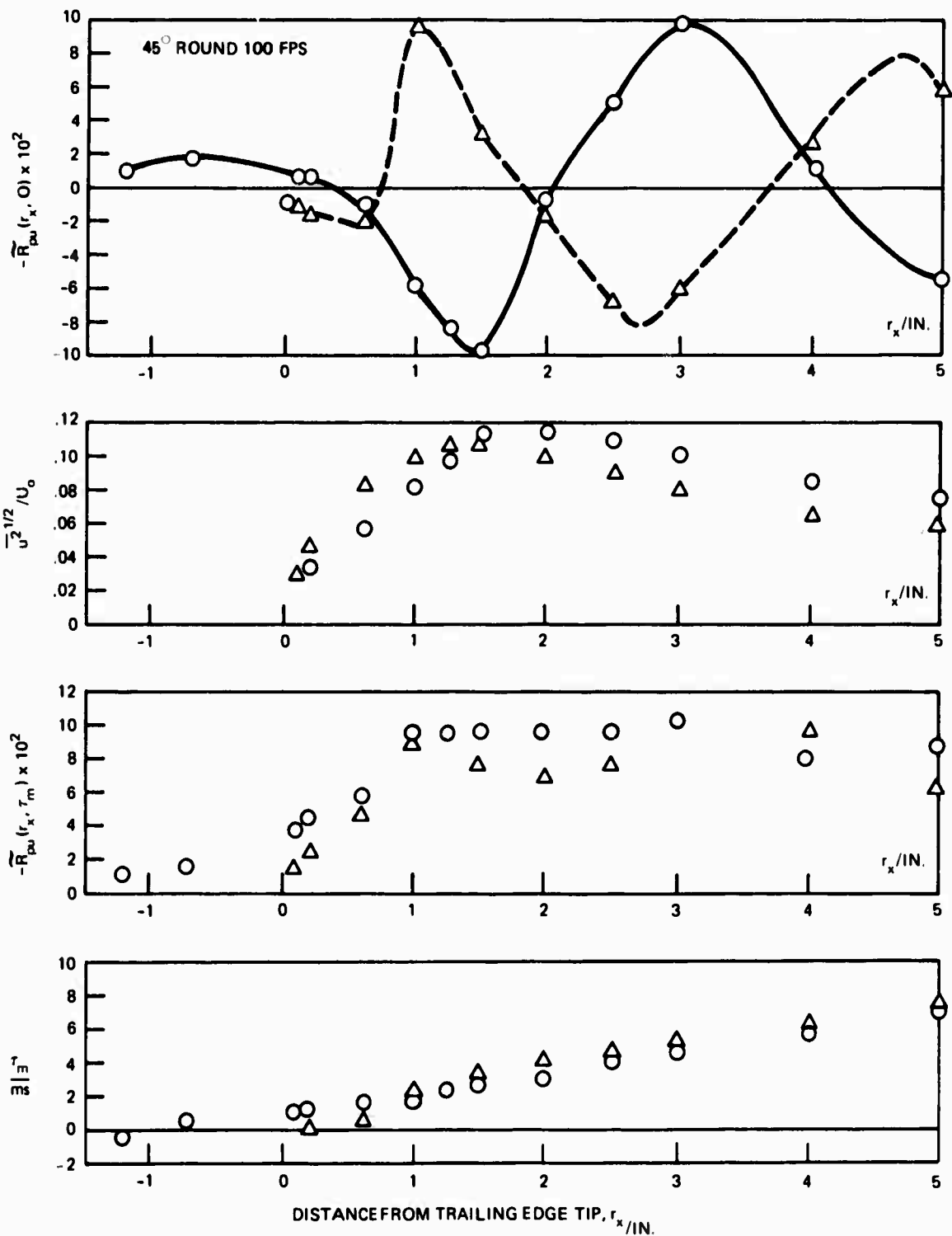


Figure 23 - Pressure-Velocity Correlations behind 45-Degree--
Rounded-Beveled Edge at $U_\infty = 100$ Feet per Second;

Distances r_x are Measured from Tip of Edge
(Points marked \circ along $y = y_u$, Δ along $y = y_l$)

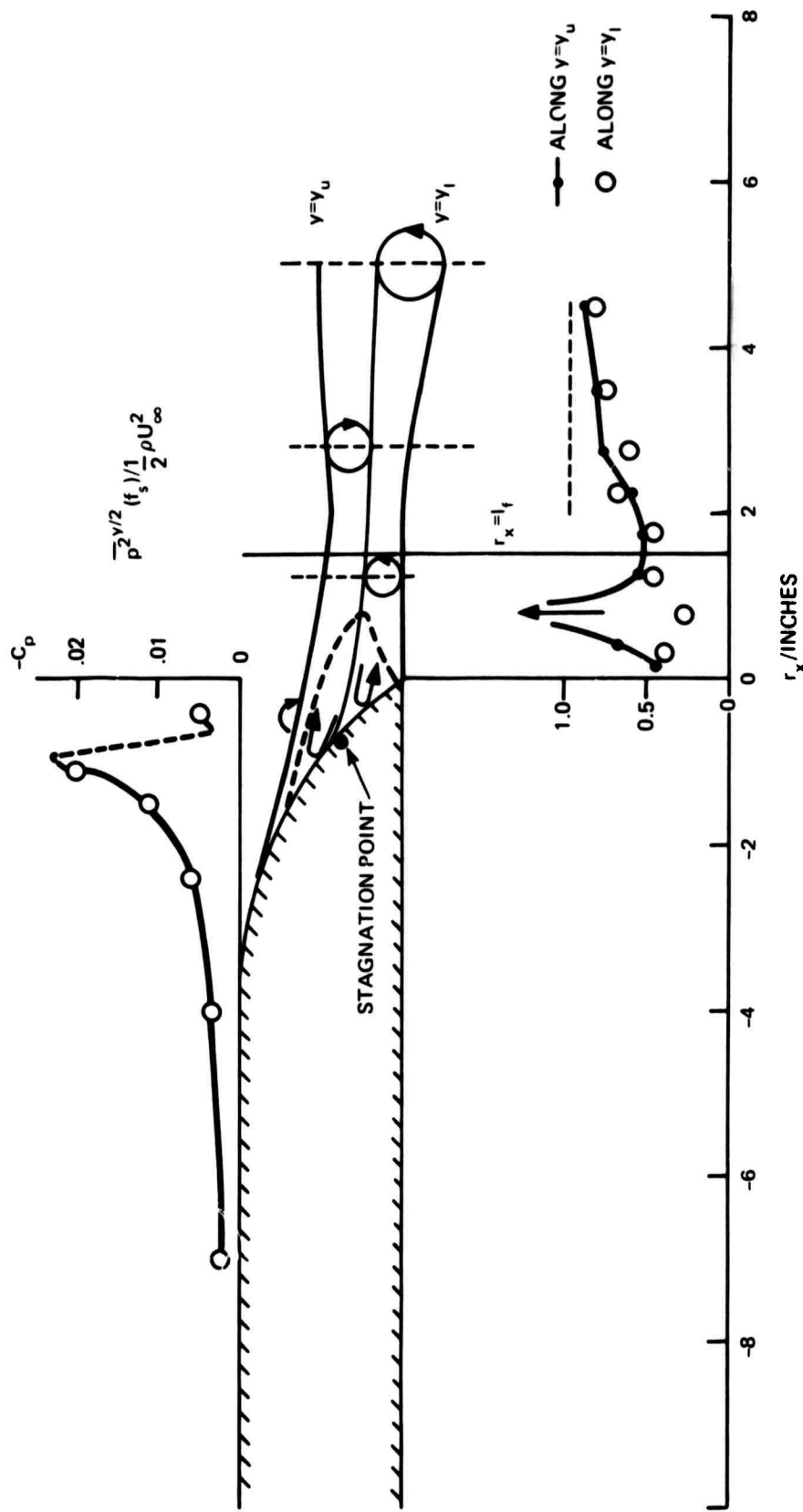


Figure 24 - Vortex Geometry in Near Wake, Corresponding to Pressure-Velocity Correlations for Upper Shear Layer

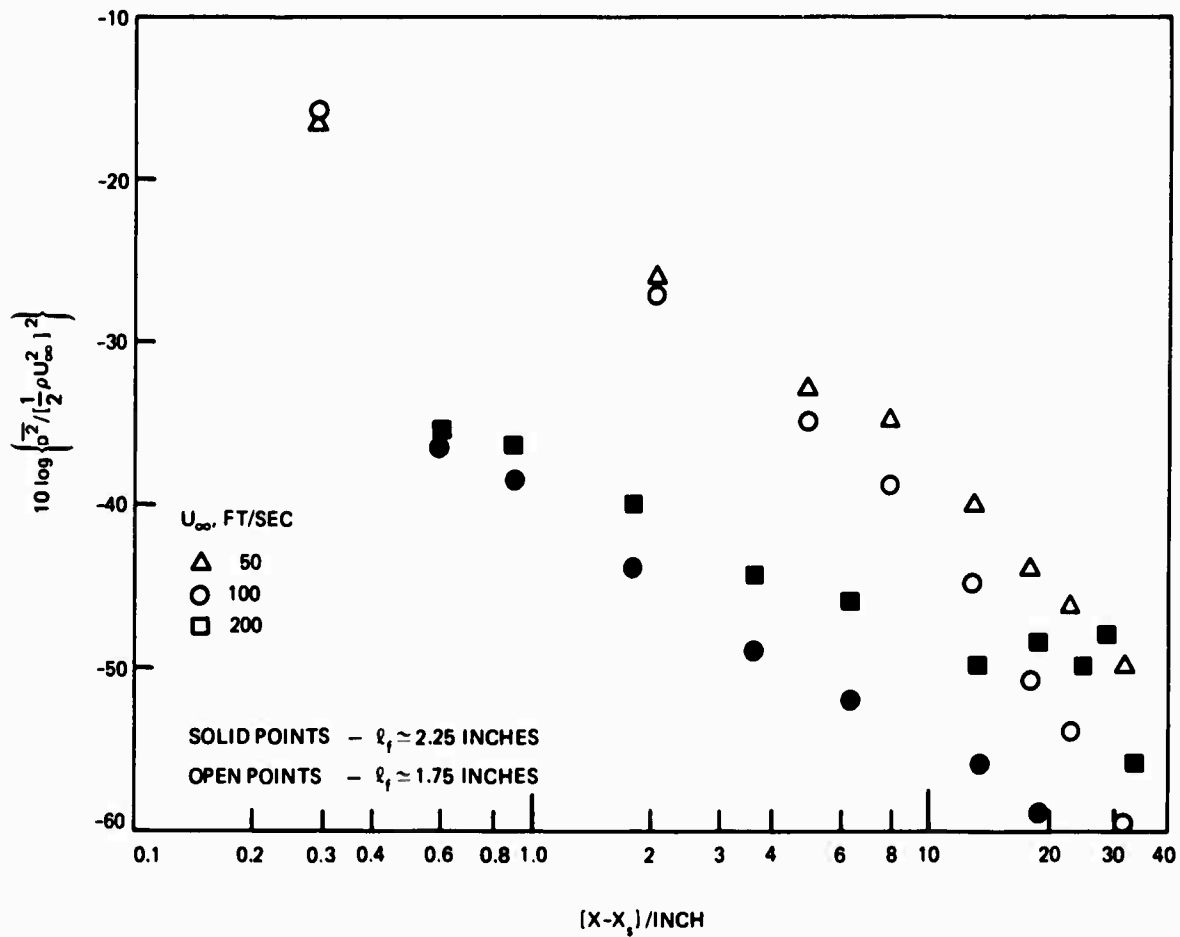


Figure 25 - Mean-Square Pressures Measured at various Streamwise Distances x Forward of Trailing-Edge Stagnation Point x_s

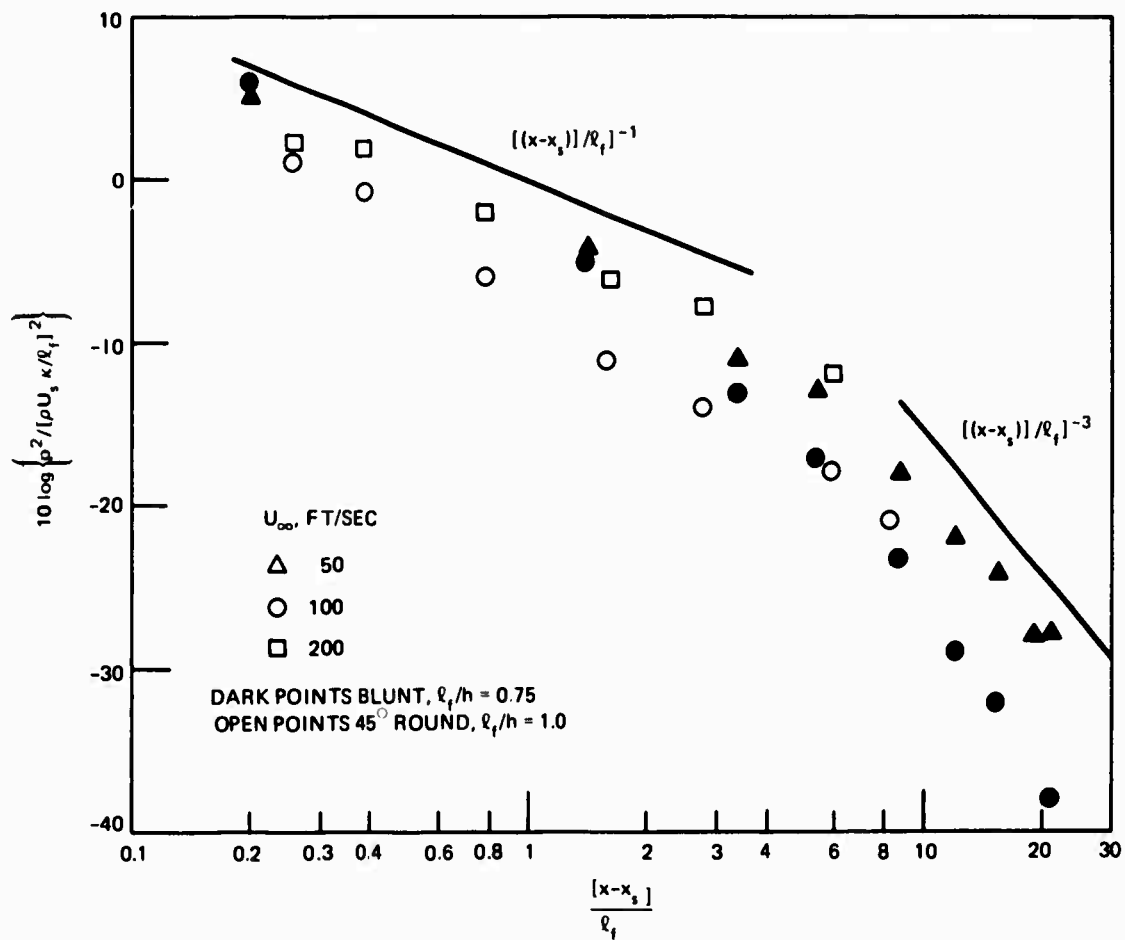


Figure 26 - Chordwise Distribution of Fluctuating Pressures Normalized on Flow-Separation Speed U_s , Vortex Strength, and Formation Length

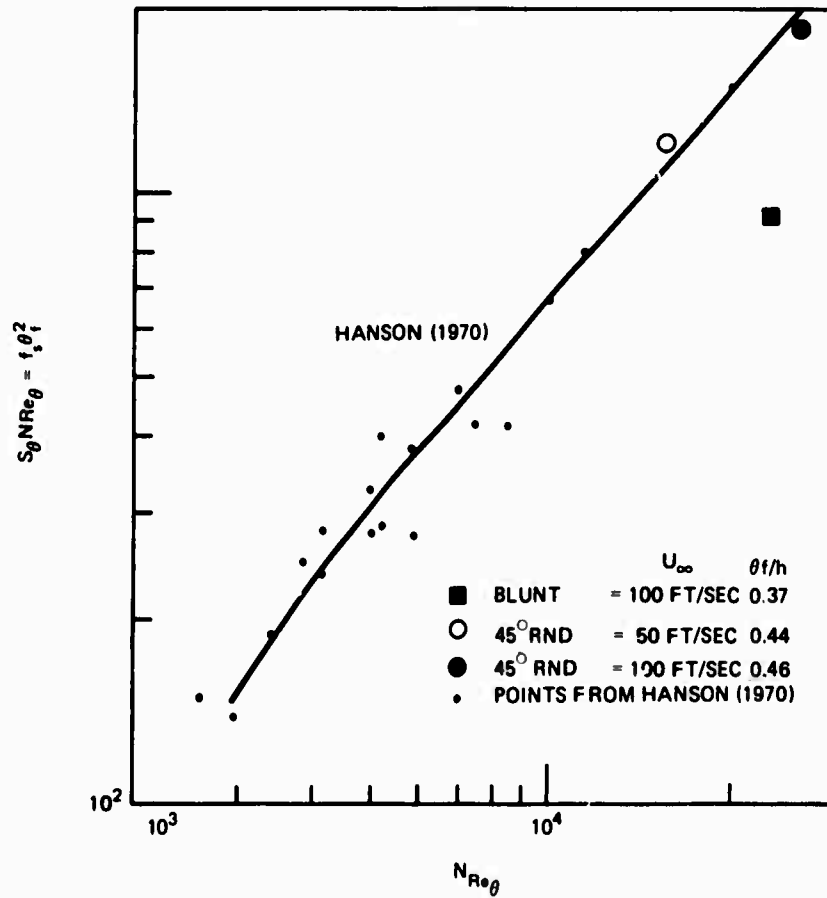


Figure 27 - Dimensionless Vortex-Shedding Frequencies Based on Momentum Thickness

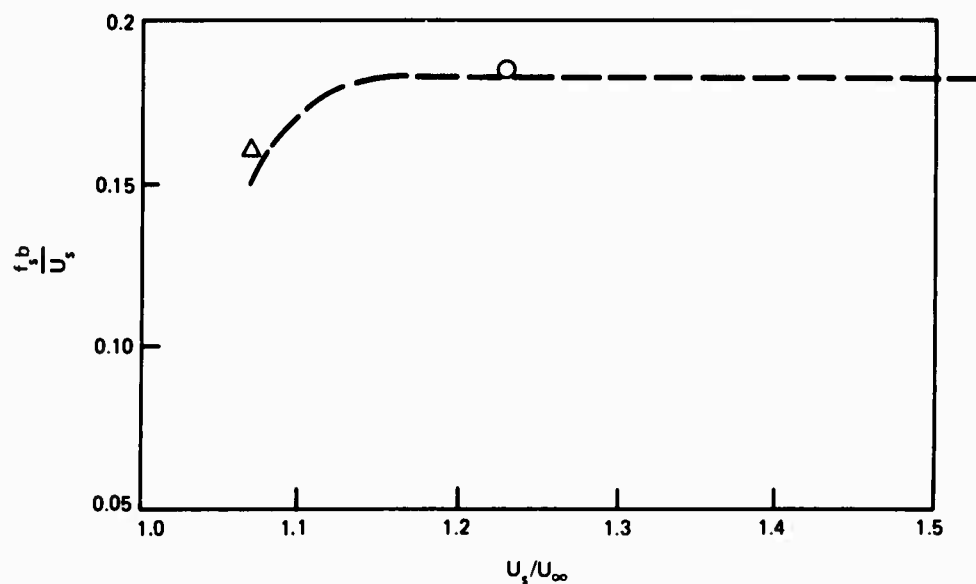


Figure 28 - Universal Strouhal Number of Bearman (1967) versus U_s/U_∞
 for Blunt and 45-Degree--Rounded-Trailing Edges
 (Δ 45-degree round, 100 feet per second, 0 blunt,
 100 feet per second; --- representative
 body shapes.)

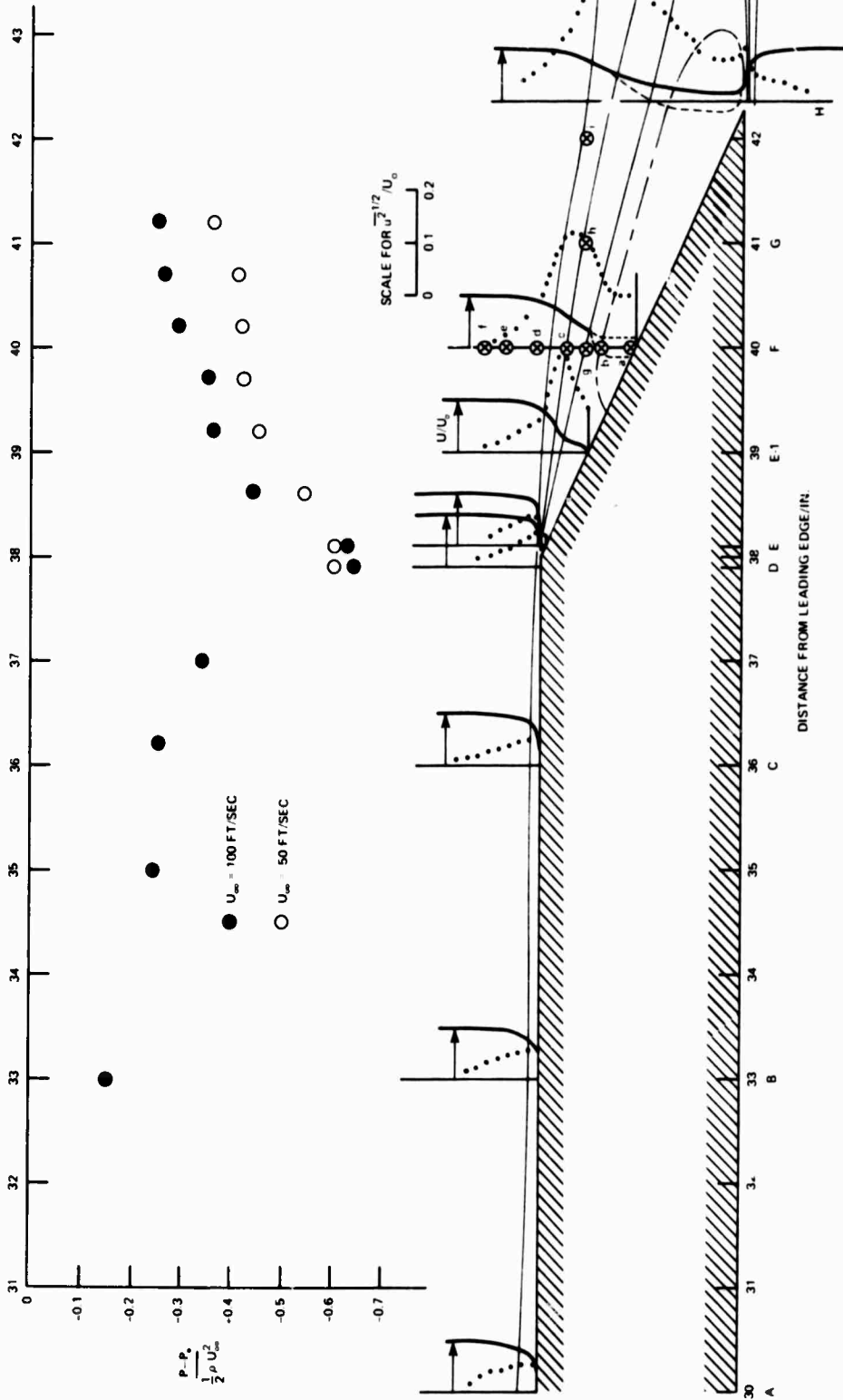


Figure 29 - Flow Patterns and Static Pressure Distributions on 25-Degree--Knuckle-Beveled Edge
(Flow patterns are shown for $U_\infty = 100$ feet per second; static pressures for speeds shown.)

$$R_{uu}(x_F, y, r_S \approx 0.5'', r_n = 0, r_z \approx 0.13'')$$

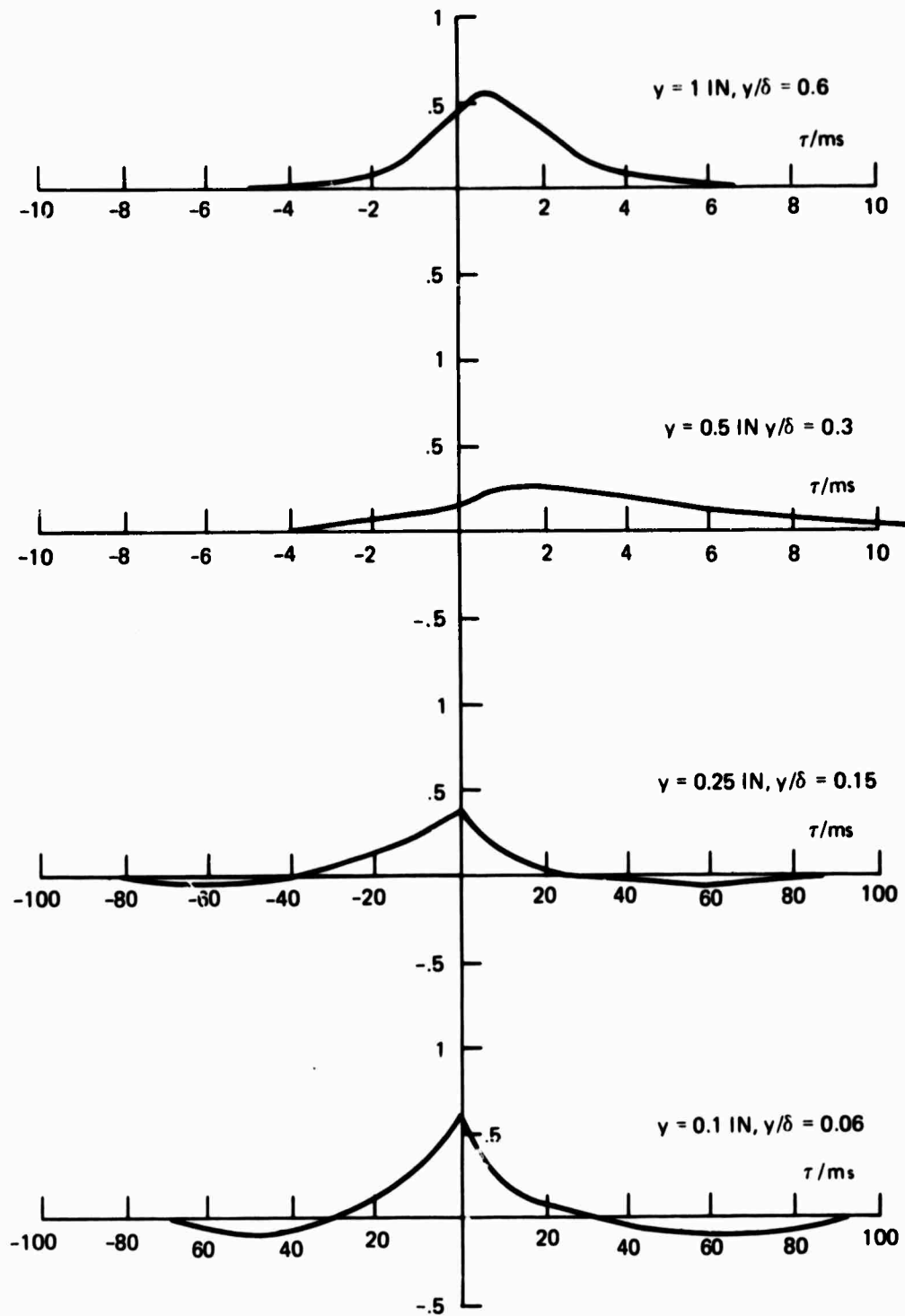
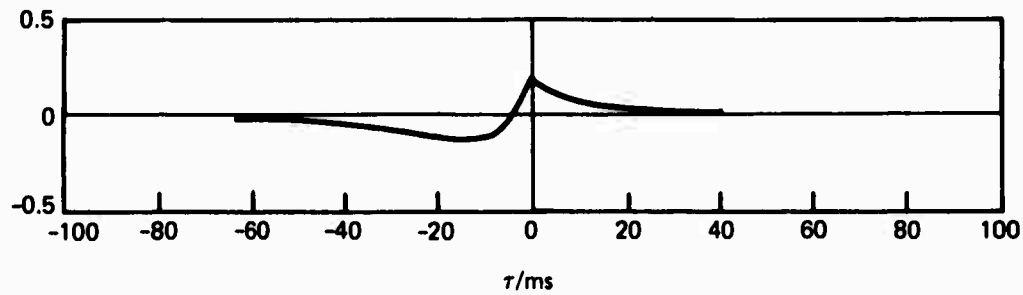


Figure 30 - Space-Time Velocity Correlations above Position F on 25-Degree--Knuckle Edge at $U_\infty = 50$ Feet per Second
(Separations of probes are in streamwise direction.)

R_{uu} ($x_F, y = 0.1$ IN, $r_s = 0, r_n = 0.22'', r_z = 0.13''$)



R_{uu} ($x_F, y = 0.1$ IN, $r_s = 0, r_n = 0.44'', r_z = 0.16''$)

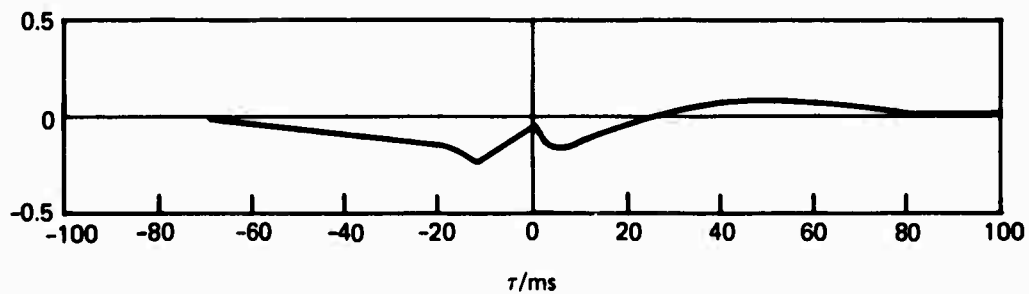


Figure 31 - Space-Time Velocity Correlations above Position F on 25-Degree--Knuckle Edge, Using Vertical Separations of Probes ($U_\infty = 50$ feet per second; $\delta = 1.69$ inch.)

Figure 32 - Spectra of Longitudinal Turbulent Velocity at Positions F and H on Knuckle Edge

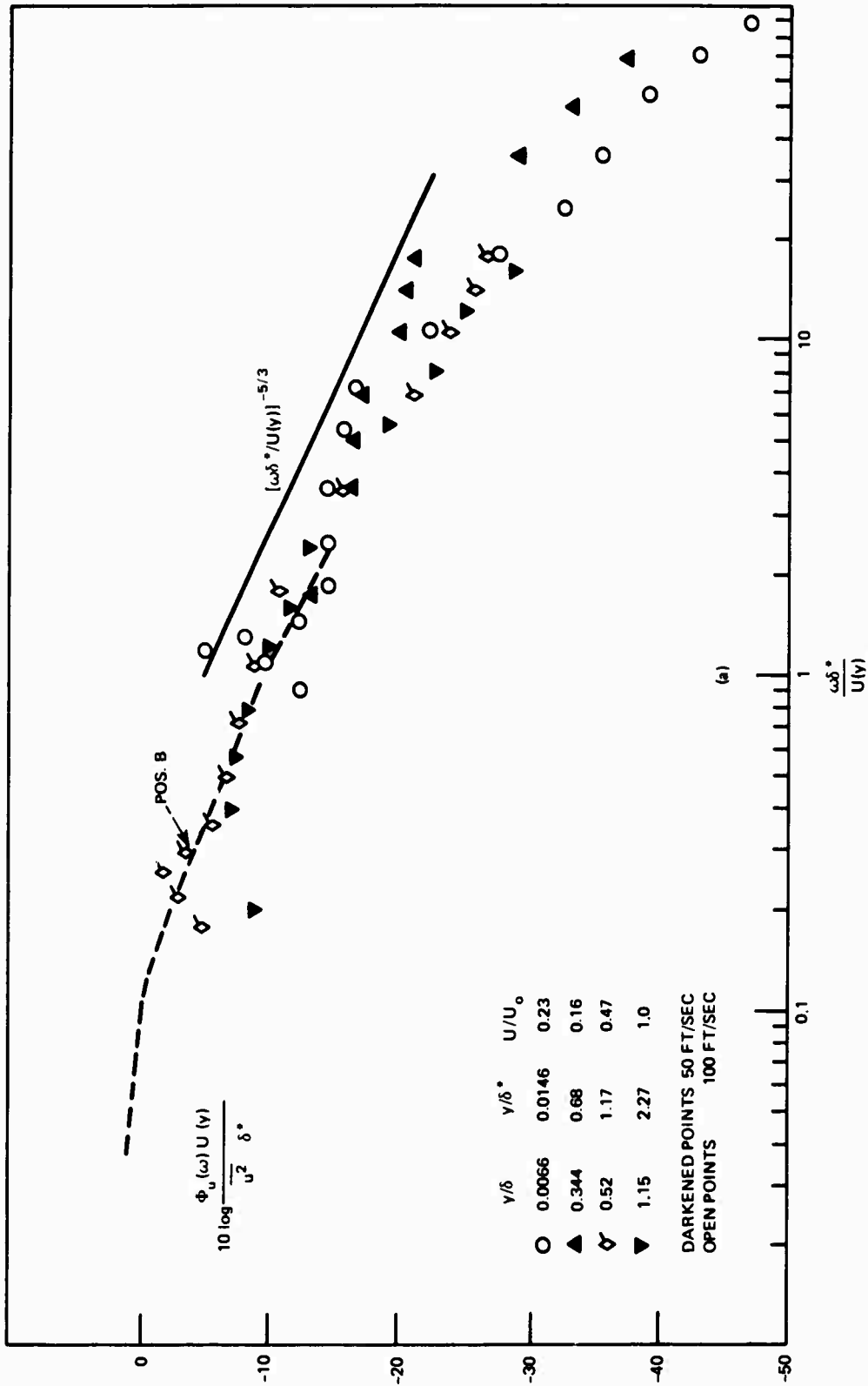


Figure 32a - Position F

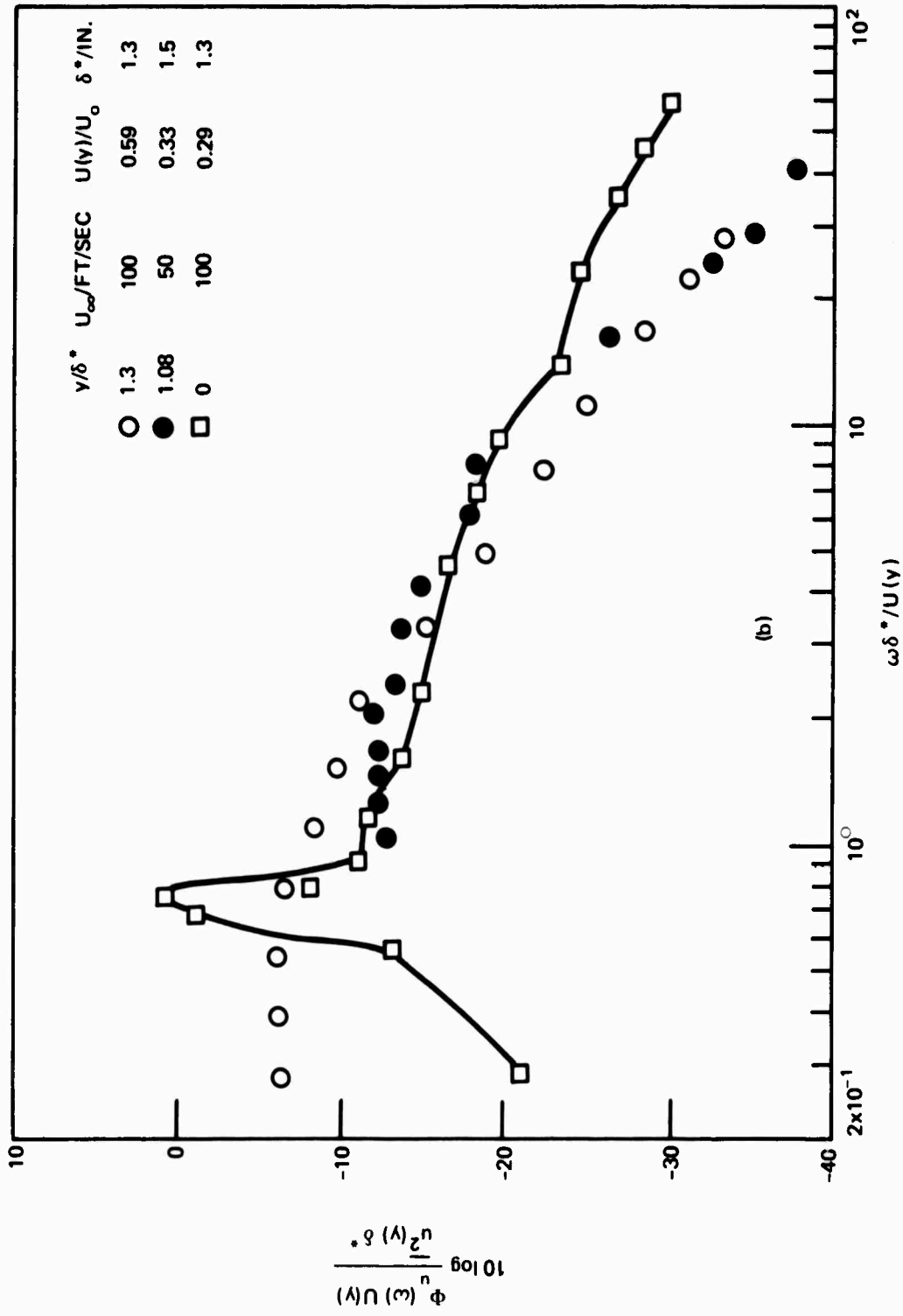


Figure 32b - Position H

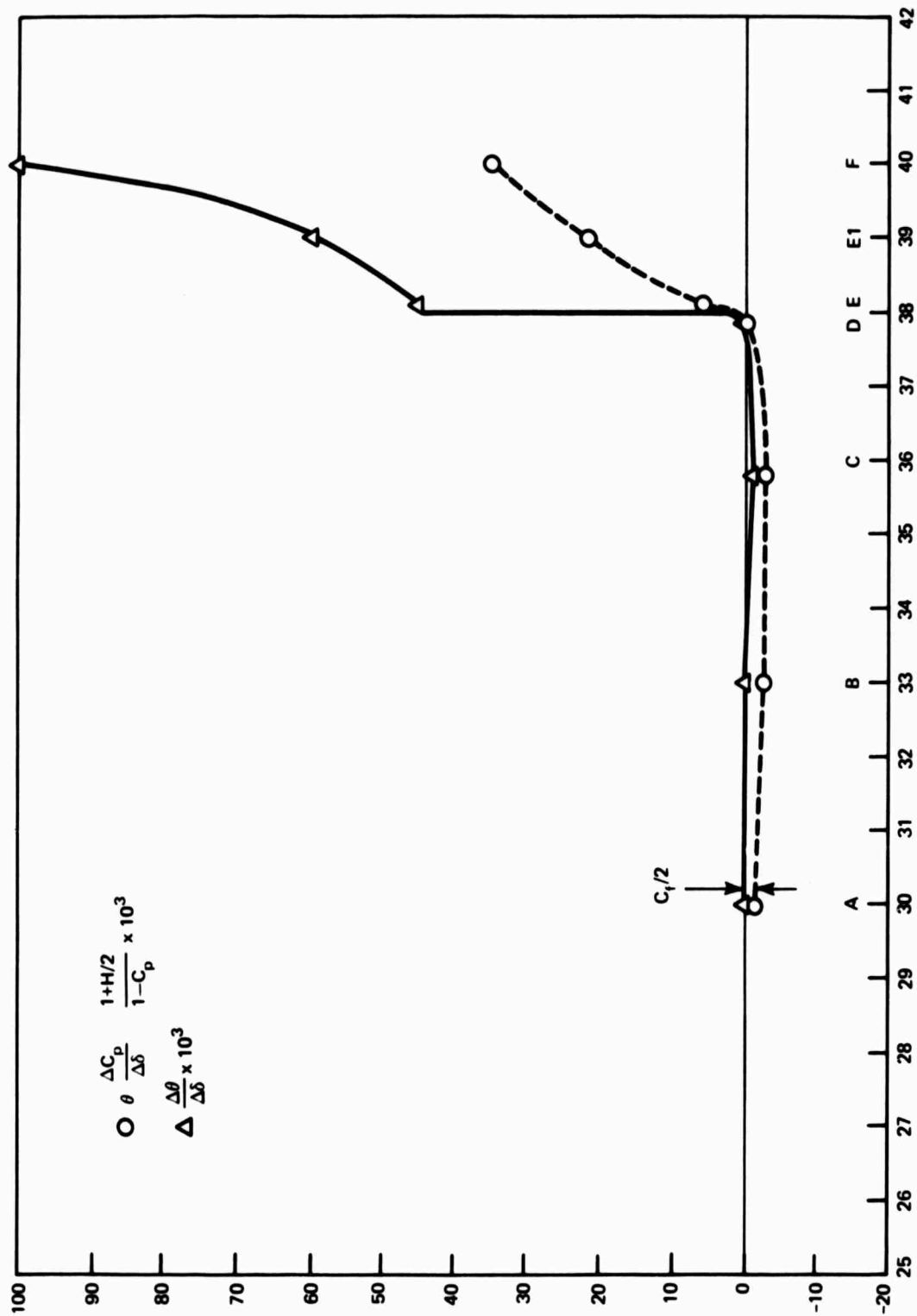


Figure 33 - Momentum Balance for 25-Degree Knuckle Edge
 at $U_\infty = 100$ Feet per Second

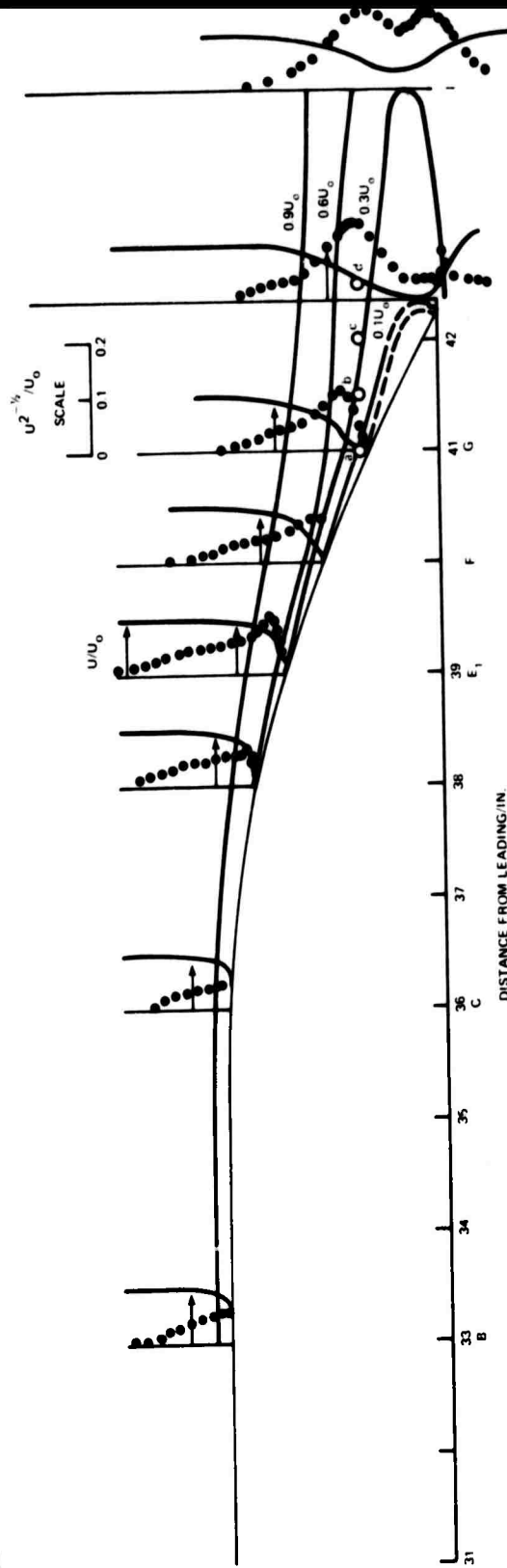
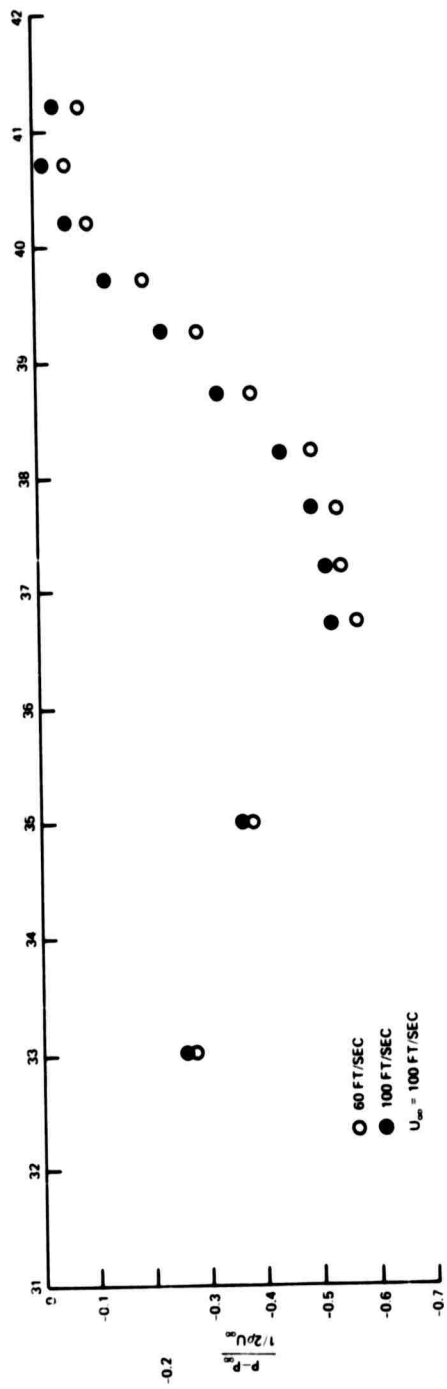


Figure 34 - Flow Patterns at $U_\infty = 100$ Feet per Second and Pressure Distribution Near 25-Degree--Rounded-Beveled Edge

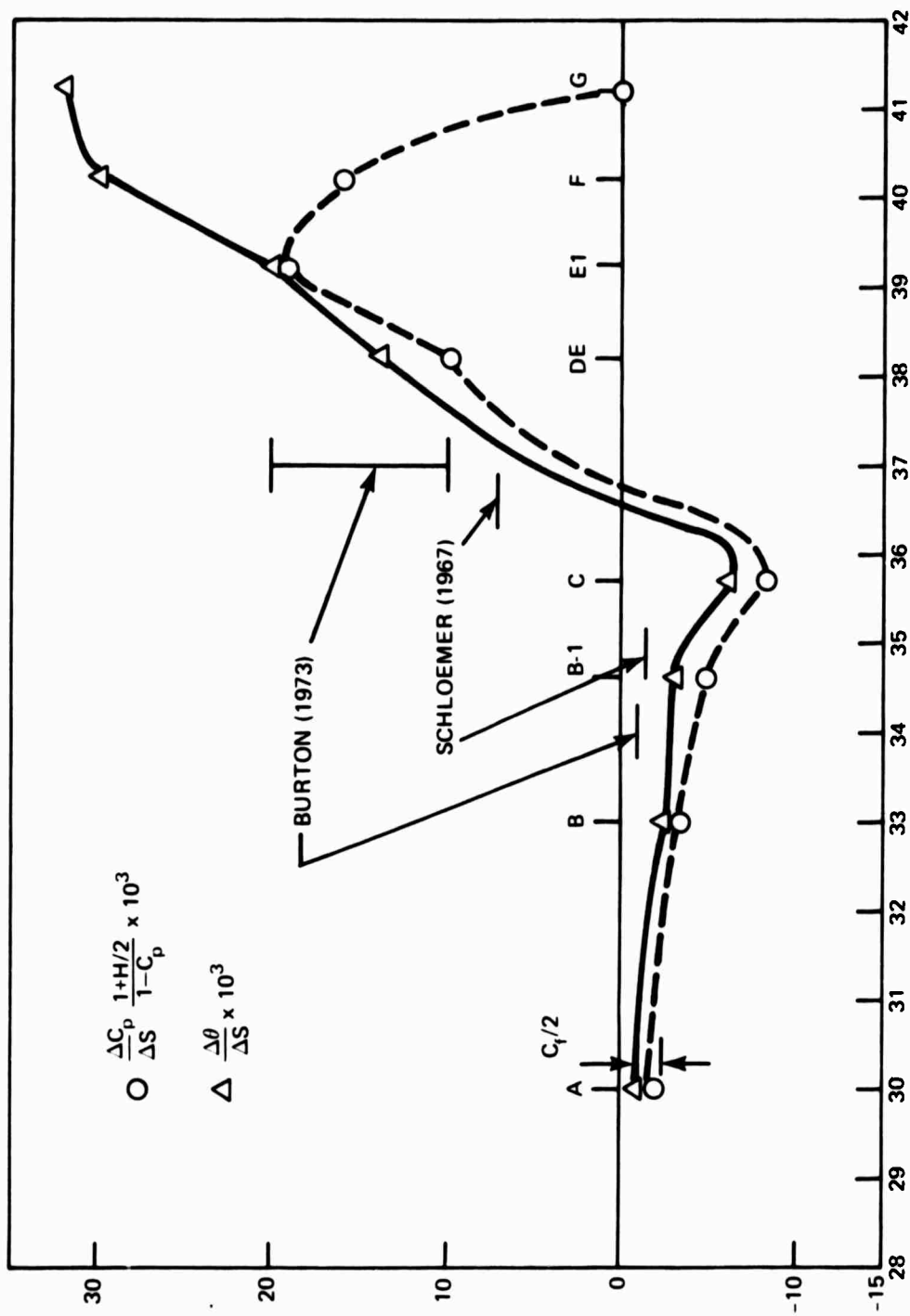


Figure 35 - Momentum Balance for 25-Degree-Rounded-Beveled Edge at 100 Feet per Second

Figure 36 - Autocorrelation of Turbulent Velocity Fluctuating over 25-Degree--Rounded-Beveled Edge

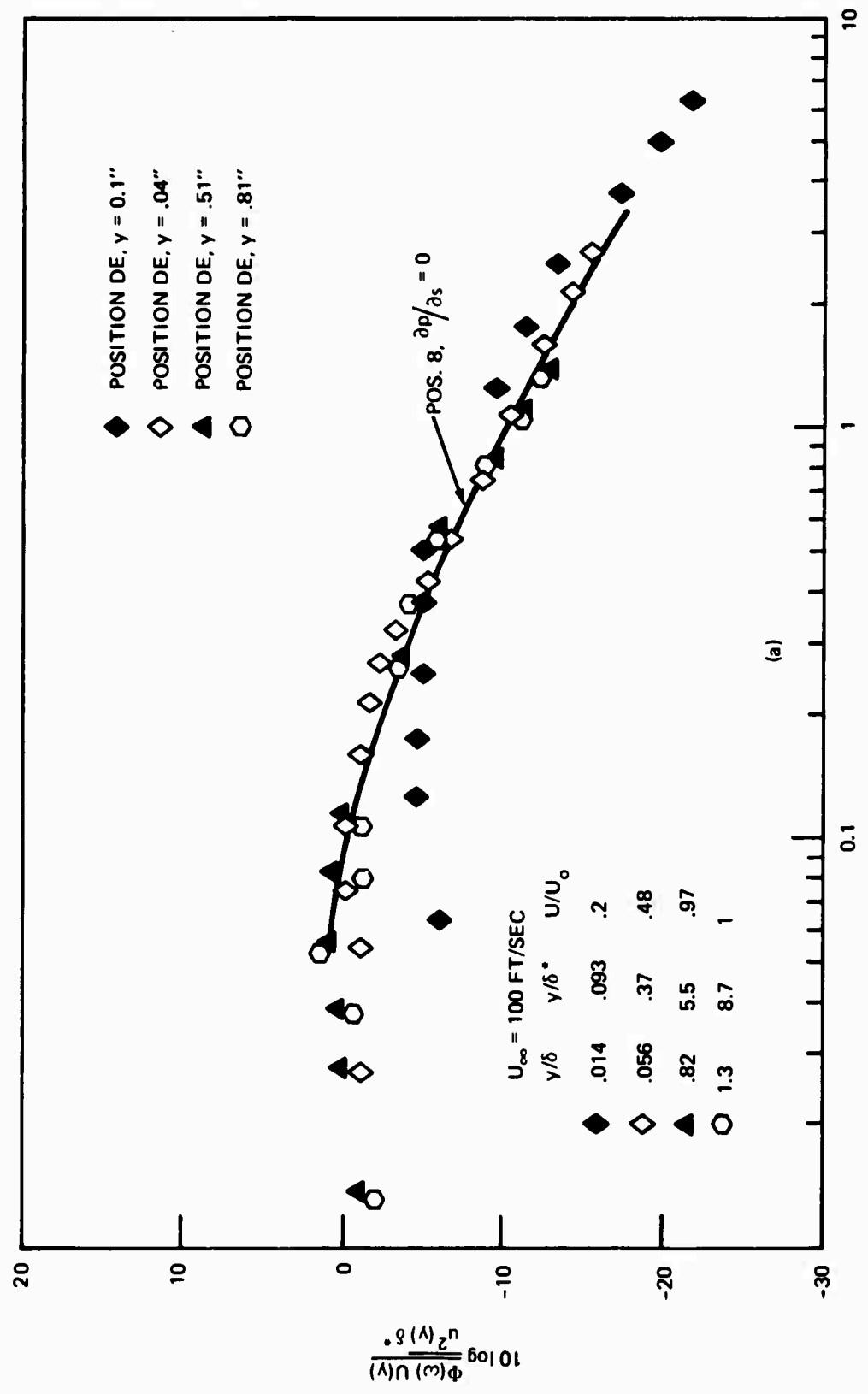


Figure 36a - Position DE

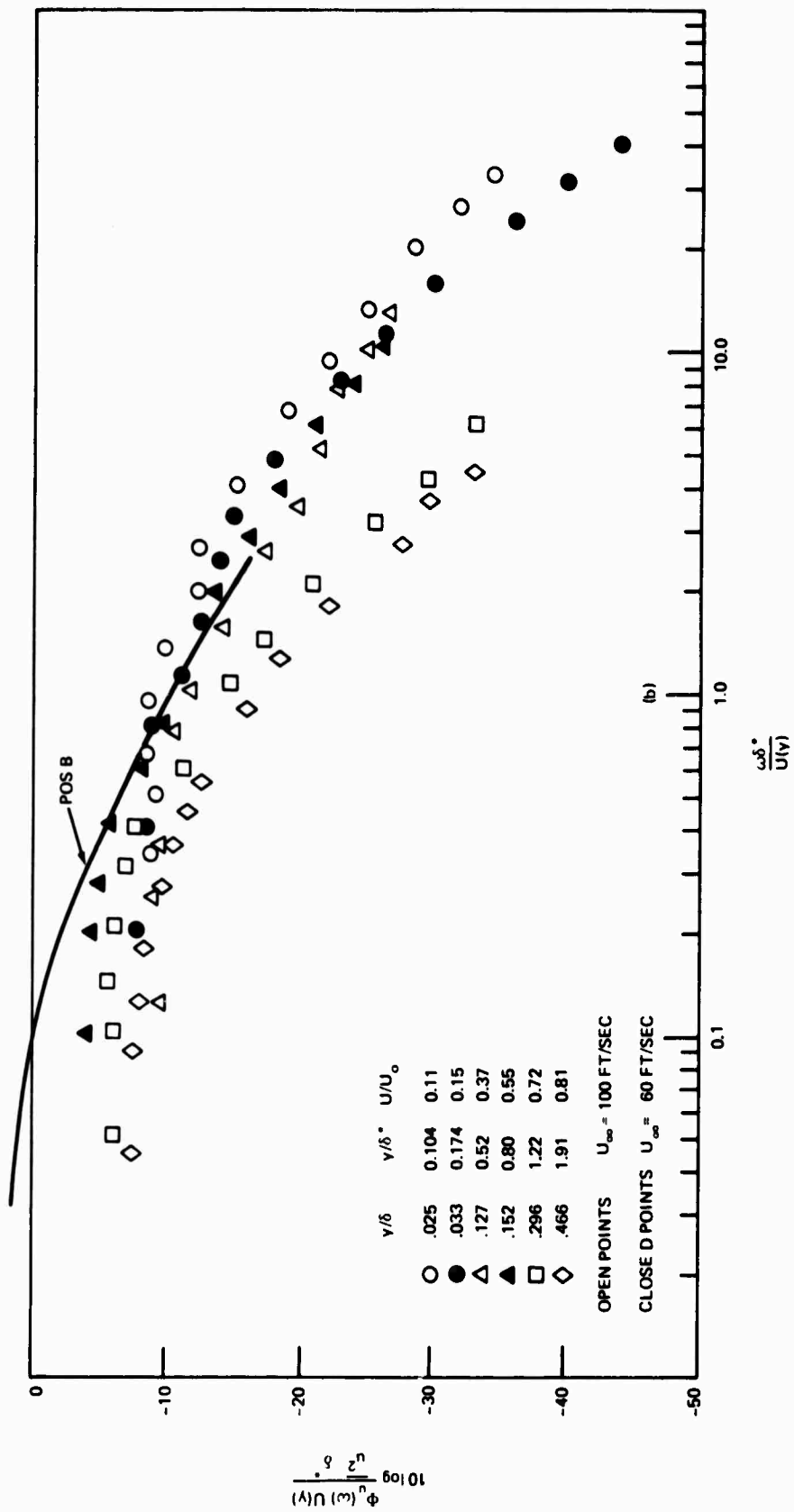


Figure 36b - Position F

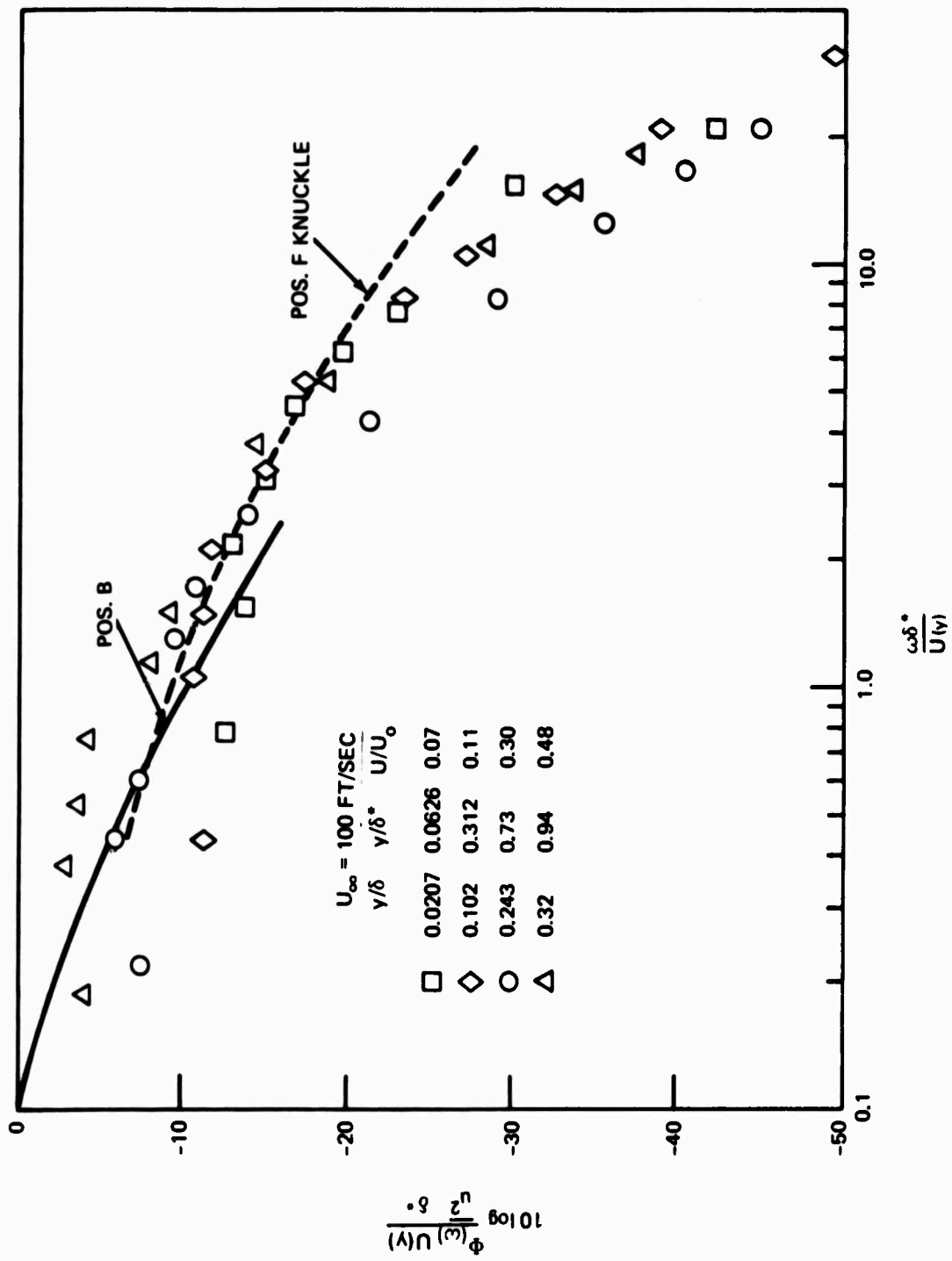


Figure 36c - Position G

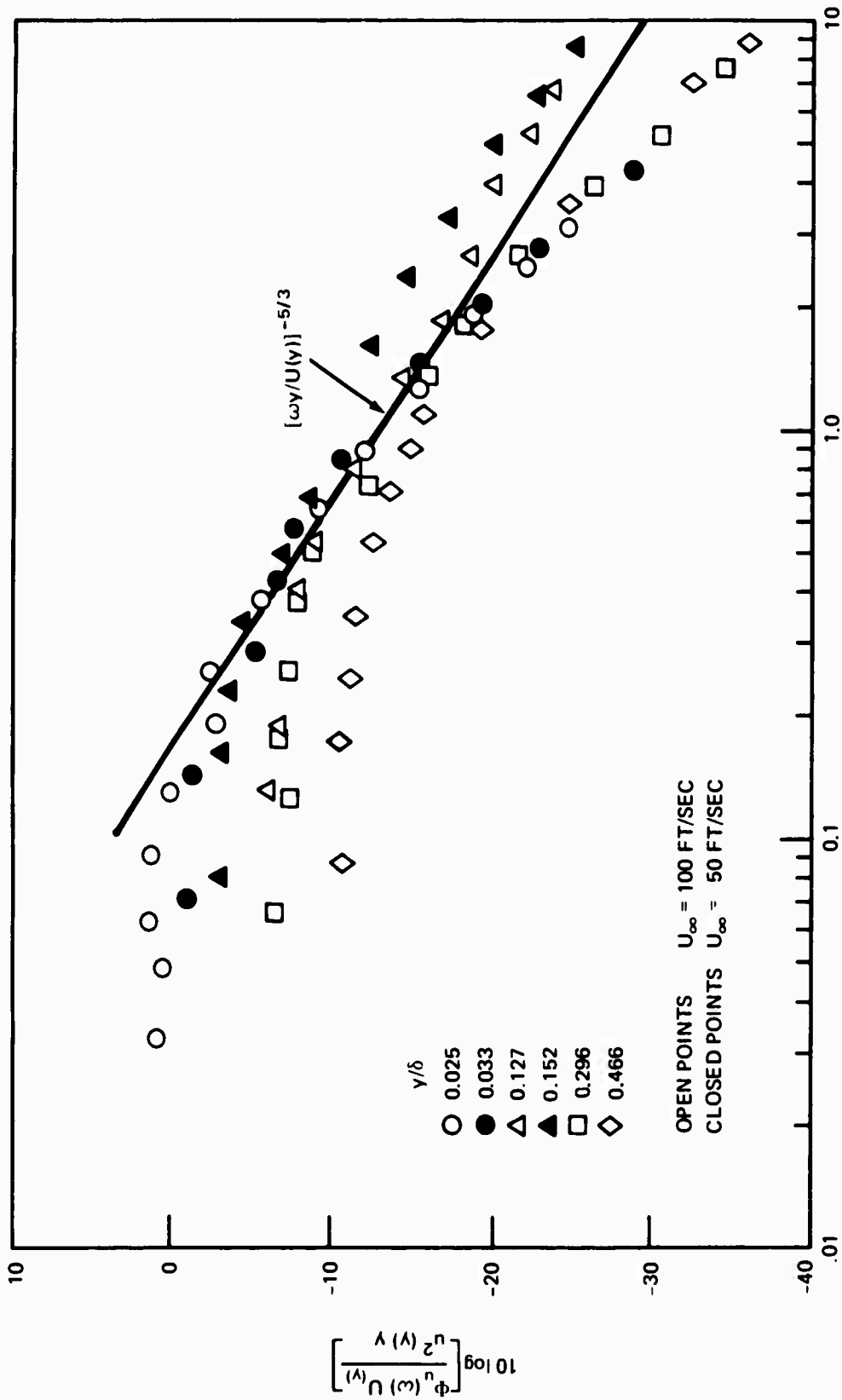


Figure 37 - Autospectra at Position F on 25-Degree--Rounded-Beveled Edge Nondimensionalized on Distance from Wall (Data are taken from Figure 36b.)

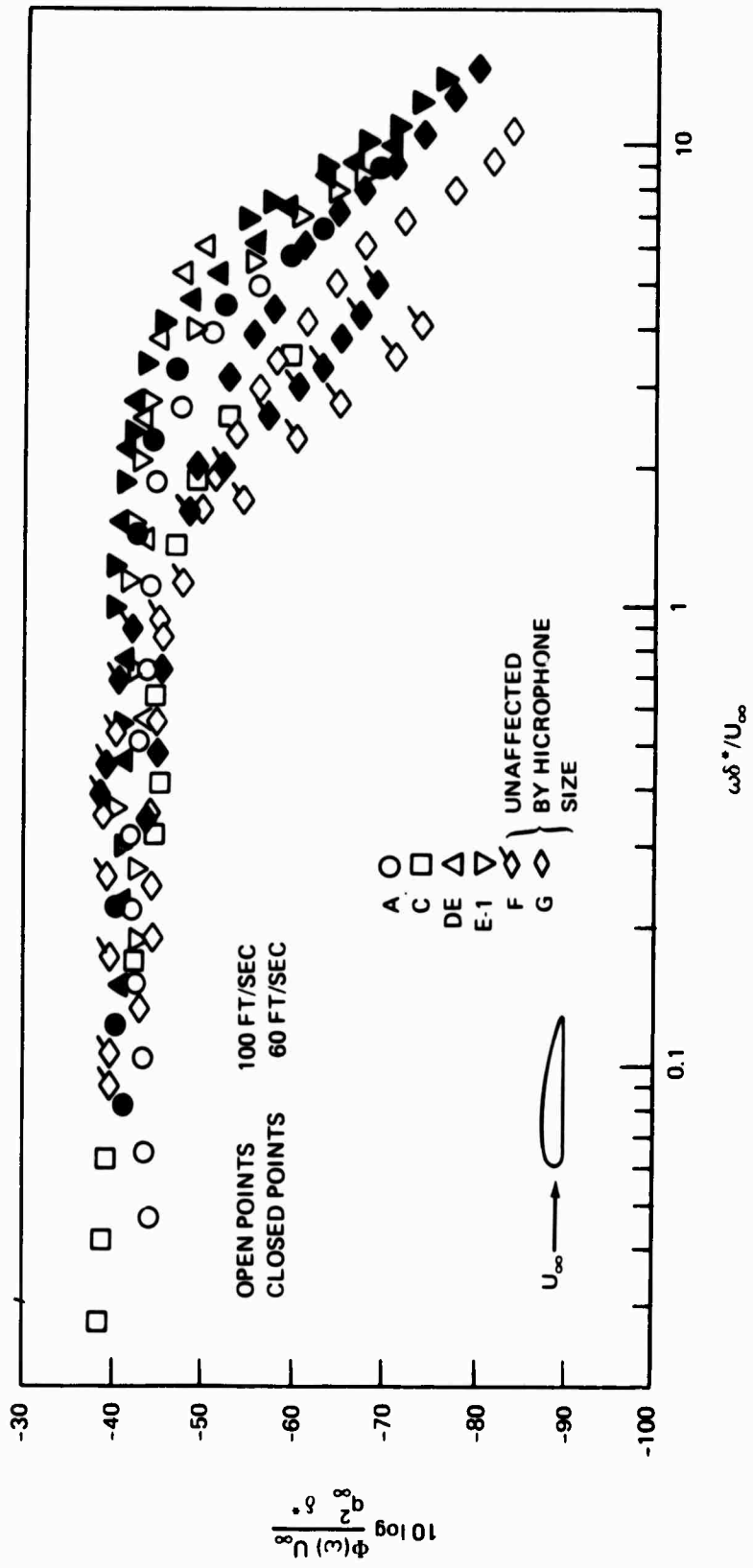


Figure 38 - Dimensionless Pressure Spectra on 25-Degree--
Rounded-Beveled Trailing Edge

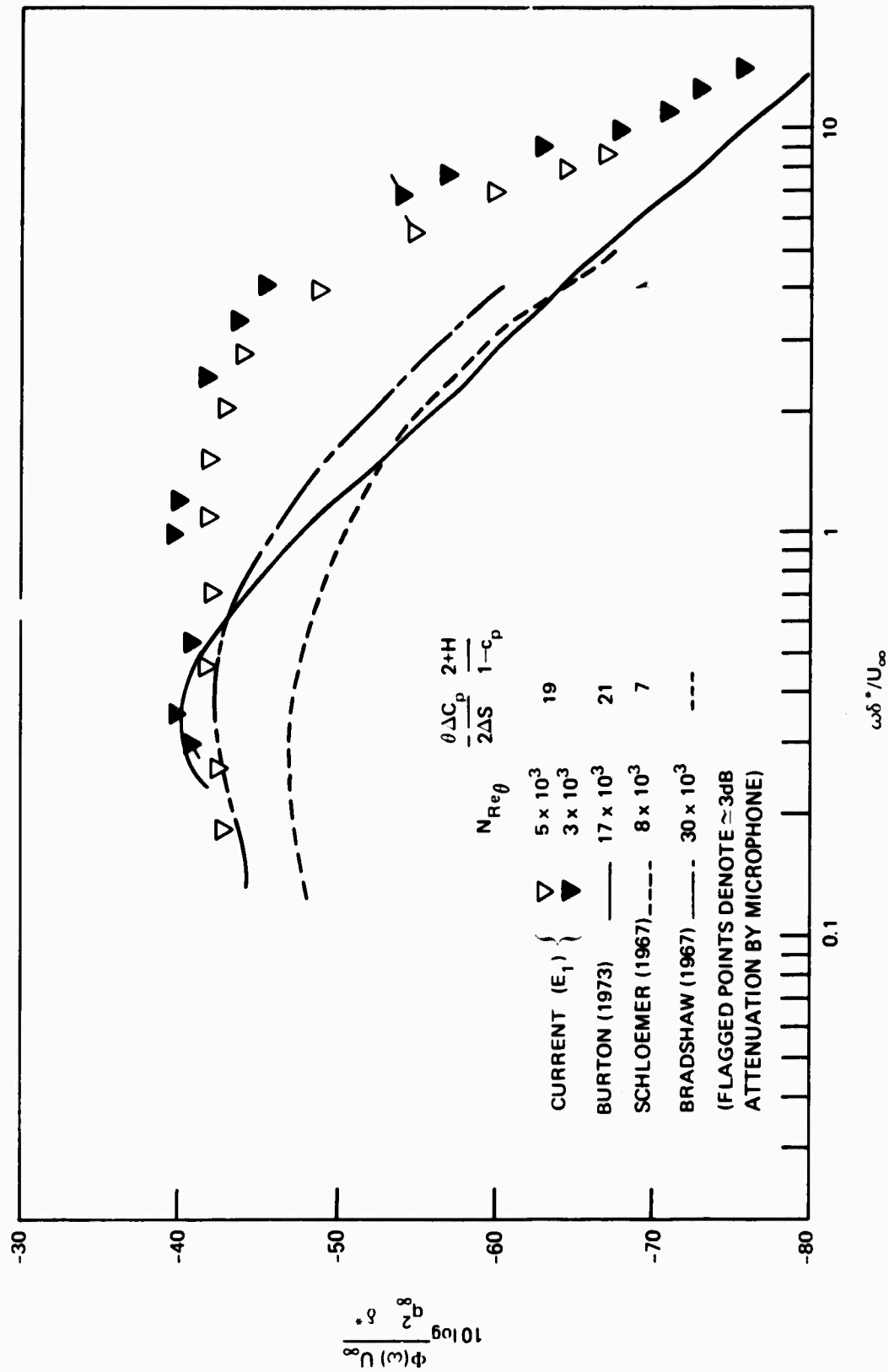


Figure 39 - Comparison of Various Measurements of Autospectra of Wall Pressures in Adverse Pressure Gradients

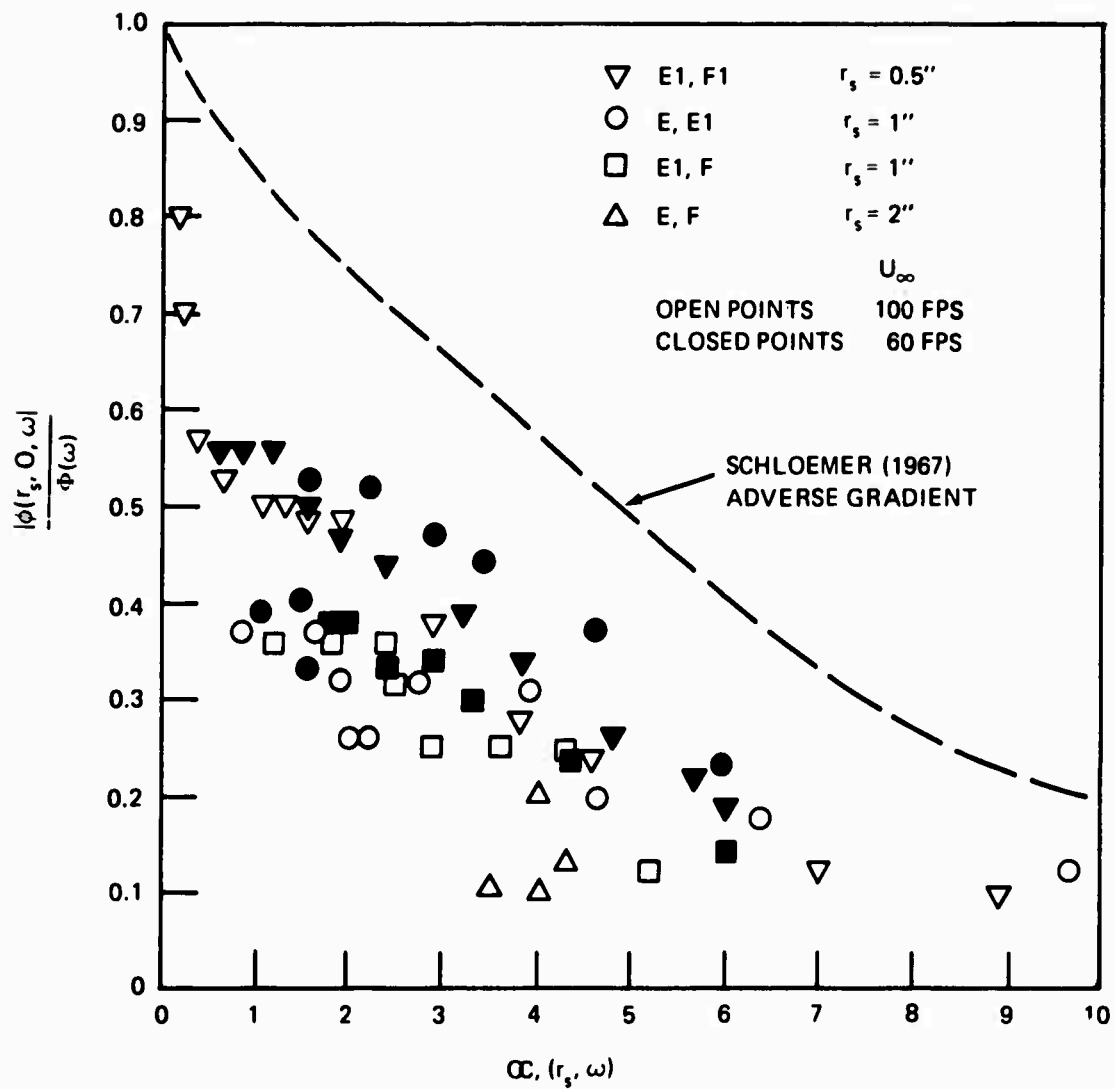


Figure 40 - Normalized Longitudinal Cross Spectral Density Magnitudes of Fluctuating Surface Pressures on 25-Degree--Rounded-Beveled Edge

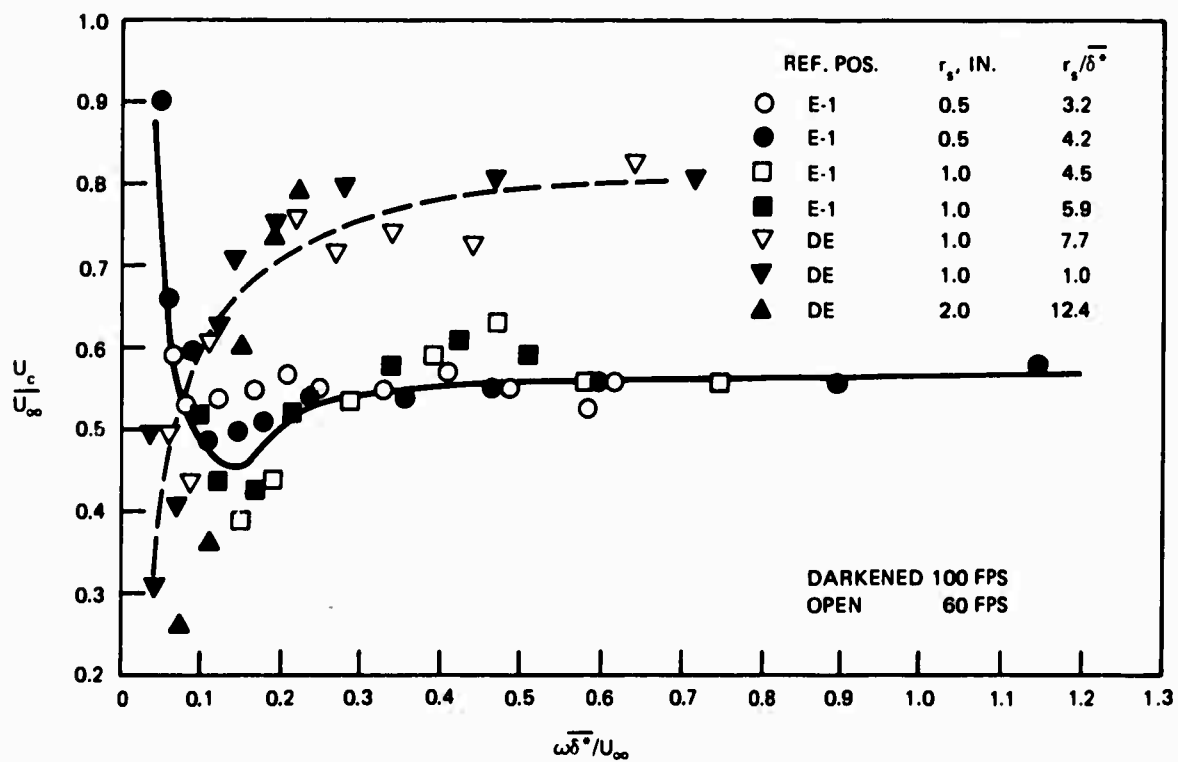
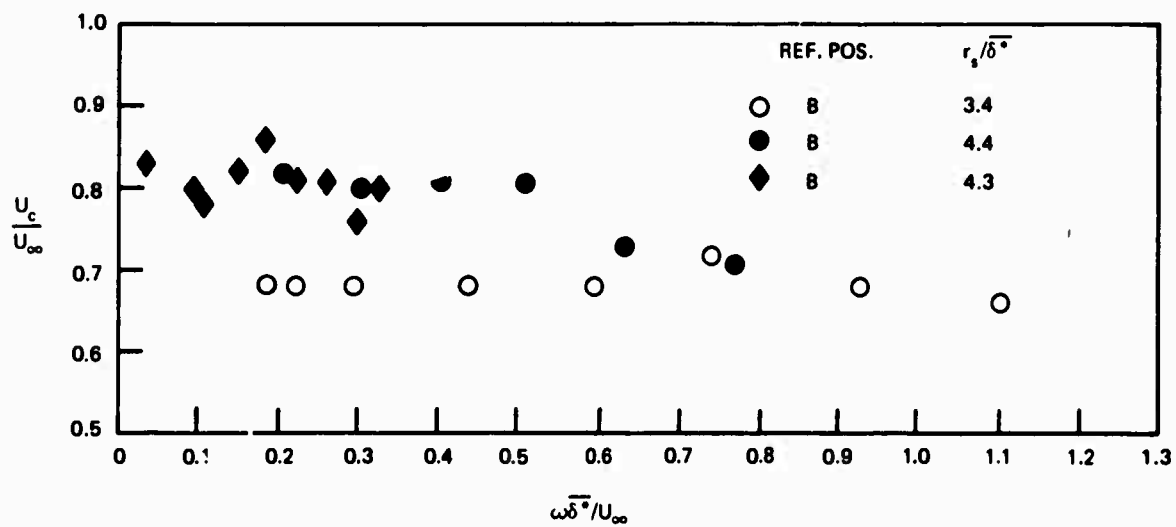


Figure 41 - Wall Pressure Convection Velocities at Two Positions on Strut with 25-Degree--Rounded-Beveled Trailing Edge

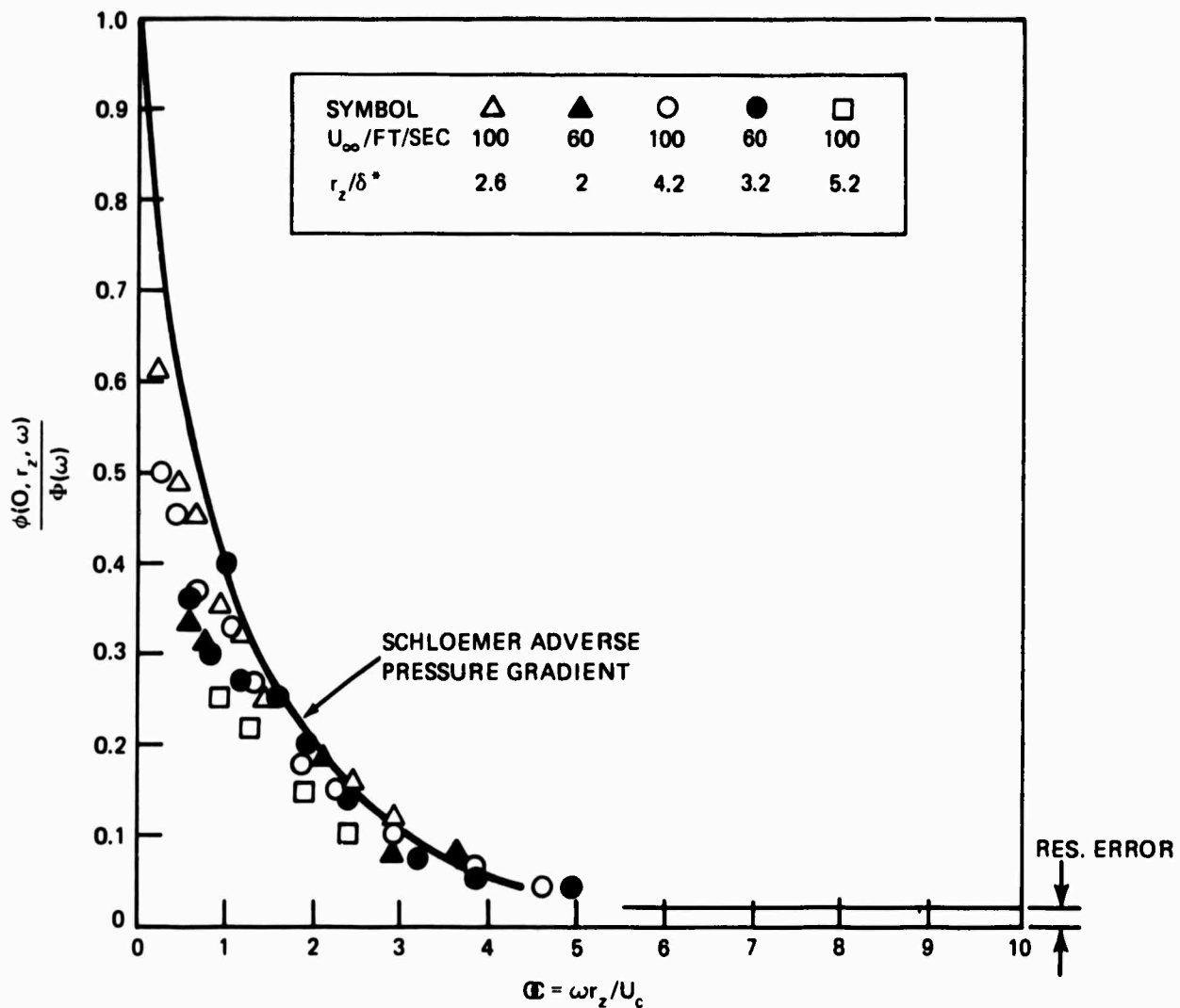


Figure 42 - Normalized Lateral Cross Spectral Density Magnitudes of Fluctuating Surface Pressure at Position E1 on 25-Degree--Rounded-Beveled Edge

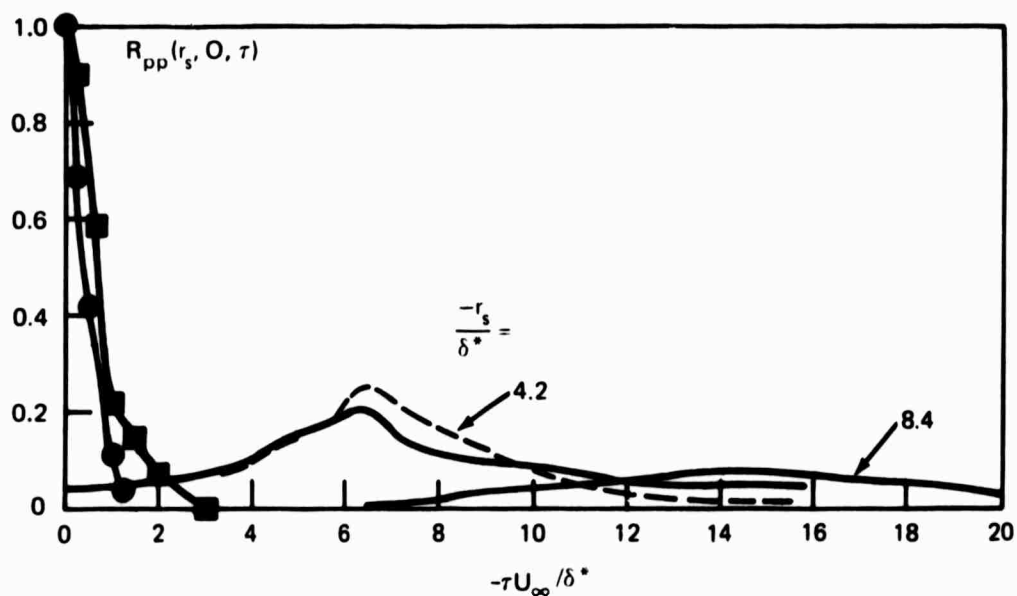
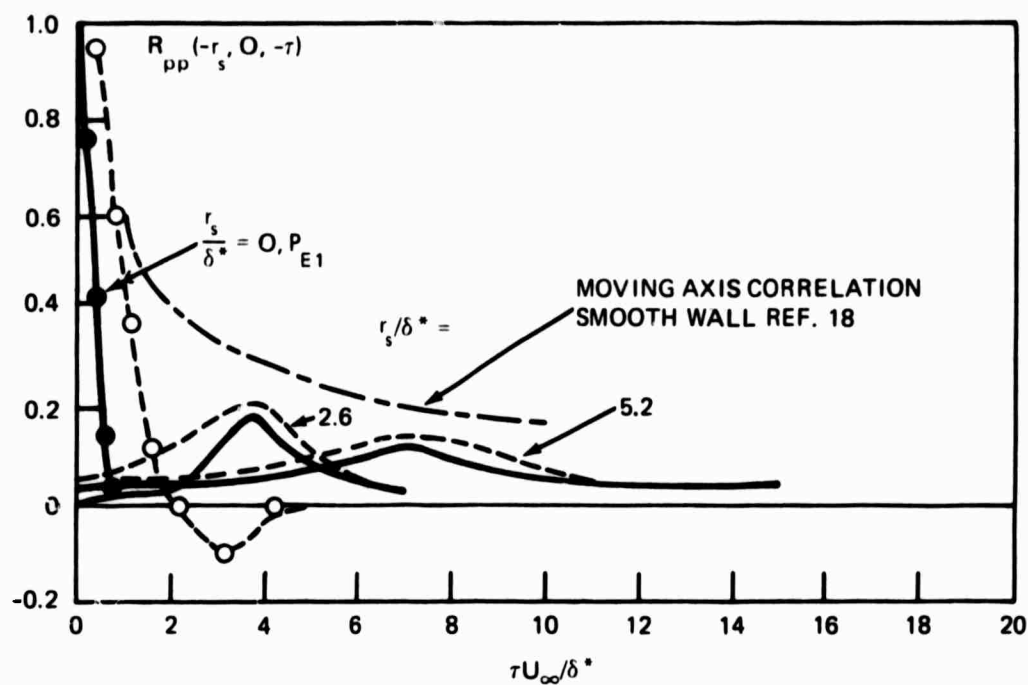


Figure 43 - Broadband Space-Time Correlations of Pressures at Position E1 on 25-Degree--Rounded-Trailing Edge ($\delta^* \approx 0.12$ inch selected at position E1 for $U_\infty = 100$ feet per second)

(--- 60 feet per second, — 100 feet per second; autocorrelations: ○ 60 feet per second, ● 100 feet per second)

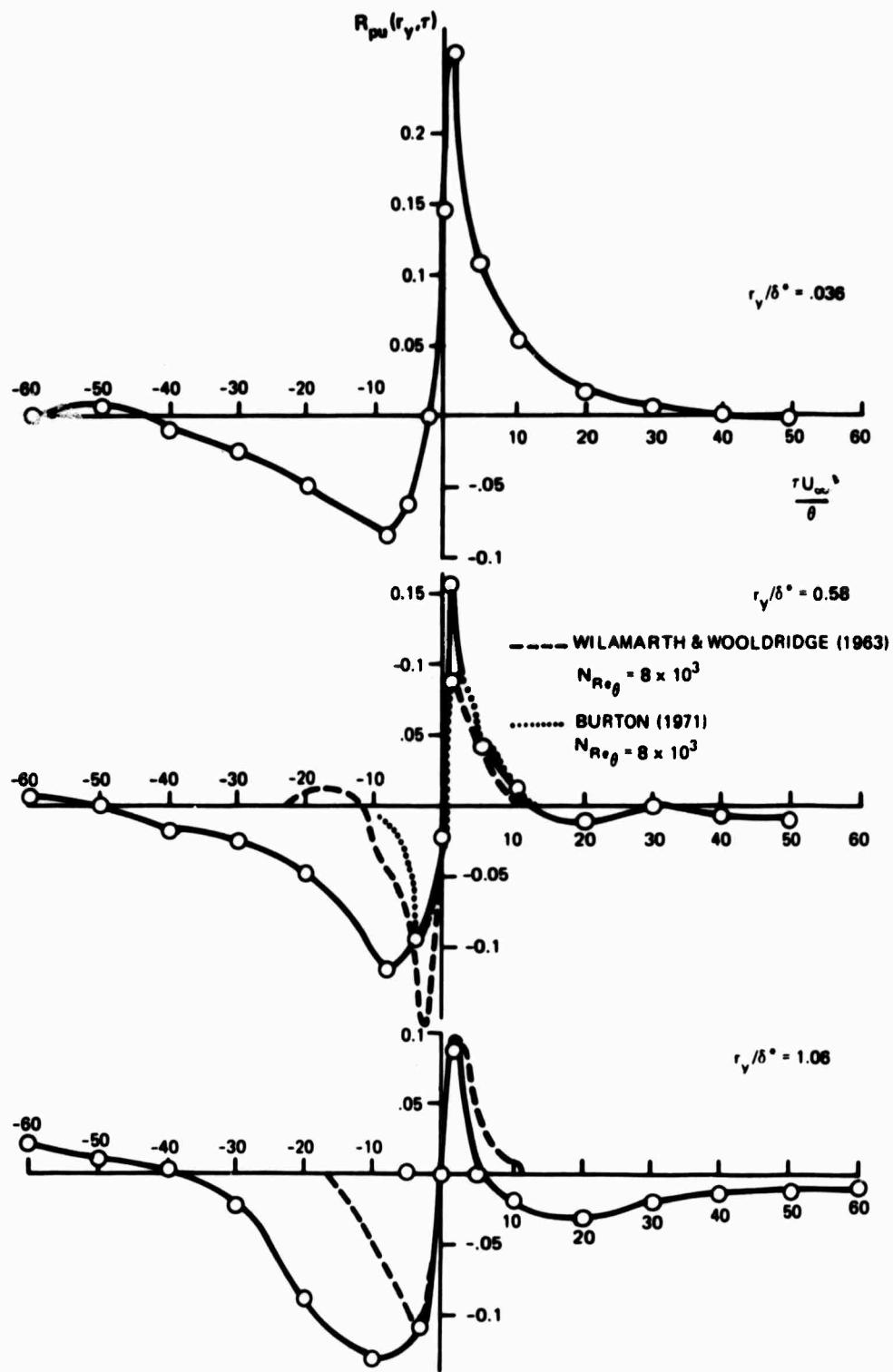


Figure 44 - Pressure-Velocity Correlations at Position B on
25-Degree--Rounded Edge
(60 feet per second, $N_{Re_\theta} = 8 \times 10^3$)

Figure 45 - Pressure-Velocity Correlations at Position F on Rounded Edge

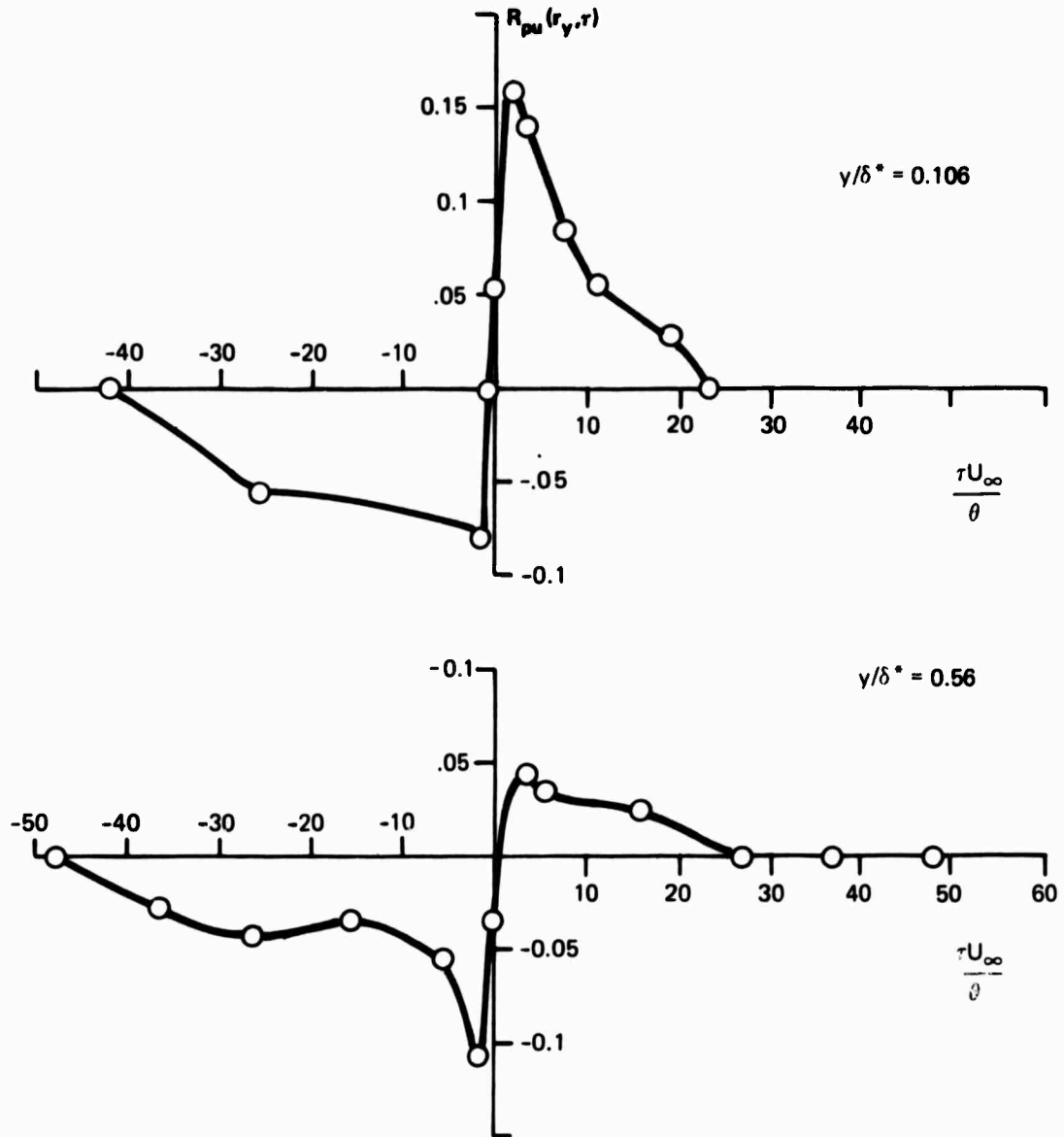


Figure 45a - $U_\infty = 60$ Feet per Second

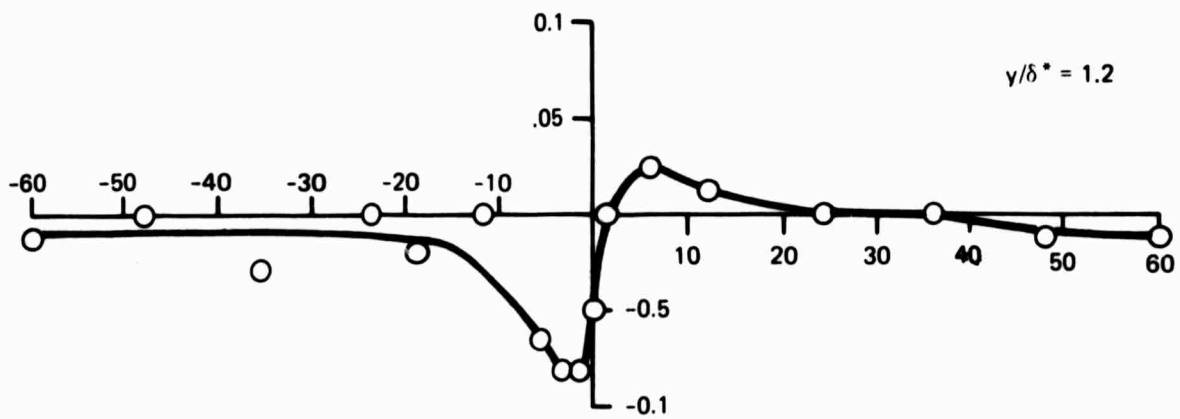
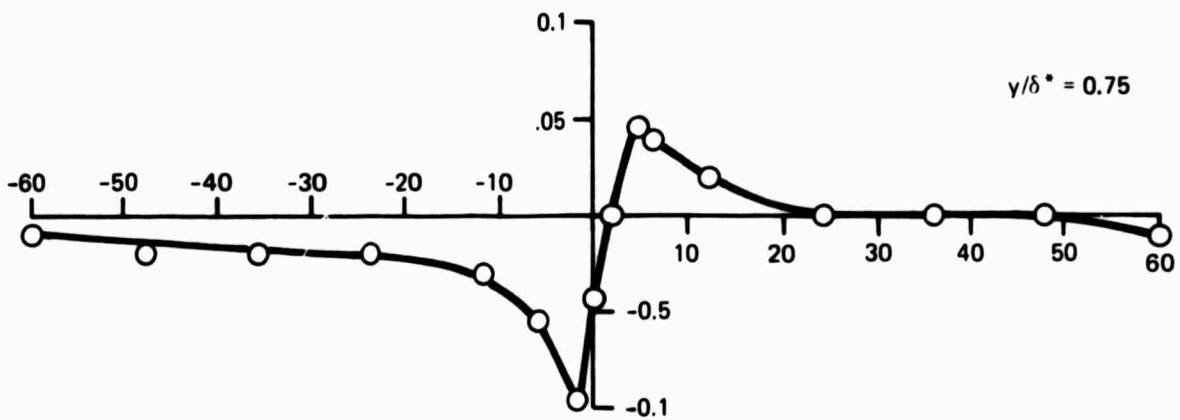
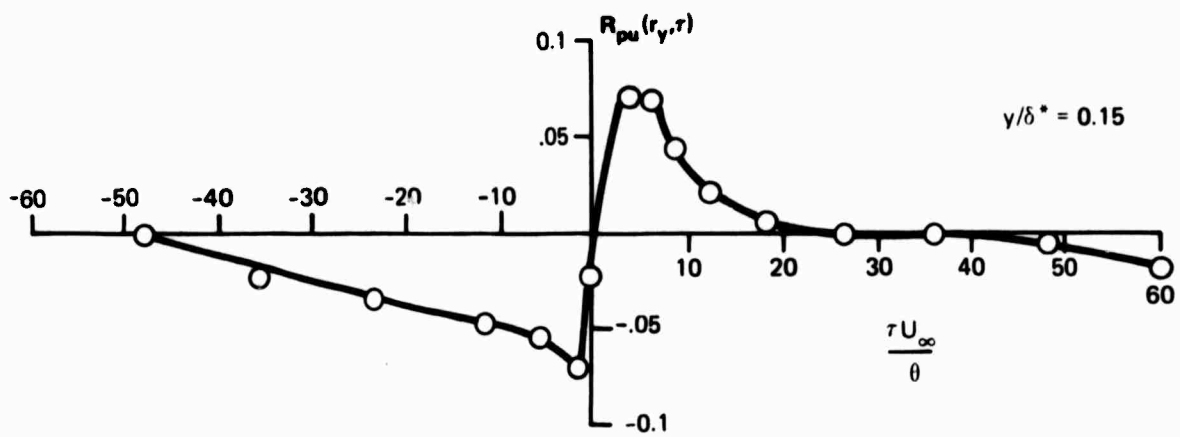


Figure 45b - $U_\infty = 100$ Feet per Second

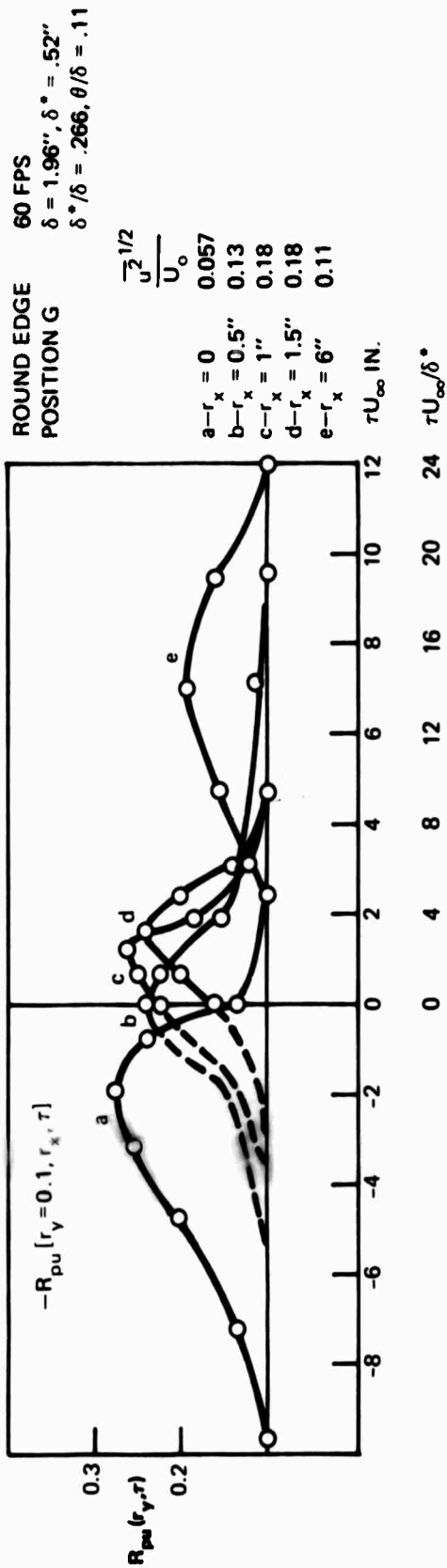


Figure 46 - Broadband Space-Time Cross Correlations of Pressure at Position G and Fluctuating Velocity in Wake of 25-Degree---Rounded Edge at 60 Feet per Second

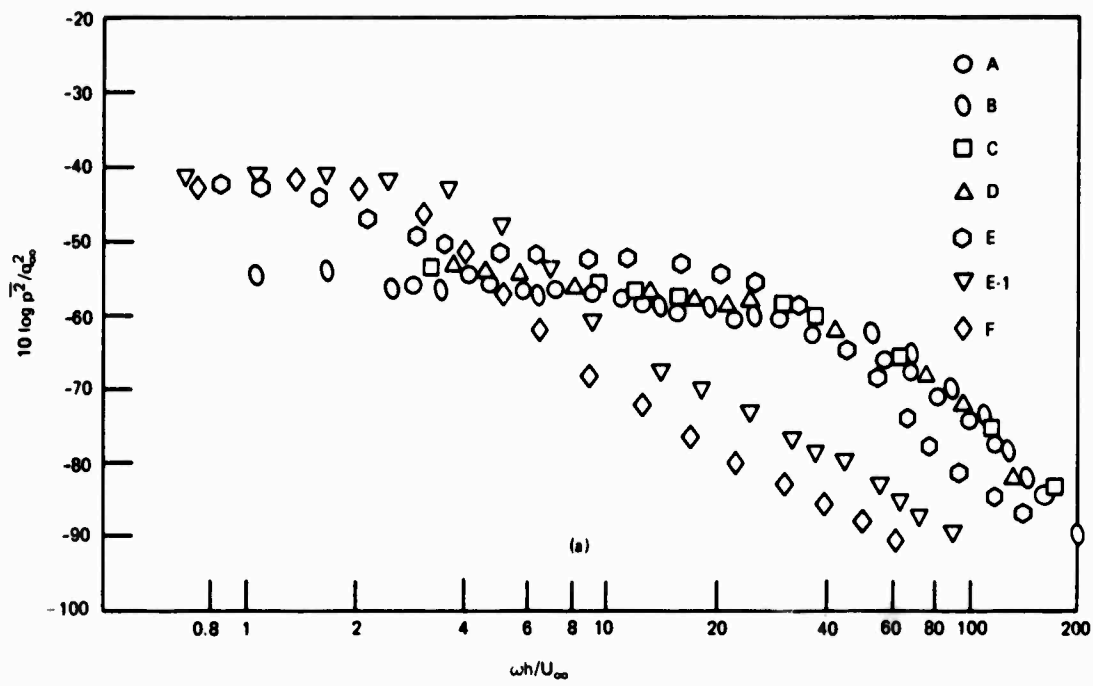


Figure 47a - $U_\infty = 50$ Ft/Sec

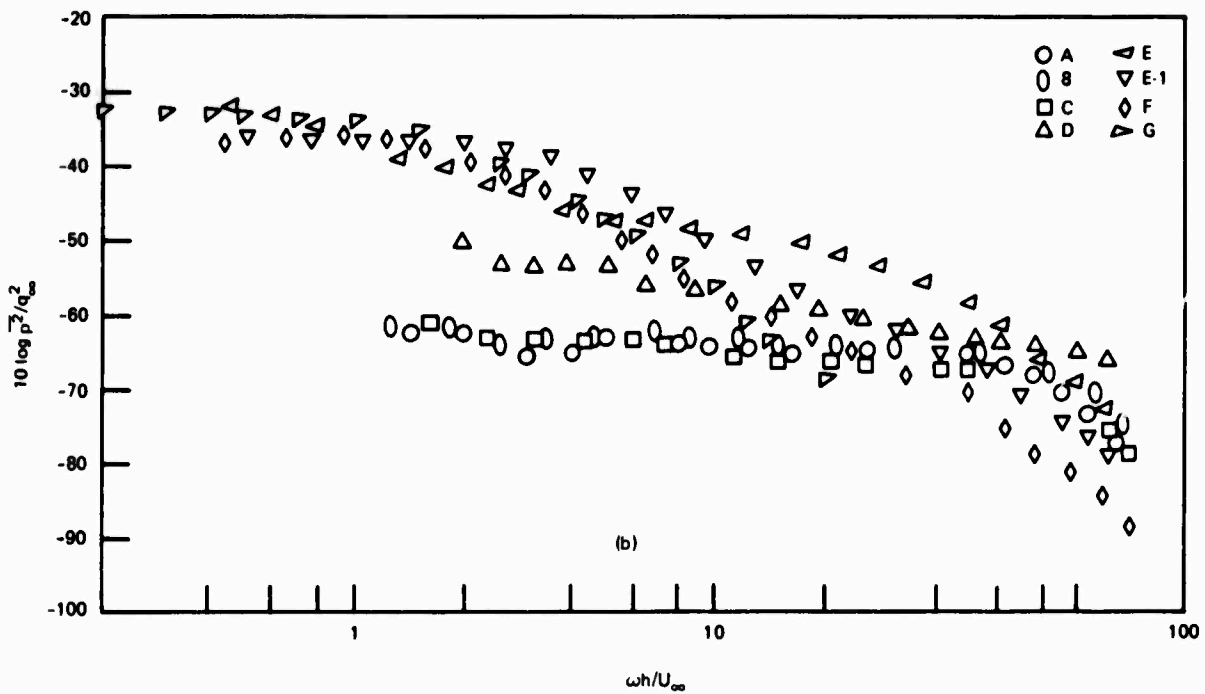


Figure 47b - $U_\infty = 100$ Ft/Sec

Figure 47 - Narrowband Mean-Square Pressure Levels, Measured in 62.5-Hertz Bands at Various Positions on 25-Degree Knuckle Edge

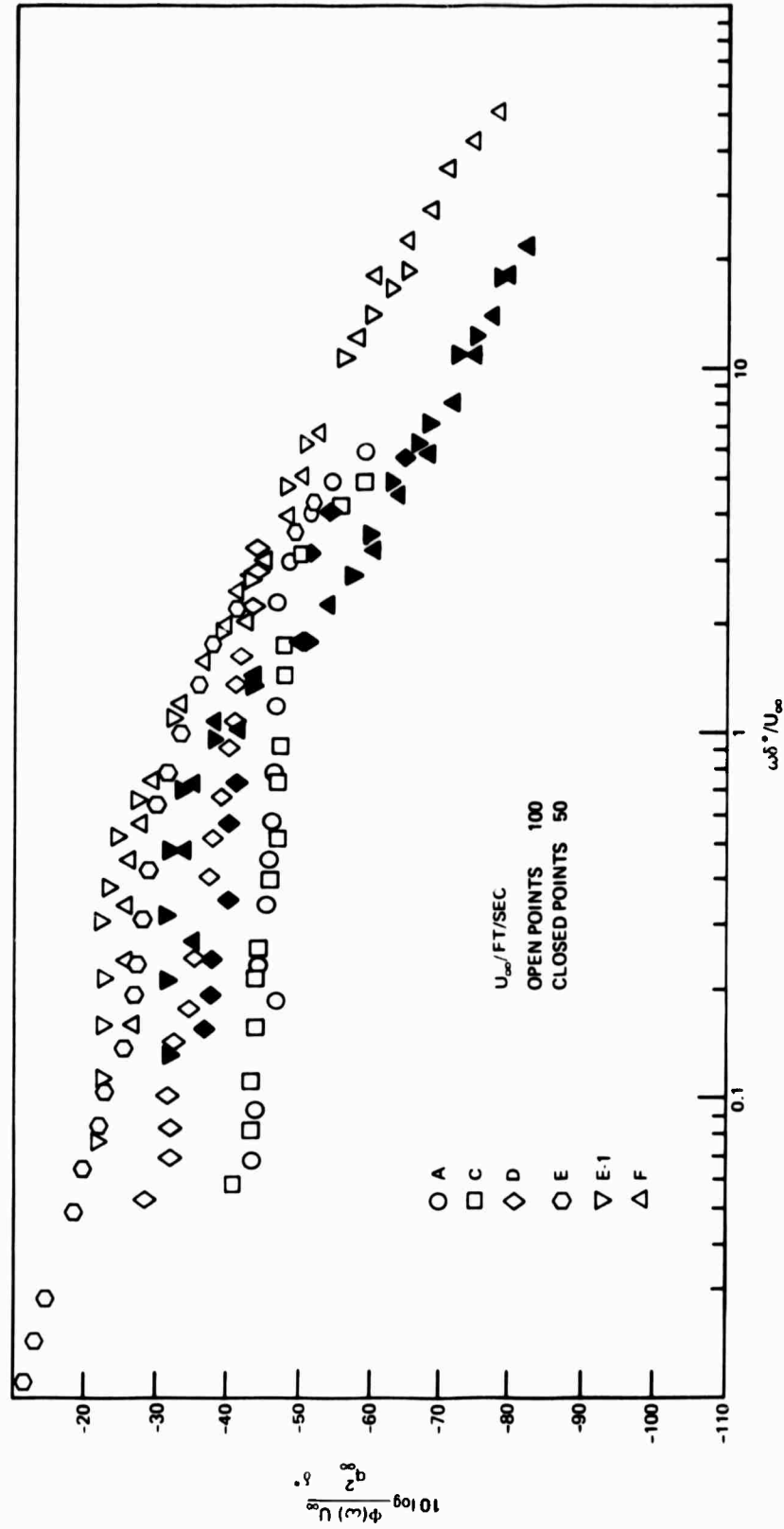


Figure 48 - Dimensionless Pressure Spectra of 25-Degree--
Knuckle-Trailing Edge

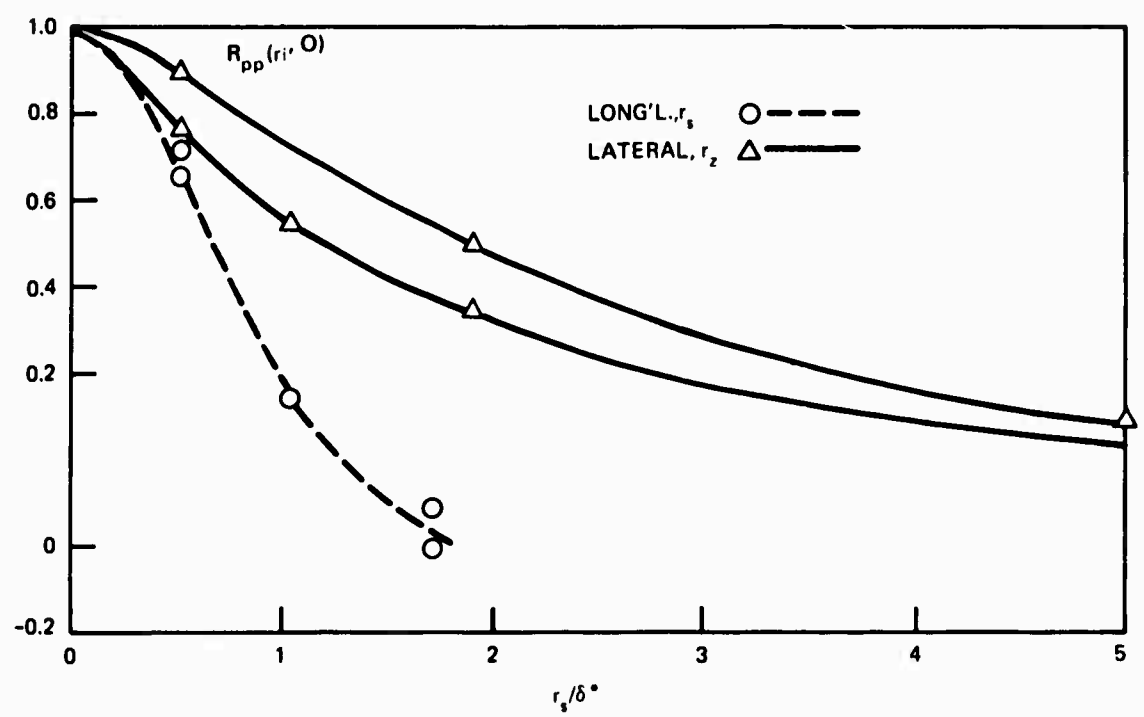
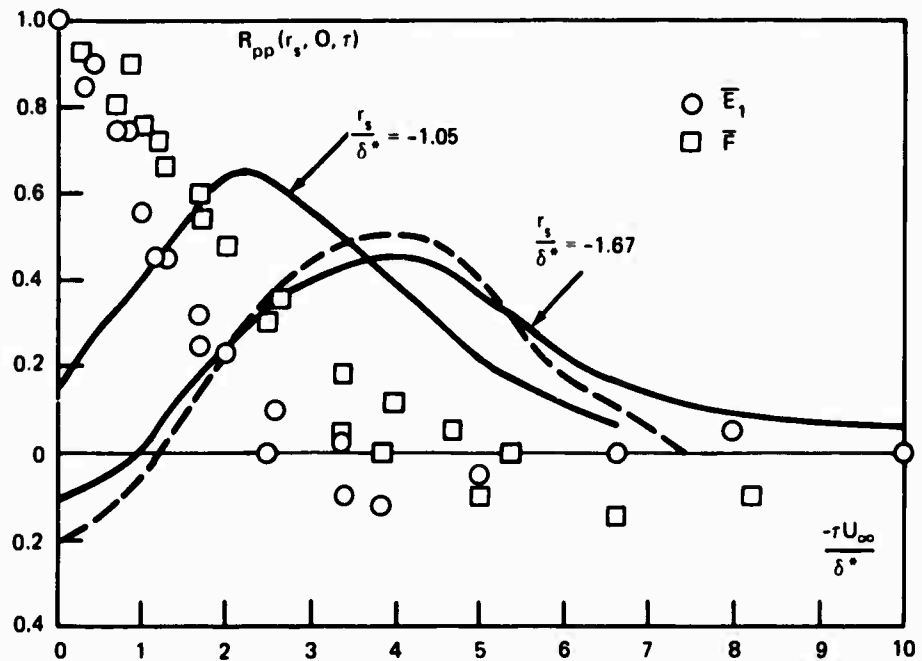


Figure 49 - Broadband Space-Time Correlations of Pressures at Position F on 25-Degree Knuckle; Separations Measured from Position F, $\delta^* = 0.05$ Foot

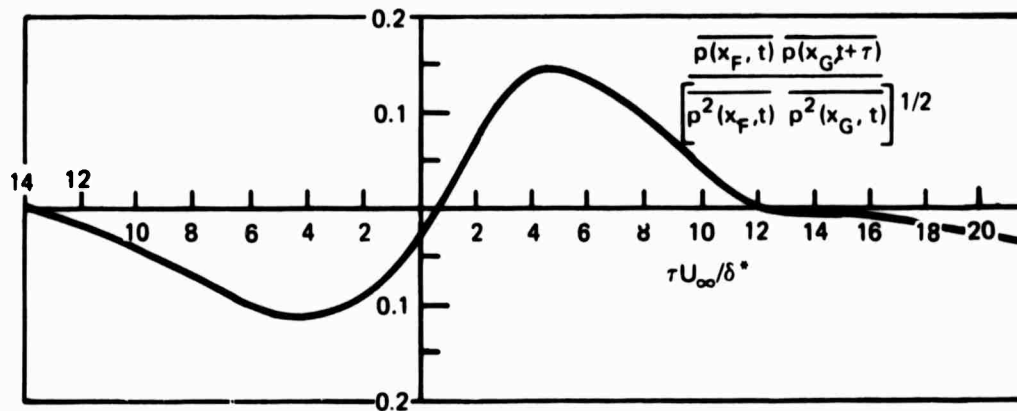


Figure 50 - Broadband Correlation of Pressures at Positions F and G
 on 25-Degree Knuckle with $U_\infty = 100$ Feet per Second,
 $r_s/\delta^* = 1.66$ -- δ^* Evaluated at Position F

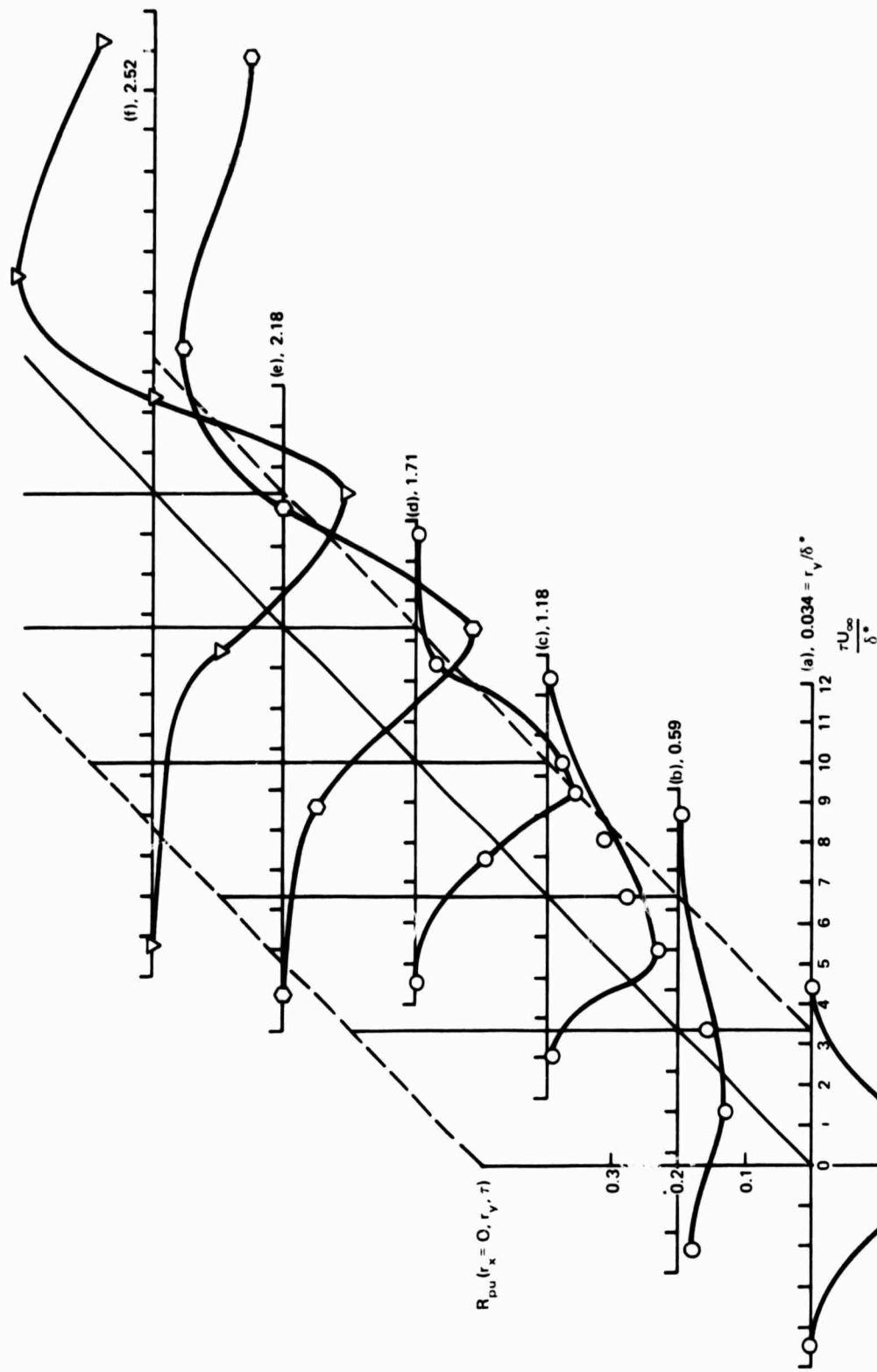


Figure 51 - Broadband Space-Time Correlations of Pressure and Velocity above 25-Degree Knuckle Edge
 (Pressure is measured at position F; velocity, above microphone $\delta^* = 0.596$ inch.)

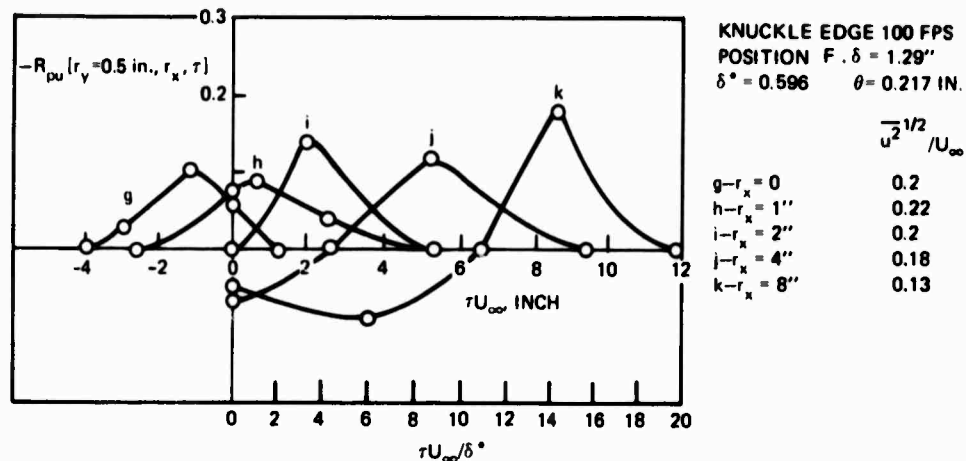


Figure 52 - Broadband Space-Time Correlations on 25-Degree Knuckle Edge of Pressures at Position F and Velocities in Wake for $U_\infty = 100$ Feet per Second

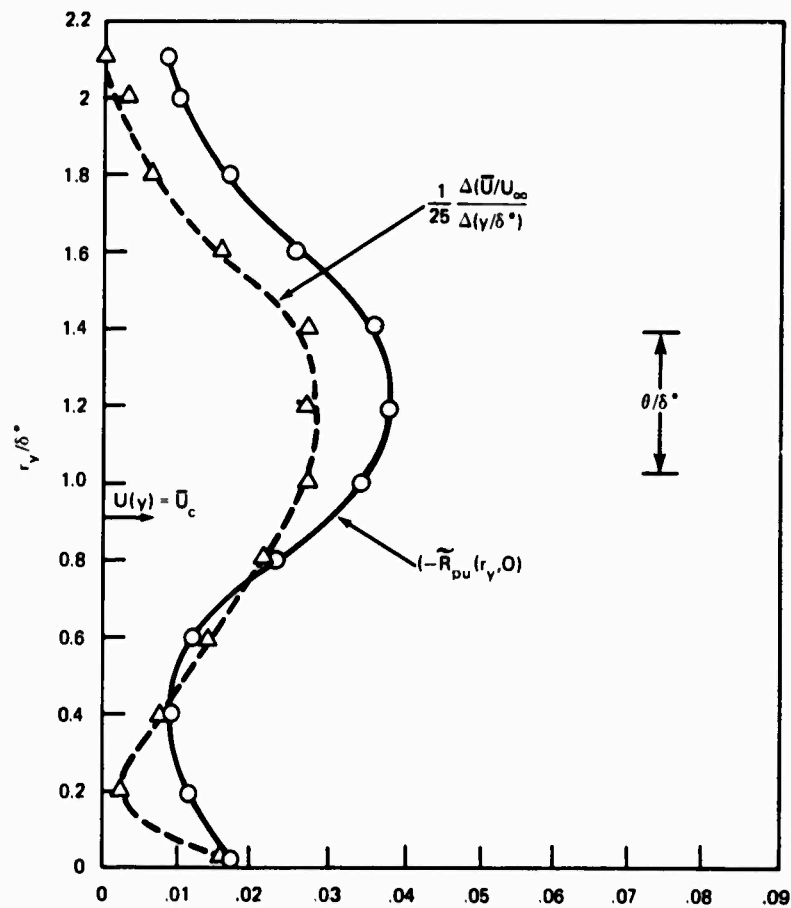


Figure 53 - Correspondence of Pressure-Velocity Correlation with Mean Shear for Position F on 25-Degree Knuckle Edge at 100 Feet per Second

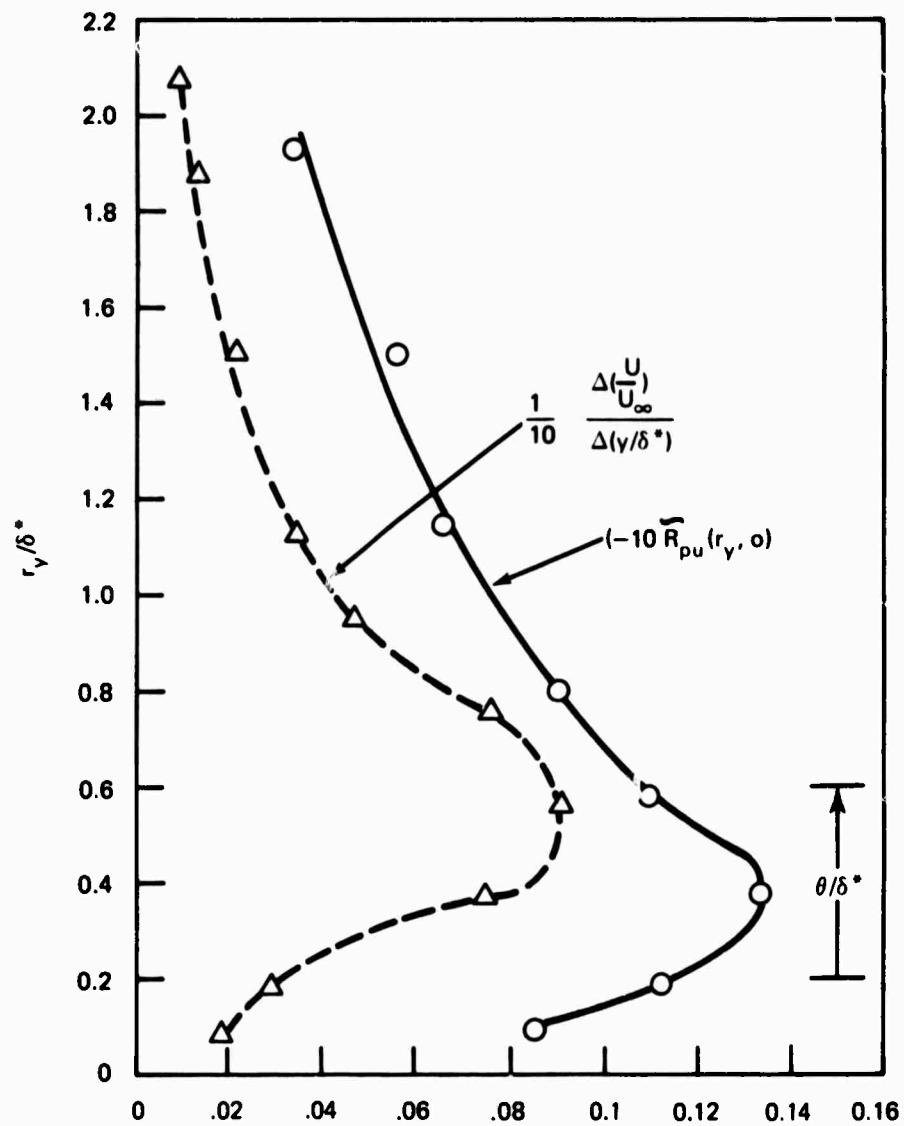


Figure 54 - Correspondence of Pressure-Velocity Correlation with Mean Shear for Position G on 25-Degree Rounded Edge at 60 Feet per Second

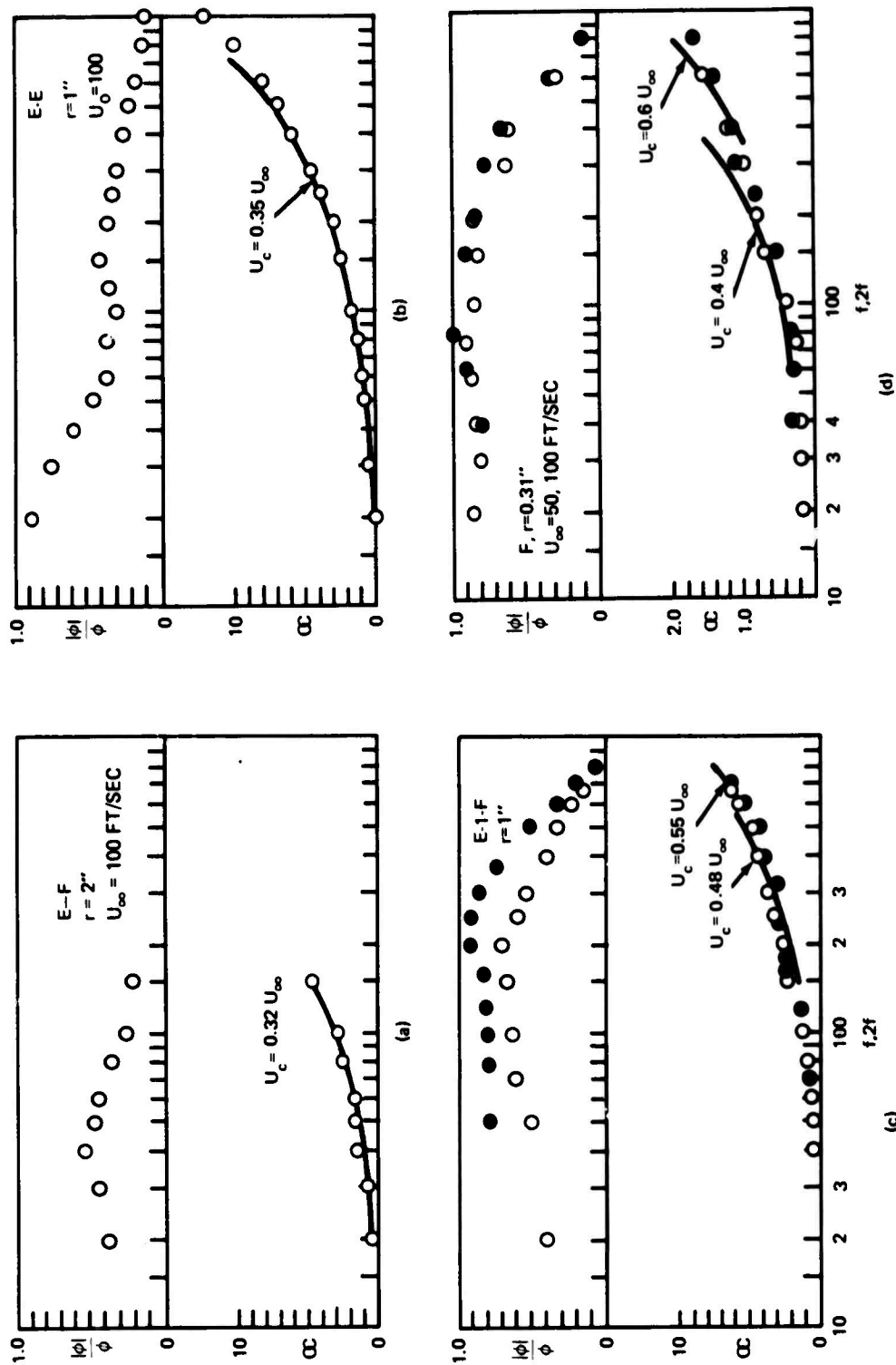


Figure 55 - Normalized Cross Spectral Density Magnitudes (ϕ) and Phases (α) for Knuckle Edge
 (Flow speeds 50 feet per second and 100 feet per second; frequencies doubled for $U_0 = 50$ feet per second. Phase is in radians, 100 feet per second, 50 feet per second.)

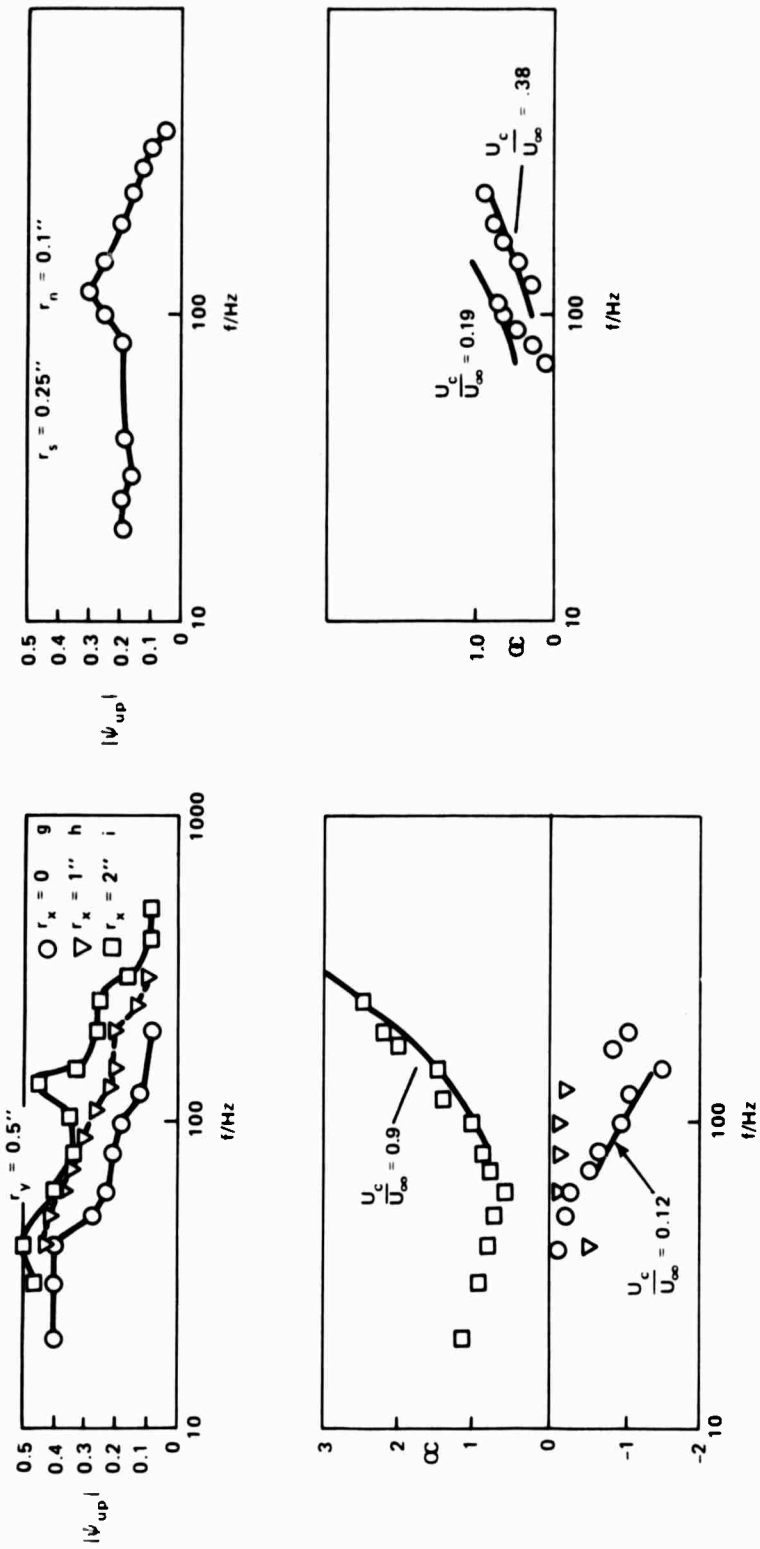


Figure 56 - Normalized Pressure-Velocity Cross Spectral Densities
for Pressures at Position F on Knuckle Edge at
100 Feet per Second
(Phase is in radians)

$$|\psi_{up}| = |\phi_{up}(f)| / [|\phi_{uu}(f)\phi_{pp}(f)|]^{1/2}$$

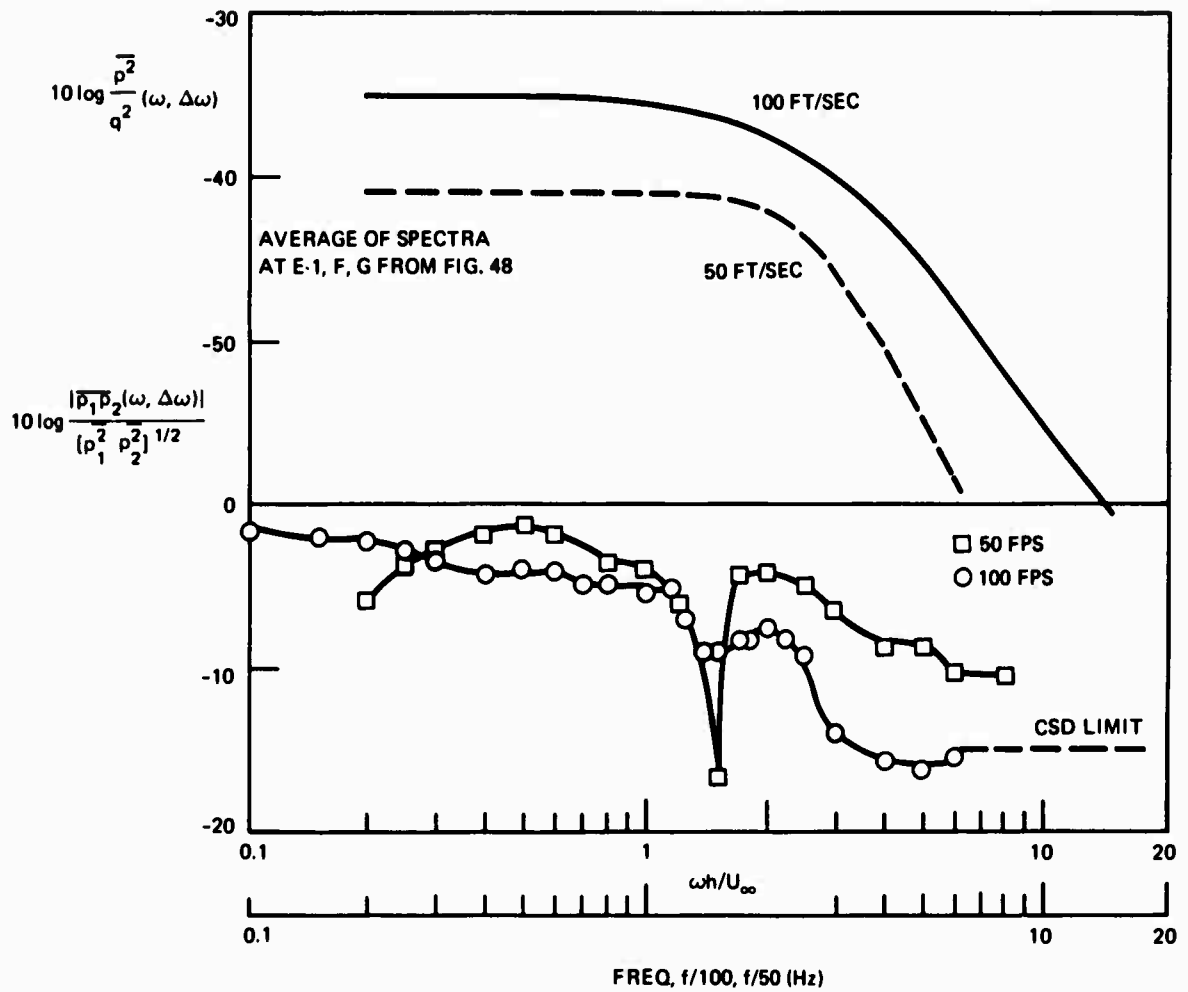


Figure 57 - Comparison of Autospectra of Pressures on 25-Degree Wedge with Cross Spectrum of Pressures on Opposite Sides of Trailing Edge (Measurements made in 12.5-hertz bands at El.)

APPENDIX A

VARIANCE OF ESTIMATE OF CROSS SPECTRAL DENSITY

In the fast Fourier transform analyses, the random variables $x(t)$ and $y(t)$ are transformed as

$$X_i(f) = \frac{1}{T_1} \int_{-T_1/2}^{T_1/2} x_i(t) e^{2\pi ift} dt \quad (26)$$

where $X_i(f)$ is the calculated transform of the i th sample, and T_1 is the sample length. The variables $X_i(f)$ and $Y_i(f)$ are random variables and the sample of the cross spectral density $[X_i(f)Y_i^*(f)] = [XY]_i$ is also a random variable; a total of N independent samples are taken. The ideal cross spectral density function is

$$\phi_{xy}(f) = \langle X_i(f)Y_i^*(f) \rangle = (\overline{XY}) \quad (27)$$

where the brackets $\langle \rangle$ denote a true ensemble average.

The estimate of the cross spectral density is

$$\tilde{\phi}_{xy}(f) = \frac{1}{N} \sum_{i=1}^N X_i(f)Y_i^*(f) = (\tilde{XY}) \quad (28)$$

Now, we define the variance of the sample estimate

$$\sigma_{xy}^2 = \langle (\tilde{XY} - \overline{XY})^2 \rangle \quad (29)$$

$$= \langle \frac{1}{N} \sum_{i=1}^N [(XY)_i - \overline{XY}]^2 \rangle$$

and the sample mean as

$$\begin{aligned}\mu_{xy} &= \langle (XY)_1 - \overline{XY} \rangle \\ &= 0\end{aligned}\tag{30}$$

Expanding Equation (29) we obtain

$$\begin{aligned}\sigma_{xy}^2 &= \frac{1}{N^2} \langle \sum_{i=1}^N [(XY)_i - \overline{XY}]^2 \rangle \\ &+ \frac{1}{N^2} \langle \sum_{i=1}^N \sum_{\substack{j=1 \\ j \neq i}}^N [(XY)_i - \overline{XY}][(XY)_j - \overline{XY}] \rangle \\ &= \frac{1}{N} [\overline{(XY)^2} - (\overline{XY})^2]\end{aligned}\tag{31}$$

The variables $[(XY)_i - \overline{XY}]$ and $[(XY)_j - \overline{XY}]$ are statistically independent and so (Cramer (1945)³⁶)

$$\begin{aligned}\langle [(XY)_i - \overline{XY}][(XY)_j - \overline{XY}] \rangle &= \langle (XY)_i - \overline{XY} \rangle \langle (XY)_j - \overline{XY} \rangle \\ &= 0\end{aligned}$$

Assuming that the random variables x and y are Gaussian distributed, the correlation function satisfies the relationship (Frenkiel and Klebanoff (1967)³⁷)

$$\overline{x^2 y^2} = \overline{x^2} \overline{y^2} + 2[\overline{x^2} \overline{y^2}]^{1/2} (\overline{xy})^2\tag{32}$$

³⁶Cramer, H., "Mathematical Methods of Statistics," Princeton University Press, Princeton, N.J. (1945).

³⁷Frenkiel, F.N. and P.S. Klebanoff, "Higher Order Correlations in a Turbulent Field," Physics of Fluids, Vol. 10, p. 507 (1967).

Substituting Equation (32) into Equation (31) we obtain

$$\sigma_{xy}^2 = \frac{1}{N} [\overline{X^2 Y^2} + 2(\overline{X^2} \overline{Y^2})^{1/2} \overline{XY} - (\overline{XY})^2]$$

In terms of the spectral density, this can be written

$$\frac{\sigma^2(\phi_{xy})}{[\phi_{xx}(f)]^2} = \frac{1}{N} \left[1 + \frac{2\phi_{xy}(f)}{\phi_{xx}(f)} - \left(\frac{\phi_{xy}(f)}{\phi_{xx}(f)} \right)^2 \right] \quad (33)$$

We have assumed that $\phi_{xx}(f) = \phi_{yy}(f)$. When x and y are uncorrelated, $\phi_{xy}(f) \equiv 0$ so that the standard deviation of the estimate is

$$\frac{|\sigma(\phi_{xy})|}{\phi_{xx}(f)} = \sqrt{\frac{1}{N}} \quad (34)$$

When x and y are identical, the $\phi_{xy}(f) \equiv \phi_{xx}(f)$ so that the standard deviation of the estimate of the auto spectrum is

$$\frac{|\sigma(\phi_{xy})|}{\phi_{xx}(f)} = \sqrt{\frac{2}{N}} \quad (35)$$

In the case of an analog cross spectrum analysis $N = 2\Delta f T$, where Δf is the analysis bandwidth, and T is the averaging time. Equation (35) is the well-known expression for the error in the estimate of an autospectral density.

APPENDIX B

DIMENSIONLESS PROFILES OF MEAN AND TURBULENT VELOCITIES

Most of the boundary-layer profiles of mean and turbulent velocity are given as functions of U_0 and y/δ . The streamline velocity component is the unfiltered--broadband-root-mean-squared value. With only a few exceptions the profiles are given in each instance for two speeds $U_\infty = 50$ or 60 ft/sec and $U_\infty = 100$ feet per second. Measurements are given for all the beveled trailing edges; see Figures 58 through 66.

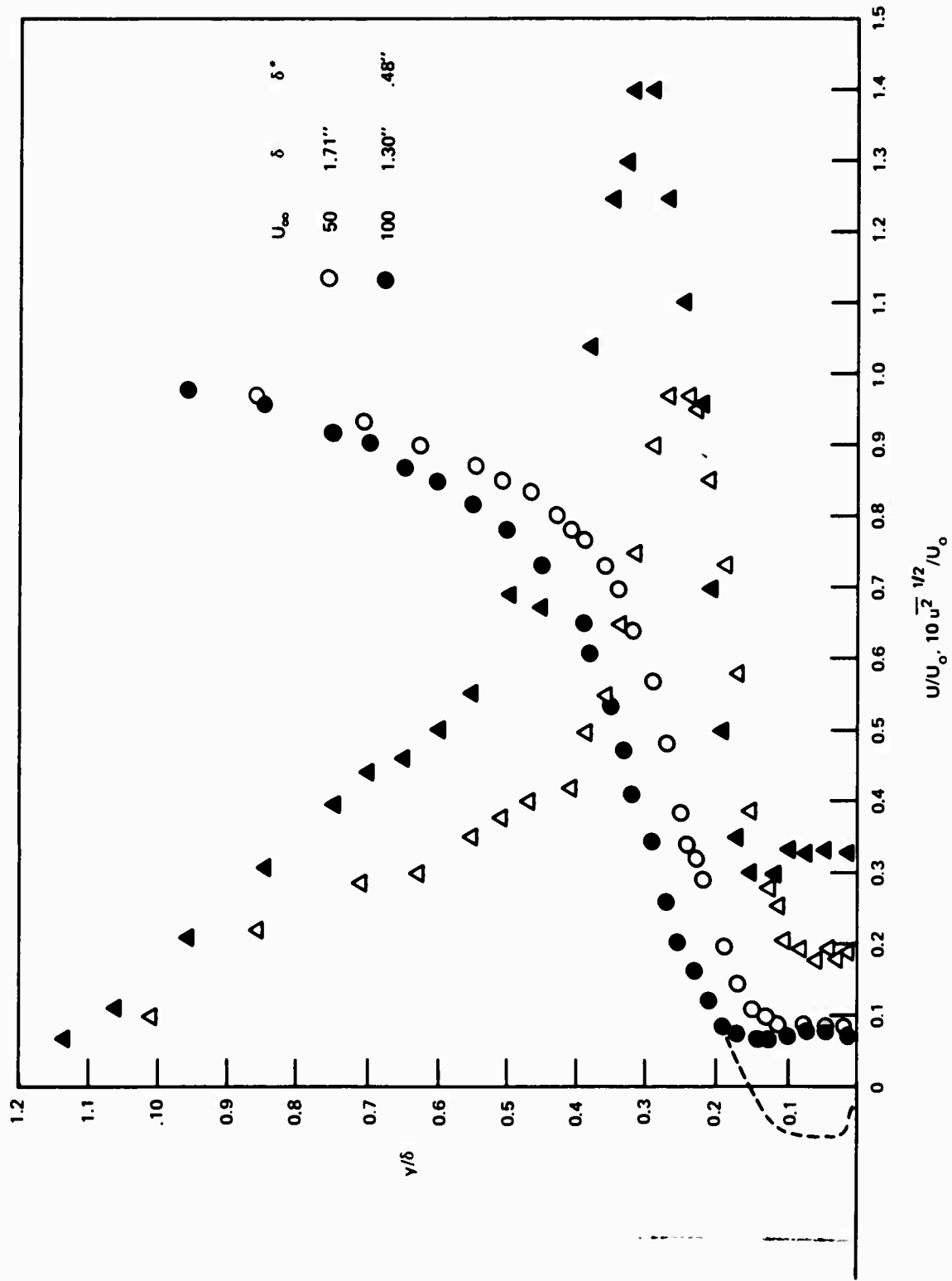


Figure 58 - Mean and Turbulent Velocity Profiles at Position G on 45-Degree--Rounded-Beveled Edge

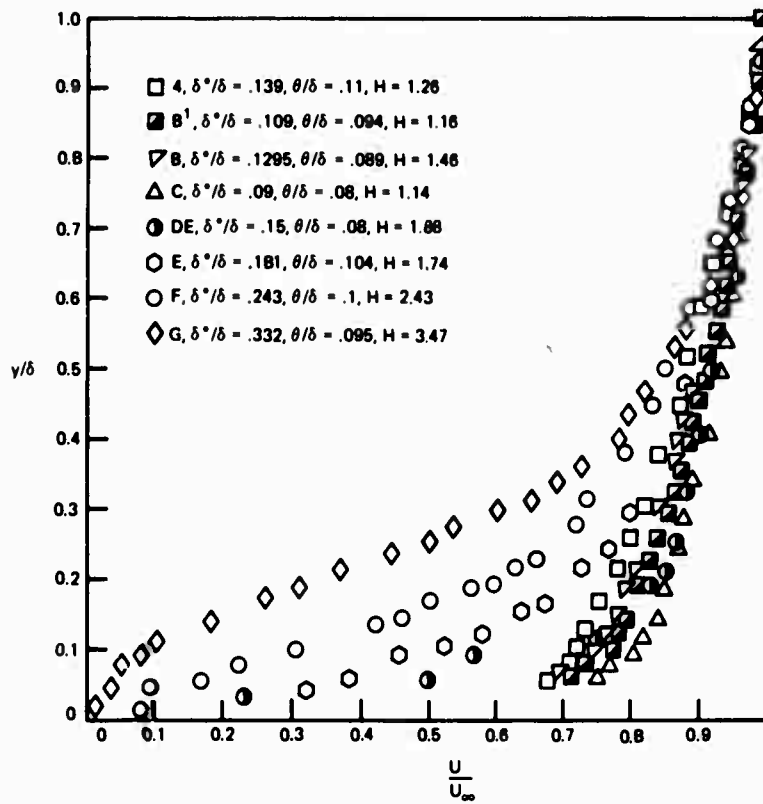


Figure 59 - Mean Velocity Profiles on 25-Degree--Rounded-Beveled Edge at $U_\infty = 100$ Feet per Second

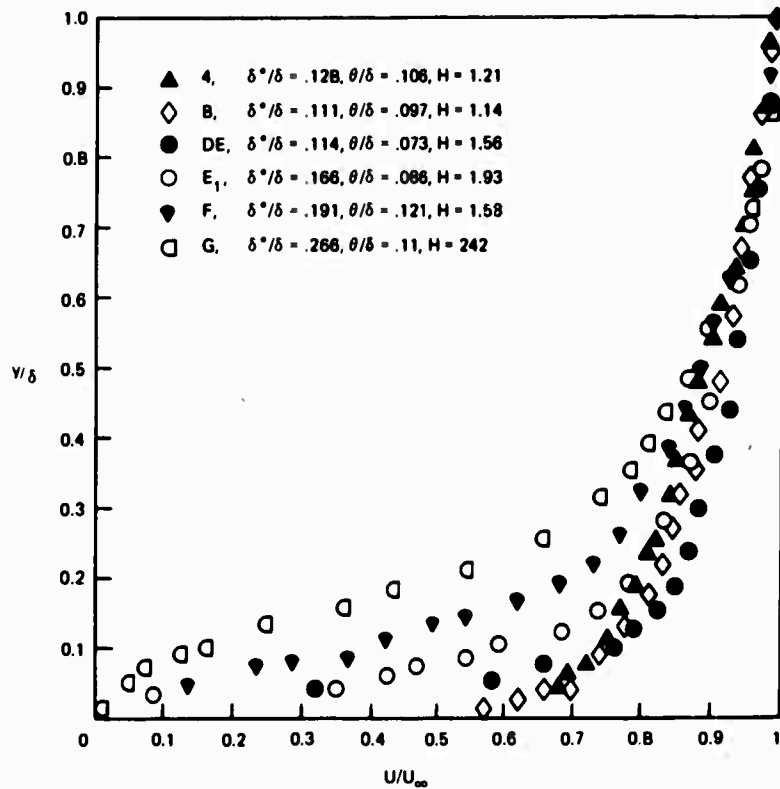


Figure 60 - Mean Velocity Profiles on 25-Degree--Rounded-Beveled Edge at $U_\infty = 60$ Feet per Second

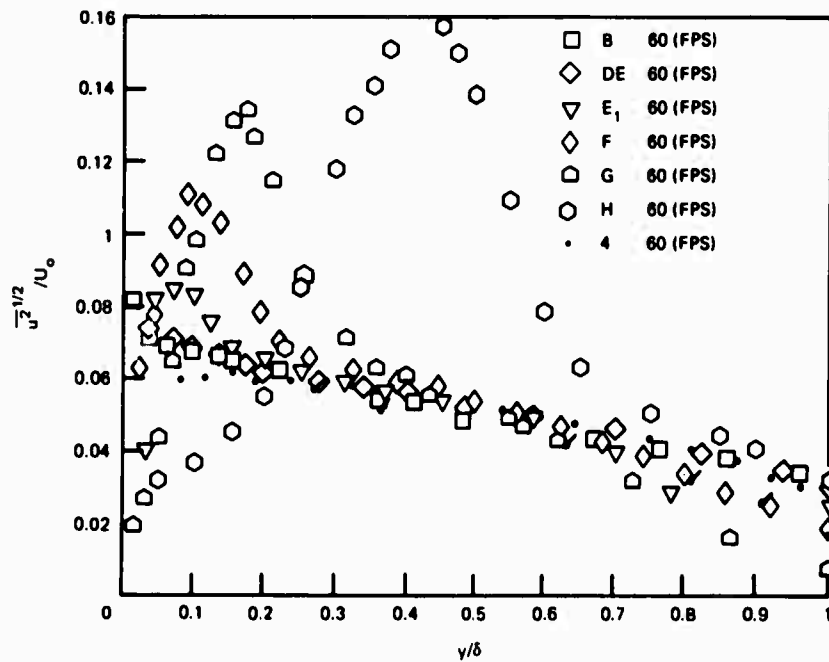


Figure 61 - Turbulence Intensity Profiles above 25-Degree--Rounded-Beveled Edge at $U_\infty = 60$ Feet per Second

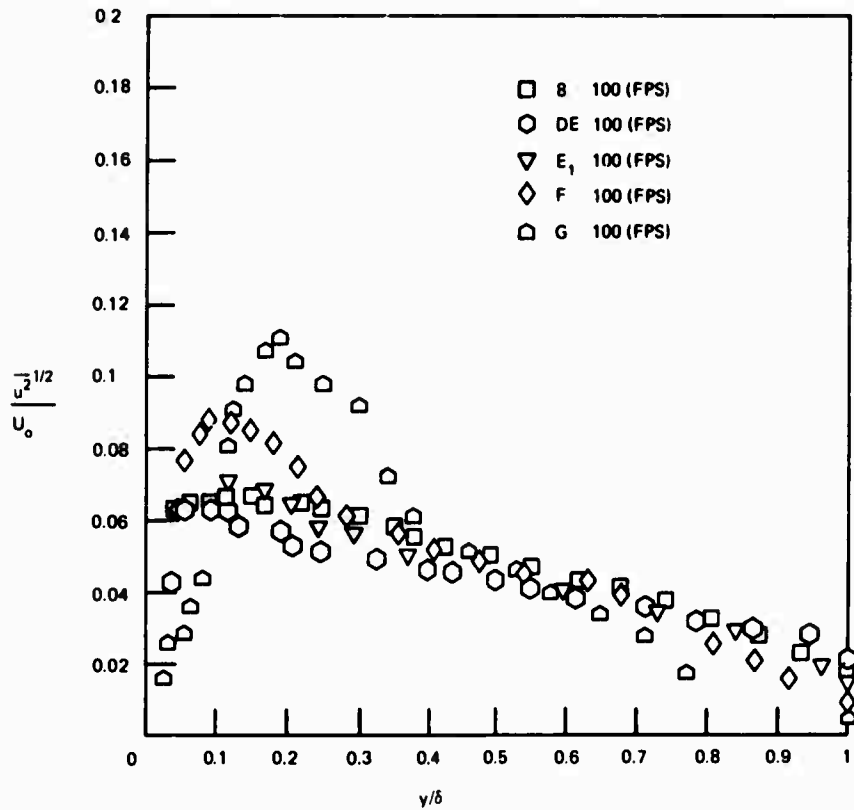


Figure 62 - Turbulence Intensity Profiles above 25-Degree--Rounded-Beveled Trailing Edge at $U_\infty = 100$ Feet per Second

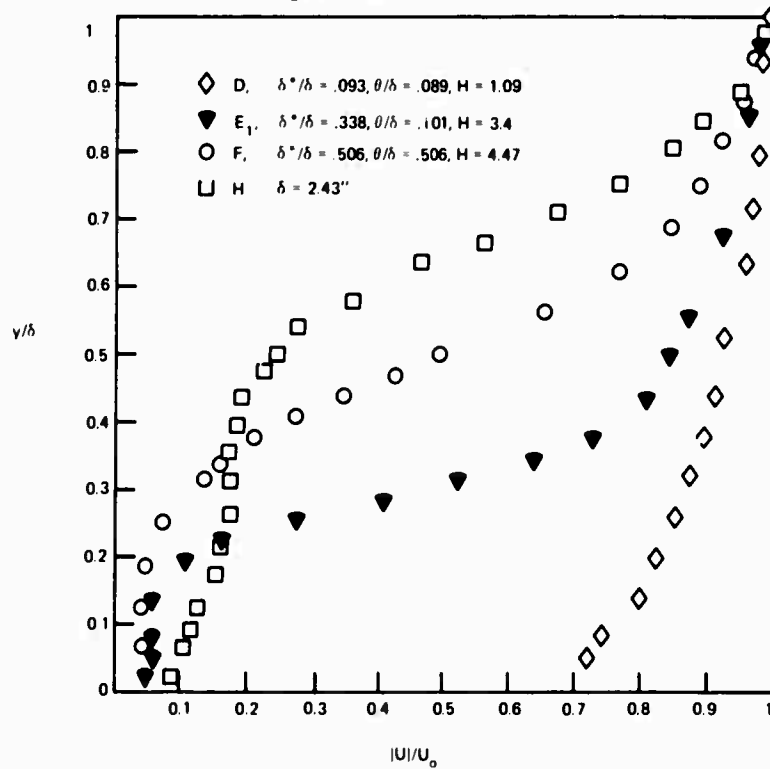


Figure 63 - Mean Velocity Profiles above 25-Degree Knuckle Edge at $U_\infty = 50$ Feet per Second

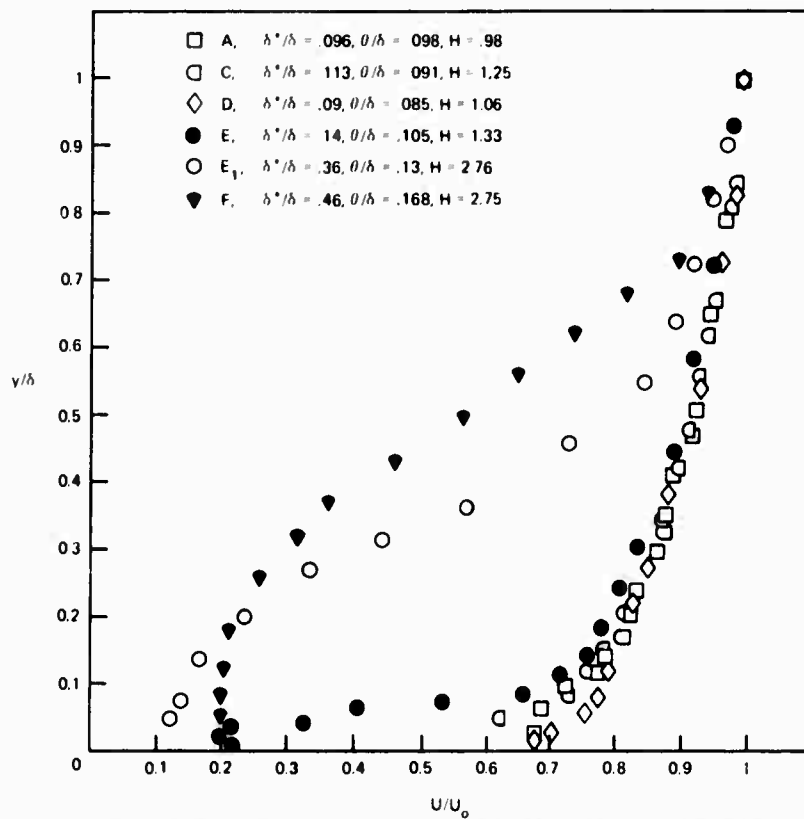


Figure 64 - Mean Velocity Profiles above 25-Degree Knuckle Edge at 100 Feet per Second

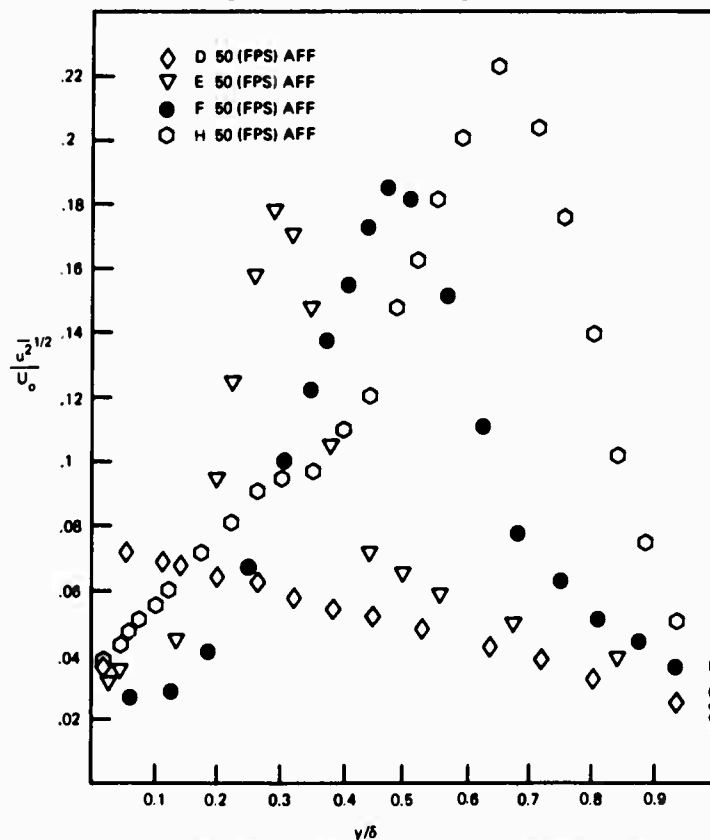


Figure 65 - Turbulence Intensity Profiles above 25-Degree--Knuckle-Trailing Edge at $U_0 = 50$ Feet per Second

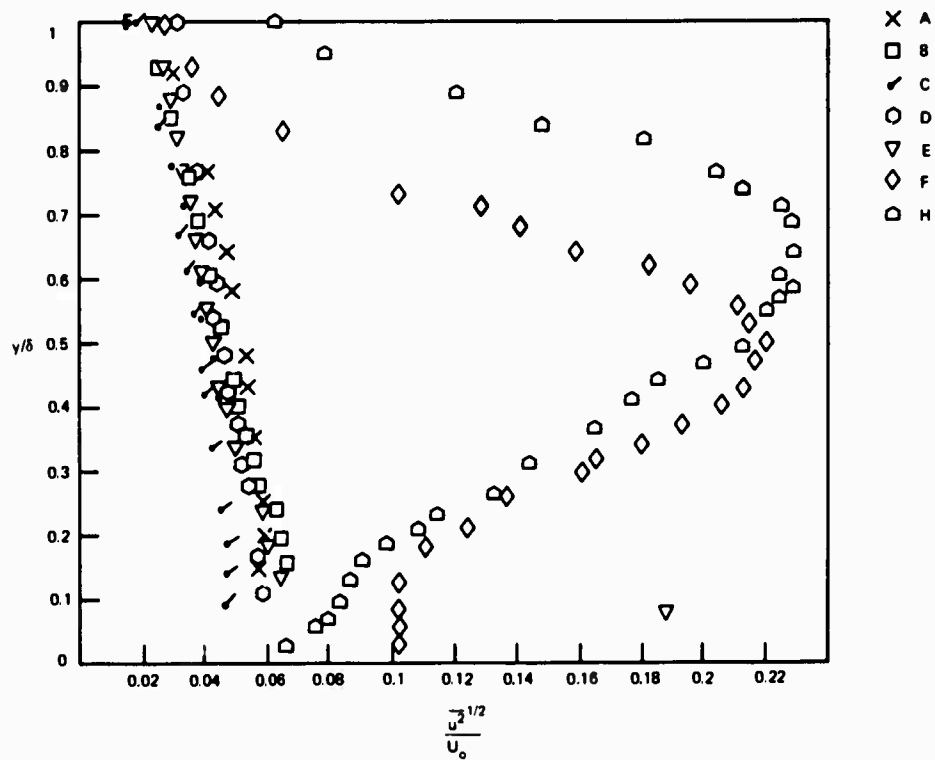


Figure 66 - Turbulence Intensity Profiles above 25-Degree--
Knuckle-Trailing Edge at $U_\infty = 100$ Feet per Second

APPENDIX C
STABILITY ANALYSIS OF WAKES

Several characteristics of the velocity and pressure fields of the trailing edges suggest that the flow may be examined using wave mechanics. The growth of coherent disturbances in the wakes are shown in Figures 16, 22, and 23 as well as the wavelike translation of velocity perturbations downstream show the plausibility of calculating the stability of disturbances. Similar efforts were undertaken by Hanson¹⁰ for turbulent wakes and by Crow and Champagne (1971)³⁸ for turbulent jets.

In a recent publication, calculations of the stability of wakes have been undertaken for laminar cases by Sato and Kuriki.²³ In their experiments, they characterized the downstream growth of perturbations in the streamline velocity in the laminar near wake of a flat plate. The observed amplification rates and wave speeds were closely approximated by a theory based on infinite Reynolds number. Use of the stability theory in cases involving turbulent flow has been attempted by Landahl³¹ who interpreted the effect of the turbulence on the stability as a forcing mechanism. He derived a nonhomogeneous Orr-Sommerfeld equation

$$(U(y)-c) (\phi''-k^2\phi) - U''\phi + \frac{i}{\alpha N_{Re}} (\phi^{IV} - 2k^2\phi'' + k^4\phi) = \hat{q}/\alpha k \quad (36)$$

for small disturbances in an incompressible shear flow of velocity distribution $U(y)$. The wavelike perturbation velocities have been assumed to be of the form

³⁸Crow, S.C. and F.H. Champagne, "Orderly Structure in Jet Turbulence," *Journal of Fluid Mechanics*, Vol. 48, pp. 547-591 (1971).

$$\hat{u} = \hat{u}(y) e^{i\alpha(x-ct)+i\beta z}$$

$$\hat{v} = \hat{v}(y) e^{i\alpha(x-ct)+i\beta z} \equiv -i\alpha\phi(y) e^{i\alpha(x-ct)-i\beta z} \quad (37)$$

$$\hat{w} = \hat{w}(y) e^{i\alpha(x-ct)+i\beta z}$$

where $k = \sqrt{\alpha^2 + \beta^2}$ is the wave number of the disturbance with wave speed $C_R = \omega/\alpha$. Velocity perturbations are assumed to be much less than $U(y)$. The function q involves all of the turbulence terms; the wavelike dynamics which are assumed to be given entirely by the left hand side of Equation (36) are linearly driven by \hat{q} . For the current discussion all velocities have been normalized on U_0 ; all distances, on a cross stream length scale,* e.g., b .

The solution of Equation (36) for finite Reynolds number is a difficult task and would have been outside the scope of the current study. However, Landahl had developed a complete numerical solution procedure (Landahl (1966)³⁹ and Kaplan (1964)⁴⁰) which was modified slightly for this study to be applicable to wake dynamics. The procedure utilizes an interactive digital computer program, originally developed for a time-sharing capability at Massachusetts Institute of Technology. At the Center the program language was translated to Fortran as well as updated to handle complex arithmetic more efficiently. Subroutines applicable to the wake stability were included in the program.

The computation routine utilizes a Runge-Kutta integration inward from a limiting coordinate in the undisturbed free stream, for instance,

* For discussions in this appendix all velocities are assumed to be referred to the local free-stream velocity U_0 .

³⁹Landahl, M.T., "A Time-Shared Program System for the Solution of the Stability Problem for Parallel Flows over Rigid and Flexible Surfaces," Massachusetts Institute of Technology Acoustics and Vibrations Laboratory Report 116-4 (Oct 1966).

⁴⁰Kaplan, R.E., "The Stability of Laminar Incompressible Boundary Layers in the Presence of Compliant Boundaries," Massachusetts Institute of Technology Acoustics and Vibrations Laboratory Report TR 116-1 (Jun 1964).

$y = y_1$ where $U(y_1) = 1$ to the wake centerline, $y = 0$ where $U(0) = U_m < U(y)$. The solution is controlled by a linear superposition of the two functions $\phi_1(y)$ and $\phi_3(y)$. The function $\phi_3(y)$ is the same as the viscous solution, and $\phi_1(y)$ is the inviscid, $N_{Re} \rightarrow \infty$, solution of the homogeneous Orr-Sommerfeld equation as discussed by Kaplan.⁴⁰ Boundary conditions are that

$$\phi_1(y) = e^{-k(y-y_1)} \text{ and } \phi_3 = e^{-\gamma(y-y_1)}, y \geq y_1$$

where

$$\gamma^2 = i\alpha N_{Re} (1-C) + k^2, R_e\{\gamma\} > 0$$

At the centerline, it is stipulated that the admittances of the disturbances behave as $\hat{v}/\hat{p} \rightarrow \infty$ and $\hat{u}/\hat{p} \equiv 0$; p is the pressure disturbance. That u/p vanishes is a statement of antisymmetry about $y = 0$. In the computation α is real, and the wave speed is complex, $C = C_R + iC_I$.

The mean velocity profile in the shear layer $U(y)$ is given the same expression as that used by Sato and Kuriki²³

$$U(y) = 1 - (1 - U_m) \exp[-P^2 y] \quad (38)$$

The cross wake length scale b is selected so that

$$U(b) = \frac{1+U_m}{2}$$

A series of sample profiles is shown in Figure 67; they roughly approximate those that were measured at $r_x = 0.1$ inch, and 1.25, 2, and 4 inches behind the 45-deg--rounded-beveled trailing edge with $U_\infty = 100$ feet per second. The fifth profile is given to indicate dependence on the factor P . An increasing value of P increases the slope $dU(y)/dy$, and it produces a more narrow wake. Table 4 lists a series of parameters which are descriptive of the profiles in Figure 67. The momentum thickness is

TABLE 4 - SHEAR-LAYER LENGTH AND FREQUENCY SCALES

U_m	P	$\frac{\theta}{2b}$	$\frac{y_f}{b}$	C_R	α_m	$\alpha_m \theta/b$	$\alpha_m y_f/b$	$\frac{\omega y_f}{U_o}$
-0.1	0.69	0.518	1.7	0.52	0.94	0.48	1.6	0.85
0	0.69	0.62	1.7	0.56	0.90	0.56	1.5	0.84
0.308	0.69	0.752	1.7	0.69	0.9	0.68	1.5	1.0
0.6	0.69	0.	1.7	0.63	-	-	-	-
0.22	1.20	0.572	1.3	0.69	1.1	0.63	1.42	0.95

based on the full wake $-\infty < y < \infty$, and y_f is the cross wake distance between points of vanishing curvature. The profile for which $P = 0.69$ and $U_m = 0.308$ also describes that of Sato and Kuriki.²³

Stability calculations were made by checking with the cases considered by Sato and Kuriki. Straight crested, unidirectional waves for which $\beta = 0$ were assumed for all calculations. Agreement between their measured and current calculated values of wave speed, amplification rates, and disturbance amplitude $u(y)$ were excellent. In the process of calculation, the stability diagram of Figure 68 was determined. The magnitude of the velocity disturbance can be written

$$|u| = u(y) \exp \left(\alpha \frac{C_I}{C_R} \frac{x}{b} \right) \quad (39)$$

thus for $C_I < 0$ the wake is stable to small disturbances. For Reynolds numbers greater than 8.4 this particular profile is unstable; for Reynolds numbers greater than 300, the variation of C_I with α appears to be independent of $N_{R_e} = \frac{U_o b}{\nu}$. For the profiles behind the 45-deg rounded edge, the Reynolds number based on b is 1.5×10^4 for $U_o \approx U_\infty = 50$ feet per second. In all of the cases calculated no effect of Reynolds number was observed for $N_{R_e} > 700$.

Figure 69 shows the calculated intensity eigenfunction $u(y)$, compared with the measured intensity at the position downstream of the 45-deg rounded trailing edge corresponding to $r_x = 1.25$ inch. The absolute amplitudes have no significance; the value $u(y)$ expresses the intensity eigenfunction corresponding to the designated velocity profile. Other calculations were performed for the series of profiles shown in Figure 67 at Reynolds numbers of approximately 4800. Calculated values of the spatial amplification rate, which is defined in Equation (39), are shown in Figure 70 for the profiles in Figure 67. The wave number α has been adjusted to be equivalent to the dimensionless frequency $\omega y_f / U_o$. The maximum amplification factor in each case occurred at a wave number, $\alpha_m = \omega_m b / C_R$, where C_R is the propagation phase velocity. Table 4 summarizes the dimensionless wave numbers and frequencies for each profile. The most similar dimensionless wave number for all cases is $\alpha_m y_f / b = \omega_m y_f / C_R$. The alternative from $\omega_m y_f / U_o$ is calculated because it would seem to have a more practical significance. The fact that these dimensionless frequencies are all near unity gives support to the frequency scaling adopted in Section 4. The alternative scale $\omega_m \theta / U_o$ can be seen by inspection of the table to be not a constant number over the range of profiles. The profile for which $U_m = 0.6$ is shown to be stable for all wave numbers. The correspondence of calculated values of C_R with the measured values of U_c / U_∞ along $y = y_L$ in Figure 24 is encouraging, and it raises a question about the validity of the high values of U_c near $r_x = 0.8$ inch.

Finally, we consider the spatial amplification of disturbances given by

$$|u(y)| = u_o \exp \left[\int_0^{x/b} \alpha \frac{C_I}{C_R} (x/b) d \left(\frac{x}{b} \right) \right] \quad (40)$$

The integral form of the amplification factor is made necessary by the fact that C_I / C_R is a function of x , i.e., $C_I / C_R (x/b)$. The form of the integral in Equation (40) reflects the assumption that the gradient

$\partial(C_I/C_R)/\partial(x/b)$ has not a strong influence in the growth process. Amplification factors evaluated at $\alpha C_R y_f/b = 0.9$ in Figure 70 for the profiles of Figure 67 are shown at the bottom of Figure 71. For $x/b > 6$ the disturbances are lightly damped, and in reality the wake should begin its decay process. The evaluation of Equation (40), assuming that $u_o = 0.04$, is shown at the top of Figure 71. Data along both $y = y_l$ and $y = y_u$ in Figure 23 are shown for comparison. It can be seen that the calculated growth rate is approximately half of that which was measured. A similar comparison was drawn in the case of Crow and Champagne³⁸ in the case of jet instability at high Reynolds number. Perhaps a breakdown in the linearized theory leading to the Orr-Sommerfeld equation is responsible for the underestimated amplification rates.

Also, a comparison of Figures 70 and 20 shows that although the dimensionless forms $\omega y_f/U_s$ or $\omega y_f/U_o$ (in the theoretical case we must accept $U_s = U_o$) align the peaks of the disturbances, their bandwidths are notably dissimilar. Thus, physically the amplification rates are higher, and the bandwidth of the amplification is more selective, than theory would indicate.

Landahl (1972)⁴¹ has considered the influences of large-amplitude disturbances on the generation of waves. The initial disturbance predictable by the linear theory is considered to have reached sufficient amplitude to initiate a second instability which in turn interacts with the first. This causes a complex breakdown in the wake structures which could give rise to the high-level, selectively-amplified disturbances which are experimentally observed. The alternative theoretical consideration by Abernathy and Kronauer²² examines the larger amplitude disturbances as being caused by a nonlinear interaction of the parallel shear layers in the wakes. These interactions culminate in the formation of distinct and localized regions of vorticity. The vorticity regions have a spatial organization that is similar to that observed in vortex streets. A complete theory of the overall development of coherent

⁴¹Landahl, M.T., "Wave Mechanics of Breakdown," Journal of Fluid Mechanics, Vol. 56, pp. 775-802 (1972).

wake disturbances would incorporate both the linear and the nonlinear behavior. The linear calculations as presented in this appendix would be expected to provide the growth rate and wavelength of a preferred, initially unstable disturbance. This disturbance would be an initial value for the nonlinear problem. The wavelength of the least stable linear disturbance corresponds to the calculated streamline separation of the vortices of the nonlinear theory of Abernathy and Kronauer.²² Their results can be interpreted in terms of our wave number α . That theory has shows a decreasing number of vorticity concentrations with increasing values of α ; for $\alpha = 0.88$, two oppositely phased vorticity regions are formed within a given wavelength. This value is very close to the values of α_m calculated by the linear theory of small disturbances as tabulated in Table 4. The equivalence indicates a consistence which makes matching the linear and nonlinear theories extremely attractive.

ACKNOWLEDGMENTS

An investigation of this scope required the cooperation of many individuals. In this regard, the author appreciates the assistance of L. Maga, G. Finkelstein, and R. Dwyer at various stages of the experimental work; of V. Ally for assistance in programing the stability calculations for the computer, and of C. Miglicco and J. Kolhafer for their cooperation in assembling experimental fixtures. Assistance of Prof. M. Landahl in the wake-stability analysis is especially appreciated.

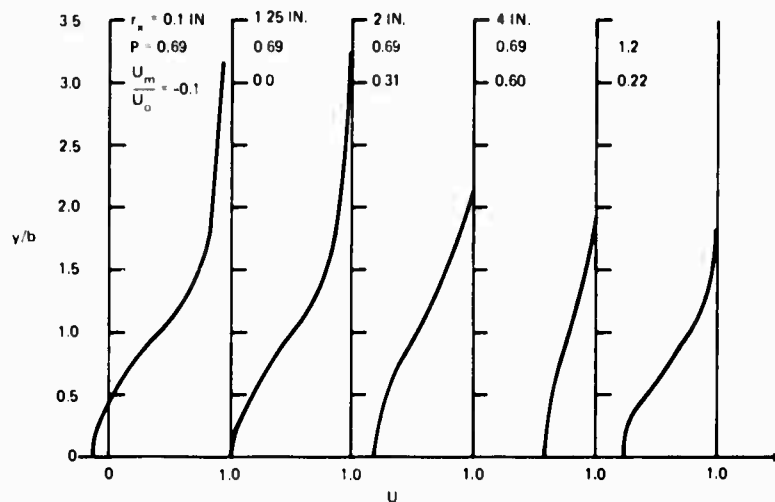


Figure 67 - Mean Velocity Profiles Which Approximate Those Measured behind the 45-Degree--Rounded-Trailing Edge at Various Positions r_x
 (Factor b is taken to be $b = 0.6$ inch; velocity is normalized on U_0 .)

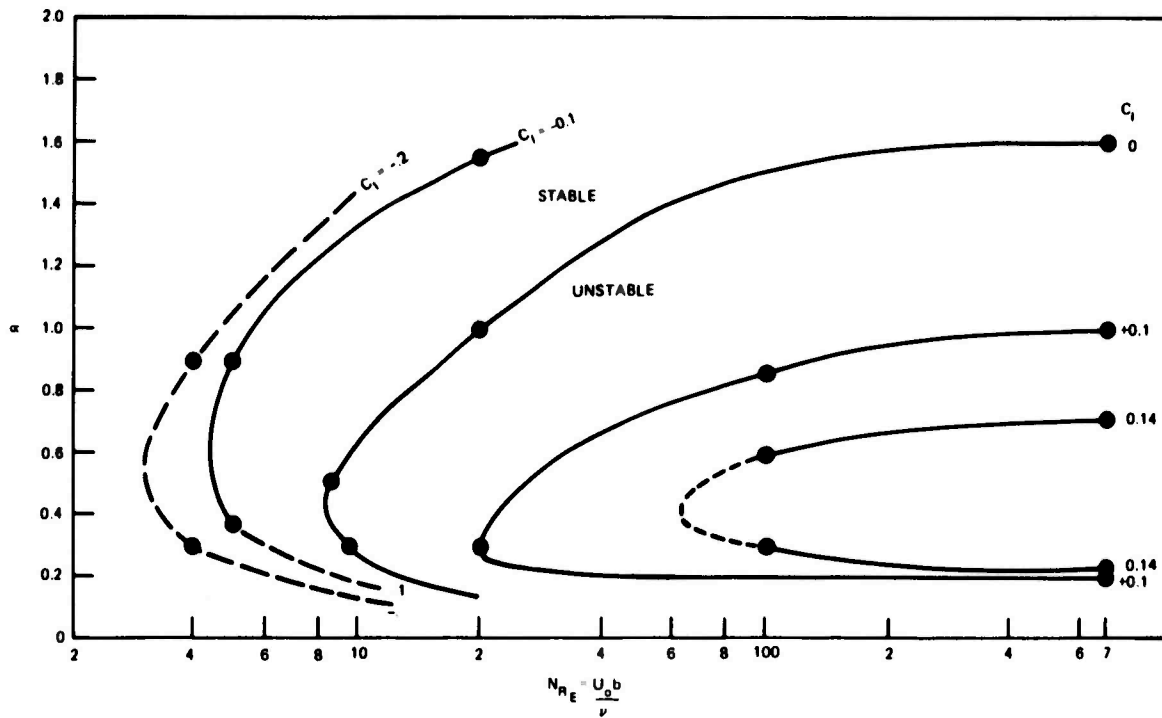


Figure 68 - Diagram of the Stability of a Two-Dimensional Wake: $P = 0.69$ and $U_m = 0.31$

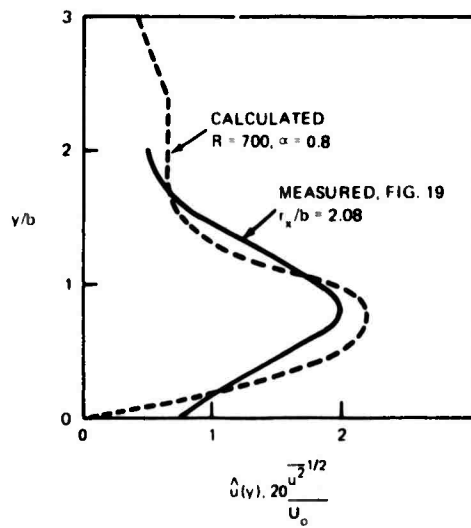


Figure 69 - Cross Wake Distribution of Streamline Velocity Perturbations for Velocity Profile $P = 0.69$ and $U_m = 0.31$

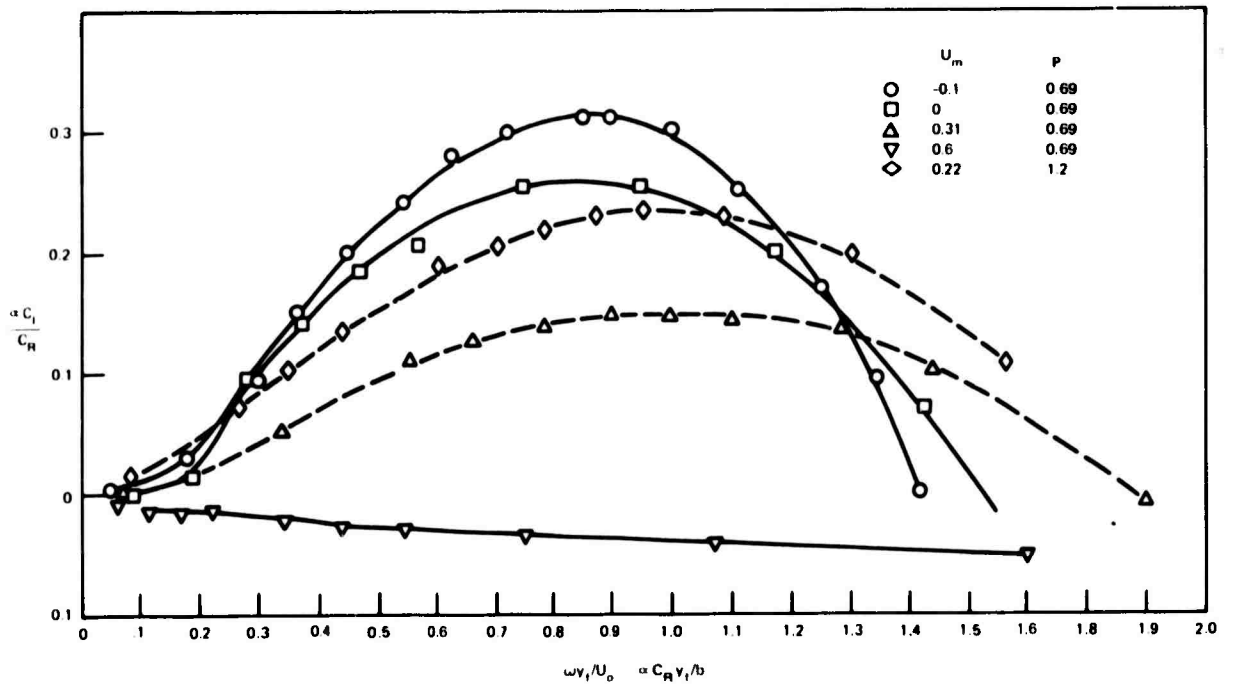


Figure 70 - Amplification Factors Computed for Velocity Profiles of Figure 67

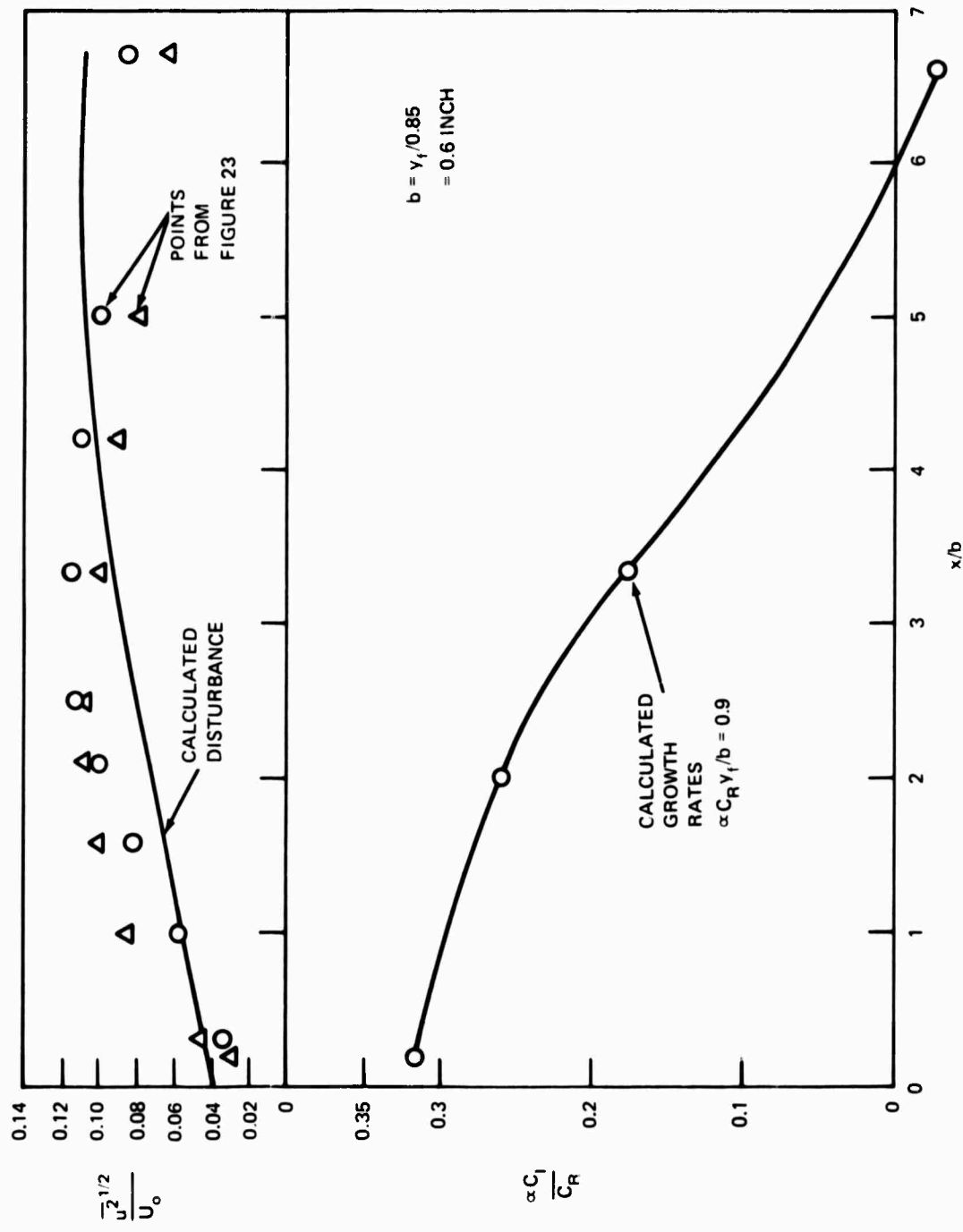


Figure 71 - Streamline Variations of Measured and Calculated Disturbances, u^2/U_0 , and Calculated Growth Rates, $\alpha C_I/C_R$, for Profiles of Figure 67

REFERENCES

1. Heskestad, G. and D.R. Olberts, "Influence of Trailing Edge Geometry on Hydraulic-Turbine-Blade Vibration Resulting from Vortex Excitation," Transactions of the American Society of Mechanical Engineers, Journal of Engineering For Power, Vol. 82, pp. 103-110 (Apr 1960).
2. Toebs, G.H. and P.S. Eagleson, "Hydroelastic Vibrations of Flat Plates Related to Trailing Edge Geometry," Transactions of the American Society of Mechanical Engineers, Journal of Basic Engineering, pp. 1-8 (1961).
3. Eagleson, P.S. et al., "Turbulence In the Early Wake of a Fixed Flat Plate," Massachusetts Institute of Technology Hydrodynamics Laboratory Report 46 (Feb 1961).
4. Greenway, M.E. and C.J. Wood, "The Effect of a Beveled Trailing Edge on Vortex Shedding and Vibration," Journal of Fluid Mechanics, Vol. 61, pp. 323-335 (1973).
5. Bearman, P.W., "Investigation of the Flow Behind a Two-Dimensional Model with a Blunt Trailing Edge and Fitted with Splitter Plates," Journal of Fluid Mechanics, Vol. 21, pp. 241-255 (1965).
6. Gongwer, G.A., "A Study of Vanes Singing In Water," Journal of Applied Mechanics, Vol. 19 (1952).
7. Bearman, P.W., "On Vortex Street Wakes," Journal of Fluid Mechanics, Vol. 28, pp. 625-641 (1967).
8. Roshko, A., "On the Drag and Shedding Frequency of Two-Dimensional Bluff Bodies," National Advisory Committee for Aeronautics Technical Note 3969 (1954).
9. Kronauer, R.E., "Predicting Eddy Frequency in Separated Wakes," Paper presented at the International Union of Theoretical and Applied Mathematics Symposium on Concentrated Vortex Motions in Fluids, University of Michigan, Ann Arbor, Mich. (6-11 Jul 1964); also, referred to by Bearman (1967).

10. Hanson, C.E., "An Investigation of the Near-Wake Properties Associated with Periodic Vortex Shedding from Airfoils," Massachusetts Institute of Technology Acoustics and Vibration Laboratory Report 76234-5 (1970).
11. DeMetz, F.C. and M.J. Casarella, "An Experimental Study of the Intermittent Properties of the Boundary Layer Pressure Field During Transition on a Flat Plate," NSRDC Report 4140 (Nov 1973).
12. Bowers, B.E., "The Anechoic Flow Facility--Aerodynamic Calibration and Evaluation (U)," NSRDC Evaluation Report SAD-48E-1942 (May 1973).
13. Chang, P.K., "Separation of Flow," Pergamon Press, Oxford, England (1970).
14. Schlichting, H., "Boundary Layer Theory," McGraw-Hill Fourth Edition, New York (1960).
15. Klebanoff, P.S., "Characteristics of Turbulence in a Boundary Layer with Zero Pressure Gradient," National Advisory Committee for Aeronautics Report 1247 (1955).
16. Blake, W.K., "Turbulent Boundary Layer Wall Pressure Fluctuations on Smooth and Rough Walls," Massachusetts Institute of Technology Acoustics and Vibration Laboratory Report 70208-1 (1969).
17. Perry, A.E. and P.N. Joubert, Journal of Fluid Mechanics, Vol. 17, p. 193 (1963).
18. Blake, W.K., "Turbulent Boundary-Layer Wall Pressure Fluctuations on Smooth and Rough Walls," Journal of Fluid Mechanics, Vol. 44, p. 1 (1970).
19. Corcos, G.M., "On the Resolution of Pressure in Turbulence," Journal of the Acoustical Society of America, Vol. 35, p. 192 (1963).
20. Bull, M.K., "Wall Pressure Fluctuations Associated with Subsonic Turbulent Boundary Layer Flow," Journal of Fluid Mechanics, Vol. 28, p. 719 (1967).

21. Schaefer, J.W. and S. Eskinazi, "An Analysis of the Vortex Street Generated in a Viscous Fluid," *Journal of Fluid Mechanics*, Vol. 6, p. 241 (1959).
22. Abernathy, F.H. and R.E. Kronauer, "The Formation of Vortex Streets," *Journal of Fluid Mechanics*, Vol. 13, pp. 1-20 (1962).
23. Sato, H. and K. Kuriki, "The Mechanism of Transition in the Wake of a Thin Flat Plate Placed Parallel to a Uniform Flow," *Journal of Fluid Mechanics*, Vol. 11, p. 321 (1961).
24. Favre, A.J. et al., "Space Time Double Correlations in a Turbulent Boundary Layer," *Journal of Fluid Mechanics*, Vol. 2, p. 313 (1957).
25. Favre, A.J. et al., "Further Space Space-Time Correlations of Velocity in a Turbulent Boundary Layer," *Journal of Fluid Mechanics*, Vol. 3, p. 344 (1957).
26. Bidwell, J.M., "Application of the von Kármán Momentum Theorem to Turbulent Boundary Layers," *National Advisory Committee for Aeronautics TM 2571* (1951).
27. Schloemer, H.H., "Effects of Pressure Gradients on Turbulent Wall Pressure Fluctuations," *Journal of the Acoustical Society of America*, Vol. 42, pp. 93-113 (1967).
28. Burton, T.E., "Wall Pressure Fluctuations at Smooth and Rough Walls Beneath a Turbulent Boundary Layer with Favorable Adverse Free-Stream Pressure Gradients," *Massachusetts Institute of Technology Acoustics and Vibration Laboratory Report 70208-9* (1973).
29. Chandiramani, K.L., "Integration of Wall Pressure Measurements Under a Turbulent Boundary Layer," *Bolt Beranek and Newman, Inc., Report 1310* (1965).
30. Corcos, G.M., "The Structure of the Turbulent Pressure Field in Boundary Layer Flows," *Journal of Fluid Mechanics*, Vol. 18, pp. 353-378 (1964).

31. Landahl, M.T., "A Wave-Guide Model for Turbulent Shear Flow," *Journal of Fluid Mechanics*, Vol. 29, pp. 441-459 (1967).
32. Willmarth, W.W. and E.F. Wooldridge, "Measurement of the Correlation Between the Fluctuating Velocities and the Fluctuating Pressures in a Thick Turbulent Boundary Layer," *Advisory Group for Aerospace Research and Development Report 456* (1963).
33. Burton, T.E., "On the Generation of Wall Pressure Fluctuations for Turbulent Boundary Layers over Rough Walls," *Massachusetts Institute of Technology Acoustics and Vibrations Laboratory Report 70208-4* (1971).
34. Kraichnan, R.H., "Pressure Fluctuations in Turbulent Flow over a Flat Plate," *Journal of the Acoustical Society of America*, Vol. 28, p. 378 (1956).
35. Coles, D., "The Law of the Wake in the Turbulent Boundary Layer," *Journal of Fluid Mechanics*, Vol. 1, pp. 191-226 (1956).
36. Cramer, H., "Mathematical Methods of Statistics," *Princeton University Press, Princeton, N.J.* (1945).
37. Frenkiel, F.M. and P.S. Klebanoff, "Higher Order Correlations in a Turbulent Field," *Physics of Fluids*, Vol. 10, p. 507 (1967).
38. Crow, S.C. and F.H. Champagne, "Orderly Structure in Jet Turbulence," *Journal of Fluid Mechanics*, Vol. 48, pp. 547-591 (1971).
39. Landahl, M.T., "A Time-Shared Program System for the Solution of the Stability Problem for Parallel Flows over Rigid and Flexible Surfaces," *Massachusetts Institute of Technology Acoustics and Vibrations Laboratory Report TR 116-1* (Jun 1964).
40. Kaplan, R.E., "The Stability of Laminar Incompressible Boundary Layers in the Presence of Compliant Boundaries," *Massachusetts Institute of Technology Acoustics and Vibrations Laboratory Report TR 116-1* (Jun 1964).
41. Landahl, M.T., "Wave Mechanics of Breakdown," *Journal of Fluid Mechanics*, Vol. 56, pp. 775-802 (1972).

INITIAL DISTRIBUTION

Copies		Copies	
2	ONR 1 Code 468, H.M. Fitzpatrick 1 Code 439, Dr. Perrone	1	American Univ Attn: Prof. Mark Harrison, Chairman Dept of Physics
3	NRL 1 Dr. Hansen 1 O.M. Griffin 1 R.A. Skop	3	California Institute of Technology 1 Dr. A.J. Acosta 1 Dr.F.R. Hama 1 Dr. A. Roshko
3	USNA 1 Dr. Bruce Johnson 1 Dr. S. Elder 1 Lib	1	Univ of California, Los Angeles Attn: Prof. W.C. Meecham Dept of Engineering
1	NAVPGSCOL, Monterey, Calif Attn: Dr. Targut Sarpkaya	2	Univ of California, San Diego 1 Prof. J.W. Miles Institute of Geophysics & Planetary Physics 1 T.T. Yeh
1	USNROTC & NAVADMINUMIT		
1	NAVWARCOL		
2	NAVSEA 1 SEA 037 1 SEA 0372 (Paladino)	2	Univ of Southern California, Los Angeles 1 Dr. J. Laufer, Dept Aero Space Engineering 1 Dr. R. Blackwelder
3	NUC, San Diego 1 Dr. A. Fabula 1 Dr. J. Hoyt 1 Mr. H. Patrick	3	Catholic Univ of America 1 Dr. F.A. Andrews 1 Dr. M. Casarella 1 Dr. R. Smith
3	NLONLAB NUSC 1 Dr. H. Bakewell 1 Dr. H. Schloemer 1 Dr. W. Strawderman	2	Georgia Institute of Technology 1 Dr. A.D. Pierce 1 Dr. A.W. Morris
1	NEWPORT, NUSC Attn: R.N. Brown	1	Harvard Univ Attn: Dr. R.E. Kronauer Div of Eng & Applied Physics
2	NAVSEC 1 SEC 6110 1 SEC 6148	1	Univ of Houston Attn: Dr. A.K.M.F. Hussain, Dept of Mech Eng.
1	National Bureau of Standards Attn: Mr. P.S. Klebanoff		
12	DDC		

Copies

- 1 Illinois Institute of Technology
Attn: M.V. Morkovin, Dept of Mechanical & Aerospace Engineering
- 1 McMaster Univ, Ontario, Canada
Attn: Dr. D.S. Weaver
- 7 MIT.
1 Dr. R.H. Lyon, Dept, Mech E
1 Dr. S. Crandall, Dept, Mech E
1 Dr. P. Leehey, Dept, NAME
1 Dr. Ira Dyer, Dept, NAME
1 Prof. P.M. Morse, Dept, Physics
1 Prof. K.U. Ingard, Dept, Physics
1 Prof. S. Widnall, Dept. Aeronautics and Astronautics
- 1 Univ of Michigan, Dept of Aeronautical & Astronautical Engineering
Attn: Prof. W.W. Willmarth
- 2 Univ of Minnesota
1 Prof. R. Plunkett
1 Prof. B. Lambert
- 1 St. Anthony Falls Hydraulic Lab, Univ of Minnesota
Attn: Dir. Mr. J.M. Killen
- 1 Montana State Univ
Attn: Dept of Aerospace & Mechanical Engineering
- 1 Univ of New Brunswick, Fredricton, N.B. Canada
Attn: Prof. H.G. Davies
- 2 Univ of Notre Dame
Engineering Sciences Dept
1 Dr. A.F. Strandhagen
1 Prof. A.A. Szewczyk

Copies

- 2 Ohio State Univ, Columbus, Ohio
1 Dr. Robert S. Brodkey
1 Dr. Harry C. Hershey
- 1 Oregon State Univ, Corvallis, Oregon
School of Engineering
Attn: Prof. Larry S. Slotta
- 6 ARL, Penn State Univ
1 Dr. B. Parkin
1 Dr. E.J. Skudrzyk
1 Dr. R. Arndt
1 Dr. R. Henderson
1 Dr. D. Thompson
1 Dr. J. Lumley
- 2 Royal Institute of Technology
Stockholm, Sweden
1 Prof. M.T. Landahl
1 Dr. F. Bark
- 1 Stanford Univ
Attn: Dr. S. Kline
- 3 Institute of Sound & Vibration Research, Univ of Southampton
Southampton, England
1 Dr. G.H. Koopmann
1 Dr. F.J. Fahey
1 Dr. P.E. Doak
- 1 Univ of Toronto, Canada
Attn: Dr. H. Ribner
- 2 SWRI
1 Dr. Wilfred Baker
1 Editor, Applied Res Review
- 2 SIT/DL
1 Dr. J. Breslin
1 Dr. R.J. Nickerson
- 1 Argonne National Lab.
Attn: H. Chung

Copies

1 Binary Systems Inc, L.I., N.Y.
Attn: Mr. S. Gardner

1 BHRA Fluid Engineering
Attn: Dr. Roger King

1 Bolt Beranek & Newman Inc.
Arlington, Va.
Attn: Dr. F. Jackson

9 Bolt Berarek & Newman Inc.
Cambridge, Mass.
1 Dr. N.A. Brown
1 Dr. D. Chase
1 Dr. P. Smith
1 Dr. K.L. Chandiramani
1 Dr. J. Barger
1 Mr. R. Hayden
1 Dr. P. Jameson
1 Dr. C.E. Hanson
1 Dr. R. Collier

1 Cambridge Acoustical Associates
Attn: Dr. M.C. Junger

1 Ecole Centiale De Lyon
Laboratoire de Mechanique des
Fluides, Ecully, France
Attn: G. Cornte-Bellot

1 Gen Applied Sciences Lab. Inc.
Westbury, L.I.,N.Y.
Attn: Dr. F. Lane

4 Electric Boat Div, General
Dynamics Corp
1 Mr. William Ezell
1 Mr. Michael Pakstys, Jr.
1 Dr. T. Graham
1 Mr. R. Gorman

1 Hydrospace Res Corp.
Attn: Lib

1 Tetrattech Inc.
Attn: Dr. D. Ross

Copies

1 Dr. Ewald G. Eichler
101 Trowbridge St
Cambridge, Ma. 02138

1 Dr. A.A. Hudimac
12100 Devilwood Dr.
Rockville, Md. 20854

CENTER DISTRIBUTION

Copies	Code
1	1505
1	154
3	1544
	1 M.L. Miller
	1 Dr. T. Brockett
3	1552
	1 Dr. T.T. Huang
	1 Dr. F.B. Peterson
1	19
1	1901
1	1902
1	1903
3	1926
	1 S.G. Solomon
	1 R. Tompkins
1	1932
1	1933
2	194
	1 F. Schloss
1	1941
29	1942
	1 Dr. F.C. DeMetz
	1 F.E. Geib
	1 L.J. Maga
	1 R.W. Brown
	1 B.E. Bowers
	1 Dr. A.J. Tucker
	1 P.J. Granum
	1 G. Wilson
	1 G. Finkelstein
20	Dr. W.K. Blake
3	1945
	1 Dr. M.L. Rumerman
	1 F.W. Desiderati

Copies Code

1	196
1	1962
2	1966
	1 Dr. Y. Liu
30	5211 Report Distribution
1	5221 Library (C)
1	5222 Library (A)

DTNSRDC ISSUES THREE TYPES OF REPORTS

(1) DTNSRDC REPORTS, A FORMAL SERIES PUBLISHING INFORMATION OF PERMANENT TECHNICAL VALUE, DESIGNATED BY A SERIAL REPORT NUMBER.

(2) DEPARTMENTAL REPORTS, A SEMIFORMAL SERIES, RECORDING INFORMATION OF A PRELIMINARY OR TEMPORARY NATURE, OR OF LIMITED INTEREST OR SIGNIFICANCE, CARRYING A DEPARTMENTAL ALPHANUMERIC IDENTIFICATION.

(3) TECHNICAL MEMORANDA, AN INFORMAL SERIES, USUALLY INTERNAL WORKING PAPERS OR DIRECT REPORTS TO SPONSORS, NUMBERED AS TM SERIES REPORTS; NOT FOR GENERAL DISTRIBUTION.